分类号__________　　　　　　　　　　　　　　　　　　　　　密　级__________

UDC__________　　　　　　　　　　　　　　　　　　　　　　单位编号__________

中国科学院研究生院
GRADUATE UNIVERSITY OF CHINESE ACADEMY OF SCIENCES

博士后论文

基于 WHIE-LBM 法暨并行 CPU-GPU 平台的同震广义电磁破坏机理研究

Hybird wave time-domain hypersingular integral equation-lattice Boltzmann method to earthquae fault slip problem in the coseismic process under multi temporal-spatial scales and coupled electromagnetothermoforce fields in parallel CPU-GPU system

博　　士　　后：朱伯靖

合　作　导　师：石耀霖院士

流动站（一级学科）：地球物理学

专业(二级学科)：固体地球物理学

研　究　方　向：计算地球动力学

研　究　期　限：2008.01－2010.09

中国科学院研究生院

2010 年 09 月

Hybird wave time-domain hypersingular integral equation-lattice Boltzmann method to earthquake fault slip problem in the coseismic process under multi temporal-spatial scales and coupled electromagnetothermoforce fields in parallel CPU-GPU system

By

BO-JING ZHU

(Prof YaoLin Shi, Supervisor)

Submitted in partial satisfaction of the requirements for the postdoctoral programme

in

SOLID GEOPHYSICS

in the

KEY LAB OF COMPUTATIONAL GEODYNAMICS

of the

COLLEGE OF SCIENCE, GRADUATE UNIVERSITY OF CHINESE ACADEMY OF SCIENCES

Beijing

17 Sep 2010-9-18

Approved

Taiyan Qin

Professor

Fracture Mechanics

Yaolin Shi

Professor

Geophysics and geodynamics

Wenke Sun

Professor

Geophysics and Geodesy

Tianyou Fan

Professor

Fracture Mechanics

Huai Zhang

Professor

Geodynamics and Mathematics

Jian Zhang

Professor

Geophysics and Geodynamics

Shoubiao Zhu

Professor

Geodynamics and Geomechanics

Han Li

Professor

Geophysics and Astronomy

答辩委员会主席：	孙文科	教授	中国科学院研究生院
答辩委员会成员：	范天佑	教授	北京理工大学理学院
	张 健	教授	中国科学院研究生院
	张 怀	教授	中国科学院研究生院
	秦太验	教授	中国农业大学理学院
	朱守彪	研究员	中国地震局地壳力学所
	李 菡	研究员	中国科学院天文台
	石耀霖	院士	中国科学院研究生院

独 创 性 声 明

本人声明所呈交的出站报告是我个人在合作导师指导下进行的研究工作及取得的研究成果。尽我所知，除了文中特别加以标注和致谢的地方外，报告中不包含其他人已经发表或撰写过的研究成果，也不包含为获得中国科学院研究生院或其它教育机构的博士后出站报告使用过的材料。与我一同工作的同志对本研究所做的任何贡献均已在报告中作了明确的说明并表示了谢意。

博士后签名：　　　　　　　　　　　　时间：　　　年　月　日

关于出站报告使用授权的说明

本人完全了解中国科学院研究生院有关保留、使用博士后出站报告的规定，即：学校有权保留送交报告的复印件和磁盘，允许报告被查阅和借阅，可以采用影印、缩印或扫描等复制手段保存、汇编报告。同意中国科学院研究生院可以用不同方式在不同媒体上发表、传播报告的全部或部分内容。

(保密的学位论文在解密后应遵守此协议)

博士后签名：　　　　　　　　　　　　时间：　　　年　月　日

合作导师签名：　　　　　　　　　　　时间：　　　年　月　日

基于 WHIE-LBM 暨并行 CPU-GPU 平台的同震广义电磁破坏机理研究

Hybird wave time-domain hypersingular integral equation-lattice Boltzmann method to earthquae fault slip problem in the coseismic process under multi temporal-spatial scales and coupled electromagnetothermoforce fields in parallel CPU-GPU system

博　士　后：朱伯靖 .

合 作 导 师：石耀霖院士 .

流动站（一级学科）：地球物理学 .

专业（二级学科）：固体地球物理学 .

研 究 方 向：计算地球动力学 .

研 究 期 限：2008.01－2010.09 .

中国科学院研究生院

2010 年 09 月

前言

波动时域超奇异积分法(WHIE)是分析三维断裂裂尖应力和位移间断的方法，格子玻尔兹曼法(LBM)是分析多孔介质流体问题的方法，两者结合可对流-固接触区破坏进行机理研究；并行 CPU 平台为大规模数值模拟提供了硬件支持, GPU 平台为其结果可视化提供了硬件支持，两者结合为应用 WHIE-LBM 解决复杂地球物理学问题提供了理论基础和数值模拟平台。

2007 年底，我有幸与石耀霖院士当面交流，谈到："能否把你博士期间磁电热弹多场耦合三维动态裂纹破坏研究，应用到地震破坏机理研究中来"；2008 年 1 月我进入中国科学院研究生院计算地球动力学重点实验室，在石老师指导下进行孕同震广义电磁破坏机理理论和数值模拟研究 。

期间开始接触计算地球动力学领域，对同震点源广义电磁破坏、考虑孔隙压（远、近场）同震点源广义电磁破坏、磁电热弹多场耦合三维界面任意多裂纹、多时空尺度渗流广义电磁驱动破坏破坏等问题进行研究，并把这些研究成果逐渐应用到实际地球物理学问题中（如：三维渗水层渗流过程、二维地表径流和渗流过程、多时空尺度水库渗流与断层库伦应力、通过实测地应变计算断层地应力等）；每当遇到困难或进入误区时，都是石老师的及时指点，使我迅速走出困境，每一点研究进展的取得都离不开导师的帮助和指导。作为一名普通博士研究生，能在博士后期间，如攻读博士学位一样，在科研上得到进一步深入、系统和全方面的训练和培养，使自己的科研素养在理论（Science）、应用(Technology)和工程(Engineering)三个方面都得到提高，是让我受益终生的事，也我一生中最幸运的事情！

三载时光，白驹过隙，出站之际，略抒感慨；感谢身边每个人，你们的激励，让我在科研上保持激情；你们的帮助，让我在科研上保持兴趣；你们的信任，让我遇到困难时能坚持下来 。

最后谨以此文献给教我做人、做事、做学问的导师石耀霖院士！您的悉心指导，让我人格成熟了许多，懂得了如何把握科研方向，取得了一些科研进展；也献给为我提供良好学习、生活和工作环境的中国科学院研究生院各位老师，特别是晓慧老师，您们的帮助，使我能在科研最困难和最紧张时能够坚持下来；同时献给为我提供科研经费支持的全国博士后基金委员会和国家自然科学基金委员会各位老师，您们的支持，使的科研活动能够正常进行下去 。

摘要

本报告总结了作者在中国科学院研究生院地球科学学院计算地球动力学实验室开展博士后研究工作期间，应用波动时域超奇异积分方程和格子波耳兹曼方法，在并行CPU及GPU平台上，对孕、同震过程中广义电磁破坏问题研究中获得的进展。研究工作包括。

1. 进一步发展了波动时域超奇异积分方程方法，把经典断裂力学理论与Coulomb-Navier-Mohr破坏理论、Anderson理论断层滑动理论相结合，建立了两者间关系，研究点源情形下同震广义电磁破坏机理。

2. 在上述工作基础上，应用相场法和超奇异积分方程方法，对考虑到断层孔隙渗流作用的同震广义流体驱动破坏问题进行研究，得到同震时刻近场及远场渗水层孔隙压力与地震P波、S波传播关系。

3. 应用混合波动时域超奇异积分方程和格子波耳兹曼方法，在并行CPU平台上，建立了磁电热力多场耦合的D3Q27模型，对高渗透率渗水层的广义流体驱动破坏问题进行研究；在并行CPU及GPU平台上，对同震时刻水库与地震断层相互作用进行研究。

关键词： 超奇异积分方程，格子波耳兹曼，CPU及GPU，同震广义电磁破坏机理，多时空尺度，多物理场耦合

Abstract

Based on the the Hybird wave time-domain hypersingular integral equation-lattice Boltzmann method, the earthquake fault slip problem in the coseismic process under multi temporal-spatial scales and coupled electromagnetothermoforce fields have been studyed under parallel CPU-GPU system, the main achievement progress include:

1. An extended hypersingular intergro-differential equation (E-HIDE) method for modeling the 3D interface crack problem in fully coupled electromagnetothermoelastic anisotropic multiphase composites under extended electro-magneto-thermo-elastic coupled loads through theoretical analysis and numerical simulations. Based on the extended boundary element method, the 3D interface crack problem is reduced to solving a set of E-HIDEs coupled with extended boundary integral equations, in which the unknown functions are the extended displacement discontinuities. Then, the behavior of the extended singular stress indices around the interface crack front terminating at the interface is analyzed by the extended main-part analysis. The extended stress intensity factors near the crack front are defined. In addition, a numerical method for a 3D interface crack problem subjected to extended loads is proposed, in which the extended displacement discontinuities are approximated by the product of basic density functions and polynomials. Finally, the radiation distribution of extended stress intensity factors at the interface crack surface are calculated, and the results are presented toward demonstrating the applicability of the proposed method.
2. A new and accurate way of theoretical and numerical description of the extended 3D fluid (electromagnetic and flow) driven crack progression in co-seismic slip under *P*- and *S*-waves was reported. First, based on the viscous fluid flow reciprocal work theorem, the hybrid hypersingular integral equation (HIE) method proposed by the author was defined by combined with the coupled extended wave time-domain HIE and the extended diffused interface phase field method. The general extended 3D fluid flow velocity wave solutions are obtained by the extended wave time-domains Green's function method. The 3D extended dynamic fluid driven crack modeling under fully coupled electromagnetothermoelastic *P*- and *S*-wave and flow field was established. Then, the problem is reduced to solving a set of extended hybrid HIEs coupled with nonlinear boundary domain integral equations, in which the unknown functions are the general extended flow velocity discontinuity waves. The behavior of the general extended singular stress indices around the crack front terminating is analyzed by hybrid time-domain

main-part analysis. The general extended singular pore stress waves (SPSWs) and the extended dynamic stress intensity factors (DSIFs) on the fluid driven crack surface are obtained from closed-form solutions. In addition, a numerical method for the problem is proposed, in which the extended velocity discontinuity waves are approximated by the product of time-domain density functions and polynomials. The extended DSIFs and general extended SPSWs are calculated, and the results are presented toward demonstrating the applicability of the proposed method.

3. Introduces a hybrid hypersingular integral equation – lattice Boltzmann method (HHIE–LBM) for analyzing extended 3D flow driven pore – crack networks problem in various porosity composites. First, the extended hybrid electronic – ionic, thermal, magnetic, electric and force coupled fields' pressure and velocity boundary conditions for HHIE–LBM model is established, and the closed form solutions of extended distribution functions are given. Second, an extended 3D flow driven pore – crack networks problem in various porosity composites is translated into a coupled of HHIE–LBM equations. Third, the extended dynamic stress intensity factors (EDSIFs) are calculated by using the parallel numerical technology and the visualization results are presented. Last, the relationship between the EDSIFs and the differential porosity are discussed, and several rules have been found, which can be utilized to understand the extended fluid flow mechanism in various porosity composites and analyze the extended fluid flow varying mechanism on coseismal slip.

Keywords: Hypersingular Integral equation; Lattice Boltzmann Method; Parallel CPU&GPU;Extended coseismic fault mechanisum; Multi temporal-spatial scales; Coupled electromagnetothermoforce fields.

目录

Chapter 1:Mixed-mode stress intensity factors of 3D interface crack in fully coupled electromagnetothermoelastic anisotropic multiphase composites

Abstract

This contribution presents a extended hypersingular intergro-differential equation (E-HIDE) method for modeling the 3D interface crack problem in fully coupled electromagnetothermoelastic anisotropic multiphase composites under extended electro-magneto-thermo-elastic coupled loads through theoretical analysis and numerical simulations. First, based on the extended boundary element method, the 3D interface crack problem is reduced to solving a set of E-HIDEs coupled with extended boundary integral equations, in which the unknown functions are the extended displacement discontinuities. Then, the behavior of the extended singular stress indices around the interface crack front terminating at the interface is analyzed by the extended main-part analysis. The extended stress intensity factors near the crack front are defined. In addition, a numerical method for a 3D interface crack problem subjected to extended loads is proposed, in which the extended displacement discontinuities are approximated by the product of basic density functions and polynomials. Finally, the radiation distribution of extended stress intensity factors at the interface crack surface are calculated, and the results are presented toward demonstrating the applicability of the proposed method.

Keywords: 3D interface crack; Boundary element method; Fully coupled electromagnetothermoelastic anisotropic multiphase composites; Hypersingular intergro-differential equation method; Extended stress intensity factors.

1. Introduction

The development of piezoelectric/piezomagnetic composites has its roots in the early work of (Davis, 1974, Jordan and Eringen, 1964a,b; Tinkham, 1974; Vandenboomgaard, et al., 1976a,b). Nowadays, electromagnetothermoelastic coupled multiphase composites (EMTE-CMCs) have wide range applications in science and engineering such as space planes, supersonic airplanes, rockets, missiles, nuclear fusion reactors and submarines. Fully coupled electromagnetothermoelastic anisotropic multiphase composites (FC-EMTE-AMCs) are special EMTE-CMCs consisting of two constituent parts whose composition change continuously along one direction. The microstructure is usually heterogeneous and the dominant failure mode is the crack initiation and propagation from the inclusions. The oscillation singularity as well as overlapping of crack surfaces near the crack tip makes it much more difficult exactly to solve the equations compared with the cases of the ordinary cracks in EMTE-CMCs.

In the field of common materials, using J_2 line integral and finite element method, Khandelwal and Chandra Kishen (Khandelwal and Chandra Kishen, 2008) predicted the stress intensity factors (SIFs) for 2D interface crack problem under arbitrary thermal loading in dissimilar materials. Pindra, et al., (Pindra, et al., 2008) studied the deformation of the front of a semi-infinite 3D interface quasistatically propagating crack problem in an infinite heterogenceous elastic body. Based on finite element method, the effect of interaction between an interfacial crack and a microcrack in ceramic/aluminum bi-materials is analyzed by Belhouari et al., (Belhouari, et al.).

In the field of multiphase composites, Singh, et al., (Singh, et al., 2008) analyzed 2D anti-plane permeable interface crack problem under combined out of plane mechanicals and in-plane electrical loads for two bonded dissimilar graded piezoelectric half-space, and obtained the relationship between SIFs and material parameters. With boundary element method, Zhao, et al., (Zhao, et al., 2008) studied arbitrary planer interface crack in 3D transversely isotropic magnetoelectroelastic bimaterials. Correa, et al.,(Correa, et al.) analyzed fibre-matrix interface crack growth in composites under transverse compression by boundary element method. With finite element method, Mankour, et al., (Mankour, et al.) analyzed the 2D interface crack between two dissimilar isotropic elastic materiasls (ceramic/metal). Using the integral transform, singular integral equation methods and the theory of residues, a 2D crack crossing the interface of functionally graded layered structure was studied analytically by Guo and Noda (Guo and Noda, 2008) , and the variations of the SIFs with nonhomogeneity constants are depicted when the crack moves from one layer into another layer.

However, relatively little work has been done on 3D interface crack problem in fully coupled electromagnetothermoelastic anisotropic multiphase composites. This seems to be due mainly to the present limitations on practical methods (such as accurate and efficient mathematical modeling) and on theoretical aspects (accurate 3D formulations of dislocation shielding and image force). These problems require a general and accurate theoretical method. The hypersingular integral method combined with the finite-part integral method (Zhu and Qin, 2007; Erdogan, 1978; Ioakimidis, 1982; Qin and Tang, 1993), provides an efficient method for analyzing this kind of 3D crack propagation problem.

In the present paper, based on the previous work (Zhu and Qin, 2008a,b; Zhu and Qin, 2007a,b), a extended hypersingular intergro-differential equation (E-HIDE) method for modeling 3D interface crack problem in FC-EMTE-AMCs under extended fully coupled loads (the mechanical load, the electrical load, the magnetic load and the thermal load) is proposed for the first time. First, based on the extended boundary element method and extended boundary conditions, the 3D interface crack problem in FC-EMTE-AMCs is reduced to solving a set of E-HIDEs coupled with extended boundary integral equations, in which the unknown functions are the general extended displacement discontinuities (the displacement discontinuity, the electric discontinuity, the magnetic discontinuity, and the thermal discontinuity). Then, the behavior of the general extended singular stress indices (the stress index, the electric density index, the magnetic density index, and the thermal density index) around the interface crack front terminating at the crack surface is analyzed by the extended main-part analysis method of E-HIDEs. The extended stress intensity factors (the stress intensity factors K_I , K_{II} and K_{III}, the electric intensity factor K_{IV} , the magnetic intensity factor K_V , and the thermal intensity factor K_{VI}) are thus defined. In addition, a numerical method of solving the E-HIDE for 3D interface crack in FC-EMTE-AMCs subjected to extended coupled loads is proposed, in which the extended displacement discontinuities are approximated by the product of the extended basic density functions and polynomials. Finally, the radiation distribution of extended stress intensity factors for fully coupled electromagnetoelastic fields at the interface crack surface are analyzed as functions of crack shape, spatial location and materials parameters. The relationship between extended stress intensity factors and the electro-magneto-thermo-elastic coupling effects is analyzed. The numerical results are then presented toward demonstrating the applicability of the proposed method.

2. Basic equations

The linear governing equations and constitutive relations (Aboudi, 2001; Perez-Aparicio and Sosa, 2004) can be expressed by tensor forms

$$\Sigma_{IJ,I} + f_J = 0 \tag{1}$$

In the present paper, summation from 1 to 3 over repeated lowercase, and of 1 to 6 in uppercase su bscripts is assumed, and a subscript comma denotes the partial differentiation with respect to the ex tended coordinates (i.e., $x_1, x_2, x_3, x_4, x_5, x_6$ or x, y, z, m, n, l).

In addition, the combined constitutive equation is written as

$$\Sigma_{IJ} = E_{IJKL} Z_{KL} \tag{2}$$

The definitions of E_{iJKl}, Z_{Kl}, Σ_{iJ} , f_J , C_{iJKl}, Π_{iJ} , U_K , σ_{ij} , D_i , B_i , ϑ_i , f_i , f_e , f_m , f_ϑ , c_{ijkl}, e_{lij} , d_{lij} , $\in_{il}$, g_{il} , μ_{il} , ι_{ij} , ς_{il} , η_{il} , λ_{ij} , u_i , ϕ , φ and Υ are given in the reference Zhu and Qin (Zhu and Qin, 2007a,b).

3. Hypersingular integral equation for an arbitrary 3D crack

Consider the FC-EMTE-AMCs containing a 3D stochastic crack as shown in Fig.1. A fixed global rectangular Cartesian system x_i (*i=1,2,3*) is chosen. Assume that the stochastic crack S $(S^+ \bigcup S^-)$ is subjected to remote the mechanical loads $p_j(P,Q)$, the electrical loads $q(P,Q)$, the magnetic loads $b(P,Q)$ and the thermal loads $\rho(P,Q)$, respectively. The local rectangular Cartesian system ξ_i are chosen, the stochastic crack is assumed to be in the $\xi_1 \xi_2^i$ plane and normal to the ξ_3 axis, the angle between the fixed global axis x_i and local Cartesian ξ_i is defined as $w_i(x_i, \xi_i)$.

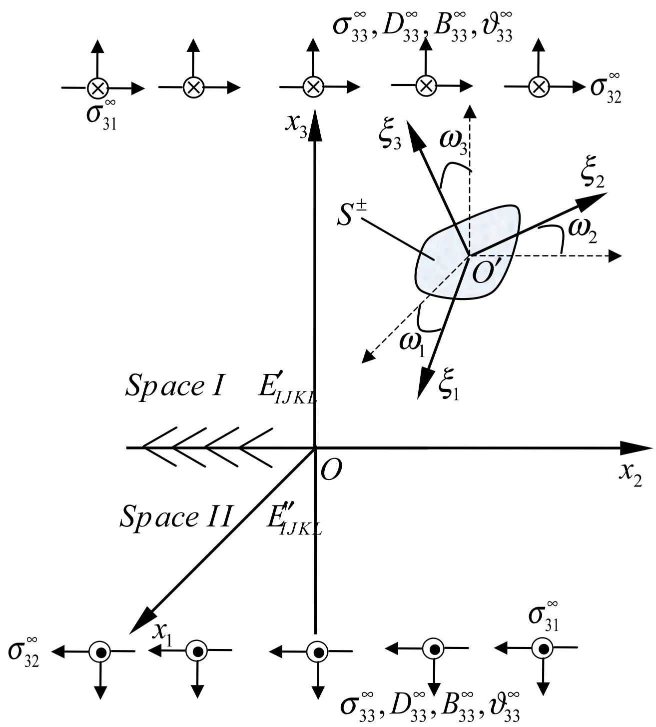

Fig.1.1. an arbitrary 3D crack in fully coupled electromagnetothermoelastic anisotropic multiphase composites

Using the EMTE form of the Somigliana identity, the extended displacement, $U_I(p)$, at interior point $p(x_1, x_2, x_3)$ is expressed as

$$U_I(p) = \int_{S^+} (U_{IJ}(p,q)T_J(q) - T_{IJ}(p,q)U_J(q))ds(q) - \int_{\Gamma} (T_{IJ}(p,q)U_J(q) + U_{IJ}(p,q)T_J(q))ds(q) + \int_{\Omega} U_{IJ}(p,q) f_J(q) ds(q) \quad (3)$$

where Ω is the domain occupied by the FC-EMTE-MCs, Γ is the external boundary, $T_J(q)$ is the extended elastic tractions on boundaries, $U_{IJ}(p,q)$ and $T_{IJ}(p,q)$ are the fundamental solutions. Using constitutive Equation (2), the corresponding extended stresses, Σ_{IJ}, is expressed as

$$\Sigma_{IJ}(p) = -\int_{S^+} S_{KiJ}(p,q)\tilde{U}_K(q)ds(q) + \int_{\Gamma} (D_{KiJ}(p,q)T_K(q) - S_{KiJ}(p,q)U_K(q))ds(q) + \int_{\Omega} D_{KiJ}(p,q) f_K(q) ds(q) \quad (4)$$

Let the source point p be taken to the boundary Γ and represented by P, applying the extended impermeable boundary conditions on the dislocations surfaces

$$D_3^+ = D_3^- = 0, B_3^+ = B_3^- = 0, \vartheta_{n3}^+ = \vartheta_3^- = 0 \quad (5)$$

where superscripts + and – denote the upper and lower dislocation surface, respectively. The hypersingular integral equations can be obtained as

$$\oint_{S^+} \left(\frac{c_{44}^2 D_0 s_0^2 (\delta_{\bar{\alpha}\bar{\beta}} - 3r_{,\bar{\alpha}} r_{,\bar{\beta}}) + (\delta_{\alpha\beta} - 3r_{,\alpha} r_{,\beta}) \sum_{i=1}^{5} \rho_i^2 t_i^2}{r^3} \hat{K}\, \tilde{u}_\beta + \frac{3r_{,\alpha} \sum_{i=1}^{5} \lambda_{33} s_i^2 t_i}{r^4} \tilde{u}_6) \right) ds = -p_\alpha \quad (6)$$

$$\oint_{S^+}\left(\frac{r_{,\alpha}\sum_{i=1}^{5}A_i^{\Upsilon}t_i^2\rho_i^1}{r^2}\tilde{u}_\alpha+\frac{\sum_{n=3}^{5}\sum_{i=1}^{5}\rho_i^m t_i^t}{r^3}\tilde{u}_n+\frac{3\lambda_{3\alpha}r_{,\alpha}\sum_{i=1}^{5}s_i^2\lambda_i^{\vartheta}\rho_i^m}{r^4}\tilde{u}_6\right)ds=-p_m \tag{7}$$

$$\oint_{S^+}\left(\frac{(\delta_{\alpha\beta}-3r_{,\alpha}r_{,\beta})\sum_{i=1}^{5}A_i^{\Upsilon}\lambda_{3\beta}t_i^2}{r^2}\tilde{u}_\beta+\frac{3\lambda_{3\alpha}r_{,\alpha}\sum_{i=1}^{5}A_i^{\Upsilon}s_i^2\lambda_i^{\vartheta}\lambda_{33}\rho_i^6}{r^4}\tilde{u}_6\right)ds=-p_6 \tag{8}$$

where p_i , $p_4(q)$, $p_5(b)$ and $p_5(\rho)$ can obtained from the solution for the loads of the solids...

4. Hypersingular intergro-differential equations for 3D interface crack

When $w_i(x_i,\xi_i)=0$ and $\xi_3(O')=0$, the crack is located in the interface of FC-EMTE-MCs , and the crack type is become a interface crack, as shown in Fig.2.

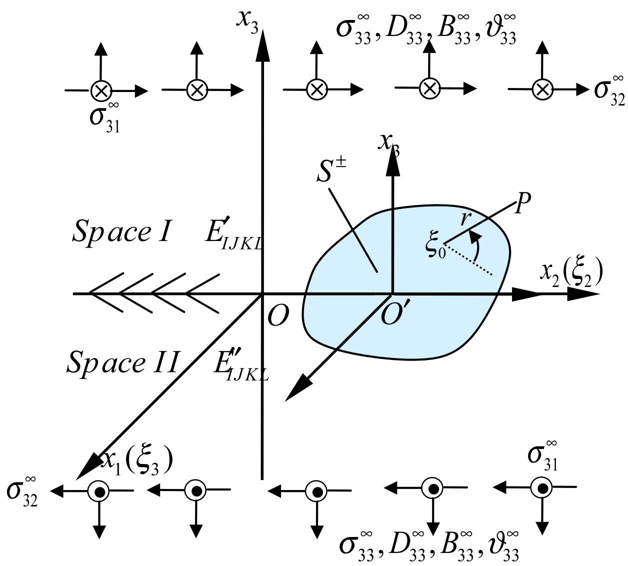

Fig.1.2. an arbitrary 3D interface crack in fully coupled electromagnetothermoelastic anisotropic multiphase composites

Using the Eq. (4) and boundary conditions Eq.(5), the hypersingular intergro-differential equations for 3D interface crack for FC-EMTE-MCs can be reduced to

$$\sum_{i=1}^{5}\rho_i^2t_i^2\sum_{m=3}^{6}\tilde{u}_{m,1}+\oint_{S^+}\left(\frac{c_{44}^2D_0s_0^2(\delta_{\bar{\alpha}\bar{\beta}}-3r_{,\bar{\alpha}}r_{,\bar{\beta}})+(\delta_{\alpha\beta}-3r_{,\alpha}r_{,\beta})\sum_{i=1}^{5}\rho_i^2t_i^2}{r^3}\hat{K}\,\tilde{u}_\beta+\frac{3r_{,\alpha}\sum_{i=1}^{5}\lambda_{33}s_i^2t_i}{r^4}\tilde{u}_6)\right)ds+\int_{S^+}K_{\alpha i}\tilde{u}_i\,ds=-p_\alpha \tag{9}$$

$$\sum_{n=3}^{5}\sum_{i=1}^{5}\rho_i^m t_i^t\sum_{m=3}^{6}\tilde{u}_{m,2}+\oint_{S^+}\left(\frac{r_{,\alpha}\sum_{i=1}^{5}A_i^{\Upsilon}t_i^2\rho_i^1}{r^2}\tilde{u}_\alpha+\frac{\sum_{n=3}^{5}\sum_{i=1}^{5}\rho_i^m t_i^t}{r^3}\tilde{u}_n+\frac{3\lambda_{3\alpha}r_{,\alpha}\sum_{i=1}^{5}s_i^2\lambda_i^{\vartheta}\rho_i^m}{r^4}\tilde{u}_6\right)ds+\int_{S^+}K_{mi}\tilde{u}_i\,ds=-p_m \tag{10}$$

$$\sum_{i=1}^{5}A_i^{\Upsilon}\lambda_{3\beta}t_i^2\tilde{u}_{\alpha,\alpha}+\oint_{S^+}\left(\frac{(\delta_{\alpha\beta}-3r_{,\alpha}r_{,\beta})\sum_{i=1}^{5}A_i^{\Upsilon}\lambda_{3\beta}t_i^2}{r^2}\tilde{u}_\beta+\frac{3\lambda_{3\alpha}r_{,\alpha}\sum_{i=1}^{5}A_i^{\Upsilon}s_i^2\lambda_i^{\vartheta}\lambda_{33}\rho_i^6}{r^4}\tilde{u}_6\right)ds+\int_{S^+}K_{6i}\tilde{u}_i\,ds=-p_6 \tag{11}$$

5. Extended singularity and extended stress intensity factors near the crack front

In the interest of investigating the singularity of the crack front, consider a local coordinate system defined as $x_2\ x_3$, in which the x_1-axis is the tangent line of the crack front at point q_0, the x_2-axis is the internal normal line of the crack plane, and the x_3-axis is the normal of the crack. Then the extended incremental displacement discontinuities gradient of the crack surface near a crack front point q_0 can be expressed as

$$U_K(q) = g_K(q_0)\xi_2^{\lambda_K} \qquad 0 < Re(\lambda_K) < 1 \tag{12}$$

where $g_k(q_0)$ is non-zero complex constant related to point q_0, and λ_k are represents the singular indices at the crack front. Consider a small semi-circle domain S_ε on the dislocation surface that includes point q_0. Using the main-part analytical method given by(Zhu and Qin, 2007a,b; Qin and Tang, 1993), the singular indices are obtained as

$$\lambda_1 = \frac{1}{2} + i\frac{1}{2\pi}\ln\left(\frac{\bar{\mu}_1 + \bar{\kappa}_1\bar{\mu}_2}{\bar{\mu}_2 + \bar{\kappa}_2\bar{\mu}_1}\right) \qquad \lambda_2 = \frac{1}{2} \qquad \lambda_n = \frac{1}{2} - i\frac{1}{2\pi}\ln\left(\frac{\bar{\mu}_1 + \bar{\kappa}_1\bar{\mu}_2}{\bar{\mu}_2 + \bar{\kappa}_2\bar{\mu}_1}\right) \qquad n = 3,4,5,6 \tag{13}$$

where $\bar{\kappa}_\alpha = 3 - 4\bar{v}_\alpha$, $\bar{\mu}_\alpha$, $\bar{v}_\alpha$ are equivalent shear module and equivalent Poisson's ratio, respectively. The extended stress intensity factors are defined as

$$K = K_1 + iK_2 = \lim_{r\to 0}\sqrt{2}[r^{\lambda_1}\sigma_{33}(r,\theta) + ir^{\lambda_2}\sigma_{31}(r,\theta)]\Big|_{\theta=0} \tag{14}$$

$$K_3 = \lim_{r\to 0}\sqrt{2}r^{\lambda_3}\sigma_{32}(r,\theta)\Big|_{\theta=0} \tag{15}$$

$$K_4 = \lim_{r\to 0}\sqrt{2}r^{\lambda_4}D_3(r,\theta)\Big|_{\theta=0} \tag{16}$$

$$K_5 = \lim_{r\to 0}\sqrt{2}r^{\lambda_5}B_3(r,\theta)\Big|_{\theta=0} \tag{17}$$

$$K_6 = \lim_{r\to 0}\sqrt{2}r^{\lambda_6}\vartheta_3(r,\theta)\Big|_{\theta=0} \tag{18}$$

where r is the distance from point p to the dislocation front point q_0.

6. Numerical method

In the procedure outlined above, the main bulk of the numerical work lies in the evaluation of the Eqs.(9-11). As we known, the most difficult parts are the hypersingular integral for those parts will decided the accurate of the numerical results. Note that the kernel functions K_{ij} are of Gauss-Chebyshev type and may be relative easily be evaluated. The extended displacement discontinuities unknown functions can be written as

$$\tilde{U}_I(\xi_1,\xi_2) = F_I(\xi_1,\xi_2)\xi_2^{\lambda_I}W_I(\xi_1,\xi_2) \tag{19}$$

where $F_I(\xi_1,\xi_2)$ can be defined as follows

$$F_1(\xi_1,\xi_2) = \sum_{\alpha=1}^{2}(1+\bar{\kappa}_\alpha)\sin\left(\bar{\varepsilon}\ln\left((a-\xi_1)(a+\xi_1)^{-1}\right)\right)\left(4\bar{\mu}_\alpha\cosh(\pi\bar{\varepsilon})\right)^{-1}\sqrt{(a^2-\xi_1^2)(b^2-\xi_2^2)} \tag{20}$$

$$F_2(\xi_1,\xi_2) = \sum_{\alpha=1}^{2}(1+\bar{\kappa}_\alpha)\sin\left(\bar{\varepsilon}\ln\left((b-\xi_2)(b+\xi_2)^{-1}\right)\right)\left(4\bar{\mu}_\alpha\cosh(\pi\bar{\varepsilon})\right)^{-1}\sqrt{(a^2-\xi_1^2)(b^2-\xi_2^2)} \tag{21}$$

$$F_m(\xi_1,\xi_2)=\sum_{\alpha=1}^{2}(1+\bar{\kappa}_\alpha)\cos\left(\bar{\varepsilon}\ln\left((a-\xi_1)(a+\xi_1)^{-1}\right)\right)\cos\left(\bar{\varepsilon}\ln\left((b-\xi_2)(b+\xi_2)^{-1}\right)\right)$$
$$\times\left(4\bar{\mu}_\alpha\cosh(\pi\bar{\varepsilon})\right)^{-1}\sqrt{(a^2-\xi_1^2)(b^2-\xi_2^2)}\quad m=3,4,5,6 \tag{22}$$

and $W_I(\xi_1,\xi_2)=\sum_{m=0}^{M}\sum_{n=0}^{N}a_{Imn}\xi_1^m\xi_2^n$, a_{Imn} are unknown constants. Substituting Eq.(19) into Eqs.(9-11), a set of algebraic equations for unknown a_{Imn} can be obtained

$$\sum_{m=0}^{M}\sum_{n=0}^{N}a_{Ish}I_{IJsh}=-p_J(x_1,x) \tag{23}$$

The non-dimensional extended stress intensity factors of the 3D interface crack front $F_{I,\lambda}$ are defined as

$$F_{,\lambda_\alpha}=F_{1,\lambda_1}+F_{2,\lambda_2}=K_{1,\lambda_1}/\sigma_{33}(r,\theta)b^{1-\lambda_1}+i\sigma_{31}(r,\theta)/\sigma_{31}(r,\theta)b^{1-\lambda_2} \tag{24}$$

$$F_{3,\lambda_3}=K_{3,\lambda_3}/\sigma_{32}(r,\theta)b^{1-\lambda_3} \tag{25}$$

7. Numerical results and discussion

In this section, the numerical results and discussions described in this paper are used in analyzing 3D interface rectangle crack problem under fully coupled electromagnetothermoelastic fields. The non-dimensional independent material constants are listed in Tab.1 in the reference Zhu and Qin (Zhu and Qin, 2007a). Consider a 3D rectangular interface crack subjected to the mechanical loads σ_{3i}^{∞}, the electric loads D_{33}^{∞} and the magnetic loads B_{33}^{∞} in infinity.

7.1 Convergence of numerical solutions

In the case of crack shape ratio is b/a=1, the collocation points are $KK=LL=20\times20$, the stress intensity factors F_{i,λ_i} at crack surface as a function of coordinate x_1/a (x_2/b) are shown in Tab.1 and compared with those given by (Qin and Noda, 2003; Wang and noda, 2001; Zhu and Qin, 2007a). Due to the symmetry, only the numerical results of stress intensity factors F_{i,λ_i} for $x_1/a\geq0$ ($-1\leq x_1/a\leq1$) and $x_2/b\geq0$ ($-1\leq x_2/b\leq1$) are given. The simulated results show that F_{i,λ_i} on $x_2=\pm b$ ($x_1=\pm a$) side decrease with increasing x_1/a (x_2/b) when $-1\leq x_1/a\leq0$ ($-1\leq x_2/b\leq0$), but increase with increasing x_1/a (x_2/b) when $0\leq x_1/a\leq1$ ($0\leq x_2/b\leq1$). F_{i,λ_i} reach a maximum value when $x_1/a=0$ ($x_2/b=0$), and F_{i,λ_i} reach a minimum value when $x_1=\pm a$ ($x_2=\pm b$).

Table.1.1. Convergence of SIFs F_{i,λ_i} for $\bar{\varepsilon}=0$ and $b/a=1$ at $x_2=\pm b$ ($x_1=\pm a$), $KK=LL=20\times 20$, $M=N=13\times 13$

x_1/a (x_2/b)	0/11	2/11	3/11	4/11	5/11	6/11	7/11	8/11	9/11	10/11
F_{I,λ_1} (Zhu and Qin, 2007)	0.7536	0.7464	0.7374	0.7244	0.7067	0.6829	0.6512	0.6092	0.5503	0.4493
F_{I,λ_1} (Qin and Noda, 2003)	0.7534	0.7462	0.7379	0.7255	0.7072	0.6821	0.6497	0.6090	0.5521	0.4464
F_{I,λ_1} (Wang and noda, 2001)	0.7534	0.7465	0.7376	0.7245	0.7066	0.6828	0.6512	0.6086	0.5492	0.4536
F_{II,λ_2} (Zhu and Qin, 2007)	0.8781	0.8710	0.8617	0.8479	0.8290	0.8039	0.7700	0.7232	0.6576	0.5541
F_{III,λ_3} (Zhu and Qin, 2007)	0.9903	0.9809	0.9686	0.8506	0.9263	0.8944	0.8526	.07978	.07240	0.6020

In the case of $\bar{\varepsilon}=0.02$, the numerical results of dimensionless stress intensity factors with increasing the polynomial exponents are given in Tab.2 for different number of collocation points, It is shown that the results are convergent, and the collocation point number 20 × 20 and the polynomial exponents M=N=13 are enough for satisfied result precision in this case.

In general, too large polynomial exponents can't give reliable results. The polynomial exponents M, N depend on the collocation point number. For the polynomial exponents M=N=15, the results of the collocation point number 20 × 20 are not good, but the ones of the collocation point number 30 × 30 are satisfied.

Table.1.2. Convergence of SIFs F_{i,λ_i} for $\bar{\varepsilon}=0.02$ and $b/a=1$ at $x_2=\pm b$ ($x_1=\pm a$), $KK=LL=20\times 20$

x_1/a	(x_2/b)	0/11	2/11	3/11	4/11	5/11	6/11	7/11	8/11	9/11	10/11
F_{I,λ_1}	m=n=13	0.7536	0.7467	0.7377	0.7246	0.7066	0.6829	0.6521	0.6105	0.5496	0.4405
	m=n=11	0.7532	0.7463	0.7373	0.7242	0.7062	0.6825	0.6518	0.6102	0.5493	0.4403
	m=n=9	0.7539	0.7470	0.7380	0.7249	0.7069	0.6832	0.6524	0.6107	0.5498	0.4407
F_{II,λ_2}	m=n=13	0.0121	0.0119	0.0117	0.0114	0.0110	0.0105	0.0099	0.0089	0.0077	0.0059
	m=n=11	0.0120	0.0119	0.0117	0.0114	0.0110	0.0105	0.0098	0.0089	0.0077	0.0058
	m=n=9	0.0118	0.0117	0.0114	0.0112	0.0108	0.0103	0.0096	0.0087	0.0076	0.0057
F_{III,λ_3} (×100)	m=n=13	0.0000	0.1998	0.3097	0.4096	0.5095	0.6293	0.7492	0.8891	1.0489	1.1987
	m=n=11	0.0000	0.1998	0.3097	0.4096	0.5194	0.6393	0.7592	0.9090	1.0589	1.1987
	m=n=9	0.0000	0.2098	0.3097	0.4196	0.5294	0.6493	0.7892	0.9390	1.0888	1.1987

7.2 Varying with the material parameter

When material parameter $\bar{\varepsilon}$ changed, it is the case of a 3D surface crack in two different materials interface. Now the polynomial exponents are taken as M=N=13, and the collocation point number is 20 × 20. Figs 3 and 4 give the stress intensity factors F_{I,λ_1} and F_{II,λ_2} as a function of x_1/a and $\bar{\varepsilon}$ for different ratios of b/a. When crack shape b/a fixed, F_{I,λ_1} increase as the $\bar{\varepsilon}$ increases, while F_{II,λ_2} decrease with increasing $\bar{\varepsilon}$ .this is the important results for interface crack on FC-EMTE-MCs interface.

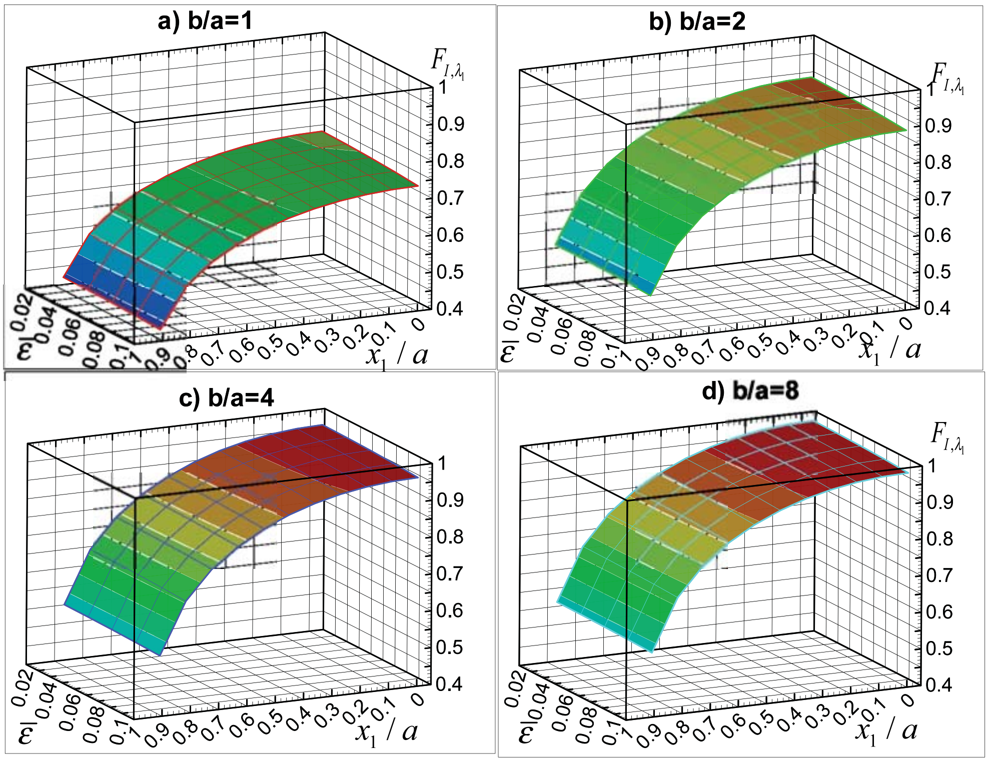

Fig.1.3. Dimensionless stress intensity factor F_{I,λ_1} **varying with** $x_1/a,\bar{\varepsilon}$ **and b/a (** $M=N=13, KK=LL=20\times 20$ **)**

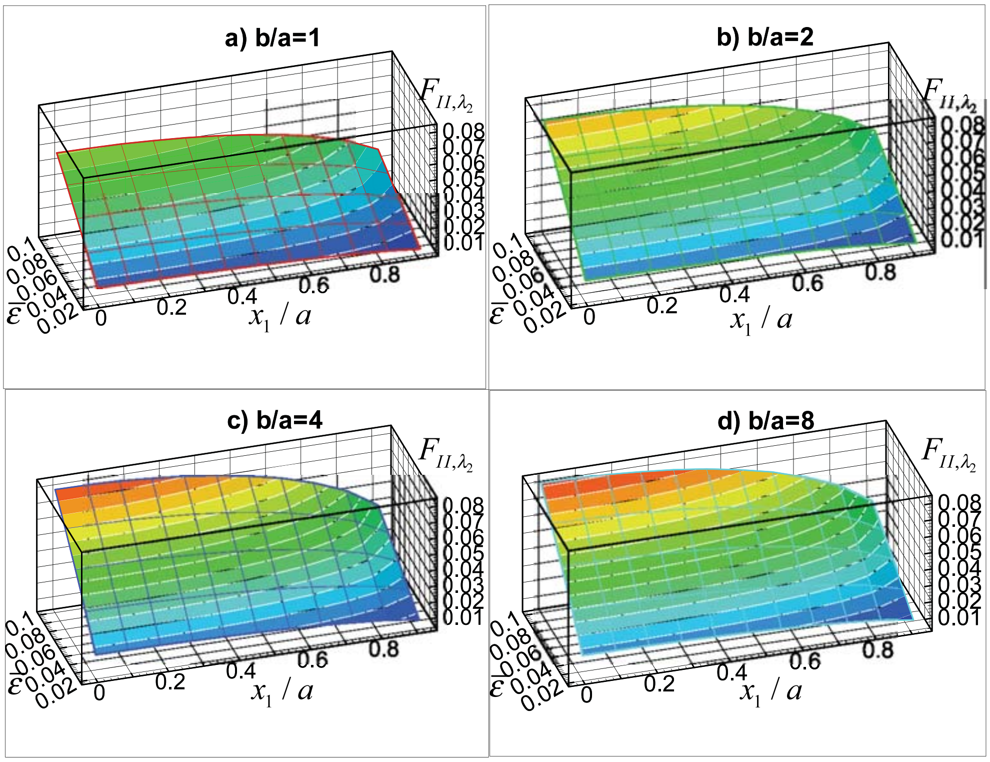

Fig.1.4. Dimensionless stress intensity factor F_{II,λ_2} **varying with** $x_1/a,\bar{\varepsilon}$ **and b/a (** $M=N=13, KK=LL=20\times 20$ **)**

7.3 Comparison with the 2D cases

As we discussed in the previous work, we know when crack shape ratio b/a=8, it is the case of a 2D surface crack in two different materials interface. Now the polynomial exponents are taken as M=N=13, and the collocation point number is 20 × 20. Tab. 3 gives the stress intensity factor F_{i,λ_i} for different $\overline{\varepsilon}$ when b/a=8.

Table1..3. F_{I,λ_1} , $F^*_{II,\lambda_2}=F_{II,\lambda_2}\times 10$, $F^*_{III,\lambda_3}=F_{III\lambda_3}\times 100$ F_{IIII} **for** $b/a=8$ **at** $x_2=\pm b$ ($x_1=\pm a$), $M=N=13$, $KK=LL=20\times 20$

$\overline{\varepsilon}$	F_{i,λ_i}	0/11	2/11	3/11	4/11	5/11	6/11	7/11	8/11	9/11	10/11
0.02	F_{I,λ_1}	0.9958	0.9866	0.9747	0.9574	0.9336	0.9024	0.8616	0.8067	0.7262	0.5820
	F^*_{II,λ_2}	0.1747	0.1728	0.1696	0.1658	0.1600	0.1524	0.1428	0.1294	0.1122	0.0848
	F^*_{III,λ_3}	0.0000	0.0890	0.1334	0.1773	0.2205	0.2622	0.3013	0.3350	0.3507	0.3576
0.04	F_{I,λ_1}	0.9949	0.9857	0.9738	0.9565	0.9327	0.9016	0.8609	0.8060	0.7255	0.5815
	F^*_{II,λ_2}	0.3459	0.3421	0.3358	0.3282	0.3168	0.3017	0.2828	0.2562	0.2222	0.1679
	F^*_{III,λ_3}	0.0000	0.1738	0.2604	0.3461	0.4305	0.5121	0.5886	0.6549	0.6870	0.6995
0.06	F_{I,λ_1}	0.9931	0.9840	0.9721	0.9548	0.9311	0.8999	0.8593	0.8045	0.7242	0.5804
	F^*_{II,λ_2}	0.5104	0.5049	0.4955	0.4844	0.4676	0.4452	0.4173	0.3782	0.3279	0.2478
	F^*_{III,λ_3}	0.0000	0.2505	0.3751	0.4989	0.6206	0.7384	0.8494	0.9458	0.9958	1.0112
0.08	F_{I,λ_1}	0.9902	0.9811	0.9692	0.9520	0.9283	0.8973	0.8568	0.8022	0.7221	0.5787
	F^*_{II,λ_2}	0.6667	0.6594	0.6472	0.6326	0.6107	0.5815	0.5450	0.4939	0.4282	0.3236
	F^*_{III,λ_3}	0.0000	0.3160	0.4735	0.6297	0.7836	0.9327	1.0731	1.1964	1.2658	1.2821
0.1	F_{I,λ_1}	0.9858	0.9768	0.9650	0.9479	0.9243	0.8934	0.8531	0.7987	0.7190	0.5762
	F^*_{II,λ_2}	0.8119	0.8030	0.7882	0.7704	0.7437	0.7082	0.6637	0.6015	0.5215	0.3941
	F^*_{III,λ_3}	0.0000	0.3689	0.5527	0.7354	0.9154	1.0900	1.2557	1.4013	1.4927	1.5053

To analyze the 2D interface crack more clearly, Figs. 5 and 6 give the stress intensity factor as a function of x_1/a and b/a for different $\overline{\varepsilon}$. From Figs.5 and 6 we observe that the stress intensity factors F_{I,λ_1} and F_{II,λ_1} increases with the increase of b/a for fixed value of $\overline{\varepsilon}$.

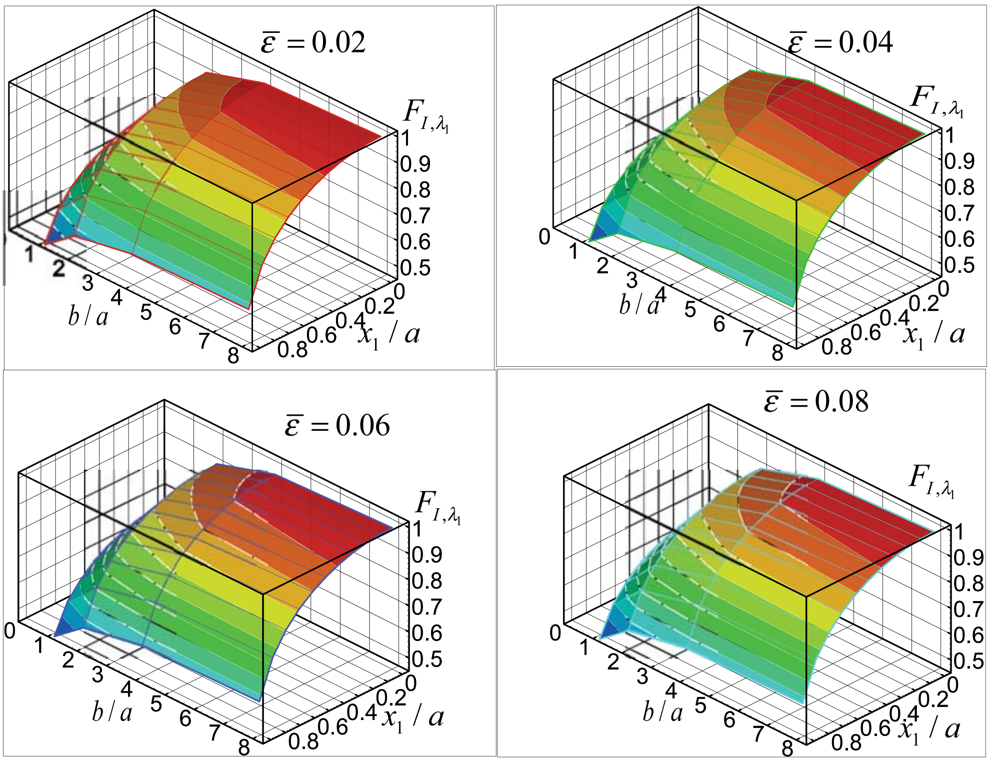

Fig.1.5. Dimensionless stress intensity factor F_{I,λ_1} varying with x_1/a and b/a ($M=N=13, K=L=20\times 20$)

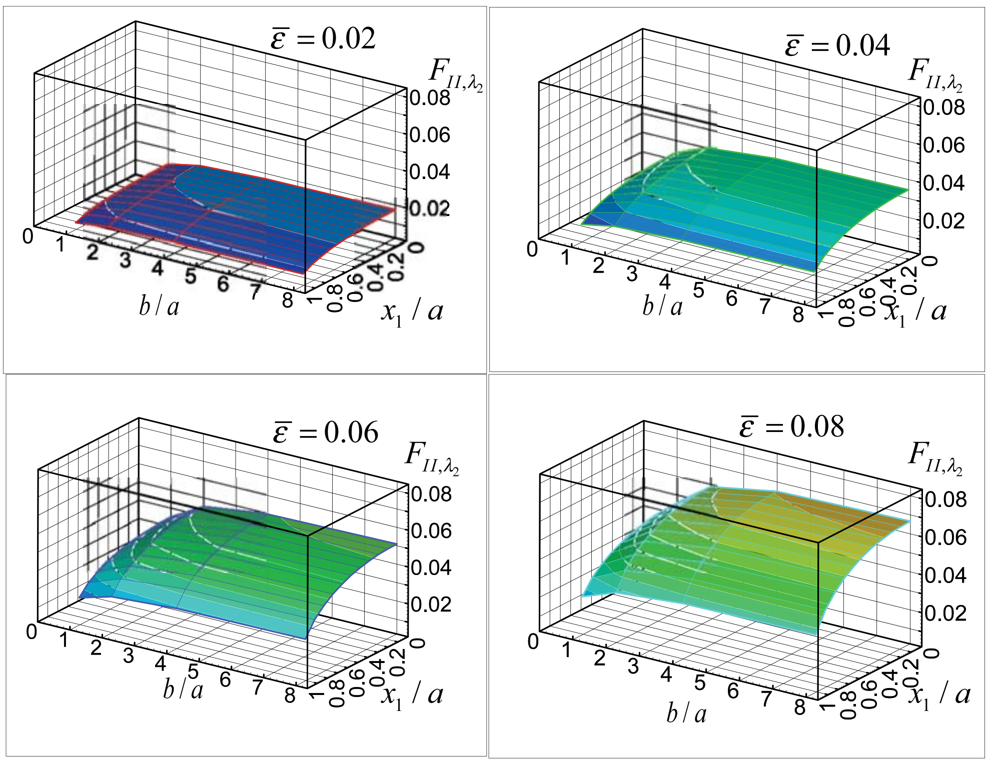

Fig.1.6. Dimensionless stress intensity factor F_{II,λ_2} varying with $\bar{\varepsilon}$ and b/a ($M=N=13, K=L=20\times 20$)

Figs 7 and 8 give the stress intensity factor as a function of $\bar{\varepsilon}$ and b/a for x_1/a changing from 0 to 1. We observer from Fig.7 that dimensionless stress intensity factors F_{I,λ_1} increases with b/a for fixed value of $\bar{\varepsilon}$ and decrease with $\bar{\varepsilon}$ for fixed value of b/a. While it can be found in Fig.8 that the F_{II,λ_2} increase with both $\bar{\varepsilon}$ and b/a.

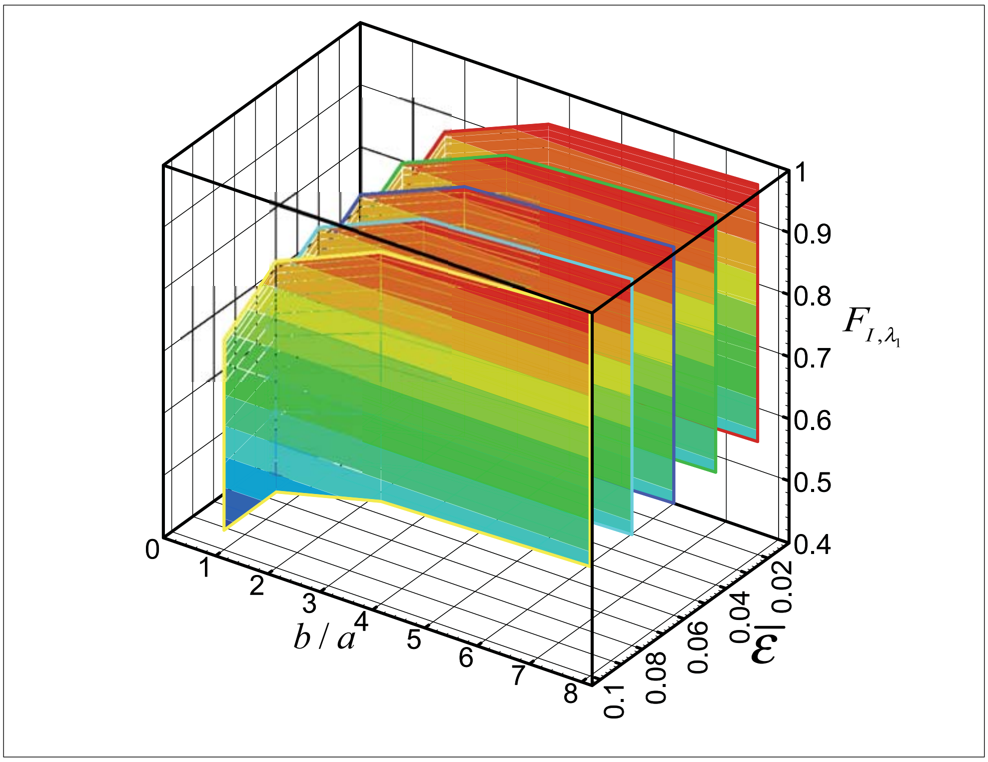

Fig.1.7. Dimensionless stress intensity factor F_{I,λ_1} varying with $\bar{\varepsilon}$ and

b/a (($M = N = 13, K = L = 20 \times 20, x_1/a \in [0,1]$)

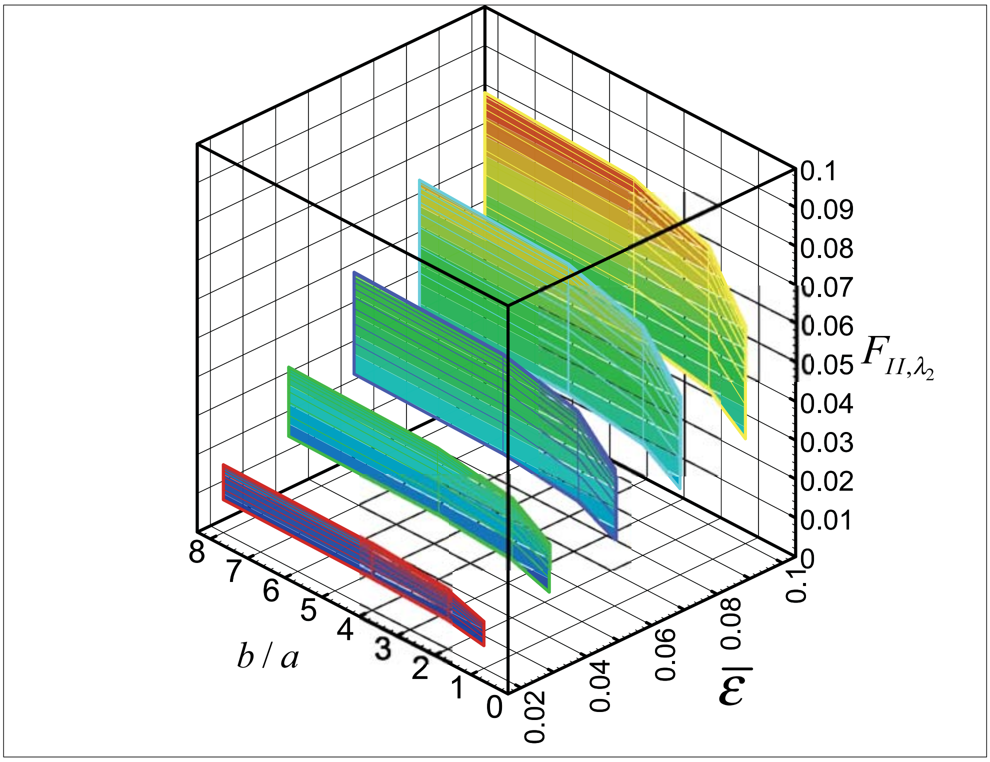

Fig.1.8. Dimensionless stress intensity factor F_{II,λ_2} varying with $\bar{\varepsilon}$ and b/a ($M=N=13, K=L=20\times20, x_1/a\in[0,1]$)

7.4 General cases

For general cases, the polynomial exponents are taken as M=N=13, and the collocation point number is 20 × 20 for the following results. When the solid is subjected to the extended loads σ_{3i}^{∞}, D_{33}^{∞} and B_{33}^{∞} in infinity, the stress intensity factors along the crack front meeting at the interface is of mixed mode II&III. Tab.5 gives the maximum stress intensity factors $F_{I\max}$ and $F_{II\max}$ for different ratios of a/b and $\bar{\varepsilon}$ at crack front points (±a,0) and (0,±b), respectively.

Table.1.5. Dimensionless stress intensity factors $F_{I\max}$ and $F_{II\max}$ varying with $\bar{\varepsilon}$ and b/a. ($M=N=13, KK=LL=20\times20$)

SIF	$F_{I\max}$ (±a,0)				$F_{II\max}$ (0,±b)			
$\bar{\varepsilon}$	b/a=1	b/a=2	b/a=4	b/a=8	b/a=1	b/a=2	b/a=4	b/a=8
0.02	0.7536	0.9062	0.977	0.9958	0.0121	0.0155	0.0171	0.0175
0.04	0.7517	0.9048	0.976	0.9949	0.0239	0.0306	0.0338	0.0346
0.06	0.7486	0.9023	0.974	0.9931	0.0351	0.0452	0.0499	0.0510
0.08	0.7441	0.8985	0.9709	0.9902	0.0458	0.0589	0.0651	0.0667
0.1	0.7381	0.893	0.9664	0.9858	0.0556	0.0716	0.0793	0.0812

Figs.9 and 10 give the dimensionless stress intensity factors F_{I,λ_1} and F_{II,λ_2} along the crack front at the interface for the different composites parameter ($\bar{\varepsilon}$) and geometrical shape parameters (x_1/a and b/a), respectively.

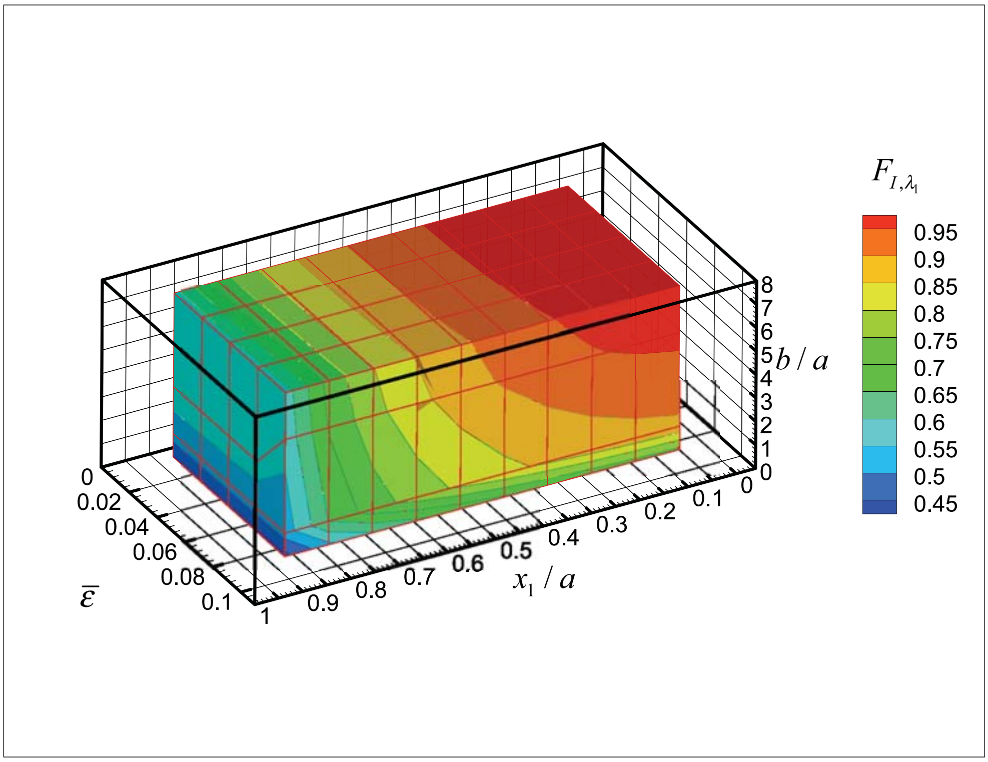

Fig.9. Dimensionless stress intensity factor F_{I,λ_1} varying with x_1/a, $\bar{\varepsilon}$ and b/a ($M=N=13, KK=LL=20\times20$)

It can be found from Fig.9 that, when $\bar{\varepsilon}$ and x_1/a are fixed, with the crack shape ratio b/a, increasing from 1 to 8, the dimensionless stress intensity factors F_{I,λ_1} increase. With the increase of b/a the numerical results convergence to a stable value, which is the same as that determined from the results of an 2D interface crack problem (b/a≥8). When b/a and x_1/a are fixed, with the material parameter $\bar{\varepsilon}$, decreasing from 0.1 to 0, the dimensionless stress intensity factors F_{I,λ_1} increase. With the decrease of $\bar{\varepsilon}$ the numerical results convergence to a stable value, which is the same as that determined from the results of a 3D crack in fully coupled electromagnetothermoelastic multiphase composites. When b/a and $\bar{\varepsilon}$ are fixed, with the x_1/a, varying from -1 to 1(Due to the symmetry, only the part of $x_1/a\in[0,1]$ is plotted), the dimensionless stress intensity factors F_{I,λ_1} increase when x_1/a increasing from -1 to 0, while decrease when x_1/a decreasing from 0 to 1, the maximum value is reached when x_1/a=0.

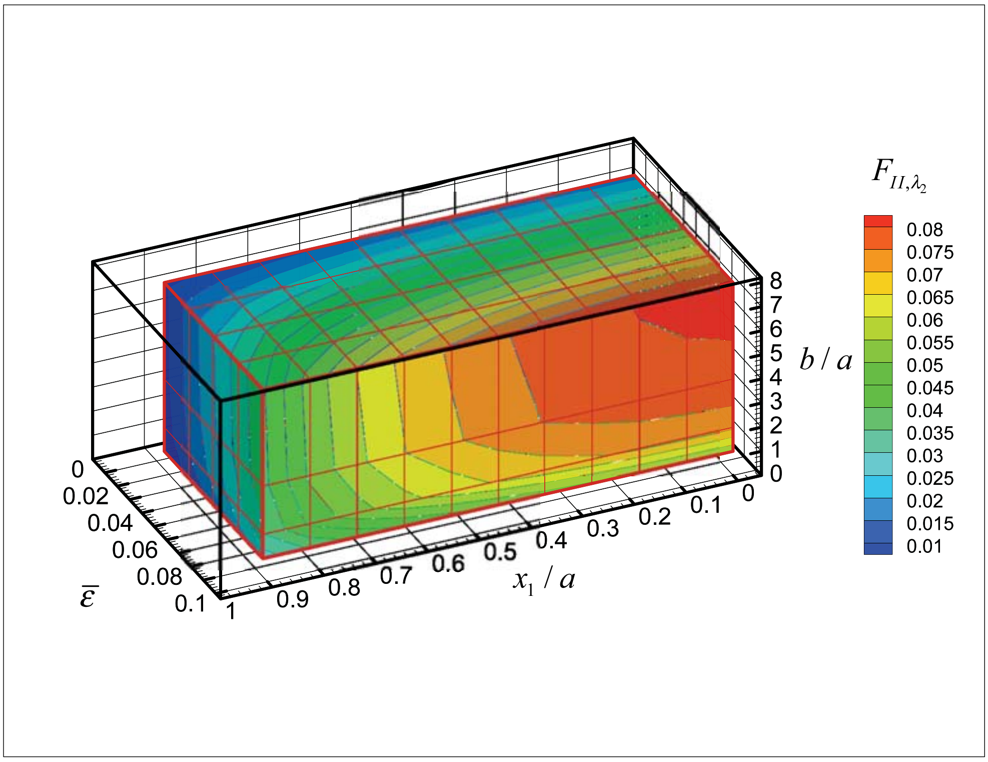

Fig.10. Dimensionless stress intensity factor F_{II,λ_2} **varying with** x_1/a , $\bar{\varepsilon}$ **and** b/a ($M = N = 13$, $KK = LL = 20\times 20$)

From Fig.10, we can obtain that, when $\bar{\varepsilon}$ and x_1/a are fixed, with the crack shape ratio b/a, increasing from 1 to 8, the dimensionless stress intensity factors F_{II,λ_1} increase. With the increase of b/a the numerical results convergence to a stable value, which is the same as that determined from the results of an 2D interface crack problem(when b/a≥8). When b/a and x_1/a are fixed, with the material parameter $\bar{\varepsilon}$, increasing from 0 to 0.1, the dimensionless stress intensity factors F_{II,λ_2} increase. When b/a and $\bar{\varepsilon}$ are fixed, with the x_1/a ,varying from -1 to 1(Due to the symmetry, only the part of $x_1/a \in [0,1]$ is plotted), the dimensionless stress intensity factor F_{II,λ_2} increase when x_1/a increasing from -1 to 0, while decrease when x_1/a decreasing from 0 to 1, the maximum value is reached when x_1/a =0.

8. Conclusions

In the present article, a 3D interface crack in FC-EMTE-AMCs under fully coupled electro-magneto-thermo-elastic loads was investigated by extended hypersingular intergro-differential equation method This method has been proposed here for the first time. The following conclusions can be drawn from our results:

Using the principles of extended finite-part integrals and the extended main-part integrals method, the 3D interface crack problem is analyzed through a set of E-HIDEs coupled with boundary integral equations. Based on the E-HIDEs, the behaviors of extended stress singularities near the crack front are obtained by the extended main-part analysis of two dimensional hypersingular integrals, and the extended singular orders are analyzed.

A numerical method for treating the 3D interface crack problem subjected to extended loads is proposed, and the radiation distribution of dimensionless extended stress intensity factors for multiple coupled fields at the crack surface have been calculated. Furthermore, the changing rule between the changing rule between the extended stress intensity factors between the crack geometry and material parameters have been analyzed.

In general, the extended SIFs not only depend on the crack geometry parameters, but also depend on the properties of the materials and the electro-magneto-elastic coupling effects. The electric-magnetic-elastic coupling fields and materials properties have a stronger influence on the extended SIFs than does the geometry parameters. Among these parameters, that of electric-magnetic-elastic coupling effect is the primary factor in determining the results of extended SIFs.

Whenever there is an interface crack on the interface of FC-EMTE-AMCs, an analysis of the type described in this paper can be utilized in order to find the critical configurations under which the structure may be most vulnerable. In such cases, the strength predictions could be much more adequate and safe if these interface crack has been taken into account.

References

Aboudi, J., 2001. Micromechanical analysis of fully coupled electro-magneto-thermo-elastic multiphase composites. Smart Materials and Structures 10, 867-877.

Belhouari, M., Gouasmi, S., Bachir bouiadjra, B., Kaddouri, K., and Serier, B., Elastic-plastic analysis of interaction between an interfacial crack and a subinterfacial microcrack in bi-materials. Computational Materials Science In Press, Corrected Proof.

Zhu, B. J., Qin, T. Y., 2007a. Application of hypersingular integral equation method to three-dimensional crack in electromagnetothermoelastic multiphase composites. International Journal of Solids and Structures 44, 5994-6012.

Zhu, B. J., Qin, T. Y.,2007b. Zhu, B. J., and Qin, T. Y., 2007. Hypersingular integral equation method for a three-dimensional crack in anisotropic electro-magneto-elastic bimaterials. Theoretical and Applied Fracture Mechanics 47, 219-232.

Zhu, B. J., Qin, T. Y.,2008a. Arbitrary 3D flaws in electromagnetothermoelastic composites under coupled multiple fields. smart materials and structures 17, 015032.

Tianyou, Fan. Intruduction of Fracture theory, Science Press.2005

Zhu, B. J.,Qin, T. Y.,2008b. 3D modeling of crack growth in electro-magneto-thermo-elastic coupled viscoplastic multiphase composites. Applied Mathematical Modelling In Press, Corrected Proof.

Correa, E., Mantic, V., and Par, F., Numerical characterisation of the fibre-matrix interface crack growth in composites under transverse compression. Engineering Fracture Mechanics In Press, Corrected Proof.

Davis, P. M., 1974. Piezomagnetic Computation of Magnetic-Anomalies Due to Ground Loading by a Man-Made Lake. Pure and Applied Geophysics 112, 811-819.

Erdogan, F., 1978. Mixed boundary value problem in mechanics. Mechanics Today, V4. Nemat-Nasser, S. ed, 44~84.

Guo, L.-C., Noda, N., 2008. Fracture mechanics analysis of functionally graded layered structures with a crack crossing the interface. Mechanics of Materials 40, 81-99.

Ioakimidis, N. I., 1982. Application of finite-part integrals to the singular integral equations of crack problems in plane and 3-D elasticity. Acta Mechanica 45, 31～47.

Jordan, N. F., Eringen, A. C., 1964a. On the static nonlinear theory of electromagnetic thermoelastic solids--I. International Journal of Engineering Science 2, 59-95.

Jordan, N. F., Eringen, A. C., 1964b. On the static nonlinear theory of electromagnetic thermoelastic solids--II. International Journal of Engineering Science 2, 97-114.

Khandelwal, R., Chandra Kishen, J. M., 2008. The use of conservative integral in bi-material interface crack problems subjected to thermal loads. International Journal of Solids and Structures 45, 2976-2992.

Mankour, A., Bachir Bouiadjra, B., and Belhouari, M., Brazilian disk test simulation intended for the study of interfacial cracks in bi-materials. Computational Materials Science In Press, Corrected Proof.

Perez-Aparicio, J. L., Sosa, H., 2004. A continuum three-dimensional, fully coupled, dynamic, non-linear finite element formulation for magnetostrictive materials. Smart Materials & Structures 13, 493-502.

Pindra, N., Lazarus, V., and Leblond, J.-B., 2008. The deformation of the front of a 3D interface crack propagating quasistatically in a medium with random fracture properties. Journal of the Mechanics and Physics of Solids 56, 1269-1295.

Qin, T. Y., Noda, N. A., 2003. Stress intensity factors of a rectangular crack meeting a bimaterial interface. International Journal of Solids and Structures 40, 2473-2486.
Qin, T. Y., Tang, R. J., 1993. Finite-Part Integral and Boundary-Element Method to Solve Embedded Planar Crack Problems. International Journal of Fracture 60, 373-381.
Singh, B. M., Rokne, J., Dhaliwal, R. S., and Vrbik, J., 2008. Antiplane crack at the interface of two bonded dissimilar graded piezoelectric materials. European Journal of Mechanics - A/Solids 27, 346-364.
Tinkham, M., 1974. Electromagnetic Properties of Superconductors. Reviews of Modern Physics 46, 587-596.
Vandenboomgaard, J., Vanrun, A. M. J. G., and Vansuchtelen, J., 1976a. Magnetoelectricity in Piezoelectric-Magnetostrictive Composites. Ferroelectrics 10, 295-298.
Vandenboomgaard, J., Vanrun, A. M. J. G., and Vansuchtelen, J., 1976b. Piezoelectric-Piezomagnetic Composites with Magnetoelectric Effect. Ferroelectrics 14, 727-728.
Wang, Q., noda, N. A., 2001. variation of stress intensity factors along the front of 3D rectangular crack by using a singular integral equation method. International Journal of Fracture 108, 119-131.
Zhao, M., Li, N., Fan, C., and Xu, G., 2008. Analysis method of planar interface cracks of arbitrary shape in three-dimensional transversely isotropic magnetoelectroelastic bimaterials. International Journal of Solids and Structures 45, 1804-1824.

Chapter 2 :Analysis of 3D fluid driven crack propagation problem in co-seismic slip under P- and S-waves by hybrid hypersingular integral method

Abstract

This work reports a new and accurate way of theoretical and numerical description of the extended 3D fluid (electromagnetic and flow) driven crack progression in co-seismic slip under *P*- and *S*-waves. First, based on the viscous fluid flow reciprocal work theorem, the hybrid hypersingular integral equation (HIE) method proposed by the author was defined by combined with the coupled extended wave time-domain HIE and the extended diffused interface phase field method. The general extended 3D fluid flow velocity wave solutions are obtained by the extended wave time-domains Green's function method. The 3D extended dynamic fluid driven crack modeling under fully coupled electromagnetothermoelastic *P*- and *S*-wave and flow field was established. Then, the problem is reduced to solving a set of extended hybrid HIEs coupled with nonlinear boundary domain integral equations, in which the unknown functions are the general extended flow velocity discontinuity waves. The behavior of the general extended singular stress indices around the crack front terminating is analyzed by hybrid time-domain main-part analysis. The general extended singular pore stress waves (SPSWs) and the extended dynamic stress intensity factors (DSIFs) on the fluid driven crack surface are obtained from closed-form solutions. In addition, a numerical method for the problem is proposed, in which the extended velocity discontinuity waves are approximated by the product of time-domain density functions and polynomials. The extended DSIFs and general extended SPSWs are calculated, and the results are presented toward demonstrating the applicability of the proposed method.

Key words： 3D fluid driven crack propagation mechanism; *P*- and *S*-waves; Extended hybrid hypersingular integral equation; Extended dynamic stress intensity factor; General extended singular pore stress waves.

1. Introduction

Strong earthquakes can have catastrophic effects on society, and therefore the precise prediction of large earthquakes is crucial for seismic hazard reduction. The genesis and occurrence of earthquakes and their subsequent effects involve complex physical processes. Studying these processes helps us understand the mechanics of earthquakes and the future physical state of the earth. Earthquake studies focus on the nucleation of rupture, thermo- and hydro-mechanical weakening of fault zones during seismic slip, fracture propagation through branched and offset fault systems, and relations between stress, seismicity, and deformation in or near continental and subduction fault systems.

Fluid driven fracture is a fundamental geophysical phenomenon operating in planetary interious on many scales, it plays a major role in chemical differentiation of the upper mantle and dynamic delayed triggering of earthquakes process. Because our ability to make direct observation of the dynamics and styles of fluid driven fracture is quite limited, our understanding of this phenomenon relies on theoretical models that use fundamental physical principles and available field data to constrain the behavior of fluid driven cracks at depth.

In the aspect of Green function method, Bouchon and Aki [**1**] studied the radiation of elastic fields from complex seismic sources in layered media by wave-number discretization of the source wave field. Bouchon [**2**] subsequently generalized the discrete wave number representation method into 3D elastic wave propagation problems. The author later obtained Green's functions for an elastic layered medium by using a double integral over frequency and horizontal wave number [**3**]. Aki and Richards [**4**] obtained a Green's function for infinite isotropic media. Okada [**5**] obtained inclined shear and tensile fault surface displacements for points and finite rectangular sources. Sánchez-Sesma et al.[6] gave a compact form of a Green's function for harmonic time dependence in an unbounded, homogeneous, isotropic elastic media, and computed the diffraction of *P, SV,* and Rayleigh waves in an elastic half-space. Liu and Huang [7] investigated the dynamic responses of a cracked elastic solid subjected to in-plane surface loadings by a hybrid method combining the FEM with a boundary integral equation. Fu and Bouchon [8, 9] studied discrete wave number solutions in piecewise heterogeneous media by a discrete wave number Green's function. Zhang [10] used Green's function to study the numerical simulation technique of long period strong ground motion at near-field. Using frequency domain traction BEM and the Green's function method, 3D Green's functions of a poroelastic half space subjected to an arbitrary buried loading was presented by Chen et al [11].

In the aspect of boundary element method, Tosaka and Onishi [12] presented 2D/3D incompressible viscous stead-state flow problem by boundary integral equations. Bush [13] analyzed steady plane flow of an incompressible, viscous Newtonian fluid past a cylindrical body of arbitrary cross-section by boundary element method. Kakuda and Tosaka [14] analyzed unsteady Navier Stokes equations by BEM. Tosaka and Kakuda [15] presented three kinds of boundary element approaches for an unsteady flow problem of incompressible viscous fluid are presented. For embrittlement crack propagation rate in liquid metal problem, [16-18] suggested that the crack propagation rates are controlled by the fluid flow characterstics of the liquid metal in the crack. Clegg [19] consider another mechanism control crack propagation rate, and he suggested that most of the fluid losses occur in a narrow region near the crack tip.

In the field of crack propagation analysis, Iturrarán-Viveros et al.[20] studied the 3D open model crack problem under elastic waves based on the indirect boundary element method, and give some numerical COD results of crack propagation under *P*-or *S*-waves. Tadeu et al. [21, 22] evaluated the 3D scattered wave field generated by the 2D empty crack problem.

However, relatively little work has been done on 3D extended fluid driven crack propagation. This seems to be due mainly to the present limitations on practical methods (such as CPU time and storage requirements) and on theoretical aspects (strongly singular domain integrals). This requires general and accurate theoretical method.

In this paper, a new and accurate way of theoretical and numerical description of extended 3D dynamic fluid (electric, magnetic and flow) driven crack progression in co-seismic slip under *P*-and *S*-waves was presented.

First, based on the viscous fluid flow reciprocal work theorem, the hybrid hypersingular integral equation (HIE) method was defined by combined with coupled extended wave time-domain HIE method [23-26] and extended diffused interface phase field method. The general extended 3D fluid flow velocity wave solutions are obtained by extended wave time-domains Green's function method. The 3D extended dynamic fluid driven crack modeling under fully coupled electromagnetothermoelastic *P*- and *S*-wave fields and flow field was established.

Then, based on the extended hybrid HIE method, the problem is reduced to solving a set of extended hybrid HIEs coupled with nonlinear boundary domain integral equations, in which the unknown functions are the general extended flow velocity discontinuity waves. The behavior of the general extended singular stress indices around the crack front terminating is analyzed by hybrid time-domain main-part analysis. The general extended singular pore stress waves (SPSWs) and the extended dynamic stress intensity factors (DSIFs) on the fluid driven crack surface are obtained from closed-form solutions.

In addition, a numerical method for the problem is proposed, in which the extended velocity discontinuity waves are approximated by the product of time-domain density functions and polynomials. The extended DSIFs and general extended SPSWs are calculated. The results are presented toward demonstrating the applicability of the proposed method.

2. Basic equations

The extended nonlinear governing equations and constitutive relationships can be expressed by incremental tensor forms

$$\Sigma_{IJ,I} + \dot{F}_J = \rho \ddot{U}_J \tag{26}$$

In the present paper, summation from 1 to 3 over repeated lowercase, and of 1 to 6 in uppercase subscripts is assumed, and a subscript comma denotes the partial differentiation with respect to the extended coordinates (i.e., $x_1, x_2, x_3, x_4, x_5, x_6$ or x, y, z, m, n, l). The extended displacement waves, U_J , can be written as follows:

$$U_K = u_i \delta_{iK} + \phi \delta_{4K} + \varphi \delta_{5K} + \Upsilon \delta_{6K} \tag{27}$$

In addition, the extended incremental stress displacement and the extended dummy incremental body loads, Σ_{iJ} and $\dot{F}_J$, are defined respectively by

$$\Sigma_{IJ} = \dot{\sigma}_{ij}\delta_{il}\delta_{jJ} + \dot{D}\delta_4\delta_{4J} + \dot{B}\delta_5\delta_{5J} + \dot{\vartheta}\delta_6\delta_{6J} \tag{28}$$

$$\dot{F}_J = (\dot{f}_j - \dot{\sigma}^n_{iJ} + f^{el-mag})\delta_{iJ} - \dot{f}_e\delta_{4J} - \dot{f}_m\delta_{5J} - \dot{f}_\vartheta\delta_{6J} \tag{29}$$

where the Maxwell stress tensor f^{el-mag} is defined as

$$f^{el-mag} = \nabla\bullet\left[\varepsilon_0(E\otimes E - 0.5E\bullet EI) + \mu_0^{-1}(B\otimes B - 0.5B\bullet BI)\right] - (\varepsilon_0 E\times B)_{,t} \tag{30}$$

The elastoplastic creep incremental constitutive equations are written as

$$\Sigma_{IJ} = E_{IJKL}\dot{Z}_{KL} \tag{31}$$

The description of the electromagnetic phenomena is given by the Maxwell equation, including Gauss' law, Faraday's law of induction conservation of a flux, and Ampere's law. These are represented respectively as follows:

$$\nabla\bullet D = q \qquad \nabla\times E = -\dot{B} \qquad \nabla\bullet B = 0 \qquad \nabla\times H = J + \dot{D} \tag{32}$$

The continuity equation for conservation of mass in inertial system can be show in the following

$$\frac{\partial\rho}{\partial t} - \frac{d\ln\rho}{dc}\left[\left(kc_{,i}\right)_{,i} + q\right] + \rho u_i\rho_{,i} = 0 \tag{33}$$

The conservation of momentum (Newton's second law) can be expressed as

$$(\rho u_i)_{,t} + (\rho u_i u_j)_{,j} = \tau_{ij,j} + \rho f_i^b \tag{34}$$

The Navier-Stokes equations can be written as

$$(\rho u_i)_{,t} + \left(\rho u_i u_j\right)_{,j} - \left(\mu(u_{i,j} + u_{j,i} - \frac{2}{3}\varepsilon_{ii}\delta_{ij}) - p\delta_{ij}\right)_{,j} - \rho f_i^b = 0 \tag{35}$$

Cahn-Hilliard-van der Waals form for the Helmoltz free energy can be written as

$$F(n_{\alpha\alpha},\varphi_\alpha) = \int_V\left[\frac{\kappa n}{2}\left|\nabla\varphi_\alpha\right|^2 + n_{\alpha\alpha}W(\varphi_\alpha) + f(n)\right] \tag{36}$$

The transport equation of two phase tube can be written as

$$\frac{\partial n_\alpha}{\partial t} = -\nabla\bullet\left(\frac{n_\alpha g}{\rho}\right) + (-1)^\alpha\nabla\bullet\Lambda\nabla\mu\,, \frac{\partial g}{\partial t} = -\nabla\bullet P - \nabla\bullet\left(\frac{gg}{\rho}\right) + \eta\nabla\bullet\left(\frac{g}{\rho}\right) \tag{37}$$

where other parameters $E_{iJKl}\ \dot{Z}_{KL}\ W$, φ_α, $\overline{\kappa}$, $\mu_i(r)$, Λ and η are listed in the Appendix B.

3. Mathematical modeling

Consider a 3D fluid driven crack propagation problem as shown in Figure 1.1. A fixed geographic Cartesian system x_i is chosen. Assume that the slip surface $S^{\pm}$ is subjected to $\dot{p}_i$, $\dot{p}_4$ or $\dot{q}_0$, $\dot{p}_5$ ($\dot{b}_0$), and $\dot{p}_6$ ($\dot{\vartheta}_0$). $\hat{x}_i$ represent the hypocenter of the coordinate systems, while the nodal plane of *P*-wave $\hat{x}_1\hat{x}_3$ and $\hat{x}_2\hat{x}_3$ denote the extended slip plane and auxiliary plane, respectively.

Coordinates $x_{\phi s}$ and x_{λ} represent the fault strike and the fault slip, respectively. $w_i = \angle(x_i;\hat{x}_i)$, $\theta_2 = \delta = \angle(\hat{x}_1\hat{}x_3; x_1x_2)$, $\theta_3 = \lambda = \angle(\hat{x}_1\hat{}x_3; x_1x_2)$.

Figure 1.1. An extended 3D fluid driven crack propagation model on co-seismic slip under multiple fields

a) **General sketch of the slip** *b*) **General model of 3D fluid crack** *c*) **Fluid flow model on crack surface**

4. Boundary conditions

4.1 Weak coupled boundary conditions

For permeable conditions, the normal extended incremental displacement rate and extended incremental potential rate should be continuous across the crack surface:

$$\dot{D}_3^+ = \dot{D}_3^-, \dot{\phi}^+ = \dot{\phi}^-, \dot{B}_3^+ = \dot{B}_3^-, \dot{\varphi}^+ = \dot{\varphi}^-, \dot{\vartheta}_3^+ = \dot{\vartheta}_3^-, \dot{\Upsilon}^+ = \dot{\Upsilon}^- \tag{38}$$

where the superscripts + and – denote the upper and lower crack surface, respectively. The proposed impermeable conditions on the crack faces are represented by the following relation:

$$\dot{D}_3^+ = \dot{D}_3^- = 0, \dot{\phi}^+ = \dot{\phi}^- = 0, \dot{B}_3^+ = \dot{B}_3^- = 0, \dot{\varphi}^+ = \dot{\varphi}^- = 0, \dot{\vartheta}_3^+ = \dot{\vartheta}_3^- = 0, \dot{\Upsilon}^+ = \dot{\Upsilon}^- = 0 \tag{39}$$

4.2 Strong coupled boundary conditions

The strong coupled boundary conditions for crack propagation in co-seismic slip under coupled multiple fields can be determined as

$$|Tn| = 0;\ |u| = 0;\ |D \bullet n| = q_s;\ |E \times n| = 0;\ |B \bullet n| = 0;\ |n \times H| = J_s \tag{40}$$

The present article presents an analysis for crack propagation problems based on boundary conditions (14) and (15).

5. Boundary domain integral equations for viscous fluid flows

Based on the reciprocal work theorem for viscous fluid flow, consequently, the following boundary domain integral equation can be obtained,

$$\dot{U}_I = \int_{-\infty}^{+\infty}\int_{-\infty}^{+\infty}\Big\{\int_\Gamma (\dot{U}_{IJ}\dot{T}_J - \dot{T}_{IJ}\dot{U}_J)dS + \int_\Omega (\dot{U}_{IJ}\dot{F}_J + \dot{\varepsilon}_{IJk}\dot{\sigma}^n_{Jk})dV + \int_\Omega [\dot{U}_{,IJ}\rho_k u_j u_k + \dot{U}_{IJ}\rho_J\dot{F}_J - \dot{U}_{It}(\rho u)_{,j} + \dot{U}_{,IJ}p]dV - \int_\Gamma \dot{U}_{IJ}\eta_J u_k u_j dS_k\Big\}d\tau\, d\tau' \tag{41}$$

The above equation is a general boundary domain integral equation valid for steady, unsteady, compressible and incompressible. The extended incremental traction wave, $\dot{T}_J$, on the boundary can be defined as

$$\dot{T}_J = E_{kJMn}\dot{U}_{IM,n} n_k = \left((\dot{\sigma}_{jl} - f^{el-mag})n_l - \dot{\sigma}^n_{iJ,i}\right)\delta_{iJ}\delta_{jJ} + (\dot{D}_l \eta_l)\delta_{4J} + (\dot{B}_l \eta_l)\delta_{5J} + (\dot{\vartheta}_{,J}\eta_l)\delta_{6J} \tag{42}$$

The extended incremental displacement discontinuity wave gradient is written as

$$\dot{\tilde{U}}_J = \begin{cases} \dot{\tilde{u}}_j = \dot{u}_j^+ - \dot{u}_j^- & J = j = 1,2,3 \\ \dot{\tilde{\phi}}_j = \dot{\phi}_j^+ - \dot{\phi}_j^- & J = 4 \\ \dot{\tilde{\varphi}}_j = \dot{\varphi}_j^+ - \dot{\varphi}_j^- & J = 5 \\ \dot{\tilde{\Upsilon}}_j = \dot{\Upsilon}_j^+ - \dot{\Upsilon}_j^- & J = 6 \end{cases} \tag{43}$$

where $\hat{P}$ and $\hat{S}$ are the source point and the field point, respectively. The extended incremental displacement wave solutions in Eq. (16) can be rewritten as

$$\dot{U}_I = \int_{-\infty}^{+\infty}\int_{-\infty}^{+\infty}\left\{\int_\Gamma (\dot{U}_{IJ}\dot{T}_J - \dot{T}_{IJ}\dot{\tilde{U}}_J)dS + \int_\Omega (\dot{U}_{IJ}\dot{F}_J + \dot{\varepsilon}_{IJk}\dot{\sigma}''_{Jk})dV + \int_\Omega [\dot{U}_{,IJ}\rho_k u_j u_k + \dot{U}_{IJ}\rho\dot{F}_J - \dot{U}_{IJ}(\rho u)_{,j} + \dot{U}_{,IJ}p]dV - \int_\Gamma \dot{U}_{IJ} n_j u_k u_j dS_k\right\}d\tau\, d\tau' \tag{44}$$

6. General extended displacement wave solutions

Using the method[5, 26-37], the general extended displacement wave solutions under *P*- and *S*-waves can be written as an explicit expression. .

$$G_{1J}(\hat{P},\hat{S},t,\tau,\tau') = \sum_{i=1}^{5}\left[D_0\omega_4^* + D_i\omega_5^* + \rho^{-1}(R_i^{-1}\omega_6^* + \dot{R}_0^{-1}\omega_7^*)\right] + \pi^{-1}\mu^{-1}R_i^{-1}(7\delta_{IJ} + R_{,i}R_{,J})/32 \tag{45}$$

$$G_{2J}(\hat{P},\hat{S},t,\tau,\tau') = \sum_{i=1}^{5}\left[D_0\omega_4^* + D_i\omega_5^* + \rho^{-1}(R_i^{-1}\omega_6^* + \dot{R}_0^{-1}\omega_7^*)\right] + \pi^{-1}\mu^{-1}R_i^{-1}(7\delta_{IJ} + R_{,i}R_{,J})/32 \tag{46}$$

$$G_{mJ}(\hat{P},\hat{S},t,\tau,\tau') = \sum_{i=1}^{5}R_i^{-1}(A_{im}\omega_9^* + \omega_8^*\rho^{-1}) + \pi^{-1}\mu^{-1}R_i^{-1}(7\delta_{IJ} + R_{,i}R_{,J})/32 \tag{47}$$

the parameters ω_8^* and ω_9^* are listed in the Appendix A

7. Wave time-domain hypersingular integral equations

Using the boundary conditions in Eqs. (14) and (15), and the main-part method given by [25], Eq. (19) can be reduced to

$$\begin{aligned}&\int_{-\infty}^{+\infty}\int_{-\infty}^{+\infty}\oint_{S^+}\Big(r^{-3}(c_{44}^2 D_0 s_0^2(\delta_{\bar{\alpha}\bar{\beta}} - 3r_{,\bar{\alpha}}r_{,\bar{\beta}}) + (\delta_{\alpha\beta} - 3r_{,\alpha}r_{,\beta})\sum_{i=1}^{5}\rho_i^2 t_i^2)\tilde{u}_\beta + 3r^{-4}r_{,\alpha}\sum_{i=1}^{5}\lambda_{33}s_i^2 t_i^1\tilde{u}_6\Big)dSd\tau\, d\tau'\\&+\int_{-\infty}^{-\infty}\int_{-\infty}^{+\infty}\int_{S^+}\big(r^{-7}K_{\alpha\beta1} + r^{-5}K_{\alpha\beta2} + r^{-3}K_{\alpha\beta3}\big)\tilde{u}_\beta dSd\tau\, d\tau' + \int_{-\infty}^{-\infty}\int_{-\infty}^{+\infty}\int_{S^+}\bar{K}_{\alpha\beta}\tilde{u}_\beta dSd\tau\, d\tau' = -p_\alpha\end{aligned} \tag{48}$$

$$\begin{aligned}&\int_{-\infty}^{+\infty}\int_{-\infty}^{+\infty}\int_{S^+}\Big(r^{-2}r_{,\alpha}\sum_{i=1}^{5}A_i^\Upsilon t_i^2\rho_i^1\tilde{u}_\alpha + r^{-3}\sum_{n=3}^{5}\sum_{i=1}^{5}\rho_i^m t_i^t\tilde{u}_n + 3r^{-4}\lambda_{3\alpha}r_{,\alpha}\sum_{i=1}^{5}v_i^2\lambda_i^\vartheta\rho_i^m\tilde{u}_6\Big)dSd\tau\, d\tau'\\&+\int_{-\infty}^{-\infty}\int_{-\infty}^{+\infty}\int_{S^+}\big(r^{-7}K_{mJ1} + r^{-5}K_{mJ2} + r^{-3}K_{mJ3}\big)\tilde{u}_J dSd\tau\, d\tau' + \int_{-\infty}^{-\infty}\int_{-\infty}^{+\infty}\int_{S^+}\bar{K}_{mJ}\tilde{u}_J dSd\tau\, d\tau' = -p_m\end{aligned} \tag{49}$$

$$\begin{aligned}&\int_{-\infty}^{+\infty}\int_{-\infty}^{+\infty}\oint_{S^+}\Big(r^{-2}(\delta_{\alpha\beta} - 3r_{,\alpha}r_{,\beta})\sum_{i=1}^{5}A_i^\Upsilon\lambda_{3\beta}t_i^2\tilde{u}_\beta + 3r^{-4}\lambda_{3\alpha}r_{,\alpha}\sum_{i=1}^{5}A_i^\Upsilon v_i^2\lambda_i^\vartheta\lambda_{33}\rho_i^6\tilde{u}_6\Big)dSd\tau\, d\tau'\\&+\int_{-\infty}^{-\infty}\int_{-\infty}^{+\infty}\int_{S^+}\sum_{i=1}^{5}\big(r^{-7}K_{6J1} + r^{-5}K_{6J2} + r^{-3}K_{6J3}\big)\tilde{u}_J dSd\tau\, d\tau' + \int_{-\infty}^{-\infty}\int_{-\infty}^{+\infty}\int_{S^+}\sum_{i=1}^{5}\bar{K}_{6J}\tilde{u}_J dSd\tau\, d\tau' = -p_6\end{aligned} \tag{50}$$

The above equations are the wave time-domain hypersingular integral equations for the 3D fluid driven crack propagation problem under fully coupled electromagnetothermoelastic *P*- and *S*-wave fields. $\dot{p}_i$, $\dot{p}_4(\dot{q}_0)$ $\dot{p}_5(\dot{b}_0)$ and $\dot{p}_6(\dot{\vartheta}_0)$ can be obtained from the solutions for the loads of un-cracked solids. The hypersingular kernel function K_{KIJ} and Cauchy kernel function $\bar{K}_{IJ}$ are given in Appendix C. It is shown that the time-domain hypersingular integral equations have structures that are similar to those studied by [38-40]. If the electromagnetothermoelastic weak boundary conditions are neglected, the above equations can be simplified to the following relations:

$$\int_{-\infty}^{+\infty}\int_{-\infty}^{+\infty}\oint_{S^+}\left(\frac{K_{KI1}}{r^7} + \frac{K_{KI2}}{r^5} + \frac{K_{KI3}}{r^3}\right)\tilde{u}_I dSd\tau\, d\tau' + \int_{-\infty}^{-\infty}\int_{-\infty}^{+\infty}\int_{S^+}\bar{K}_{KI}\tilde{u}_I dSd\tau\, d\tau' = -\frac{4\pi\rho}{\mu^2}p_K \tag{51}$$

8. Crack propagation parameters

In the interest of investigating the singularity of the crack front, consider a local coordinate system defined as x_2 x_3, in which the x_1-axis is the tangent line of the crack front at point q_0, the x_2-axis is the internal normal line of the crack plane, and the x_3-axis is the normal of the crack. Then the extended velocity discontinuities gradient of the crack surface near a crack front point $\hat{q}_0$ can be expressed as

$$\dot{\tilde{U}}_{i,J} = g_k \xi_2^{\lambda_k} \qquad 0 < \mathrm{Re}(\lambda_k) < 1 \tag{52}$$

where g_k are non-zero constants related to point $\hat{q}_0$, and λ_k represents the singular indices at the crack front. The singular index can be determined by

$$\cot(\lambda_1\pi) = 0 \,, \cot(\lambda_2\pi) = 0 \,, \cot(\lambda_3\pi) = 0 \,, \cot(\lambda_4\pi) = 0 \,, \cot(\lambda_5\pi) = 0 \,, \cot(\lambda_6\pi) = 0 \tag{53}$$

The extended dynamic stress intensity factors are defined as

$$K_1 = \lim_{r\to 0}\sqrt{2r}\sigma_{33}\Big|_{\hat{\hat{\theta}}=0} , K_2 = \lim_{r\to 0}\sqrt{2r}\sigma_{31}\Big|_{\theta=0} , K_3 = \lim_{r\to 0}\sqrt{2r}\sigma_{32}\Big|_{\theta=0} \tag{54}$$

$$K_4 = \lim_{r\to 0}\sqrt{2r}D_3\Big|_{\hat{\hat{\theta}}=0} , K_5 = \lim_{r\to 0}\sqrt{2r}B_3\Big|_{\theta=0} , K_6 = \lim_{r\to 0}\sqrt{2r}\vartheta_3\Big|_{\hat{\theta}=0} \tag{55}$$

The extended singular pore stress waves field around the crack front can be expressed as follows:

$$\begin{aligned}\dot{\sigma}_{13} &= -0.25c_{44}v_0 g_1(rr_0)^{-0.5}\cos\dot{\theta}_0 \\ &+\mu^2\rho^{-1}\left\{\begin{aligned}&-\frac{5(2\omega_3 x_1 w_{11}^1 + x_1 w_{13}^1 + x_3 w_{11}^1)}{r^7} + \frac{2\omega_3 w_{11}^2 + w_{13}^2 + w_{11}^6}{r^6} + \frac{2\omega_3 w_{11}^3 + w_{13}^3 + w_{11}^7}{r^5} + \frac{2\omega_3 w_{11}^4 + w_{13}^4 + w_{11}^8}{r^4} + \frac{w_{23}^{10} + w_{21}^4}{r^4} \\ &+\frac{2\omega_3 w_{11}^5 + w_{13}^5 + 1 - 3\omega_1 + \tilde{\delta}_4}{r^3} + \frac{\beta^{-3}\tilde{\delta}_3'[4\omega_3(1+\omega_1)+1]}{r^2} - \frac{5(x_1 w_{23}^1 + x_3 w_{21}^1)}{r^7} + \frac{w_{23}^8 + w_{21}^2}{r^6} + \frac{w_{23}^9 + w_{21}^3}{r^5} + \frac{w_{33}^4 + w_{31}^4}{r^4} \\ &\frac{\tilde{\delta}_3 - \beta^{-5}\tilde{\delta}_3''[x_1(x_1+x_2+x_3) - x_3(x_1+2x_2)]}{r^3} - \frac{\beta^{-3}\tilde{\delta}_3'}{r^2} - \frac{5(x_1 w_{33}^1 + x_3 w_{31}^1)}{r^7} + \frac{w_{33}^2 + w_{31}^2}{r^6} + \frac{w_{33}^3 + w_{31}^3}{r^5} + \\ &\frac{\tilde{\delta}_3 - 3\omega_1 - \tilde{\delta}_4 - \beta^{-5}x_1\tilde{\delta}_{31}''(x_1+x_2+x_3) + \tilde{\delta}_3(\omega_1+1)(3\omega_1+\tilde{\delta}_4)}{r^3}\end{aligned}\right\}\end{aligned} \tag{56}$$

$$\begin{aligned}\dot{\sigma}_{23} &= \sum\nolimits_{i=1}^{5}\pi(rr_i)^{-0.5}(g_6\lambda_{33}(15\lambda_{33}v_i^2\cot\theta_i(3\cos 0.25\theta_i - 3\sin^2 0.5\theta_i\cos 0.5\theta_i - 0.25\sin^2\theta_i\cos 1.5\theta_i) - 2\lambda_{33}(rr_i)^{-2}\sin^{-1}0.5\theta_i \\ &+0.5\lambda_{32}r^{-1}r_i^{-1}\sin^{-1}\theta_i(2\cos^{-1}0.5\theta_i - 3\cos 0.5\theta_i - \cos 2.5\theta_i)) + \rho_{i2}\pi\cos 0.5\theta_i(t_2 g_2 + 4\sum\nolimits_{m=3}^{5}\hat{\rho}_{im}g_m) + \hat{w}_2\dot{\varepsilon}_{jK}^n\cos 0.5\theta_0) \\ &+\mu^2\rho^{-1}\left\{\begin{aligned}&-\frac{5(x_2 w_{13}^1 + x_3 w_{12}^1)}{r^7} + \frac{w_{13}^6 + w_{12}^2}{r^6} + \frac{w_{13}^7 + w_{12}^3}{r^5} + \frac{w_{13}^8 + w_{12}^4}{r^4} - \frac{4\beta^{-5}x_2 x_3\tilde{\delta}_3''}{r^3} - \frac{5(2\omega_3 x_2 w_{22}^1 + w_{23}^1 x_2 + x_3 w_{23}^1)}{r^7} \\ &+\frac{2\omega_3 w_{22}^2 + w_{23}^2 + w_{23}^5}{r^6} + \frac{2\omega_3 w_{22}^3 + w_{23}^3 + w_{23}^6}{r^5} + \frac{2\omega_3 w_{22}^4 + w_{23}^4 + w_{23}^7}{r^4} + \frac{w_{22}^5 + 2\tilde{\delta}_3 - \tilde{\delta}_3''(x_1+x_2+x_3)(x_2+x_3)}{r^3} \\ &+\frac{3\beta^{-3}\tilde{\delta}_3'}{r^2} - \frac{5(x_2 w_{33}^1 + w_{32}^1 x_3)}{r^7} + \frac{w_{33}^5 + w_{32}^2}{r^6} + \frac{\beta^{-5}\tilde{\delta}_3'' x_2[(x_1+x_2+x_3)(x_2+x_3) - x_3] + (3\omega_1 + \tilde{\delta}_4)(2\omega_3+3)}{r^3} \\ &+\frac{\beta^{-3}\tilde{\delta}_3'}{r^2} + \frac{w_{33}^6 + w_{32}^3}{r^5} + \frac{w_{33}^7 + w_{32}^4}{r^4}\end{aligned}\right\}\end{aligned} \tag{57}$$

$$\begin{aligned}\bar{\dot{\sigma}}_{3n} &= \sum\nolimits_{i=1}^{5}\rho_{in}v_i\pi\cot\theta_i((rr_i)^{-0.5}(\hat{\hat{\rho}}_{i2}g_2\cos^{-1}\dot{\theta}_i + 6\cot\dot{\theta}_i\sum\nolimits_{m=3}^{5}\rho_{im}g_m) + g_6 v_i^2\kappa_{i5}\kappa_{i1}^{-1}(rr_i)^{0.5}\cos\dot{\theta}_i)) + \\ &\sum\nolimits_{i=1}^{5}\pi(rr_i)^{-0.5}\hat{w}_n\dot{\varepsilon}_{jK}^n\cos\dot{\theta}_0 + 2\pi A_{i4}\iota_{33}((rr_i)^{0.5}\cos\dot{\theta}_i(g_2\cot\theta_i + \sum\nolimits_{m=3}^{5}\hat{\rho}_{im}g_m) + (rr_i)^{-0.5}v_i^3\lambda_{33}\kappa_{i5}\kappa_{i1}^{-1}g_6\cos\dot{\theta}_i) \\ &+\mu^2\rho^{-1}\left\{\begin{aligned}&-\frac{5x_3 w_{13}^1}{r^7} + \frac{w_{13}^9}{r^6} + \frac{w_{13}^{10}}{r^5} + \frac{w_{13}^{11}}{r^4} + \frac{w_{13}^{12}}{r^3} + \frac{2\beta^{-3}\tilde{\delta}_3'}{r^2} - \frac{5x_3 w_{23}^1}{r^7} + \frac{w_{23}^5}{r^6} + \frac{w_{23}^6}{r^5} + \frac{w_{23}^7}{r^4} + \frac{\beta^{-3}\tilde{\delta}_3'}{r^2} + \frac{\beta^{-3}\tilde{\delta}_3'}{r^2} + \frac{w_{33}^8}{r^6} + \frac{w_{33}^9}{r^5} + \frac{w_{33}^{10}}{r^4} \\ &+\frac{\tilde{\delta}_3 - \beta^{-5}x_3\tilde{\delta}_3''(x_1+x_2+x_3)}{r^3} - \frac{5x_3 w_{33}^1}{r^7} + \frac{2(\omega_3+1)(\tilde{\delta}_3 - 6\omega_1 - 2\tilde{\delta}_4) - 3\omega_1 - \tilde{\delta}_4 - \beta^{-5}x_3\tilde{\delta}_3''(x_1+x_2+x_3)}{r^3}\end{aligned}\right\} \\ &, n = 3-5\end{aligned} \tag{58}$$

$$\begin{aligned}\dot{\vartheta}_3 &= \sum_{i=1}^{5} A_{i4}\pi(rr_0)^{-0.5}(\cos\dot{\theta}_i(\lambda_{32}+4\lambda_{33}v_i^2)\sum_{m=3}^{5}\hat{\rho}_{im}\hat{}g_m + 4\lambda_{32}\rho_{i2}g_2v_i^3\kappa_{i5}\kappa_{i1}^{-1}(2/3\lambda_{32}\cos\dot{\theta}_i + \lambda_{33}(rr_0)^{-2}\sin^{-1}\dot{\theta}_i)\\ &+15rr_ig_6\lambda_{32}v_i^3\kappa_{i5}\kappa_{i1}^{-1}\cot\theta_i(3\cos 0.5\dot{\theta}_i - 6\cos\dot{\theta}_i\sin^2\dot{\theta}_i - 0.25\sin^2\theta_i\cos 3\dot{\theta}_i)(2v_i^2\lambda_{33}+\lambda_{32}(rr_0)^{-1}\sin^{-1}\theta_i))\\ &+\mu^2\rho^{-1}\left\{\begin{array}{l}\dfrac{w_{13}^9}{r^6}-\dfrac{5x_3w_{13}^1}{r^7}+\dfrac{w_{13}^{10}}{r^5}+\dfrac{w_{13}^{11}}{r^4}+\dfrac{w_{13}^{12}}{r^3}+\dfrac{2\beta^{-3}\tilde{\delta}_3'}{r^2}-\dfrac{5x_3w_{23}^1}{r^7}+\dfrac{w_{23}^5}{r^6}+\dfrac{w_{23}^6}{r^5}+\dfrac{w_{23}^7}{r^4}+\dfrac{\beta^{-3}\tilde{\delta}_3'}{r^2}+\dfrac{\beta^{-3}\tilde{\delta}_3'}{r^2}+\dfrac{w_{33}^8}{r^6}+\dfrac{w_{33}^9}{r^5}+\dfrac{w_{33}^{10}}{r^4}\\ +\dfrac{\tilde{\delta}_3-\beta^{-5}x_3\tilde{\delta}_3''(x_1+x_2+x_3)}{r^3}-\dfrac{5x_3w_{33}^1}{r^7}+\dfrac{2(\omega_3+1)(\tilde{\delta}_3-6\omega_1-2\tilde{\delta}_4)-3\omega_1-\tilde{\delta}_4-\beta^{-5}x_3\tilde{\delta}_3''(x_1+x_2+x_3)}{r^3}\end{array}\right\}\end{aligned} \tag{59}$$

where $\bar{\dot{\sigma}}_{3n} = \left[\dot{\sigma}_{33} \quad \dot{D}_3 \quad \dot{B}_3 \quad \dot{\vartheta}_3\right]$,the more detailed process are listed in the Appendix D.

9. Numerical procedure

A method proposed by [38, 41, 42] can be generalized for solving the hypersingular integral in Eqs. (23) through (25) numerically. Making use of the behavior near the crack front, the extended incremental displacement discontinuity gradient's unknown functions can be written as

$$\dot{\hat{U}}_{i,J} = F_{iJ}\xi_2^{\lambda_J}W \tag{60}$$

$a_{iJmn}(t,\tau,\tau')$ are unknown constants. A set of algebraic equations for the unknown $a_{iJmn}(t,\tau,\tau')$ can be obtained

$$\sum_{s=0}^{S}\sum_{h=0}^{H} a_{lJsh}I_{lJsh}^{i} = -\dot{p}_J \tag{61}$$

where $I_{lJsh}(x_1, x_2)$ are defined in the appendix D. The non-dimensional extended DSIFs around the 3D crack propagation front $F_{I,\lambda}$ and inner crack propagation front F_I are defined as

$$F_{1,\lambda} = K_{1,\lambda}/\sigma_{33}^{\infty}b^{1-\lambda} \qquad F_1 = K_1^{\hat{i}}/\sigma_{33}^{\infty}\sqrt{b} \tag{62}$$

$$F_{2,\lambda} = K_{2,\lambda}/\sigma_{31}^{\infty}b^{1-\lambda} \qquad F_2 = K_2/\sigma_{31}^{\infty}\sqrt{b} \tag{63}$$

$$F_{3,\lambda} = K_{3,\lambda}^{i}/\sigma_{32}^{\infty}b^{1-\lambda} \qquad F_3 = K_3/\sigma_{32}^{\infty}\sqrt{b} \tag{64}$$

$$F_{4,\lambda} = K_{4,\lambda}/D_{33}^{\infty}b^{1-\lambda} \qquad F_4 = K_4/D_{33}^{\infty}\sqrt{b} \tag{65}$$

$$F_{5,\lambda} = K_{5,\lambda}/B_{33}^{\infty}b^{1-\lambda} \qquad F_5 = K_5/B_{33}^{\infty}\sqrt{b} \tag{66}$$

$$F_{6,\lambda} = K_{6,\lambda}/\vartheta_3^{\infty}b^{1-\lambda} \qquad F_6 = K_6/\vartheta_3^{\infty}\sqrt{b} \tag{67}$$

10. Numerical solutions and discussions

In this section, the numerical solutions and calculations described in the present paper are used in analyzing a 3D rectangle fluid driven crack propagation mechanism under he mechanical loads $\dot{\sigma}_{3i}^{\infty}$, the electric loads $\dot{D}_{33}^{\infty}$, the magnetic loads $\dot{B}_{33}^{\infty}$ and the thermal loads $\dot{\vartheta}_{33}^{\infty}$ in infinity. The non-dimensional independent material constants are listed in Table 2.1 and 2.2.

Table.2.1. Material constants for solid part

Table 2.2 Material constants and initial condition for fluid part

To facility the computing and comparing, we use non-dimensional quantities as follows:

$$\bar{c}_{ij} = c_{ij}/c_{11},\ \bar{e}_{ij} = e_{ij}/\sqrt{c_{11}e_{11}}\ ,\bar{\in}_{ij} = \in_{ij}/\in_{11},\ \bar{d}_{ij} = d_{ij}/\sqrt{c_{11}\mu_{11}}\ ,\ \bar{g}_{ij} = d_{ij}/\sqrt{\in_{11}\mu_{11}} \tag{68}$$

$$\bar{\mu}_{ij} = \mu_{ij} / \mu_{11}, \bar{\phi} = \sqrt{\in_{11} / c_{11}}\phi, \bar{\varphi} = \sqrt{\mu_{11} / c_{11}}\varphi, \bar{D}_i = D_i / \sqrt{c_{11} \in_{11}}; \bar{B}_i = B_i / \sqrt{c_{11}\mu_{11}} \quad (69)$$

$$\bar{L} = \frac{L}{L}, \bar{Q} = \frac{Q}{Q}, \bar{G} = \frac{G}{G}, \bar{\rho} = \frac{\rho}{\rho}, \bar{\sigma} = \frac{\sigma}{\sigma} \quad (70)$$

$$Pe = \frac{\bar{L}^2\bar{V}}{D}, \bar{V} = \frac{5\bar{Q}}{18\bar{L}^2}, Re = \frac{\bar{\rho}\bar{L}\bar{V}}{1000\eta^*}, We = \frac{\bar{\rho}\bar{L}\bar{V}^2}{10^9\bar{\sigma}}, Ca = \frac{\eta^*\bar{V}}{10^6\bar{\sigma}} \quad (71)$$

10.1 Compliance of boundary condition and convergence of numerical solutions

Figure 2.2 shows the compliance of the boundary condition along the crack surface，it can be shown that the extended remaining incremental stress waves on the collocation points (KK=LL=20×20,) possess a stable value at the flaw surface (the blue region), though they increase sharply at the corner points (the red color region). The present numerical method for multiple 3D flaws is stable and convincing.

Fig.2.2 Extended remaining stress waves on the flaw surface when b/a=1, KK=LL=20×20

10.2 Extended dynamic stress intensity factor

The crack shape ratio is a/b=1, the polynomial exponents are $M = N = 13$, the collocation points are $KK = LL = 20 \times 20$, the delay time arising from the hypocenter is $\tau = 0$, the delay time arising from the seismic wave is $\tau' = 0$, the near-field extended dynamic stress intensity factors are $F_I\,(r,\hat{\theta},t,\tau,\tau')$, and the radiation distribution for *P*- and *S*-waves at the crack surface as a function of θ, ϕ, x_1 / a are shown in Figures 2.3 through 2.15.

10.2.1 Dynamic stress intensity factors F_i

As shown in Figure 2.3, the crack is located on the ox_1x_2 plane, the area surrounded by the red line is the crack surface, p_i (i=1, 2, 3) represents the greatest principal tension stress (the least compressive principal stress), the intermediate compressive principal stress, and the least principal tension stress (the greatest compressive principal stress) on the crack surface before the crack begins to propagate, respectively. The angle of internal friction, $\undertilde{\theta}$, is the orientation of the greatest principal stress tension axis to the x_3 axis, $\undertilde{\theta} = 0.5\tan^{-1}\undertilde{\mu}^{-1}$, and $\undertilde{\mu}$ is the coefficient of internal friction.

Figure 2.3. Sketch map of the crack model for F_i

In Figure 2.3a, the crack propagation direction is perpendicular to the crack plane ox_1x_2 as shown by the arrows C_1 and C_1' (in the $\pm x_3$ axis direction, open crack model). In Figure 2.3b, the crack propagation direction is to the crack plane ox_1x_2 as shown by the arrows C_2 and C_2' (in the $\pm x_1$ axis direction, shear crack model). In Figure 2.3c, the crack propagation direction is parallel to the crack plane ox_1x_2 as shown by the arrows C_3 and C_3' (in the $\pm x_2$ axis direction, tear crack model).

It is well known that most earthquakes arise from mechanical instabilities that result from the sudden failure of the rock to sustain the shear stresses acting across a surface; the surface may be a pre-existing fault or a new facture caused by the failure. Figure 2.3 establishes a relationship between the failure model of co-seismic slip based on the Coulomb-Navier-Mohr theory of failure and the Anderson theory [44-46], and the fracture mechanics crack model based on the classical fracture theory [47-51].

10.2.1.1. 2D dimensionless DSIFs for *P*- and *S*-waves

Figure 2.4. Two dimensionless near-field F_{i,λ_i} radiation distributions for *P*- and *S*-waves

The 2D dimensionless near-field DSIFs F_{i,λ_i} radiation distribution for *P*- and *S*- waves as a function of θ, x_1/a and x_2/b are shown in Figure 2.4. Due to the symmetry, only the numerical results of DSIFs F_{i,λ_i} for $x_1/a \geq 0$ ($-1 \leq x_1/a \leq 1$) are given. The simulated results show that the DSIFs F_{i,λ_i} on $x_2 = \pm b$ sides decrease with increasing x_1 when $-1 \leq x_1/a \leq 0$, but increase with increasing x_1 when $0 \leq x_1/a \leq 1$. DSIFs F_{i,λ_i} reach a maximum value when $x_1/a = 0$, and F_{i,λ_i} reach a minimum value when $x_1/a = \pm 1$. Apart form these; there are two other important results. First, the DSIFs F_{i,λ_i} for $-1 \leq x_1/a \leq 1$ (x_2/b is fixed) follow the same distribution principle as do those for $-1 \leq x_2/b \leq 1$ (x_1/a is fixed). Secondly, the results of the numerical simulation curves are consistent with the data of co-seismic slip displacements for *P*-waves, as the F_{i,λ_i} are symmetrically distributed about the central axis, and reach the maximum value at $\theta = \pi/4$, $\theta = 3\pi/4$, $\theta = 5\pi/4$ and $\theta = 7\pi/4$ in quadrants *I, II, III,* and *IV*, respectively [52].

From these figures it can be seen that the radiation of DSIFs F_{i,λ_i} under *S*-waves is based on the same distribution principle as their distribution under *P*-waves but with a different symmetric angle. The DSIFs F_{i,λ_i} reached the maximum value at $\theta = 0$, $\theta = \pi/2$, $\theta = \pi$, and $\theta = 3\pi/2$ in quadrants *I, II, III,* and *IV*, respectively. The numerical simulation curves are also consistent with the corresponding results of co-seismic slip displacements for *S*- waves [52].

10.2.1.2. 3D dimensionless DSIFs for *P*-waves

The numerical results in Figures 2.5 through 2.7 shows that F_{i,λ_i} varies with θ and ϕ in the area $[0,2\pi]$ for *P*-waves. The DSIFs F_{1,λ_1} (Figure 2.5), F_{2,λ_2} (Figure2.6), and F_{3,λ_3} (Figure 2.7) based on the same method and the numerical/graphical representation have the pattern of a whirl of rose petals, but with different magnitudes at different locations ($x_1 / a = 0;0.2;0.4;0.6;0.8;1.0$).

The result is a symmetrical distribution about the axis. When ϕ is fixed, the DSIF F_{i,λ_i} reaches the maximum value at $\theta = \pi / 4$, $\theta = 3\pi / 4$, $\theta = 5\pi / 4$, and $\theta = 7\pi / 4$ in quadrants *I, II, III,* and *IV*, respectively. When θ is fixed, the DSIF F_{i,λ_i} reached the maximum value at $\phi = \pm\pi / 2$.

The crack location parameters θ and ϕ have a stronger influence on the DSIFs F_{i,λ_i} than does the location parameter x_1 / a. Among these parameters, θ is the primary factor in determining the results of the DSIFs F_{i,λ_i}.

When θ and ϕ are fixed, the simulated results show that the DSIFs F_{1,λ_1}, F_{2,λ_2} and F_{3,λ_3} on $x_2 = \pm b$ sides decrease with increasing x_1 when $-1 \le x_1 / a \le 0$, but increase with increasing x_1 when $0 \le x_1 / a \le 1$. The DSIFs F_{i,λ_i} reached the maximum value when $x_1 / a = 0$, and F_{i,λ_i} reached the minimum value when $x_1 / a = \pm 1$.

Fig.2.5. 3D dimensionless near-field F_{1,λ_1} radiation distribution for *P*- wave

Fig.2.6. 3D dimensionless near-field F_{2,λ_2} radiation distribution for *P*- wave

Fig.2.7. 3D dimensionless near-field F_{3,λ_3} radiation distribution for *P*- wave

10.2.1.3. 3D dimensionless DSIFs for *S*- waves

The numerical results in Figures 2.8 through 10 show that the F_{i,λ_i} varies with θ and ϕ in the area $[0,2\pi]$ for *S*-waves. The DSIFs F_{1,λ_1} (Figure 2.8), F_{2,λ_2} (Figure 2.9), and F_{3,λ_3} (Figure 2.10) based on the same method and numerical/graphical representation have the pattern of a whirl of rose petals, but with different magnitudes at different locations ($x_1 / a = 0;0.2;0.4;0.6;0.8;1.0$).

The result is a symmetrical distribution about the axis. When ϕ is fixed, the DSIF F_i reached the maximum value at $\theta = 0$, $\theta = \pi / 2$, $\theta = 3\pi / 2$ and $\theta = 2\pi$ in quadrants *I, II, III,* and *IV*, respectively. When θ is fixed, the DSIF F_i reached the maximum value at $\phi = \pm\pi / 2$.

Fig.2.8. 3D dimensionless near-field F_{1,λ_1} radiation distribution for *S*- wave

Fig.2.9. 3D dimensionless near-field F_{2,λ_2} radiation distribution for *S*- wave

Fig.2.10. 3D dimensionless near-field F_{3,λ_3} radiation distribution for *S*- wave

It can be generally concluded that with changes in the variable θ from 0 to 2π, the DSIFs F_{i,λ_i} for *P*-waves have a symmetrical distribution of θ in quadrants *I, II, III,* and *IV*, and reach four peak values at $\theta = \pi/4$, $\theta = 3\pi/4$, $\theta = 5\pi/4$ and $\theta = 7\pi/4$.

With the change of the variable θ from 0 to 2π, the DSIFs F_{i,λ_i} for *S*-waves also show a symmetrical distribution of θ in quadrants *I, II, III,* and *IV*, and reach four peak values at $\theta = 0$, $\theta = \pi/2$, $\theta = \pi$ and $\theta = 3\pi/2$.

The DSIFs F_{i,λ_i} for *P*- and *S*-waves show a symmetrical distribution of x_1/a at $x_2/b = \pm 1$ sides and x_2/b at $x_1/a = \pm 1$ sides, respectively. It reached the maximum value at points (-1,0), (1,0), (0,-1), and (0,1), while it reached the minimum value at points (-1,-1), (-1,1), (1,-1) and (1,1). These means that F_{i,λ_i} reached maximum values at the crack side centre, while F_{i,λ_i} reached the minimum values at the horn of the crack.

The crack location parameters θ and ϕ have a stronger influence on the DSIFs F_{1,λ_1} than does the location parameter x_1/a. Among these parameters, θ is the primary factor in determining the results of the DSIFs F_{1,λ_1}.

When θ and ϕ are fixed, the simulated results show that the DSIFs F_{1,λ_1}, F_{2,λ_2}, and F_{3,λ_3} on $x_2 = \pm b$ sides decrease with increasing x_1 when $-1 \le x_1/a \le 0$, but increase with increasing x_1 when $0 \le x_1/a \le 1$. The DSIFs F_{i,λ_i} reached the maximum value when $x_1/a = 0$, and F_{i,λ_i} reached the minimum value when $x_1/a = \pm 1$.

10.2.2Electric DSIF F_{4,λ_4} and Magnetic DSIF F_{5,λ_5}

10.2.2.1 2D dimensionless electric and magnetic DSIFs for *P*- and *S*-waves

Fig.2.11. 2D dimensionless near-field F_{4,λ_4} and F_{5,λ_5} radiation distribution for *P*- and *S*- wave

The radiation distribution of 2D dimensionless near-field electric DSIFs F_{4,λ_4} and magnetic DSIFs F_{5,λ_5} for *P*- and *S*- waves as a function of θ, x_1/a and x_2/b are shown in Figures 2.11. Due to the symmetry, only the numerical results of the DSIFs F_{4,λ_4} and F_{5,λ_5} for $x_1/a \geq 0$ ($-1 \leq x_1/a \leq 1$) are given. The simulated results show that the both F_{4,λ_4} and F_{5,λ_5} decrease with increasing x_1 when $-1 \leq x_1/a \leq 0$, but increase with increasing x_1 when $0 \leq x_1/a \leq 1$ at $x_2 = \pm 1$ sides, when $x_1/a = 0$, the DSIFs F_{4,λ_4} and F_{5,λ_5} reached the maximum value. Conversely, they reached the minimum value when $x_1/a = \pm 1$. The DSIFs F_{4,λ_4} and F_{5,λ_5} for *P*-waves based on the same method and the numerical representation show the pattern of a rose curve, but with different magnitudes at different values of x_1/a. Apart form these; there are two other important results. First, the DSIFs F_{4,λ_4} and F_{5,λ_5} for $-1 \leq x_1/a \leq 1$ (x_2/b is fixed) follow the same distribution principle as do those for $-1 \leq x_2/b \leq 1$ (x_1/a is fixed). Secondly, the results of the numerical simulation curves are consistent with the data of co-seismic slip displacements for *P*-waves. The DSIFs F_{4,λ_4} and F_{5,λ_5} are symmetrically distributed through the central axis and reach the maximum value at $\theta = 7\pi/36$, $\theta = 29\pi/36$, $\theta = 43\pi/36$ and $\theta = 65\pi/36$ in quadrant *I, II ,III,* and *IV*, respectively [52].

These figures show that the radiation of DSIFs F_{4,λ_4} and F_{5,λ_5} under *S*-waves is based on a different distribution principle than its distribution under *P*-waves. The DSIFs F_{4,λ_4} and F_{5,λ_5} reached the maximum value at $\theta = 0$, $\theta = 2\pi/3$, and $\theta = 4\pi/3$ in quadrants *I, II,* and *IIII*, respectively. The DSIFs F_{4,λ_4} and F_{5,λ_5} for *S*-waves based on the same method and numerical representation show the pattern of a three leaf curve, but with different magnitudes at different values of x_1/a.

10.2.2.2. 3D dimensionless electric and magnetic DSIFs for *P*-waves

Fig.2.12. 3D dimensionless near-field F_{4,λ_4} radiation distribution for *P*- wave

Fig.2.13. 3D dimensionless near-field F_{5,λ_5} radiation distribution for *P*- wave

The numerical results show that F_{4,λ_4} and F_{5,λ_5} varying with θ and ϕ in the area $[0, 2\pi]$ for *P*-waves are symmetrically distributed about the axis, and are based on the same method and numerical/graphical representation as a double-wag-whirl-radar curve have but different magnitudes at different locations ($x_1/a = 0; 0.2; 0.4; 0.6; 0.8; 1.0$).

When ϕ is fixed, the results reached the maximum value at $\theta = \pi/4$, $\theta = 3\pi/4$, $\theta = 5\pi/4$, and $\theta = 7\pi/4$ in quadrants *I, II, III,* and *IV*, respectively. When θ is fixed, the results reached the maximum value at $\phi = \pm\pi/2$.

10.2.2.3. 3D dimensionless electric and magnetic DSIFs for *S*-waves

Fig.2.14. 3D dimensionless near-field F_{4,λ_4} radiation distribution for *S*- wave

Fig.2.15. 3D dimensionless near-field F_{5,λ_5} radiation distribution for *S*- wave

The numerical results show that the F_{4,λ_4} (Figure 2.14) and F_{5,λ_5} (Figure 2.15) varying with θ and ϕ in the area $[0,2\pi]$ for *S*-waves are symmetrically distributed about the axis, and are based on the same method and numerical/graphical representation as a double-wag-whirl-radar curve, but with different magnitudes at different locations ($x_1/a = 0;0.2;0.4;0.6;0.8;1.0$).

When ϕ is fixed, the results reached the maximum value at $\theta = 7\pi/36$, $\theta = 29\pi/36$, $\theta = 43\pi/36$, and $\theta = 65\pi/36$ in quadrants *I, II, III,* and *IV*, respectively. When θ is fixed, the results reached the maximum value at $\phi = \pm\pi/2$.

In general, the crack location parameters θ and ϕ have a stronger influence on the DSIFs F_{4,λ_4} and F_{5,λ_5} than does the location parameter x_1/a . Among these parameters, that of θ is the primary factor in determining the results of DSIFs F_{4,λ_4} and F_{5,λ_5} . When θ and ϕ are fixed, the simulated results showed that DSIFs F_{4,λ_4} and F_{5,λ_5} on $x_2 = \pm b$ sides decrease with increasing x_1 when $-1 \le x_1/a \le 0$, but increase with increasing x_1 when $0 \le x_1/a \le 1$. The DSIFs F_{4,λ_4} and F_{5,λ_5} reached their maximum value when $x_1/a = 0$ and F_{i,λ_i} reached its minimum value when $x_1/a = \pm 1$.

10.2.3 Thermal

10.2.3.1. 2D dimensionless thermal DSIFs for *P*- and *S*-waves

Fig.2.16. 2D dimensionless near-field F_{6,λ_6} radiation distribution for *P*- and *S*- wave

The radiation distribution of 2D dimensionless near-field thermal DSIFs F_{6,λ_6} for *P*- and *S*- waves as a function of θ , x_1/a and x_2/b are shown in Figures 2.16. Due to the symmetry, only the numerical results of the DSIFs F_{6,λ_6} for $x_1/a \ge 0$ ($-1 \le x_1/a \le 1$) are given. The simulated results show that the F_{6,λ_6} decrease with increasing x_1 when $-1 \le x_1/a \le 0$, but increase with increasing x_1 when $0 \le x_1/a \le 1$ at $x_2 = \pm 1$ sides. When $x_1/a = 0$, the F_{6,λ_6} reached the maximum value. Conversely, they reached the minimum value when $x_1/a = \pm 1$. The F_{6,λ_6} for *P*-waves based on the same method and the numerical representation show the pattern of a rose curve. Apart form these; there are two other important results. First, the F_{6,λ_6} for $-1 \le x_1 / a \le 1$ (x_2 / b is fixed) follow the same distribution principle as do those for $-1 \le x_2 / b \le 1$ (x_1 / a is fixed). Secondly, the results of the numerical simulation curves are consistent with the data of co-seismic slip displacements for *P*-waves. The F_{6,λ_6} **is** symmetrically distributed through the central axis and reach the maximum value at $\theta = 7\pi / 36$, $\theta = 29\pi / 36$, $\theta = 43\pi / 36$ and $\theta = 65\pi / 36$ in quadrant *I, II ,III,* and *IV*, respectively [52]. These figures show that the F_{6,λ_6} under *S*-waves is based on a different distribution principle than its distribution under *P*-waves. The F_{6,λ_6} reached the maximum value at $\theta = 0$, $\theta = 2\pi / 3$, and $\theta = 4\pi / 3$ in quadrants *I, II,* and *IIII*, respectively. The F_{6,λ_6} for *S*-wave based on the same method and numerical representation show the pattern of a three leaf curve, but with different magnitudes at different values of x_1 / a.

10.2.3.2. 3D thermal DSIFs for *P*-waves

Fig.2.17. 3D dimensionless near-field F_{6,λ_6} radiation distribution for *P*- wave

The numerical results show that F_{6,λ_6} varying with θ and ϕ in the area $[0, 2\pi]$ for *P*-waves are symmetrically distributed about the axis, and are based on the same method and numerical/graphical representation as a double-wag-whirl-radar curve have but different magnitudes at different locations ($x_1 / a = 0;0.2;0.4;0.6;0.8;1.0$). When ϕ is fixed, the results reached the maximum value at $\theta = \pi / 4$, $\theta = 3\pi / 4$, $\theta = 5\pi / 4$, and $\theta = 7\pi / 4$ in quadrants *I, II, III,* and *IV*, respectively. When θ is fixed, the results reached the maximum value at $\phi = \pm\pi / 2$.

10.2.3.3. 3D thermal DSIFs for *S*-waves

Fig.2.18. 3D dimensionless near-field F_{6,λ_6} radiation distribution for *S*- wave

The numerical results show that the F_{6,λ_6} varying with θ and ϕ in the area $[0, 2\pi]$ for *S*-waves are symmetrically distributed about the axis, and are based on the same method and numerical/graphical representation as a double-wag-whirl-radar curve, but with different magnitudes at different locations ($x_1 / a = 0;0.2;0.4;0.6;0.8;1.0$). When ϕ is fixed, the results reached the maximum value at $\theta = 7\pi / 36$, $\theta = 29\pi / 36$, $\theta = 43\pi / 36$, and $\theta = 65\pi / 36$ in quadrants *I, II, III,* and *IV*, respectively. When θ is fixed, the results reached the maximum value at $\phi = \pm\pi / 2$.

In general, the crack location parameters θ and ϕ have a stronger influence on the F_{6,λ_6} than does the location parameter x_1/a. Among these parameters, that of θ is the primary factor in determining the results. When θ and ϕ are fixed, the simulated results showed that the F_{6,λ_6} on $x_2 = \pm b$ sides decrease with increasing x_1 when $-1 \le x_1/a \le 0$, but increase with increasing x_1 when $0 \le x_1/a \le 1$. The F_{6,λ_6} reached their maximum value when $x_1/a = 0$ and F_{i,λ_i} reached its minimum value when $x_1/a = \pm 1$.

10.3 General extended singular pore stress waves

Fig.2.19. Dimensionless $\dot{\sigma}_{13}$ radiation distribution for *P*-and *S*- waves

Fig.2.20. Dimensionless $\dot{\sigma}_{23}$ radiation distribution for *P*-and *S*- waves

Fig.2.21. Dimensionless $\dot{\sigma}_{33}$ radiation distribution for *P*-and *S*- waves

The numerical results in Figures 2.19 through 2.21 shows that dimensionless singular pore stress waves $\dot{\sigma}_{i3}$ varieties with time for *P*-and S- waves. The $\dot{\sigma}_{i3}$ decrease with increasing until the time is reached to 10s.

Fig.2.22. Dimensionless electric $\dot{D}$ radiation distribution for *P*-and *S*- waves

Fig.2.23. Dimensionless magnetic $\dot{B}$ radiation distribution for *P*-and *S*- waves

Fig.2.24. Dimensionless thermal $\dot{\vartheta}$ radiation distribution for *P*-and *S*- waves

The numerical results in Figures 2.22 through 2.24 shows that dimensionless extended singular pore stress waves $\dot{D}$, $\dot{B}$, $\dot{\vartheta}$ varies with time for *P*-and S- waves. They decrease with increasing until the time is reached to 10s.

From the figures, we can obtain that force field have strongest influence on the pore stress, electric field and magnetic field have a stronger influence on the pore stress than thermal field. although, the relationship between force field pore stress, electric field pore stress, magnetic field pores stress and thermal field pore stress and time compliance with the same distribution principle.

In engineering practice, we can use electric, magnetic and thermal abnormal information to predict and analyze the co-seismic slip in place of force/displace abnormal information, compared with force field, electromagnetic and thermal is more easily detected around the co-seismic slip.

Equation Section 1**11. Conclusions**

In the present article, a 3D fluid driven crack propagation mechanism on co-seismic slips under fully coupled electromagnetothermoelastic *P*- and *S*-wave fields was investigated by hybrid hypersingular equation method. This method has been proposed here for the first time. The following conclusions can be drawn from our results:

Using the principles of extended wave time-domain finite-part integrals and the extended wave time-domain main-part integrals method, the 3D crack fluid driven propagation problem on co-seismic slips for *P*- and *S*-waves has been analyzed through a set of hybrid hypersingular equations coupled with nonlinear boundary integral equations.

Using the wave time-domain finite-part analysis method, the behavior of the general extended singular stress indices around the crack front terminating at the slip surface have been analyzed, and the general extended singular pore stress waves and the extended dynamic stress intensity factors have been obtained by a closed-form solution.

A numerical method for treating the 3D fluid driven crack propagation problem subjected to extended fully coupled loads is proposed, and the radiation distribution of 2D/3D dimensionless near-field extended DSIFs and SPSWs for *P*- and *S*-waves at the crack surface have been calculated. The results show that the extended dynamic electric stress intensity factor F_4 and the extended dynamic magnetic stress intensity factor F_5 have different changing rules than does F_i. The force field has strongest influence on the pore stress; electric field and magnetic field have a stronger influence on the pore stress than thermal field, although, they compliance with the same distribution principle.

In conclusion, an analysis of the type described in this paper can be utilized to help understand the extended electromagnetic fracture mechanism for any 3D crack propagation problem in co-seismic slip. In engineering practice, we can use electric, magnetic and thermal and water abnormal information to predict and analyze the co-seismic slip in place of force/displace abnormal information, compared with force field, electromagnetic and thermal is more easily detected around the co-seismic slip.

Acknowledgements

This work was supported by a grant from the National Natural Science Foundation of China (No.40673016), and the authors would like to thank the editors for their help and thank the anonymous reviewer’s constructive comments.

Appendix A

u_i The displacement wave

ϕ The electric field wave

φ The magnetic field wave

Υ The thermal field wave

$\dot{p}_i(t,\tau,\tau')$ The mechanical load

$\dot{p}_4(t,\tau,\tau')$, $\dot{q}_0(t,\tau,\tau')$ the electrical loads

$\dot{p}_5(t,\tau,\tau')$, $\dot{b}_0(t,\tau,\tau')$ the magnetic loads

$\dot{p}_6(t,\tau,\tau')$, $\dot{\vartheta}_0(t,\tau,\tau')$ the thermal loads

Q Flow rate

η_i Viscosity of phase i

λ Viscosity of rate

D Diffusion coefficient of molecule

L Character unit length of molecule

ρ_i Unite density of phase i

σ_i Surface tension of phase i

T Temperature ration

V_i Character velocity of phase i

t Unit time of molecule

Pe Peclet number

Re Reynolds number

We Weber number

Ca Capillarity number

G Wetting number

DX Fix lattice spacing

$\rho(t,x)$ The density of the material particle at time t and position x .

u Velocity field of the flow

φ Flow potential

k The flow diffusion coefficient

q The flow source term

c The flow material property

p The flow pressure

$\delta_{\alpha\beta}$ The Kronecker delta

μ The dynamic viscosity coefficient

e_{ij} The rate of strain tensor

f_i^b The flow body force

n_{ii} The particle number density

φ_i The molar fraction of component i

f The sum of the free energy densities the pure components

W The free energy of mixing

$\bar{\kappa}$ Boltzmann's constant

ξ The interface width

T The absolute temperatures

T_c The critical temperatures

$\mu_i(r)$ Chemical potentials,

P_{11} The normal pressure

P_{22}, P_{33} The transverse pressures.

$\Lambda = \frac{Dn}{\bar{\kappa}T}$ Constant mobility with diffusion coefficient D

η The phase dependent viscosity

C_{IK} The tensor coefficient dependent on the geometry of the boundary

x_i Fixed geographic Cartesian system

$S\ (S^+ \bigcup S^-)$ The slip surface

$\dot{p}_i(t,\tau,\tau')$ The mechanical load

$\dot{p}_4(t,\tau,\tau')$ or $\dot{q}_0(t,\tau,\tau')$ The electrical loads

$\dot{p}_5(t,\tau,\tau')$ or $\dot{b}_0(t,\tau,\tau')$ The magnetic loads

$\dot{p}_6(t,\tau,\tau')$ or $\dot{\vartheta}_0(t,\tau,\tau')$ The thermal loads

$\hat{x}_i$ The hypocenter of the coordinate systems

$\hat{x}_1\hat{x}_3$ The extended slip plane

$\hat{x}_2\hat{x}_3$ The auxiliary plane

$x_{\phi s}$ The fault strike

x_λ The fault slip

ρ Mass density

U_J The extended displacement wave

$<\bullet>$ The McAuley symbol

f^{el-mag} The Maxwell stress tensor

α Velocity of *P- wave*

β Velocity of S- *wave*

$\hat{P}$ Field point or observation point

$\hat{S}$ Epicenter point or source point

t Time

τ The delay times arising from hypocenter

τ' The delay times arising from the seismic wave

r The distance between the source point and observation point

$r_{,\hat{i}}$ The direction cosine of the field point

$\tilde{\delta}_I$ The kernel function of the general solution

K_{KIJ} The hypersingular kernel function

$\bar{K}_{IJ}$ The Cauchy kernel function

Appendix B

Equation Chapter (Next) Section 1Equation Chapter (Next) Section 2

$$E_{iJKl}=\begin{bmatrix} C_{iJKl} & -\Pi_{iJ} & 0 \\ 0 & 0 & -\lambda_{iJ} \end{bmatrix},\ \dot{Z}_{Kl}=[\dot{U}_{K,l} \quad \dot{\Upsilon}_{,l}]^T \tag{B.1}$$

$$C_{iJKl}=\begin{cases} c_{ijkl} & J,K=1,2,3 \\ e_{lij} & J=1,2,3;K=4 \\ e_{ikl} & J=4;K=1,2,3 \\ d_{lij} & J=1,2,3;K=5 \\ d_{ikl} & J=5;K=1,2,3 \\ -g_{il} & J=4;K=5orJ=5;K=4 \\ -\in_{il} & J,K=4 \\ -\mu_{il} & J,K=5 \end{cases} \tag{B.2}$$

$$\Pi_{iJ}=\begin{cases} \iota_{ij} & J=1,2,3;K=6 \\ \varsigma_{il} & J=4;K=6 \\ \eta_{il} & J=5;K=6 \end{cases} \tag{B.3}$$

$$\dot{U}_K=\begin{cases} \dot{u}_i & K=1,2,3 \\ \dot{\phi} & K=4 \\ \dot{\varphi} & K=5 \\ \dot{\Upsilon} & K=6 \end{cases} \tag{B.4}$$

$$W(\varphi)=2\bar{\kappa}T_c\varphi_\alpha(1-\varphi_\alpha)+\bar{\kappa}T\left[\varphi_\alpha\log\varphi_\alpha+(1-\varphi_\alpha)\log(1-\varphi_\alpha)\right] \tag{B.5}$$

$$\varphi_\alpha=\frac{n_\alpha}{n},\ \bar{\kappa}=\frac{\kappa}{T_c\xi^2},\ \mu_i(r)=\frac{\delta F}{\delta n_i(r)},\ \Lambda=\frac{Dn}{\bar{\kappa}T},\ \eta=\eta*h(\varphi) \tag{B.6}$$

$$h(\varphi)=\begin{cases}\dfrac{\lambda-1}{2\lambda}\tanh\left(\dfrac{\varphi-0.5}{\chi}\right)+\dfrac{\lambda+1}{2\lambda} & if\,\lambda\geq 1\\ \dfrac{\lambda-1}{2}\tanh\left(\dfrac{\varphi-0.5}{\chi}\right)+\dfrac{\lambda+1}{2} & if\,\lambda<1\end{cases} \tag{B.7}$$

$$\lambda=\frac{\eta_2}{\eta_1},\eta^*=\max\{\eta_1,\eta_2\}\quad when\ \chi\ll\varphi_2-\varphi_1,\omega_0^*=\lambda_i^w\delta_{3J}+\lambda_i^\phi\delta_{4J}+\lambda_i^\varphi\delta_{5J},x_i^*=x_i-\xi_i \tag{B.8}$$

$$\omega_1^*=(3R_{,i}R_J-\delta_{iJ})\int_{r/\beta}^{r/\alpha}\tilde{\delta}^1\tau'd\tau',\omega_2^*=\alpha^{-2}\tilde{\delta}^2-\beta^{-2}\tilde{\delta}^3,\omega_4^*=x_1^*R_0^{-1}\dot{R}_0^{-2}x_1^*\delta_{2J}-x_2^*\delta_{1J}-\dot{R}_0^{-1}\delta_{2J} \tag{B.9}$$

$$\omega_5^*=\dot{R}_i^{-1}\delta_{2J}-x_\alpha^*x_2^*R_i^{-1}(\delta_{\alpha J}\dot{R}_i^{-2}-\dot{R}_i^{-1}\omega_0^*-\lambda_i^\vartheta R_i^{-2}s_i\delta_{6J}),\omega_6^*=R_i^{-2}\omega_1^*+\delta_{iJ}\tilde{\delta}^3+R_{,i}R_{,J}\omega_3^* \tag{B.10}$$

$$\omega_7^*=\dot{R}_0^{-2}\omega_1^*+R_{,i}R_{,J}\omega_2^*+\delta_{iJ}\tilde{\delta}^3,\omega_8^*=R_i^{-2}\omega_1^*+R_{,i}R_{,J}\omega_2^*+\delta_{iJ}\tilde{\delta}^3,\ \omega_9^*=\dot{R}_i^{-1}x_\alpha^*\delta_{\alpha J}+\omega_0^*-R_i^{-2}x_\alpha^*\lambda_i^\vartheta s_i^2\delta_{6J} \tag{B.11}$$

Appendix C

Equation Section 3

$$K_{111}=4\omega_3(3x_1^2\omega_1-\omega_1-x_1^2\tilde{\delta}_4)(\omega_3+1.5)+x_2(\tilde{\delta}_4+3\omega_1)(2\omega_3x_1+2x_1+1) \tag{C.1}$$

$$K_{121}=-15x_1(x_1+x_2)\omega_1 \tag{C.2}$$

$$K_{131}=-15x_1(x_1+x_2)\omega_1 \tag{C.3}$$

$$\begin{aligned}K_{112}=&3(\tilde{\delta}_4+3\omega_1)\left[8\omega_3x_1^2(\omega_3+1.5)+5x_1x_2+x_1^2+x_1+x_2\right]+\\&x_1(\beta^{-5}\tilde{\delta}_3''-\alpha^{-5}\tilde{\delta}_2'')(2x_1^2+x_2^2+x_1)+6(3\omega_1x_1^2-\omega_1+x_1^2\tilde{\delta}_4)(\omega_3+1.5)\\&-10x_1^2(\omega_3+1)(\tilde{\delta}_3-6\omega_1-2\tilde{\delta}_4)+x_2(1-3\omega_1+\tilde{\delta}_4)\end{aligned} \tag{C.4}$$

$$K_{122}=3\omega_1-3x_1(x_1+x_2)\tilde{\delta}_3+x_1(3x_2+x_1)(3\omega_1+\tilde{\delta}_4) \tag{C.5}$$

$$K_{132}=x_1\left[\omega_1(x_1+x_2)\tilde{\delta}_3+(9x_1+6\omega_3x_1+x_2)(3\omega_1+\tilde{\delta}_4)\right] \tag{C.6}$$

$$K_{113}=2\omega_3(\omega_3+1)(\tilde{\delta}_3-6\omega_1-2\tilde{\delta}_4)-4\omega_3\beta^{-5}x_1(x_1\omega_1+x_1+0.5x_2)+1+2\tilde{\delta}_4 \tag{C.7}$$

$$K_{123}=\tilde{\delta}_3-\beta^{-5}x_1(x_1+x_2)\tilde{\delta}_3'' \tag{C.8}$$

$$K_{133}=\tilde{\delta}_3-3\omega_1-\tilde{\delta}_4-\beta^{-5}x_1\tilde{\delta}_3''(x_1+x_2)+\tilde{\delta}_3(\omega_3+1)(3\omega_1+\tilde{\delta}_4) \tag{C.9}$$

$$\begin{aligned}\bar{K}_{11}=&2x_1^3\frac{(\beta^{-3}\tilde{\delta}_3'-\alpha^{-5}\tilde{\delta}_2')(4\omega_3+3x_1x_2+x_2)-8\omega_3(\omega_3x_1+x_1+x_2)}{r^6}\\&+2\omega_3x_1\frac{4x_2+2x_1(\omega_3+1)-4\beta^{-3}\tilde{\delta}_3'(x_1\omega_1+x_1+0.5x_2)+x_1}{r^4}\\&+2\omega_3x_1\frac{x_2(\beta^{-5}\tilde{\delta}_3''-\alpha^{-5}\tilde{\delta}_2'')+2x_1^2(\omega_3+1)(2\alpha^{-5}\tilde{\delta}_2''-2\beta^{-5}\tilde{\delta}_3''-\alpha^{-3}\tilde{\delta}_2')}{r^4}\\&+\frac{\omega_2x_2^2-x_1^2(\beta^{-3}\tilde{\delta}_3'-\alpha^{-3}\tilde{\delta}_2')}{r^4}+\frac{\beta^{-3}\tilde{\delta}_3'(4\omega_3+4\omega_3\omega_1+1)}{r^2}-\frac{4\omega_2x_2^2x_1^2}{r^6}\end{aligned} \tag{C.10}$$

$$\bar{K}_{12} = x_1 \frac{\omega_2 x_2 - 3\beta^{-2}\tilde{\delta}_3'(x_1 + x_2) - x_2(3\omega_1 + \tilde{\delta}_4)(\beta^{-3}\tilde{\delta}_3' - \alpha^{-3}\tilde{\delta}_2')}{r^4} \tag{C.11}$$

$$\bar{K}_{13} = x_1 \frac{2(\omega_3 + 1)(\beta^{-2}\tilde{\delta}_3' - 2\beta^{-5}\tilde{\delta}_3'' + 2\alpha^{-5}\tilde{\delta}_2'') - (x_1 + x_2)\beta^{-2}\tilde{\delta}_3' - x_1^2(\beta^{-3}\tilde{\delta}_3' - \alpha^{-3}\tilde{\delta}_2')}{r^4} \tag{C.12}$$

$$K_{211} = 3x_1 x_2^2(3\omega_1 + \tilde{\delta}_4)(2x_1 + 1) \tag{C.13}$$

$$K_{212} = x_1\left[(\tilde{\delta}_4 + 3\omega_1)(2x_1 + 1 + 5x_2) + x_2^2(\beta^{-5}\tilde{\delta}_3'' - \alpha^{-5}\tilde{\delta}_2'')\right] \tag{C.14}$$

$$K_{213} = 0 \tag{C.15}$$

$$\bar{K}_{21} = x_1 x_2\left(x_2 \frac{3(\beta^{-3}\tilde{\delta}_3' - \alpha^{-3}\tilde{\delta}_2')(2x_1 + 1) - 4x_2\omega_2}{r^6} + \frac{4\omega_2 + \beta^{-3}\tilde{\delta}_3' - \alpha^{-3}\tilde{\delta}_2'}{r^4}\right) \tag{C.16}$$

$$K_{221} = 3x_2\left[2\omega_3(2\omega_3 x_2 + 2x_2 + x_1)(3\omega_1 x_2^2 - \omega_1 + x_2^2\tilde{\delta}_4) + 2\omega_3 x_2(3\omega_1 + \tilde{\delta}_4) - \omega_1(x_1 + x_2)\right] \tag{C.17}$$

$$\begin{aligned} K_{222} = 2\omega_3 &\begin{pmatrix} 6(x_2\omega_3 + 1)(3x_2^2\omega_1 - \omega_1 + x_2^2\tilde{\delta}_4) + 6x_2(2\omega_3 x_2 + 2x_2 + 2x_1)(3\omega_1 + \tilde{\delta}_4) + \\ x_2^3(x_2 + 2x_1)(\beta^{-5}\tilde{\delta}_3'' - \alpha^{-5}\tilde{\delta}_2'') - x_2^2(\tilde{\delta}_3 - 6\omega_1 - 2\tilde{\delta}_4) + x_1 x_2(\tilde{\delta}_3 - 3\omega_1 + \tilde{\delta}_4) \end{pmatrix} \\ &-3\omega_1 - x_2\tilde{\delta}_3(x_1 + x_2) + (x_2 x_1 - x_2^2)(3\omega_1 + \tilde{\delta}_4) + 3(3x_2^2\omega_1 - \omega_1 + x_2^2\tilde{\delta}_4) \end{aligned} \tag{C.18}$$

$$K_{223} = \tilde{\delta}_3 - 6\omega_1 - 2\tilde{\delta}_4 + \beta^{-5}x_2(x_1 + x_2)\tilde{\delta}_3' + 2\tilde{\delta}_3 - \tilde{\delta}_3''(x_1 + x_2) \tag{C.19}$$

$$\begin{aligned} \bar{K}_{22} = {} & 2\omega_3 x_2^3 \frac{3(2\omega_3 x_2 + 2x_2 + 2x_1 + 1/3)(\beta^{-3}\tilde{\delta}_3' - \alpha^{-3}\tilde{\delta}_2') - \omega_2(x_2 + 2x_1)}{r^6} \\ & + x_2 \frac{2\omega_3 x_2(\alpha^{-5}\tilde{\delta}_2'' - \beta^{-5}\tilde{\delta}_3'' - \alpha^{-3}\tilde{\delta}_2') + x_1(\alpha^{-5}\tilde{\delta}_2'' - \alpha^{-3}\tilde{\delta}_2' - \beta^{-5}\tilde{\delta}_3'')}{r^4} + \frac{3\beta^{-3}\tilde{\delta}_3'}{r^2} \\ & + \omega_2 \frac{x_1(2x_1 + x_2) + x_2(2x_2 + x_1)}{r^4} + x_2 \frac{\omega_2(x_1 + x_2) - (3\omega_1 + \tilde{\delta}_4)(\beta^{-5}\tilde{\delta}_3'' - \alpha^{-5}\tilde{\delta}_2'')}{r^4} \end{aligned} \tag{C.20}$$

$$K_{231} = -15x_2\omega_1(x_1 + x_2) \tag{C.21}$$

$$K_{232} = 2x_2(3\omega_3 x_2 + x_1)(3\omega_1 + \tilde{\delta}_4) - x_2(\tilde{\delta}_3 + \beta^{-3}\tilde{\delta}_3') - 3\omega_1 - 6x_2(\omega_3 + 1)(\tilde{\delta}_3 - 6\omega_1 - 2\tilde{\delta}_4) + (x_1 + x_2)\tilde{\delta}_3 \tag{C.22}$$

$$K_{233} = \beta^{-5}\tilde{\delta}_3'' x_2(x_1 + x_2) + (3\omega_1 + \tilde{\delta}_4)(2\omega_3 + 3) \tag{C.23}$$

$$\bar{K}_{23} = -2(\omega_3 + 1)\frac{(x_1 + x_2)x_2\beta^{-2}\tilde{\delta}_3' + 2x_1 x_2(\beta^{-3}\tilde{\delta}_3' - \alpha^{-3}\tilde{\delta}_2')}{r^4} + \frac{\omega_2(2\omega_3 x_2 + 2x_1 + 3x_2) - 2x_2\beta^{-3}\tilde{\delta}_3'(x_1 + x_2)}{r^4} + \frac{\beta^{-3}\tilde{\delta}_3'}{r^2} \tag{C.24}$$

$$K_{m12} = x_1 x_2(3\omega_1 + \tilde{\delta}_4) - 3(\omega_1 x_1^2 - \omega_1 - x_1^2\tilde{\delta}_4) \tag{C.25}$$

$$K_{m13} = 2(3\omega_1 + \tilde{\delta}_4) - \tilde{\delta}_3 \tag{C.26}$$

$$\bar{K}_{m1} = -\frac{4x_1\omega_2 x_2^2}{r^4} + \frac{2\beta^{-3}\tilde{\delta}_3'}{r^2} \tag{C.27}$$

$$K_{m22} = x_1 x_2(3\omega_1 + \tilde{\delta}_4) + 3(3x_2^2\omega_1 - \omega_1 - x_2^2\tilde{\delta}_4) \tag{C.28}$$

$$K_{m23} = \tilde{\delta}_3 \tag{C.29}$$

$$\bar{K}_{m2} = \frac{\omega_2 x_2 (x_1 + x_2)}{r^4} + \frac{\beta^{-5}\tilde{\delta}_3'}{r^2} \tag{C.30}$$

$$K_{m32} = -3\omega_1 - 3x_1\left[\tilde{\delta}_3(x_1 + x_2) - x_2(3\omega_1 + \tilde{\delta}_4)\right] \tag{C.31}$$

$$K_{m33} = 2(\omega_3 + 1)(\tilde{\delta}_3 - 6\omega_1 - \tilde{\delta}_4) - 3\omega_1 - \tilde{\delta}_4 \tag{C.32}$$

$$\bar{K}_{m3} = \frac{-3\beta^{-3}x_1\tilde{\delta}_3'(x_1 + x_2) - x_1 x_2(3\omega_1 + \tilde{\delta}_4)(\beta^{-3}\tilde{\delta}_3' - \alpha^{-3}\tilde{\delta}_2')}{r^4} + \frac{\beta^{-3}\tilde{\delta}_3'}{r^2} \tag{C.33}$$

where $\omega_3 = \dfrac{1}{1-2\nu}$, $\omega_1 = \int_{r/\beta}^{r/\alpha} \tilde{\delta}_1 \tau' d\tau'$, $\omega_2 = \alpha^{-3}\tilde{\delta}_2' - \beta^{-3}\tilde{\delta}_3', m = 3-6$

Appendix D

Equation Section 4

Consider a small semi-circular domain S_ε on the crack surface that includes point q_0. Using the time-domain main-part analytical method [25], the following relations can be derived:

$$\int_{-\infty}^{-\infty}\int_{-\infty}^{+\infty} \oint_{S_\varepsilon} r^{-3}\dot{\tilde{u}}_{I,J} d\xi_1\xi_2 d\tau d\tau' \cong -2\pi\int_{-\infty}^{+\infty}\int_{-\infty}^{-\infty} \lambda_J g_J x_2^{\lambda_J - 1}\cot(\lambda_J\pi) d\tau d\tau' \tag{D.1}$$

$$\int_{-\infty}^{+\infty}\int_{-\infty}^{+\infty} \oint_{S_\varepsilon} 3r^{-5}(x_2 - \xi_2)^2\dot{\tilde{u}}_{I,J} d\xi_1\xi_2 d\tau d\tau' \cong -4\pi\int_{-\infty}^{+\infty}\int_{-\infty}^{+\infty} \lambda_J g_J x_2^{\lambda_J - 1}\cot(\lambda_J\pi) d\tau d\tau' \tag{D.2}$$

$$\int_{-\infty}^{+\infty}\int_{-\infty}^{+\infty} \oint_{S_\varepsilon} 3r^{-5}(x_1 - \xi_1)^2\dot{\tilde{u}}_{I,J} d\xi_1\xi_2 d\tau d\tau' \cong -2\pi\int_{-\infty}^{+\infty}\int_{-\infty}^{+\infty} \lambda_J g_J x_2^{\lambda_J - 1}\cot(\lambda_J\pi) d\tau d\tau' \tag{D.3}$$

$$\int_{-\infty}^{+\infty}\int_{-\infty}^{+\infty} \int_{S_\varepsilon} r^{-3}(x_2 - \xi_2)\dot{\tilde{u}}_{I,J} d\xi_1\xi_2 d\tau d\tau' \cong 2\pi\int_{-\infty}^{+\infty}\int_{-\infty}^{+\infty} g_J x_2^{\lambda_J}\cot(\lambda_J\pi) d\tau d\tau' \tag{D.4}$$

$$\int_{-\infty}^{+\infty}\int_{-\infty}^{+\infty} \oint_{S_\varepsilon} r^{-7}x_2\xi_2(x_1 - \xi_1)^2\dot{\tilde{u}}_{I,J} d\xi_1 d\xi_2 d\tau d\tau' \cong \frac{2}{45}\pi\int_{-\infty}^{+\infty}\int_{-\infty}^{+\infty} \lambda_J(1-\lambda_J^2) g_J\, x_2^{\lambda_J - 1}\sin(\lambda_J\pi)^{-1} d\tau d\tau' \tag{D.5}$$

$$\int_{-\infty}^{+\infty}\int_{-\infty}^{+\infty} \int_{S_\varepsilon} r^{-7}x_2\xi_2(x_2 + \xi_2)^2\dot{\tilde{u}}_{I,J} d\xi_1 d\xi_2 d\tau d\tau' \cong \frac{2}{45}\pi\int_{-\infty}^{+\infty}\int_{-\infty}^{+\infty} \lambda_J(1-\lambda_J^2) g_J\, x_2^{\lambda_J - 1}\cos(\lambda_J\pi)^{-1} d\tau d\tau' \tag{D.6}$$

where r is the distance from point $\hat{P}$ to the dislocation front point q_0. Considering the relations in Eqs. (25-30), the following relations can be obtained:

$$\int_{-\infty}^{+\infty}\int_{-\infty}^{+\infty} \int_{s_\varepsilon} R_0^{-3}(1 - 3R_0^{-2}(x_2 - \xi_2)^2)\dot{\tilde{u}}_{I,J} d\xi_1\xi_2 d\tau d\tau' \cong \int_{-\infty}^{+\infty}\int_{-\infty}^{+\infty} (rr_0)^{-0.5}\pi g_J \cos 0.5\hat{\theta}_0 d\tau d\tau' \tag{D.7}$$

$$\int_{-\infty}^{+\infty}\int_{-\infty}^{+\infty} \int_{s_\varepsilon} R_0^{-3}(1 - 3R_0^{-2}v_0^2 x_3^2)\dot{\tilde{u}}_{I,J} d\xi_1\xi_2 d\tau d\tau' \cong \int_{-\infty}^{+\infty}\int_{-\infty}^{+\infty} (rr_0)^{-0.5}\pi g_J \cos 0.5\hat{\theta}_0 d\tau d\tau' \tag{D.8}$$

$$\int_{-\infty}^{+\infty}\int_{-\infty}^{+\infty} \int_{s_\varepsilon} 3R_J^{-5}v_J x_3(x_2 - \xi_2)\dot{\tilde{u}}_{I,J} d\xi_1\xi_2 d\tau d\tau' \cong \int_{-\infty}^{+\infty}\int_{-\infty}^{+\infty} (rr_J)^{-0.5}\pi g_J \sin 0.5\hat{\theta}_J d\tau d\tau' \tag{D.9}$$

$$\int_{-\infty}^{+\infty}\int_{-\infty}^{+\infty} \int_{s_\varepsilon} 3R_J^{-5}x_2 x_3\dot{\tilde{u}}_{I,J} d\xi_1\xi_2 d\tau d\tau' \cong -\int_{-\infty}^{+\infty}\int_{-\infty}^{+\infty} (rr_I)^{-0.5}4\pi g_J \cos 0.5\hat{\theta}_J d\tau d\tau' \tag{D.10}$$

$$\int_{-\infty}^{+\infty}\int_{-\infty}^{+\infty} \int_{s_\varepsilon} 30R_J^{-7}x_2^2 x_3\dot{\tilde{u}}_{I,J} d\xi_1\xi_2 d\tau d\tau' \cong \int_{-\infty}^{+\infty}\int_{-\infty}^{+\infty} (rr_I)^{-1.5}\pi g_J \sin^{-1}\theta_I(2\cos^{-1}0.5\hat{\hat{\hat{\theta}}}_J - 3\cos 0.5\theta_J - \cos 2.5\theta_J) d\tau d\tau' \tag{D.11}$$

$$\int_{-\infty}^{+\infty}\int_{-\infty}^{+\infty}\int_{S_\varepsilon} r^{-7}x_3(x_2+\xi_2)^3\tilde{u}_J(\hat{P},\hat{S},t,\tau,\tau')d\xi_1 d\xi_2 d\tau d\tau' \cong \int_{-\infty}^{+\infty}\int_{-\infty}^{+\infty} \frac{2\pi\lambda g_J(\xi_0)\, r^{\lambda-1}}{15\sin(\lambda\pi)}[3\sin(\lambda\pi+\theta-\lambda\theta)+(1-\lambda)\sin\theta\cos(\lambda\pi+2\theta-\lambda\theta)]d\tau d\tau' \quad (D.12)$$

$I_{lJsh}(x_1,x_2)$ are defined as follows:

$$I_{11sh}=\int_{-\infty}^{+\infty}\int_{-\infty}^{+\infty}\int_S\left(r^{-7}K_{111}+r^{-5}K_{112}+r^{-3}K_{113}+r^{-3}\left(K_{11}(1-3r_{,2}^2)+K_{12}(1-3r_{,1}^2)\right)\right)\xi_1^s\xi_2^{\lambda_1+h}W\,d\xi_1\,d\xi_2\,d\tau d\tau' \quad (D.13)$$

$$I_{12sh}=\int_{-\infty}^{+\infty}\int_{-\infty}^{+\infty}\int_S\left(r^{-7}K_{121}+r^{-5}K_{122}+r^{-3}K_{123}+r^{-3}(K_{11}+K_{12})\right)\xi_1^s\xi_2^{\lambda_1+h}W\,d\xi_1\,d\xi_2\,d\tau d\tau' \quad (D.14)$$

$$I_{mnsh}=\int_{-\infty}^{+\infty}\int_{-\infty}^{+\infty}\int_S\left(\sum_{i=1}^3(r^{-7}K_{mi1}+r^{-5}K_{mi2}+r^{-3}K_{mi3})+r^{-3}K_{mn}\right)\xi_1^s\xi_2^{\lambda_n+h}W\,d\xi_1\,d\xi_2\,d\tau d\tau' \quad (D.15)$$

$$I_{21sh}=-\int_{-\infty}^{+\infty}\int_{-\infty}^{+\infty}\int_S\left(r^{-7}K_{211}+r^{-5}K_{212}+r^{-3}K_{213}+3r^{-3}(K_{11}+K_{12})r_{,1}r_{,2}\right)\xi_1^s\xi_2^{\lambda_1+h}W\,d\xi_1\,d\xi_2\,d\tau d\tau' \quad (D.16)$$

$$I_{22sh}=\int_{-\infty}^{+\infty}\int_{-\infty}^{+\infty}\int_S\left(r^{-7}K_{221}+r^{-5}K_{222}+r^{-3}K_{223}+r^{-3}\left(K_{11}(1-3r_{,1}^2)+K_{12}(1-3r_{,2}^2)\right)\right)\xi_1^s\xi_2^{\lambda_2+h}W\,d\xi_1\,d\xi_2\,d\tau d\tau' \quad (D.17)$$

$$I_{1KI}=\int_{-\infty}^{+\infty}\int_{-\infty}^{+\infty}\int_S\left(\sum_{i=1}^3 r^{-7}K_{1i1}+r^{-5}K_{1i2}+r^{-3}K_{1i3}+r^{-3}\left(\hat{\hat{K}}_{11}(1-3r_{,1}^2)-K_{12}r_{,1}r_{,2}\right)\right)\xi_1^s\xi_2^{\lambda_1+h}W\,d\xi_1\,d\xi_2\,d\tau d\tau' \quad (D.18)$$

$$I_{66sh}=\int_{-\infty}^{+\infty}\int_{-\infty}^{+\infty}\int_S\left(r^{-7}K_{631}+r^{-5}K_{632}+r^{-3}K_{633}+3r^{-4}K_{66}\lambda_{3\alpha}r_{,\alpha}\right)\xi_1^s\xi_2^{\lambda_6+h}W\,d\xi_1\,d\xi_2\,d\tau d\tau' \quad (D.19)$$

$$I_{m6sh}=\int_{-\infty}^{+\infty}\int_{-\infty}^{+\infty}\int_S\left(r^{-7}K_{m31}+r^{-5}K_{m32}+r^{-3}K_{m33}+3r^{-4}\hat{K}_{m6}\lambda_{3\alpha}r_{,\alpha}\right)\xi_1^s\xi_2^{\lambda_6+h}W\,d\xi_1\,d\xi_2\,d\tau d\tau' \quad (D.20)$$

$$I_{62sh}=\int_{-\infty}^{+\infty}\int_{-\infty}^{+\infty}\int_S\left(r^{-7}K_{621}+r^{-5}K_{622}+r^{-3}K_{623}+r^{-3}\left(\hat{\hat{K}}_{12}(1-3r_{,2}^2)-3K_{11}r_{,1}r_{,2}\right)\right)\xi_1^s\xi_2^{\lambda_2+h}W\,d\xi_1\,d\xi_2\,d\tau d\tau' \quad (D.21)$$

$$I_{\alpha 6sh}=\int_{-\infty}^{+\infty}\int_{-\infty}^{+\infty}\int_S\left(r^{-7}K_{\alpha 31}+r^{-5}K_{\alpha 32}+r^{-3}K_{\alpha 33}+3r^{-4}K_{\alpha 6}r_{,\alpha}\right)\xi_1^s\xi_2^{\lambda_6+h}W\,d\xi_1\,d\xi_2\,d\tau d\tau' \quad (D.22)$$

$$I_{m\alpha sh}=\int_{-\infty}^{+\infty}\int_{-\infty}^{+\infty}\int_S\left(r^{-7}K_{m\alpha 1}+r^{-5}K_{m\alpha 2}+r^{-3}K_{m\alpha 3}+r^{-2}K_{m1}r_{,\alpha}\right)\xi_1^s\xi_2^{\lambda_\alpha+h}W\,d\xi_1\,d\xi_2\,d\tau d\tau' \quad (D.23)$$

References

Bouchon M, Aki K. Discrete wave number representation of seismic source wave field. Bulletin of the Seismological Society of America 1977;67(2):259-77.
Bouchon M. Discrete wave number representation of elastic wave fields in three-space dimensions. Journal of Geophysical Research-Solid Earth 1979;84(B7):3609-14.
Bouchon M. A simple method to calculate Green's functions for elastic layered media. Bulletin of the Seismological Society of America 1981;71(4):959-71.
Aki K, Richards PG. Quantitative Seismology Theory and Methods. 1-2 1980;Freeman, San Francisco:1-932.
Okada Y. Surface deformation due to shear and tensile faults in half-space. Bulletin of the Seismological Society of America 1985;75(4):1135-54.
Sánchez-Sesma F.J., M. Campillo. Diffraction of P, SV and Rayleigh waves by topographic features: A boundary integral formulation. Bulletin of the Seismological Society of America 1991;81(6):2234-53.
Liu SW, Huang JH. Transient dynamic responses of a cracked solid subjected to in-plane loadings. International Journal of Solids and Structures 2003;40(18):4925-40.
Fu LY. Seismogram synthesis for piecewise heterogeneous media. Geophysical Journal International 2002;150(3):800-8.
Fu LY, Bouchon M. Discrete wavenumber solutions to numerical wave propagation in piecewise heterogeneous media - I. Theory of two-dimensional SH case. Geophysical Journal International 2004;157(2):481-98.
Zhang DL. Simulation of long period strong groudn motion at near-field by numerical Green function method. Institute of Engineering Mechanics China Earthquake Adminstration(PhD dissertation) 2005;Harbin China.
Chen SL, Chen LZ, Pan E. Three-dimensional time-harmonic Green's functions of saturated soil under buried loading. Soil Dynamics and Earthquake Engineering 2007;27(5):448-62.
Tosaka N, Onishi K. Boundary integral equation formulations for steady Navier-Stokes equations using the Stokes fundamental solutions. Engineering Analysis 1985;2(3):128-32.
Bush MB. Modelling two-dimensional flow past arbitrary cylindrical bodies using boundary element formulations. Applied Mathematical Modelling 1983;7(6):386-94.
Kakuda K, Tosaka N. the generalized boundary element approach for viscous fluid flow problems. boundary element methods in applied mechanics, Editors: MTanaka & TACruse 1988;Pergamon Press(305-314).
Tosaka N, Kakuda K. Development of BEM for convective viscous flow problems. Int J Solids Struct 1994;31(12-13):1847-59.
Kamdar M. Liquid metal embrittlement. In:Briant CL, Banerji SK, editors Embrittlement of Engineering Alloys, London: Academic 1982:362-455.

Perrone N, Liebowitz H. Effect of capillary action on fracture due to liquid metal embrittlement. In: First International Conference on Fracture, Sendai, Japan 1965;2065-2073.
Gordon P. Metal induced embrittlement of metals - An evaluation of embrittler transport mechanisms. Metallurgical Transactions A 1978;9(2):267-73.
Clegg RE. A fluid flow based model to predict liquid metal induced embrittlement crack propagation rates. Engineering Fracture Mechanics 2001;68(16):1777-90.
Iturrarán-Viveros U, Sánchez-Sesma F, Luzón F. Boundary element simulation of scattering of elastic waves by 3-D cracks. Journal of Applied Geophysics 2008;64(3-4):70-82.
Tadeu A, Godinho L, Antonio J, Amado Mendes P. Wave propagation in cracked elastic slabs and half-space domains--TBEM and MFS approaches. Engineering Analysis with Boundary Elements 2007;31(10):819-35.
Tadeu A, Godinho L, Santos P. Performance of the BEM solution in 3D acoustic wave scattering. Advances in Engineering Software 2001;32(8):629-39.
Erdogan F. Mixed boundary value problem in mechanics. Mechanics Today, V4 Nemat-Nasser, S ed 1978:44~84.
Ioakimidis NI. Application of finite-part integrals to the singular integral equations of crack problems in plane and 3-D elasticity. Acta Mechanica 1982;45:31～47.
Qin TY, Tang RJ. Finite-Part Integral and Boundary-Element Method to Solve Embedded Planar Crack Problems. International Journal of Fracture 1993;60(4):373-81.
Zhu BJ, Qin TY,. Application of hypersingular integral equation method to three-dimensional crack in electromagnetothermoelastic multiphase composites. International Journal of Solids and Structures 2007;44(18-19):5994-6012.
Banerjee PK. The Boundary Element Methods in Engineering. McGraw-Hill book Company Europe 1994.
Hörmander L. Linear Partial Differential Operators. Springer-Verlag, Berlin 1965.
Tosaka N. Numerical Methods for Viscous Flow Problems Using an Integral Equation. In: Wang, SY, Shen, HW, Ding, L Z (eds): River sedimentation 1986;The University of Mississippi:1514-25.
Camacho RGR, Barbosa JR. The boundary element method applied to incompressible viscous fluid flow. Journal of the Brazilian Society of Mechanical Sciences and Engineering 2005;27(4):456-62.
Pan E. Three-dimensional Green's functions in anisotropic magneto-electro-elastic bimaterials. Z Angew Math Phys 2002;53(5):815-38.
Ding HJ, Jiang AM, Hou PF, Chen WQ. Green's functions for two-phase transversely isotropic magneto-electro-elastic media. Eng Anal Bound Elem 2005;29(6):551-61.
Chen WQ, Lee KY, Ding H. General solution for transversely isotropic magneto-electro-thermo-elasticity and the potential theory method. Int J Eng Sci 2004;42(13-14):1361-79.
Zhu H, H, Chen Q, J, Yang L, D. Boudary element method ans its application in rock soil engineering. Tong ji university Publication 1996:162-9.
Bigoni D, Capuani D. Green's function for incremental nonlinear elasticity: shear bands and boundary integral formulation. Journal of the Mechanics and Physics of Solids 2002;50(3):471-500.
Bigoni D, Capuani D. Time-harmonic Green's function and boundary integral formulation for incremental nonlinear elasticity: dynamics of wave patterns and shear bands. Journal of the Mechanics and Physics of Solids 2005;53(5):1163-87.
Chen YT, Seismic parameter_Application of digital seismic method in earthquake prediction, Earthquake press.2003
Qin TY, Noda NA. Analysis of a three-dimensional crack terminating at an interface using a hypersingular integral equation method. Journal of Applied Mechanics-Transactions of the Asme 2002;69(5):626-31.
Qin TY, Noda NA. Application of hypersingular integral equation method to a three-dimensional crack in piezoelectric materials. Jsme International Journal Series a-Solid Mechanics and Material Engineering 2004;47(2):173-80.
Qin TY,Yu YS, N.A.Noda. Finite-part integral and boundary element method to solve three-dimensional crack problems in piezoelectric materials. Int J Solids Struct 2007;In Press, Corrected Proof.
Qin TY, Noda NA. Stress intensity factors of a rectangular crack meeting a bimaterial interface. Int J Solids Struct 2003;40(10):2473-86.
Zhu BJ, Qin TY. 3D modeling of crack growth in electro-magneto-thermo-elastic coupled viscoplastic multiphase composites. Applied Mathematical Modelling 2008;In Press, Corrected Proof.
Li JY. Magnetoelectroelastic multi-inclusion and inhomogeneity problems and their applications in composite materials. International Journal of Engineering Science 2000;38(18):1993-2011.
Coulomb CA. Sur une application des règles de Maximis et Minimis a quelques problèmes de stratique relatifis à l'Architecture. Acad Roy des Sciences Memoires de math et de physique par divers savans 1773;7:343-82.
Anderson EM. The dynamics of faultiong and dyke formation with applications to britain. 2nd edn, 1951;Edinburgh, Oliver and Boyd.
Jagger Jc. Elasticity , Fracture and Flow. 2nd edn, 1962;London, Methuen.
Griffith AA. The phenomena of rupture and flow in solids. Philosophical Transactions of the Royal Society of London, Series A, Mathematical and Physical Sciences 1920;221(587):163-98.
Griffith AA. The theory of rupture. In Proceedings of the First Applied Mechanics. Delft J Waltman Jr Publishers: Delft 1924(55-63).
Irwin GR. Fracture. Hanbuch der Physik. 6(Edited by S Flügge) 1958;Springer-Verlag, Berlin(551-590).
Kassir MK, Sih GC. Griffith's theory of brittle fracture in three dimensions. International Journal of Engineering Science 1967;5(12):899-918.
Sih GC, Liebowitz H. On the Griffith energy criterion for brittle fracture. International Journal of Solids and Structures 1967;3(1):1-22.
Chen Y, Gu H. Fundamentals of epicentre theory. Institute of Geophysics, China Earthquake Administration;School of Earth and Space Sciences, Peking University;Graduate University of Chinese Academy of Science 2007.

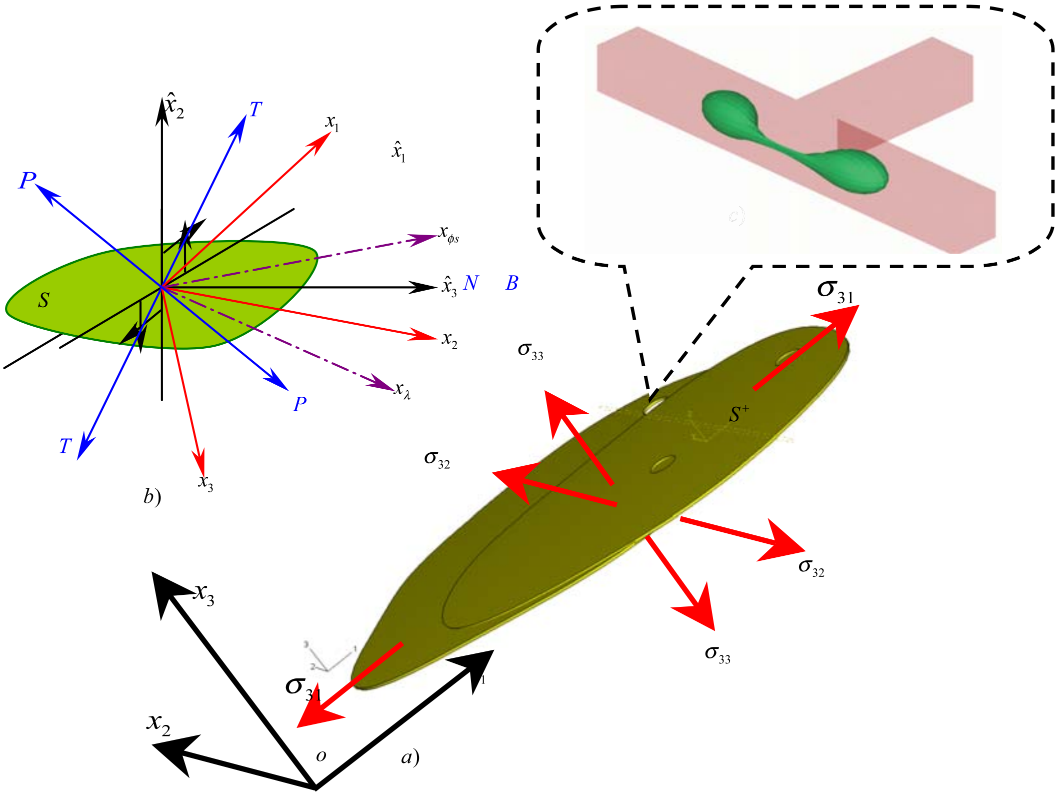

Figure 2.1. A extended 3D fluid driven crack propagation model on co-seismic slip under multiple fields

a) **General sketch of slip** *b*) **General model of 3D fluid crack** *c*) **Fluid flow model on crack surface**

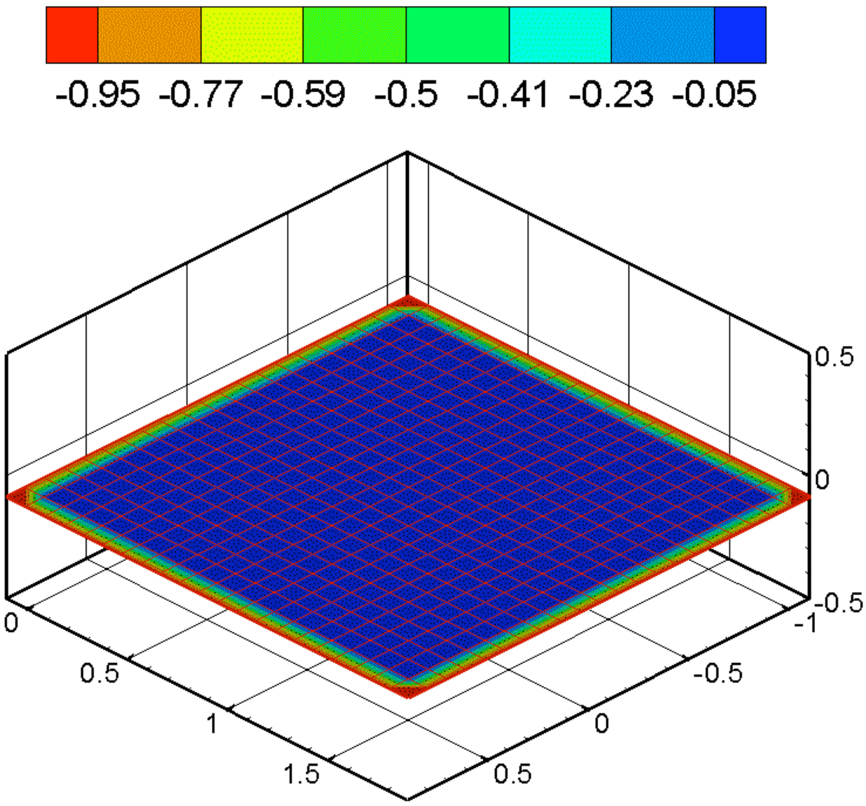

Fig.2.2 Extended remaining stresses wave on the flaw surface when b/a=1, KK=LL=20×20

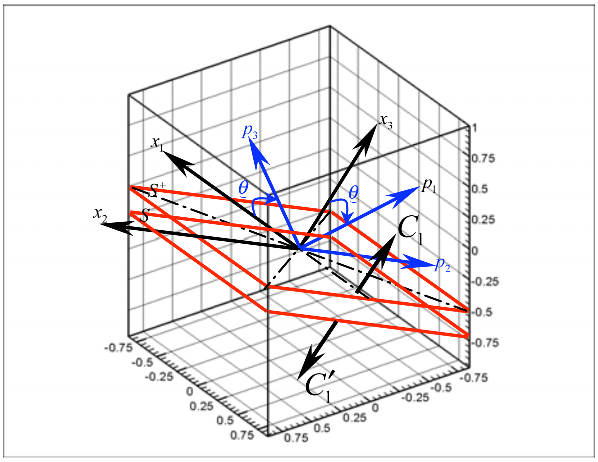

a) Open crack model for F_1

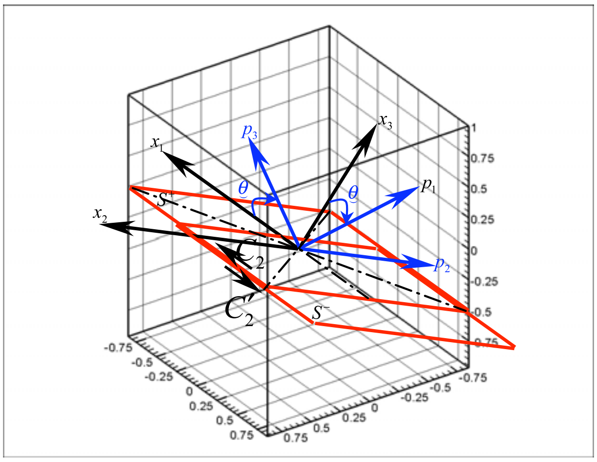

b) Shear crack model for F_2

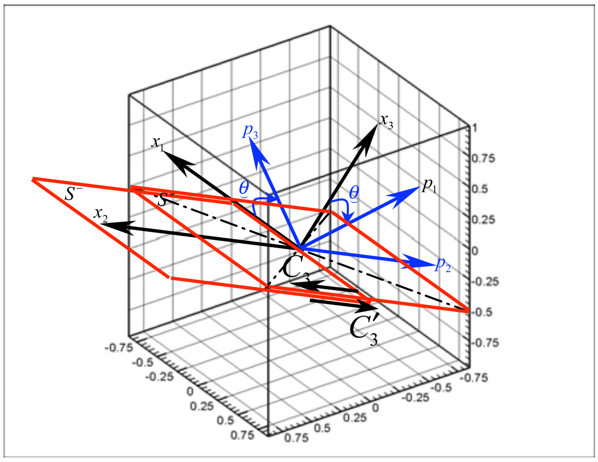

c) Tear crack model for F_3

Fig.2.3. Sketch map of crack model for F_i

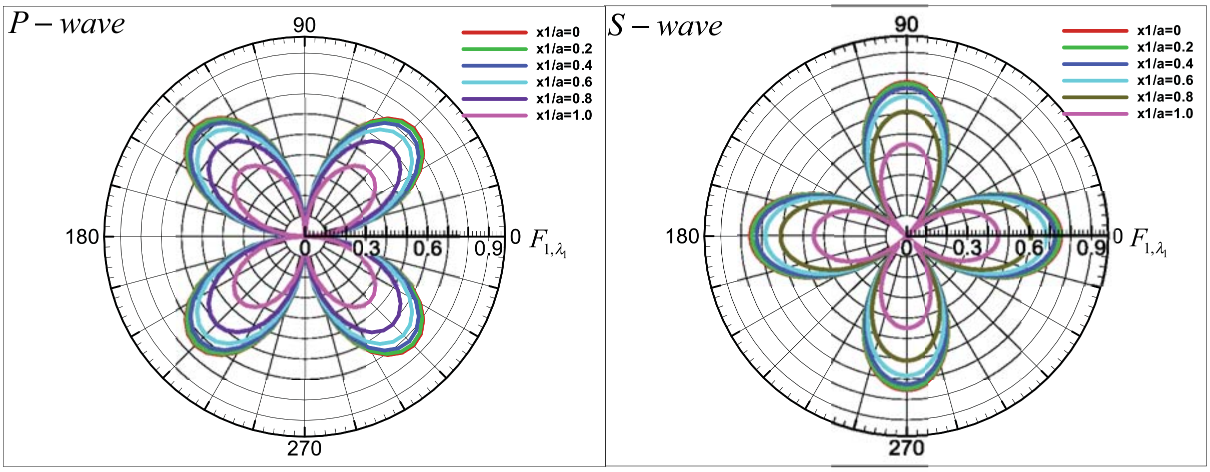

a) F_{1,λ_1}

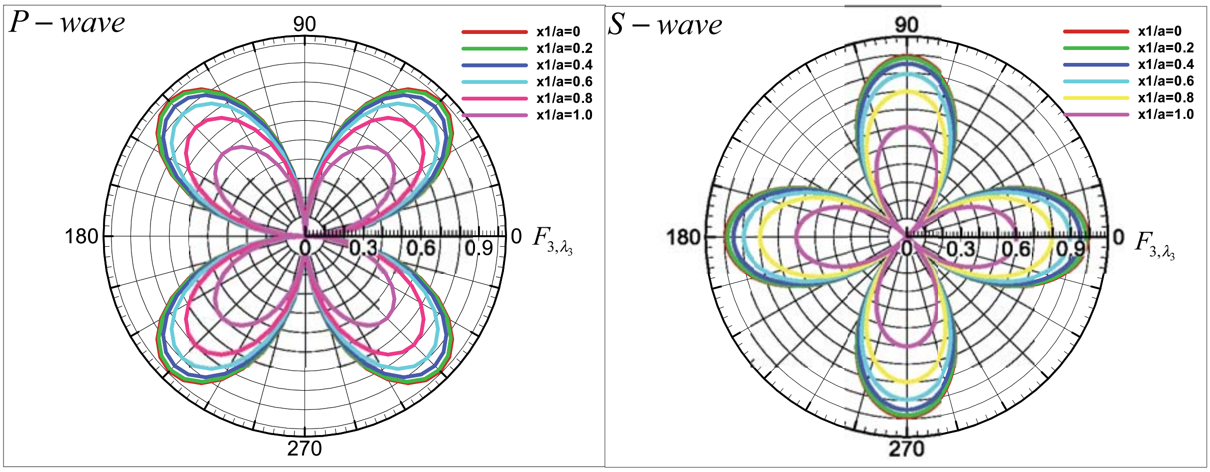

b) F_{2,λ_2}

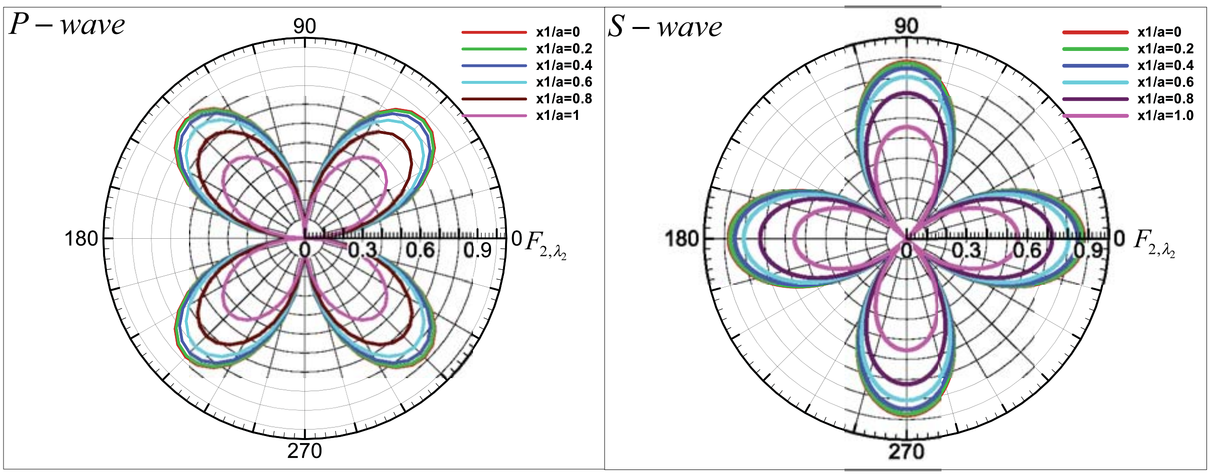

c) F_{3,λ_3}

Figure 2.4. Two dimensionless near-field F_{i,λ_i} radiation distributions for *P*- and *S*-waves

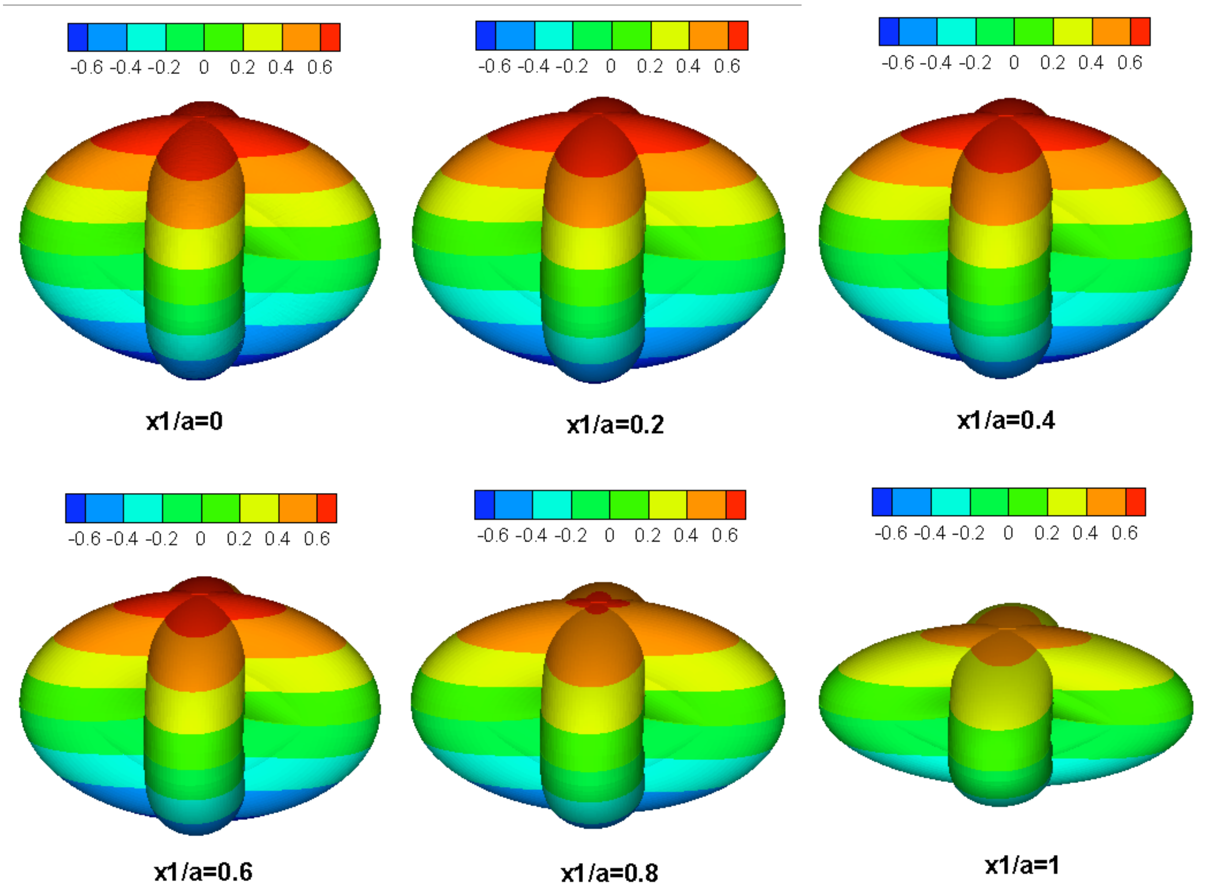

Fig.2.5. 3D dimensionless near-field F_{1,λ_1} radiation distribution for *P*- wave

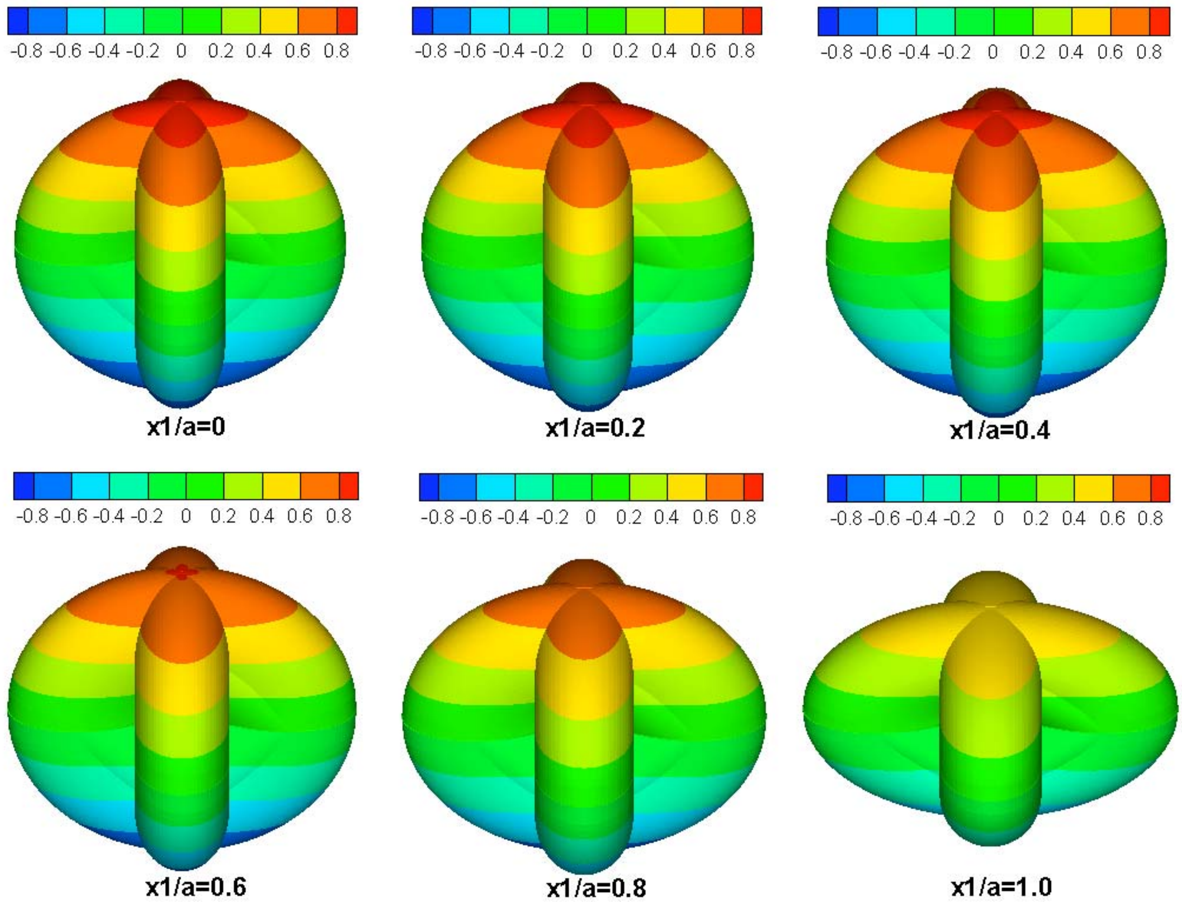

Fig.2.6. 3D dimensionless near-field F_{2,λ_2} radiation distribution for *P*- wave

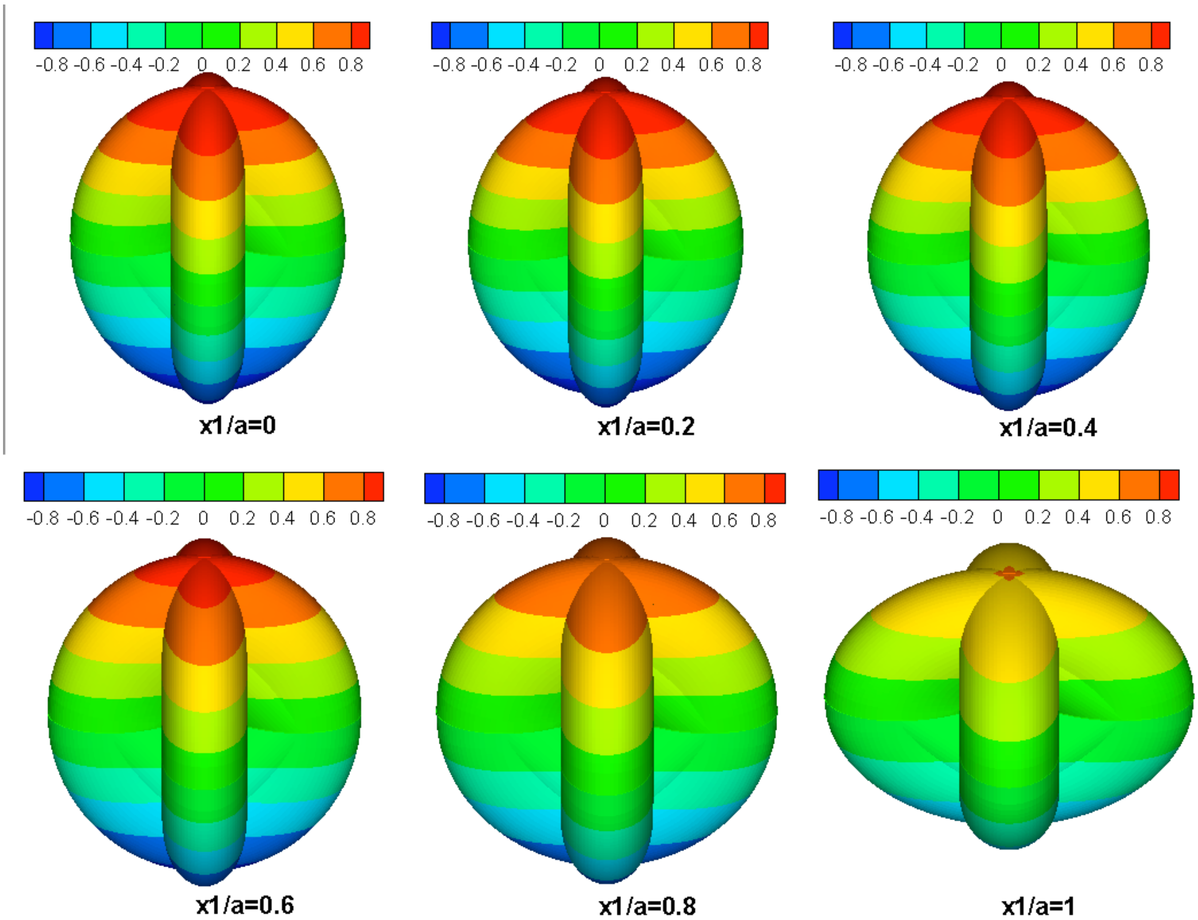

Fig.2.7. 3D dimensionless near-field F_{3,λ_3} radiation distribution for *P*- wave

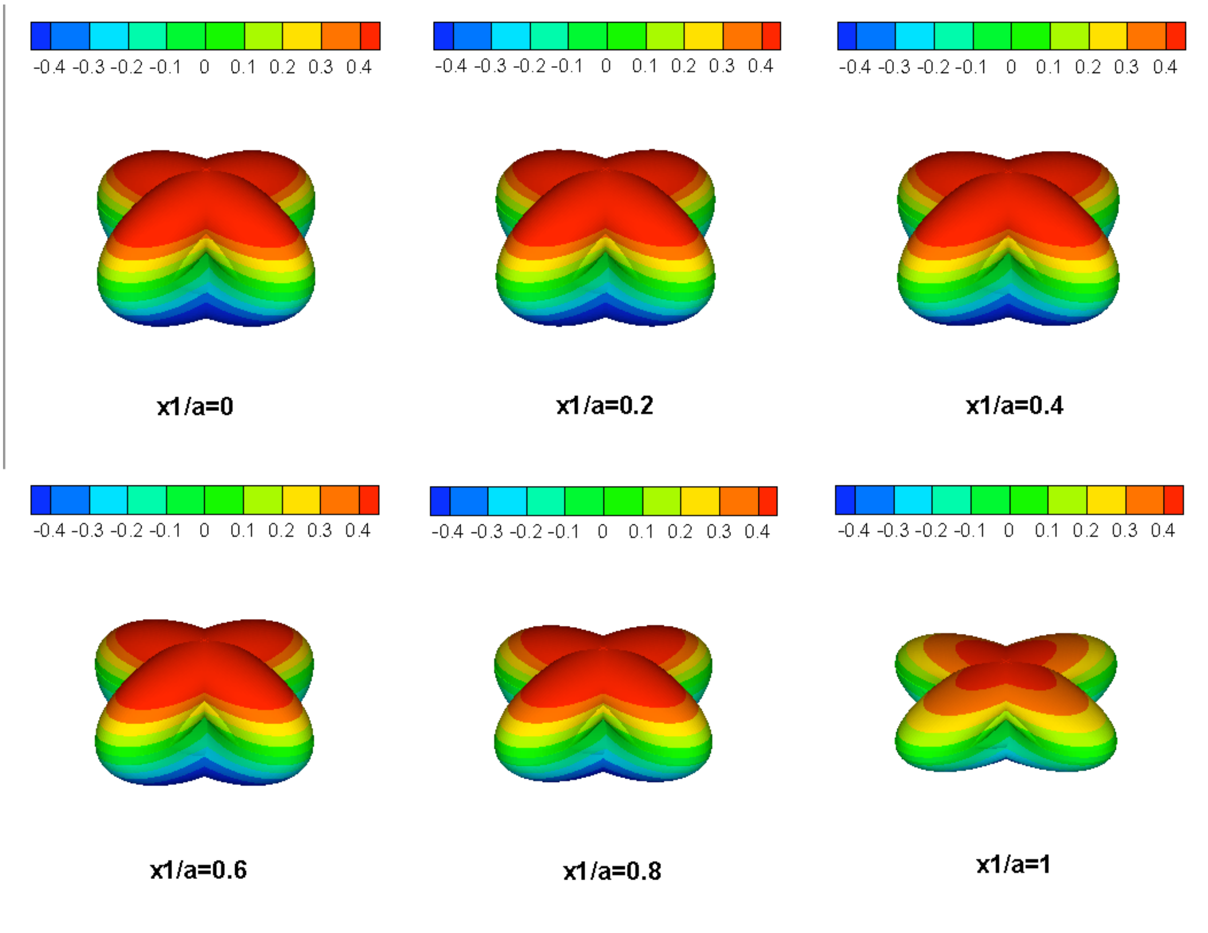

Fig.2.8. 3D dimensionless near-field F_{1,λ_1} radiation distribution for *S*- wave

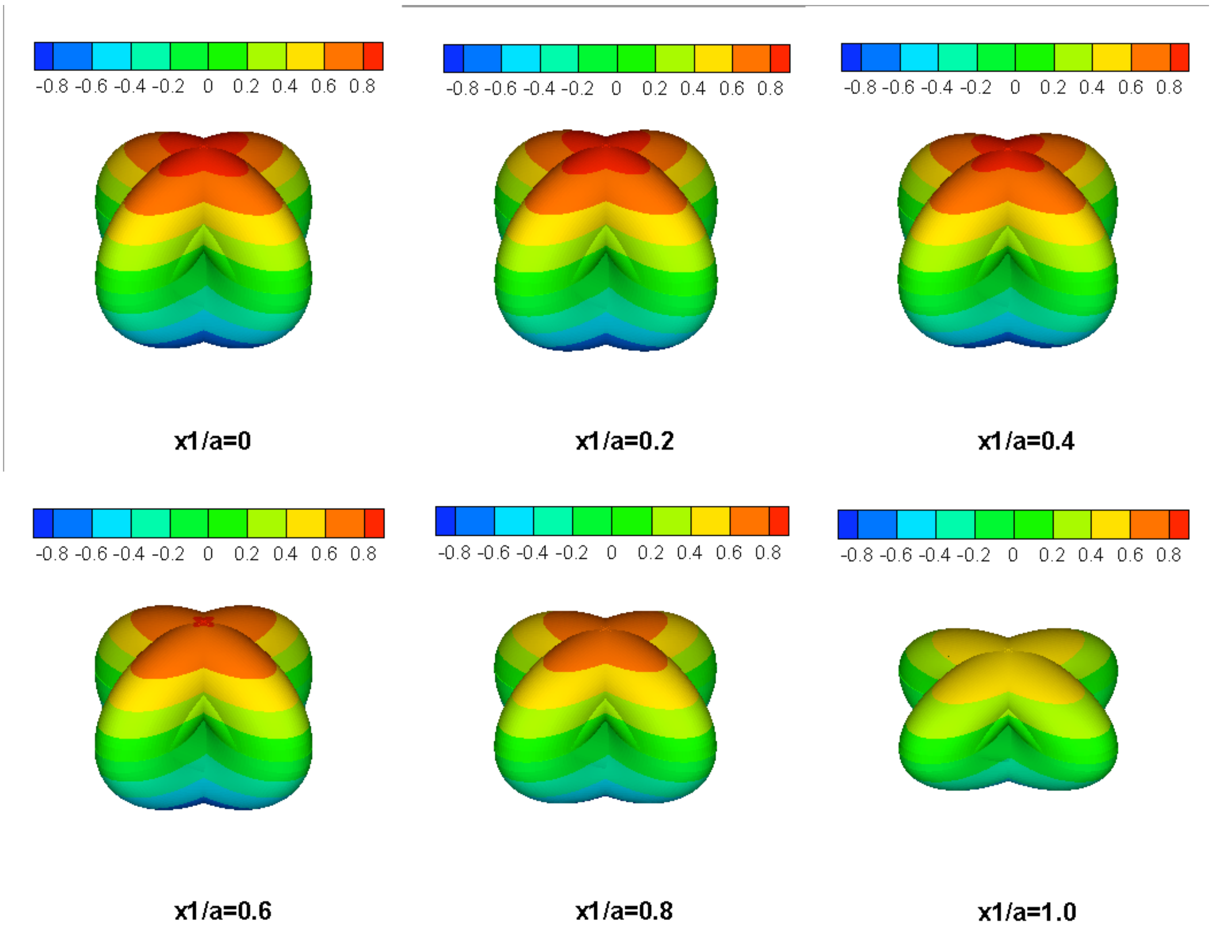

Fig.2.9. 3D dimensionless near-field F_{2,λ_2} radiation distribution for *S*- wave

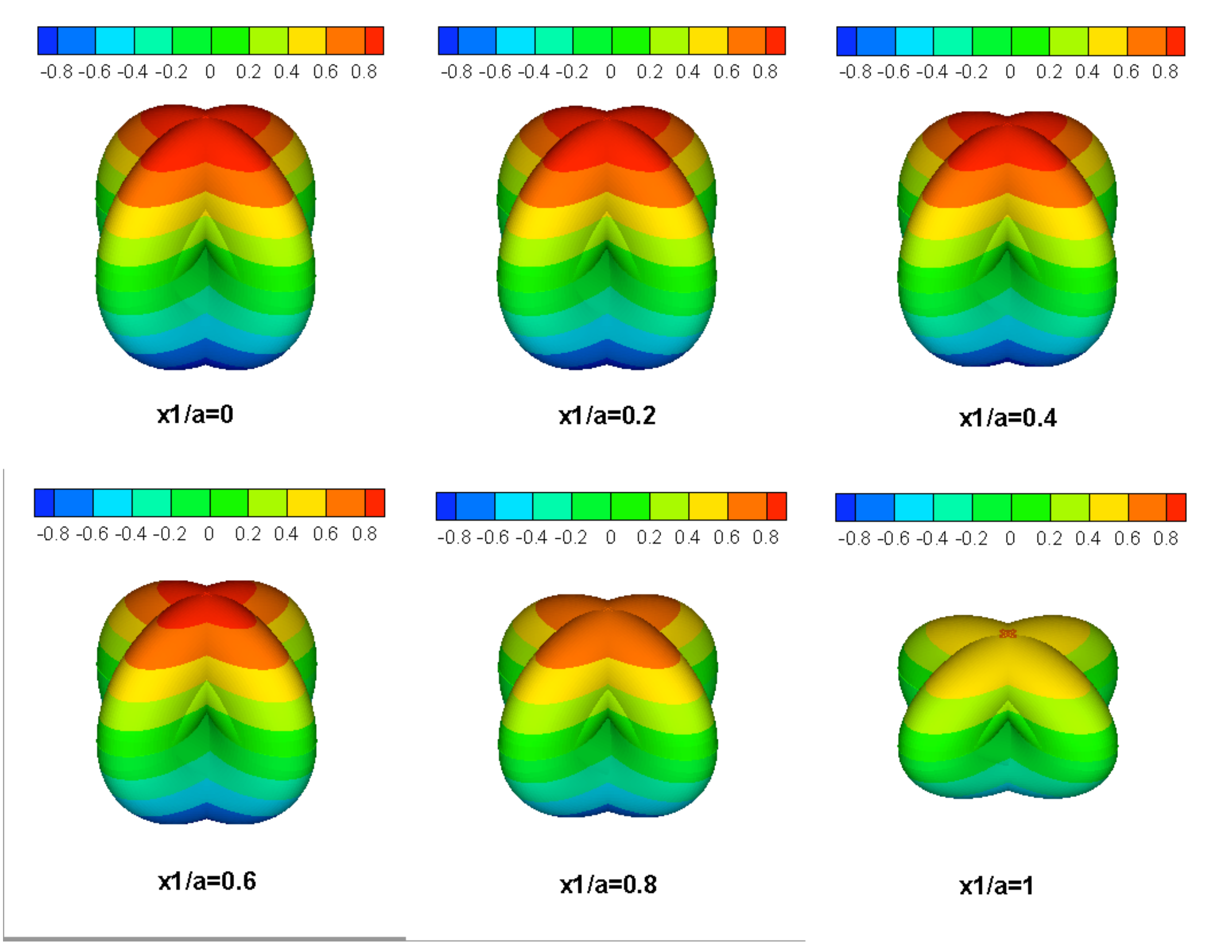

Fig.2.10. 3D dimensionless near-field F_{3,λ_3} radiation distribution for *S*- wave

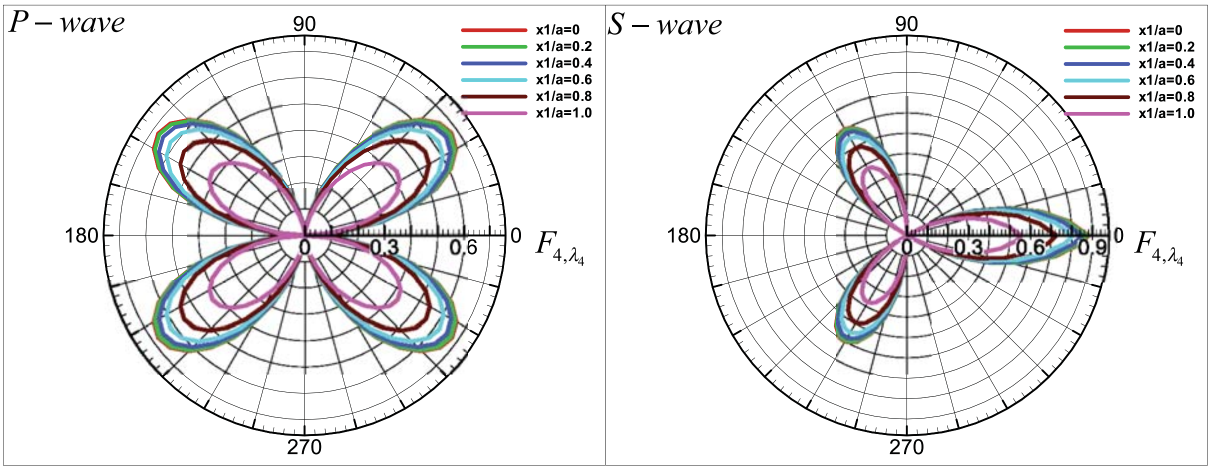

d) F_{4,λ_4}

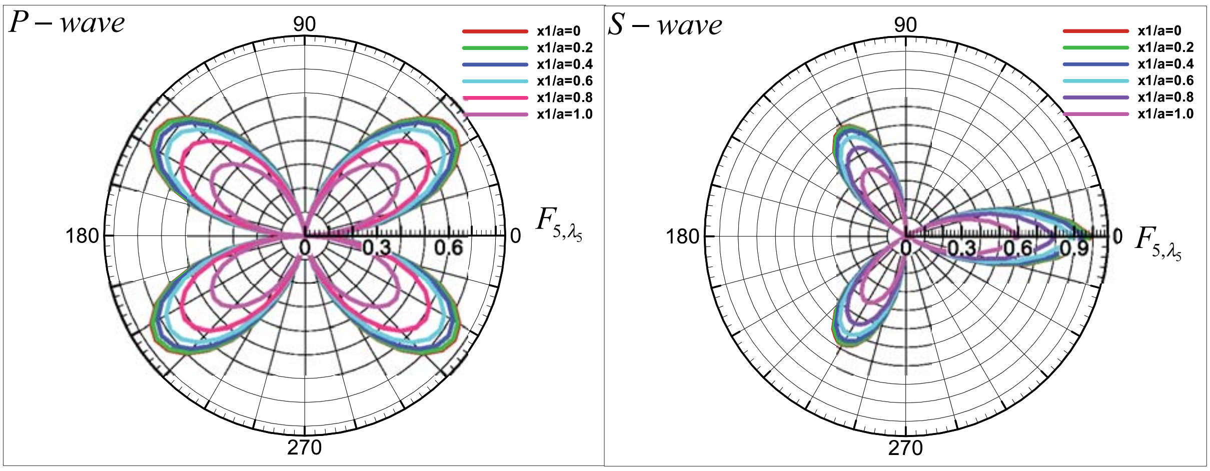

e) F_{5,λ_5}

Fig.2.11. 2D dimensionless near-field F_{4,λ_4} and F_{5,λ_5} radiation distribution for *P*- and *S*- wave

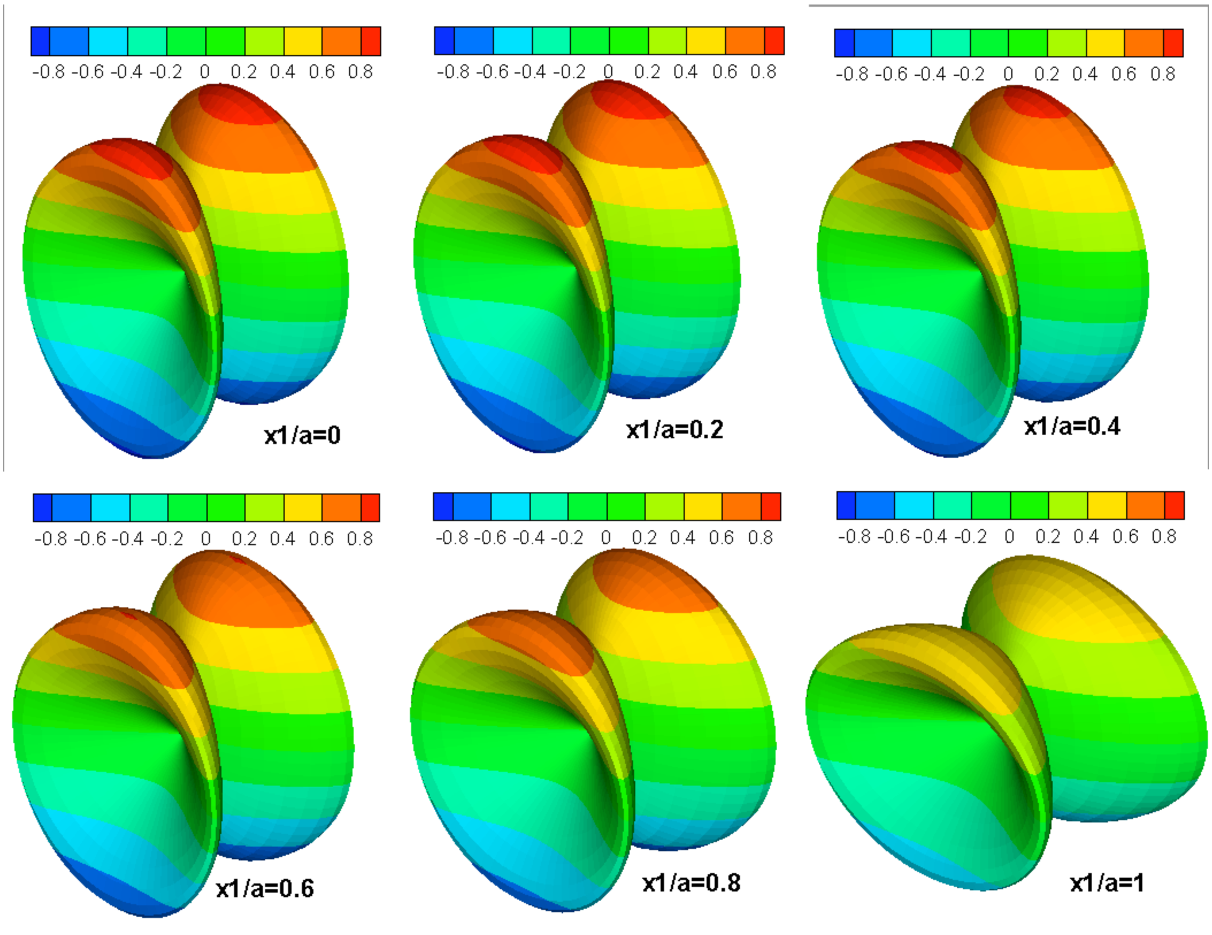

Fig.2.12. 3D dimensionless near-field F_{4,λ_4} radiation distribution for *P*- wave

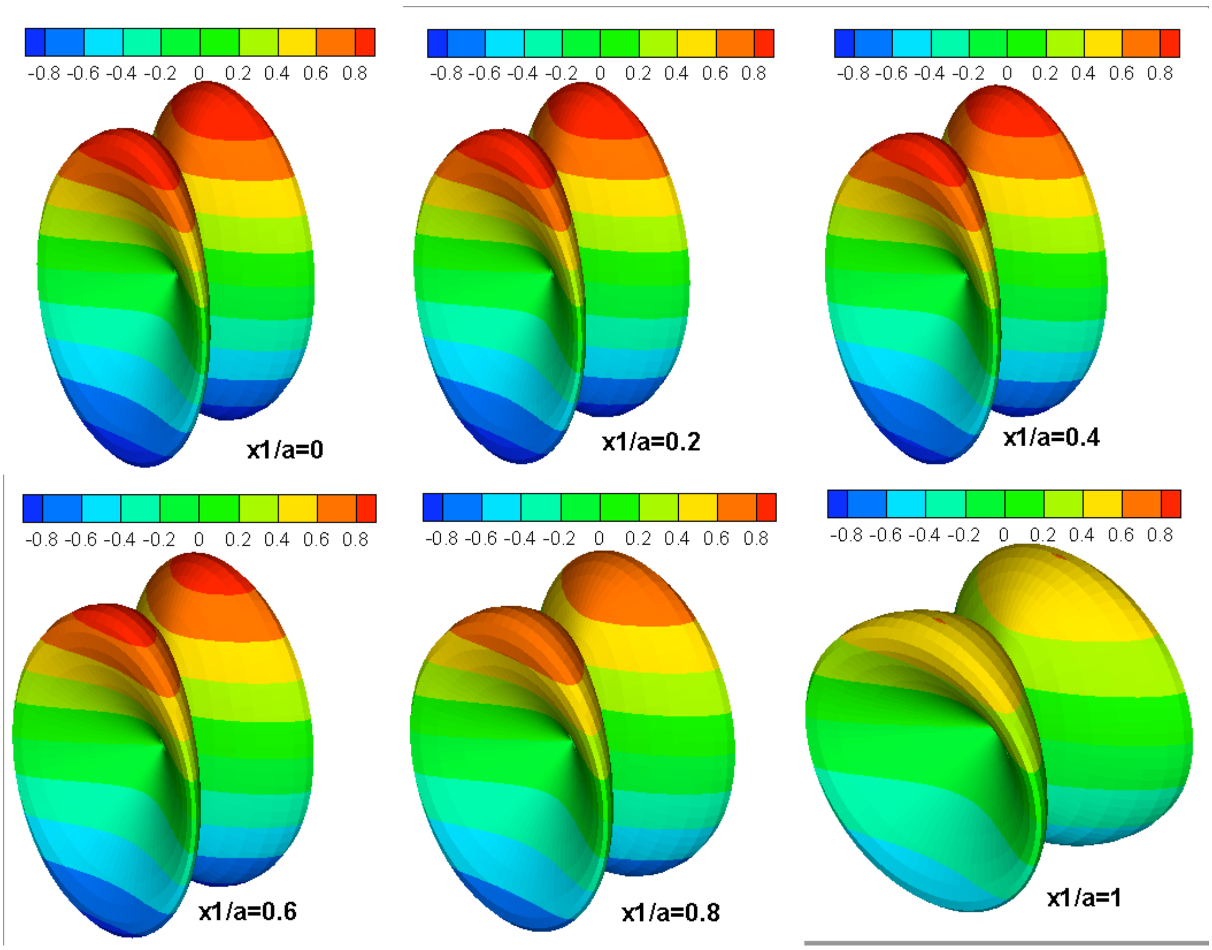

Fig.2.13. 3D dimensionless near-field F_{5,λ_5} radiation distribution for *P*- wave

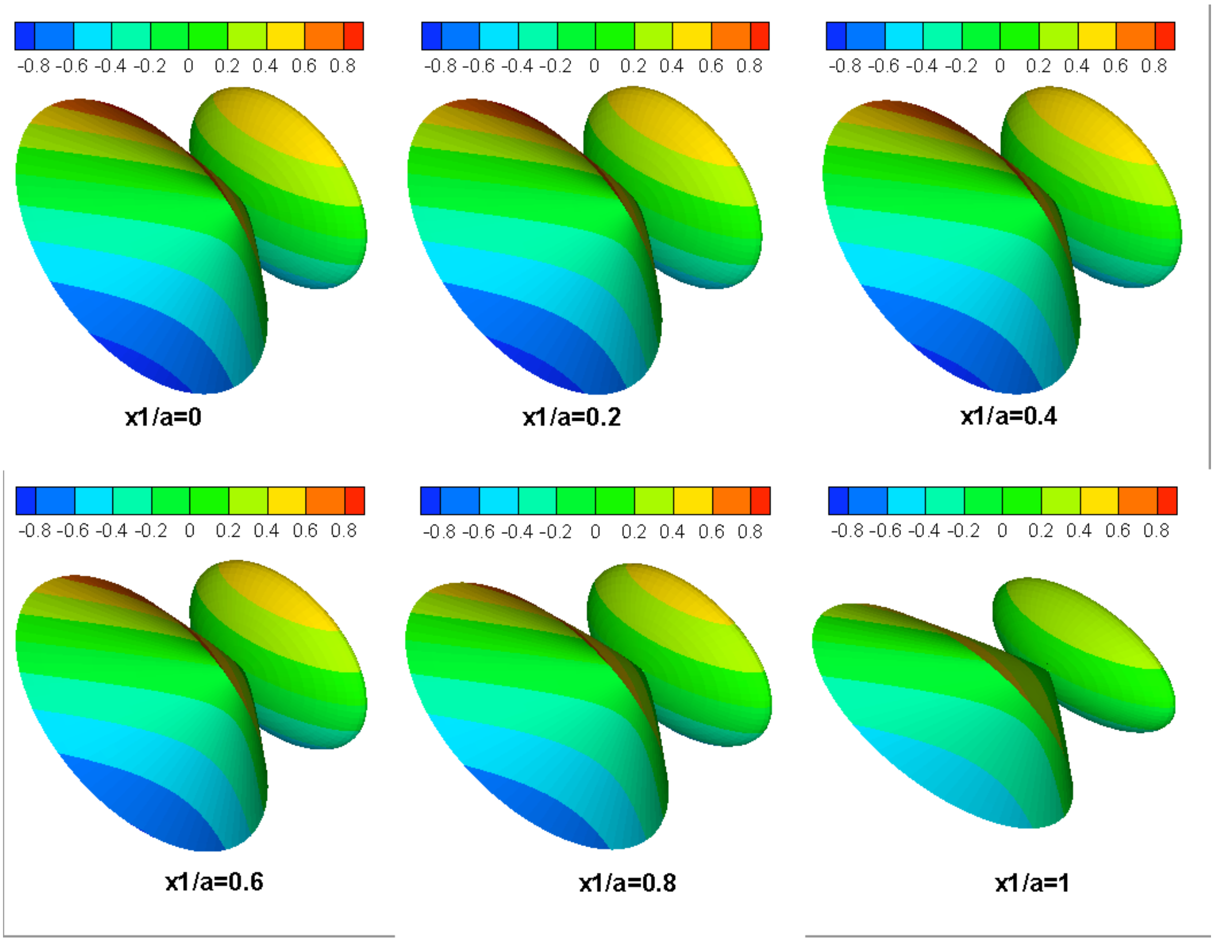

Fig.2.14. 3D dimensionless near-field F_{4,λ_4} radiation distribution for *P*- wave

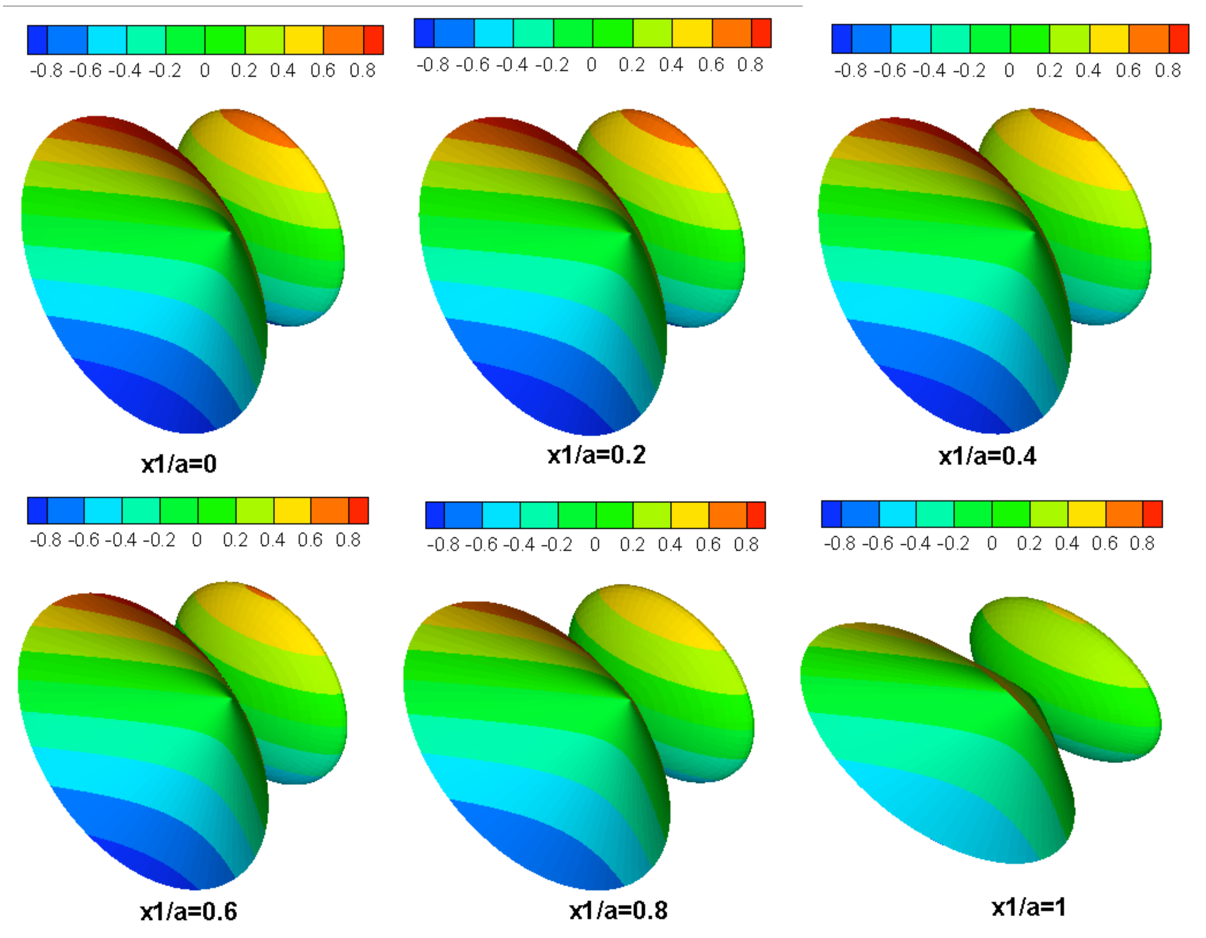

Fig.2.15. 3D dimensionless near-field F_{5,λ_4} radiation distribution for *P*- wave

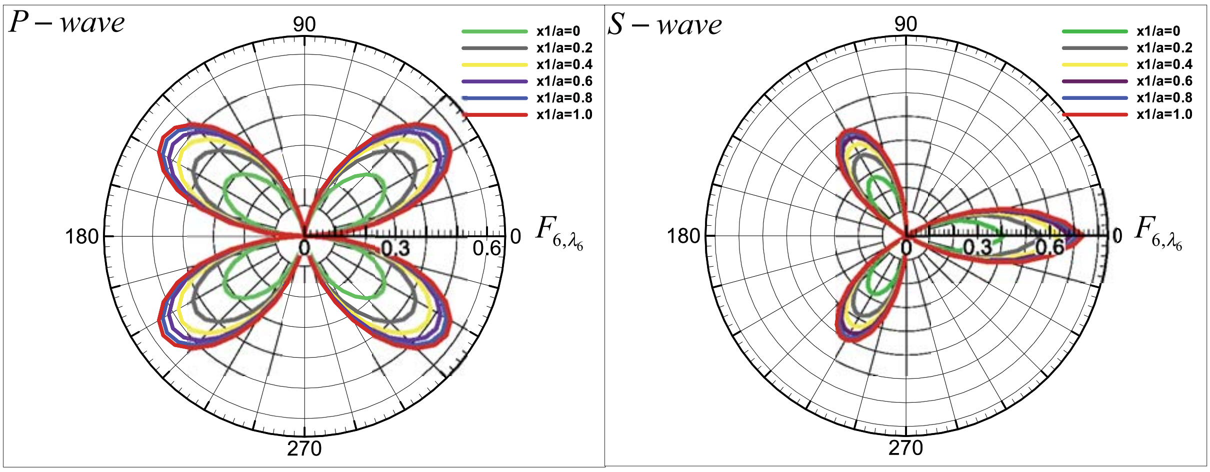

Fig.2.16. 2D dimensionless near-field F_{6,λ_6} radiation distribution for *P*- and *S*- wave

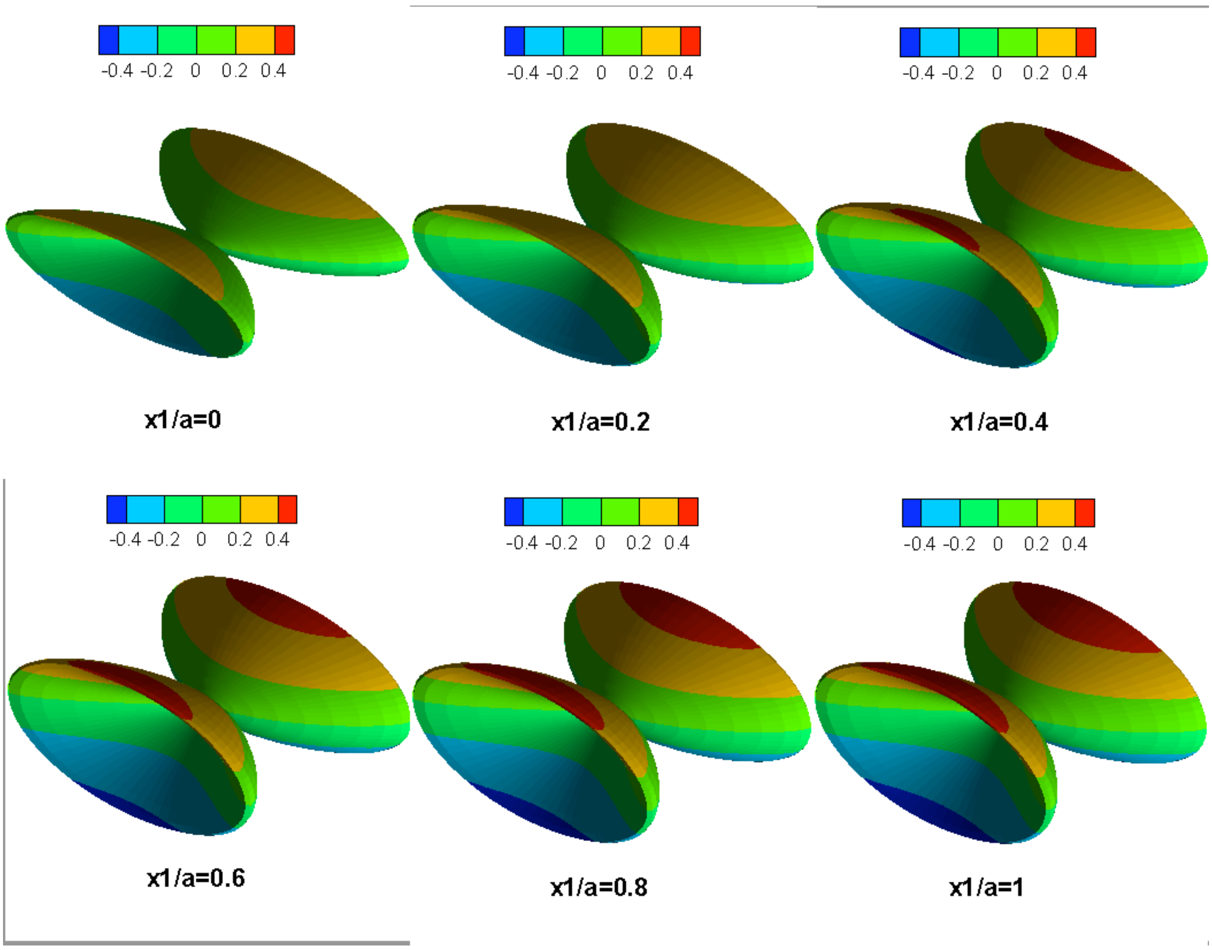

Fig.2.17. 3D dimensionless near-field F_{6,λ_6} radiation distribution for *P*- wave

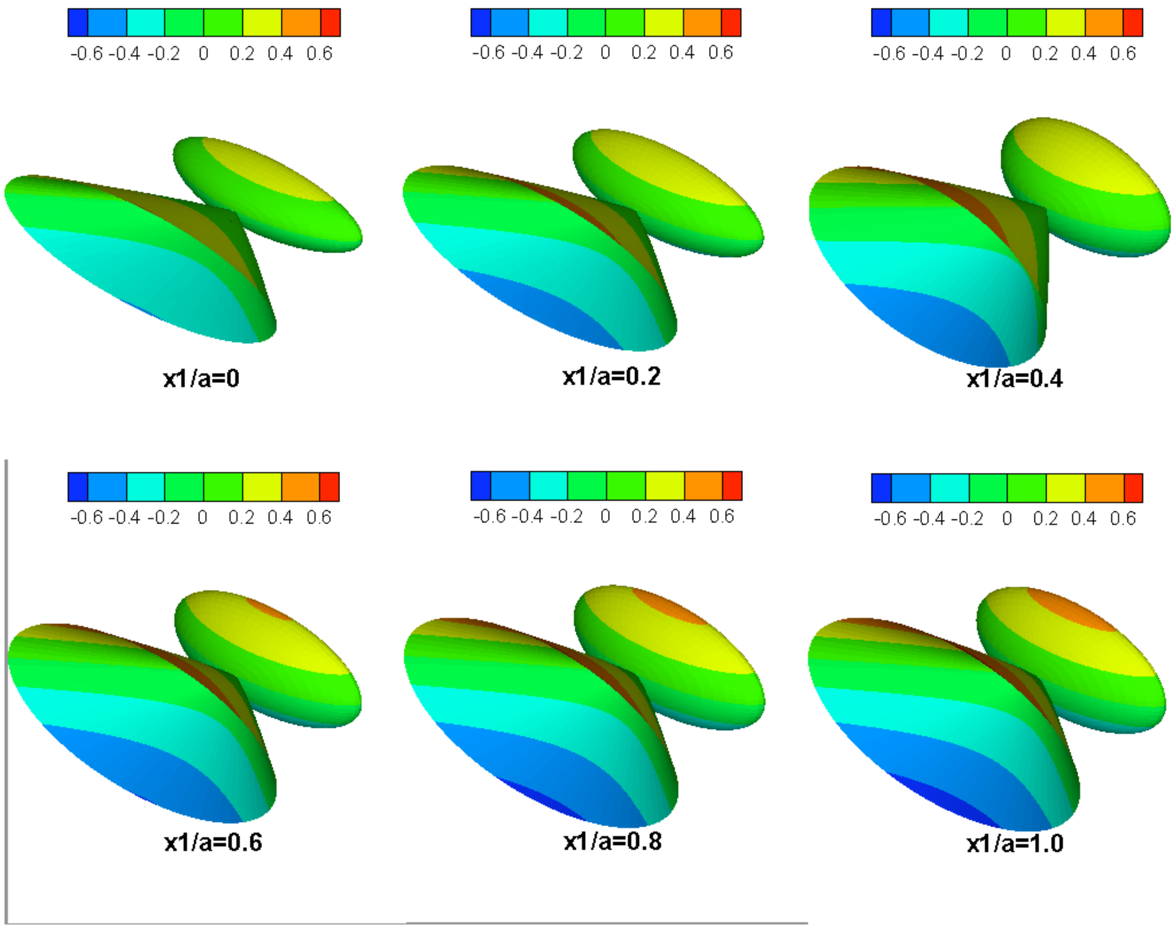

Fig.2.18. 3D dimensionless near-field F_{6,λ_6} radiation distribution for *S*- wave

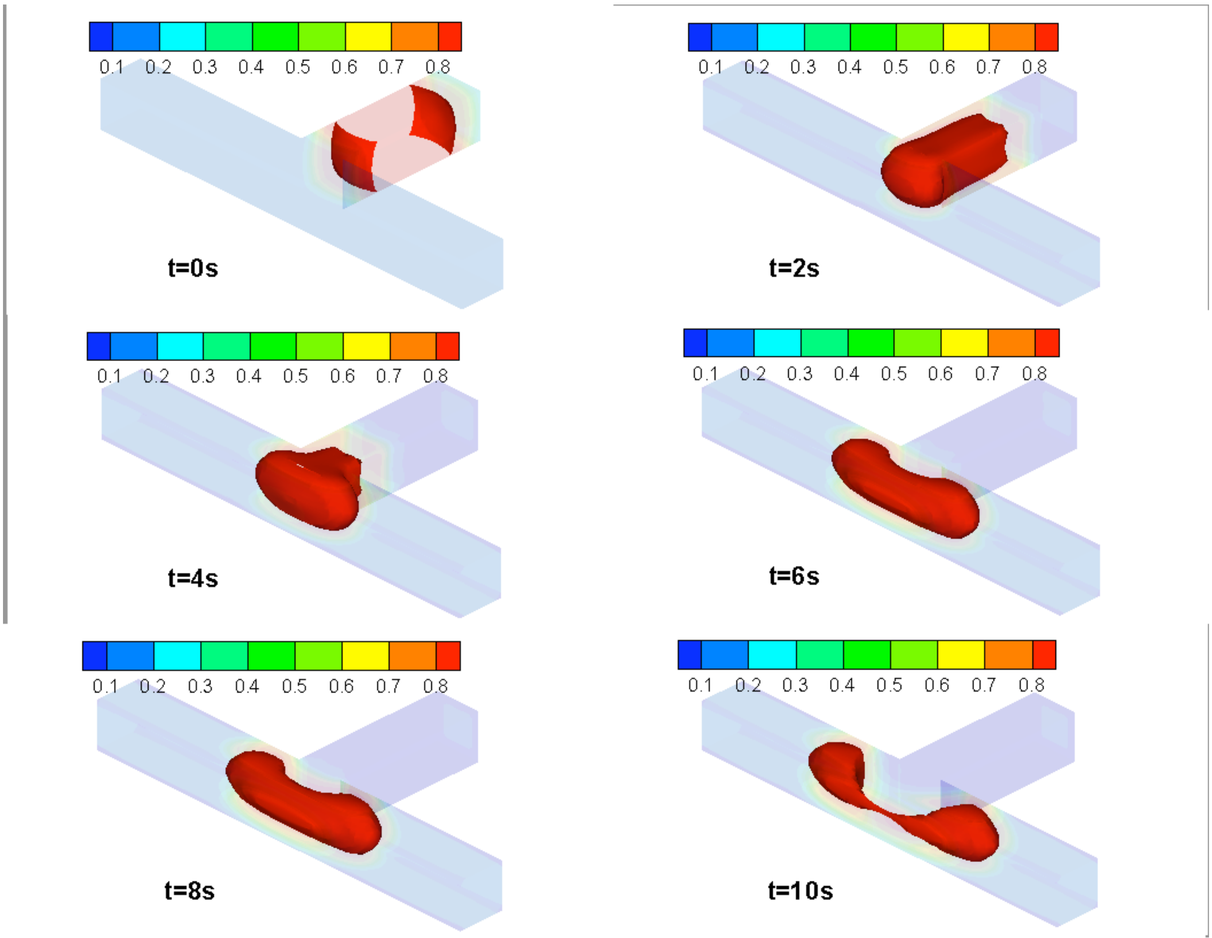

Fig.2.19. Dimensionless $\dot{\sigma}_{13}$ radiation distribution for *P*-and *S*- waves

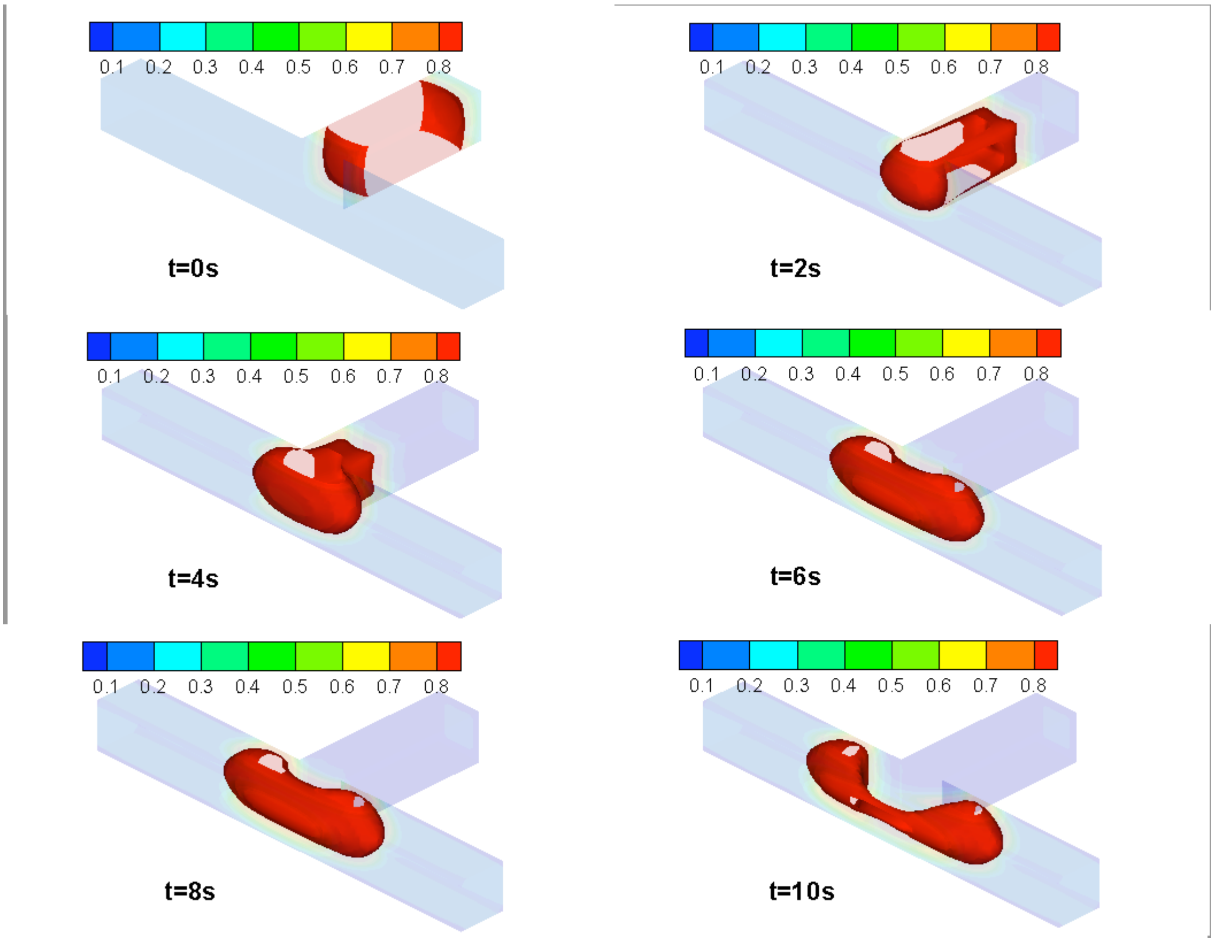

Fig.2.20. Dimensionless $\dot{\sigma}_{23}$ radiation distribution for *P*-and *S*- waves

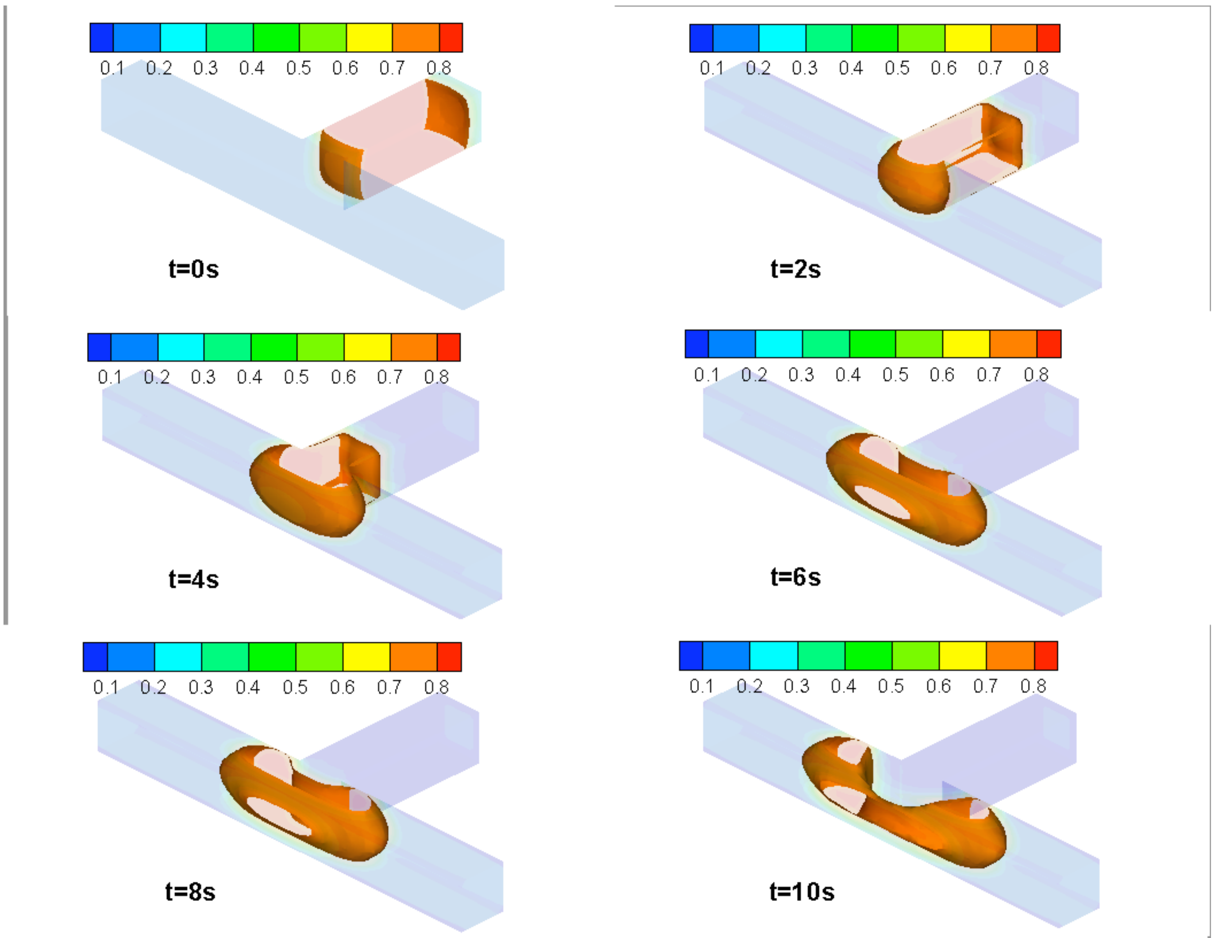

Fig.2.21. Dimensionless $\dot{\sigma}_{33}$ radiation distribution for *P*-and *S*- waves

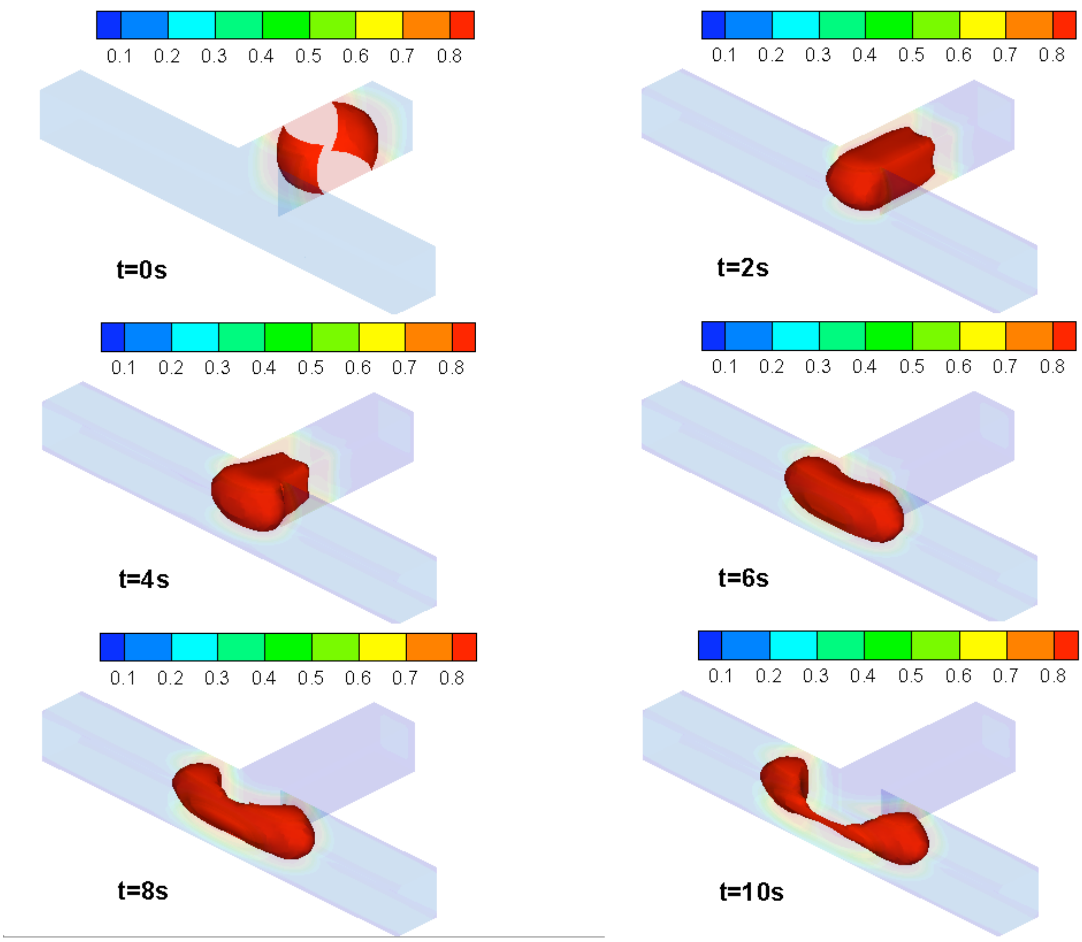

Fig.2.22. Dimensionless electric $\dot{D}$ radiation distribution for *P*-and *S*- waves

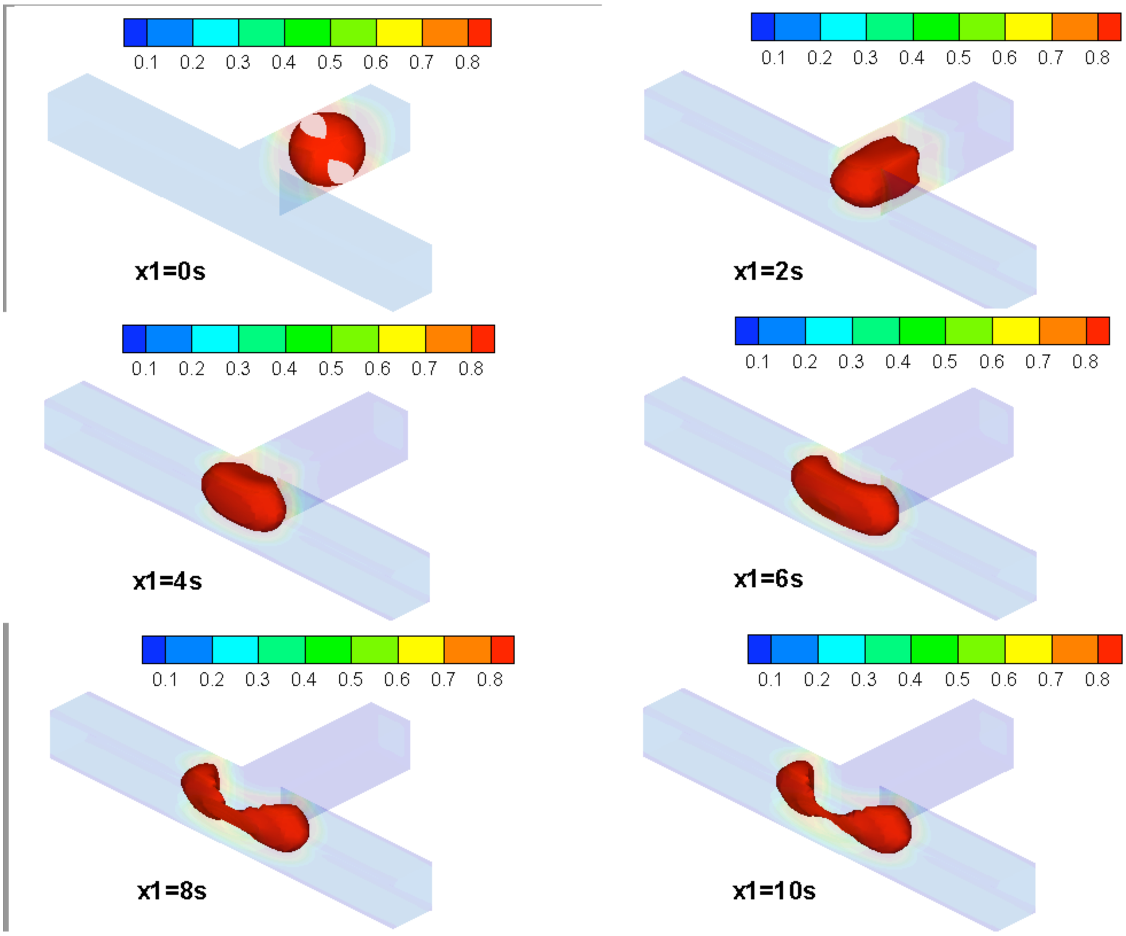

Fig.2.23. Dimensionless magnetic $\dot{B}$ radiation distribution for *P*-and *S*- waves

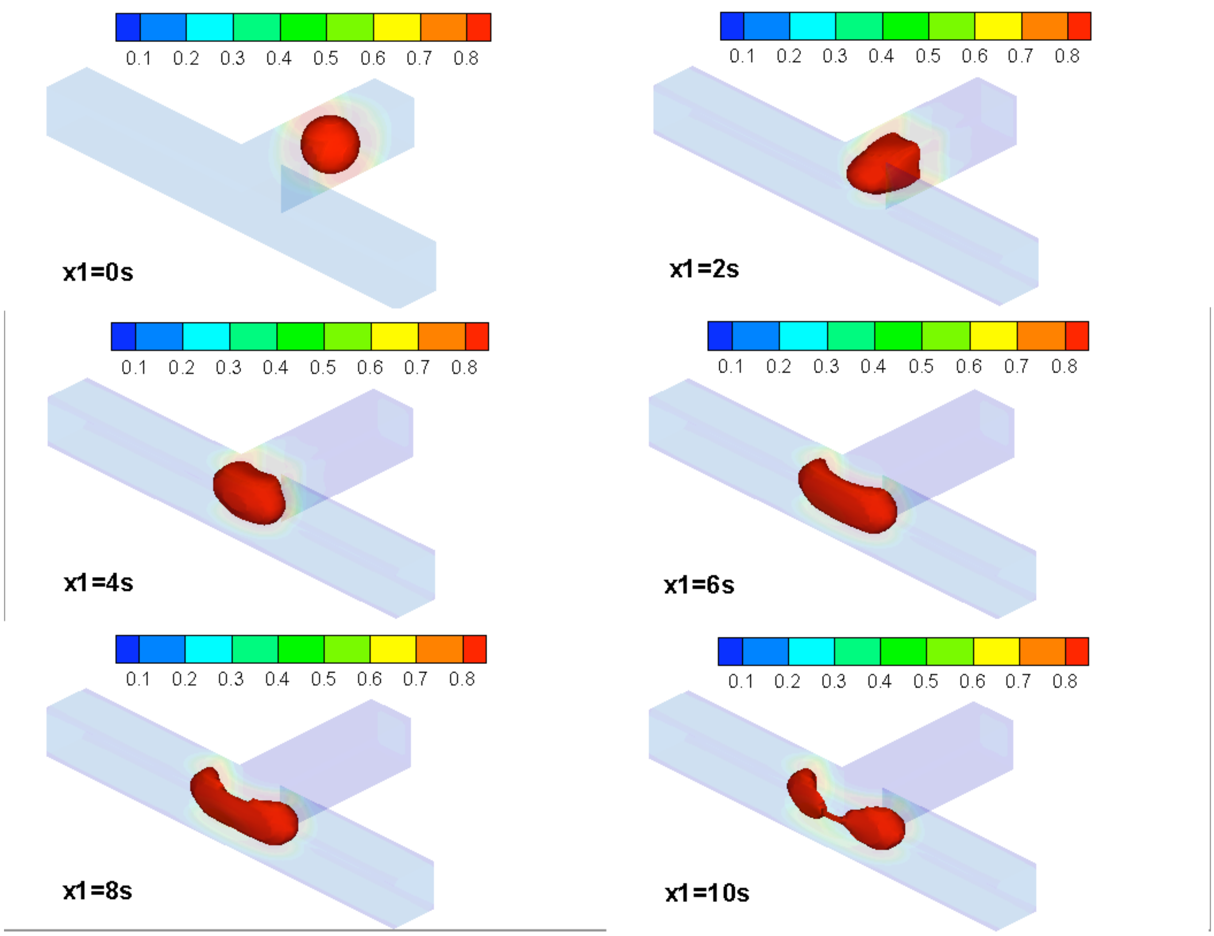

Fig.2.24. Dimensionless thermal $\dot{\vartheta}$ radiation distribution for *P*-and *S*- waves

Chapter 3:HHIE-LBM for extended 3D flow driven pore−crack networks in various porosity composites

Abstract

This study introduces a hybrid hypersingular integral equation − lattice Boltzmann method (HHIE−LBM) for analyzing extended 3D flow driven pore − crack networks problem in various porosity composites. First, the extended hybrid electronic − ionic, thermal, magnetic, electric and force coupled fields' pressure and velocity boundary conditions for HHIE−LBM model is established, and the closed form solutions of extended distribution functions are given. Second, an extended 3D flow driven pore − crack networks problem in various porosity composites is translated into a coupled of HHIE−LBM equations. Third, the extended dynamic stress intensity factors (EDSIFs) are calculated by using the parallel numerical technology and the visualization results are presented. Last, the relationship between the EDSIFs and the differential porosity are discussed, and several rules have been found, which can be utilized to understand the extended fluid flow mechanism in various porosity composites and analyze the extended fluid flow varying mechanism on coseismal slip.

Key words

Hypersingular integral equation method; Lattice Boltzmann method; Flow driven pore − crack networks; Stress intensity factor; Various porous composites.

1. Introduction

Fluid driven fracture is one of important geophysical phenomenon, especially for seismic trigger events at seismogenic zone during inter − seismic period [1, 2]. Groundwater has an important role in the whole water resources system, with the increasing demand of the information on groundwater hydrology and hydraulics, the mechanism of fluid and fluid flow driven pore − crack networks in the aquifer need special attention as the main resources of groundwater.

As one of the most popular fluid simulation method, lattice Boltzmann method has been widely applied in studying of fluid problem, and a lot of landmark achievements have been obtained [3-15]. On boundary condition aspect, [16] developed a hexagonal lattice gas model and modeling the 2D Navier-Stokes equation. [17] presented a cellular automaton model to simulate the process of seismogenesis. [11] proposed a supplementary rule for computing the boundary distribution, and presented 3D body-centered-cubic lattices are presented for Poiseuille flow. [12] developed a hydrodynamic boundary condition for lattice Boltzmann simulations. [10] proposed the pressure and velocity boundary for 2D/3D lattice Boltzmann BGK model.

Extended Fluid (electronic-ionic, thermal, magnetic, electric and force) flow pore−crack network problem is an interdisciplinary issues, a lot of research results have been obtained in different fields of study. [18] simulated 2D falling drops under gravity for some range of Eotvos and Ohnesorge numbers. Based on the work in [19] , [20] addressed the problem of stress intensity factors statistics in a randomly cracked solid and found that SIF distribution follows the Gnedenko-Gumber asymptotic rule. [21] deal with the solute transport in a single fracture with the combination of the lattice Boltzmann method and modified moment propagation method, and this study provide a new path of applying the LBM in solute transport simulation in fractures.

But there is little research about the extended 3D flow driven pore − crack networks problem in various porosity composites under multiple coupled electronic- − ionic, thermal, magnetic, electric and force fields.

In this paper, bases on the multiple scale fracture mechanics/physics theory[22-27], the hybrid hypersingular integral equation − lattice Boltzmann method (HHIE−LBM) proposed by the authors is defined by combined with extended hypersingular integral equation method [3, 4, 7, 8, 28-32] and 3D lattice Boltzmann method [3, 4, 7, 8, 32], and one typical extended 3D flow driven pore − crack networks model for various porosity composites is analyzed by using this method.

First, the extended hybrid multiple coupled D3Q27 lattice cubic is created and the extended hybrid electronic − ionic, thermal, electromagnetic (weak and strong coupled) and force coupled fields pressure and velocity boundary conditions for the HHIE−LBM model is established.

Then, using the HHIE−LBM method, the extended 3D flow driven pore − crack networks problem in various porosity composites is translated into a set of coupled HHIE−LBM equations, in which the unknown functions are the extended displacement ratio discontinuities.

Third, the extended dynamic stress intensity factors (EDSIFs) are calculated by using the parallel numerical technology and the visualization results are calculated. The results are presented toward demonstrating the applicability of the proposed method.

In addition, the relationship between the EDSIFs and differential porosity are discussed, and several rules have been found, which can be utilized to help understand the extended fluid flow mechanism in various porosity composites and analyze the extended fluid flow varying mechanism on coseismal slip.

2. Basic equation

In the present paper, summation from 1 to 3 over repeated lowercase, and of 1 to 7 in uppercase subscripts is assumed, and a subscript comma denotes the partial differentiation with respect to the extended coordinates.

The constitutive relationships can be written as

$$\left(E_{IJKL}\dot{Z}_{KL}\right)_{,I} + \dot{F}_{J} = \rho \ddot{U}_{J} \tag{24}$$

The Gauss' law, Faraday's law and Ampere's law can be written as

$$\nabla \bullet D = q \quad \nabla \times E = -\dot{B} \quad \nabla \bullet B = 0 \quad \nabla \times H = J + \dot{D} \tag{25}$$

The continuity equation, the conservation of momentum and the Navier-Stokes equations can be written as

$$\frac{\partial \rho}{\partial t} - \frac{d \ln \rho}{dc}[(kc_{,i})_{,i} + q] + \rho u_i \rho_{,i} = 0 \tag{26}$$

$$(\rho u_i)_{,t} + (\rho u_i u_j)_{,j} = \tau_{ij,j} + \rho f_i^b \tag{27}$$

$$(\rho u_i)_{,t} + (\rho u_i u_j)_{,j} - [\mu(u_{i,j} + u_{j,i} - 2\varepsilon_{ii}\delta_{ij}/3) - p\delta_{ij}]_{,j} - \rho f_i^b = 0 \tag{28}$$

The Helmholtz free energy and transport equation can be written as

$$F(n_{\alpha\alpha}, \varphi_\alpha) = \int_V \left[\frac{\kappa n}{2} \left| \nabla \varphi_\alpha \right|^2 + n_{\alpha\alpha} W(\varphi_\alpha) + f(n) \right] \tag{29}$$

$$\frac{\partial n_\alpha}{\partial t} = -\nabla \bullet \left(\frac{n_\alpha g}{\rho} \right) + (-1)^\alpha \nabla \bullet \Lambda \nabla \mu \tag{30}$$

$$\frac{\partial g}{\partial t} = -\nabla \bullet P - \nabla \bullet \left(\frac{gg}{\rho} \right) + \eta \nabla \bullet \left(\frac{g}{\rho} \right) \tag{31}$$

The electronic − ionic density, velocity and equilibrium distribution functions for incompressible and compressible model can be defined as [33-35]

$$\rho_{in\_ini}^{mi} u_\alpha^{mi} = \sum_{i=0}^{18} f_i^{mi} e_{i\alpha}^{mi} \tag{32}$$

$$\rho_{in}^{mi} = \sum_{i=0}^{18} f_i^{mi} \tag{33}$$

$$f_{i\_incom}^{eq\_mi}(x,t) = \alpha_i^{mi} \rho_{in}^{mi} + \alpha_i^{mi} \rho_{in\_ini}^{mi} \left(\frac{e_i^{mi} u_\alpha^{mi}}{c_s^2} + \frac{(e_i^{mi} u_\alpha^{mi})^2}{2c_s^4} - \frac{(u_\alpha^{mi})^2}{2c_s^2} \right) \tag{34}$$

$$f_{i\_com}^{eq\_mi}(x,t) = \alpha_i^{mi} \rho_{in}^{mi} + \alpha_i^{mi} \rho_{in}^{mi} \left(\frac{e_i^{mi} u_\alpha^{mi}}{c_s^2} + \frac{(e_i^{mi} u_\alpha^{mi})^2}{2c_s^4} - \frac{(u_\alpha^{mi})^2}{2c_s^2} \right) \tag{35}$$

where $\alpha_i^{mi} = \frac{1}{3}\delta_{i0} + \frac{1}{18}\delta_{im} + \frac{1}{36}\delta_{in} \quad m = 1 \sim 6 \quad n = 7 \sim 18$.

After we define the similar lattice velocity e_i^f and distribution function f_i^f (i=0, 18) at position $X(x, y, z)$ and time t for the fluid flow, we can obtain the pressure and velocity boundary conditions for fluid flow problem (force field).

The thermal flow density, velocity and equilibrium distribution function for incompressible and compressible model can be defined as

$$\rho_{in\_ini}^t u_\alpha^t = \sum_{i=0}^{14} f_i^t e_{i\alpha}^t \tag{36}$$

$$\rho_{in}^{t} = \sum_{i=0}^{14} f_i^{t} \tag{37}$$

$$f_i^{eq-t}(x,t) = \alpha_i^t \rho_{in}^t + \alpha_i^t \rho_{in\_ini}^t \left[\frac{e_i^t u_\alpha^t}{c_s^2} + \frac{9(e_i^t u_\alpha^t)^2}{2c_s^4} - \frac{3(u_\alpha^t)^2}{2c_s^2} \right] \tag{38}$$

$$f_i^{eq-t}(x,t) = \alpha_i^t \rho_{in}^t + \alpha_i^t \rho_{in}^t \left[\frac{e_i^t u_\alpha^t}{c_s^2} + \frac{9(e_i^t u_\alpha^t)^2}{2c_s^4} - \frac{3(u_\alpha^t)^2}{2c_s^2} \right] \tag{39}$$

where $\alpha_i^t = \frac{2}{9}\delta_{i0} + \frac{1}{9}\delta_{im} + \frac{1}{72}\delta_{in} \quad m = 1 \sim 6 \quad n = 7 \sim 14$.

The strong couple electromagnetic density, velocity and equilibrium distribution functions for incompressible and compressible model can be defined as

$$\rho_{in\_ini}^{mw} u_\alpha^{mw} = \sum_{i=0}^{12} f_i^{mw} e_{i\alpha}^{mw} \tag{40}$$

$$\rho_{in}^{mw} = \sum_{i=0}^{12} f_i^{mw} \tag{41}$$

$$f_i^{eq-mw}(x,t) = \alpha_i^{mw} \rho_{in}^{mw} + \alpha_i^{mw} \rho_{in\_ini}^{mw} \left[\frac{3e_i^{mw} u_\alpha^{mw}}{c_s^2} + \frac{9(e_{\boldsymbol{i}}^{mw} u_\alpha^{mw})^2}{4c_s^4} - \frac{3(u_\alpha^{mw})^2}{2c_s^2} \right] \tag{42}$$

$$f_i^{eq-mw}(x,t) = \alpha_i^{mw} \rho_{in}^{mw} + \alpha_i^{mw} \rho_{in}^{mw} \left[\frac{e_i^{mw} u_\alpha^{mw}}{c_s^2} + \frac{9(e_{\boldsymbol{i}}^{mw} u_\alpha^{mw})^2}{4c_s^4} - \frac{3(u_\alpha^{mw})^2}{2c_s^2} \right] \tag{43}$$

where $\alpha_i^{mw} = 0\delta_{i0} + \frac{1}{8}\delta_{im} \quad m = 1 \sim 12$.

After we define similar the lattice velocity e_i^e and the distribution function f_i^e (i=0, 12) at position $X(x,y,z)$ and time t for the electric fluid flow, we can obtained the similar pressure and velocity boundary conditions for electric fluid flow field. The extended magnetic density, velocity and equilibrium distribution functions for incompressible and compressible model are defined as

$$\rho_{in\_ini}^{m} u_\alpha^{m} = \sum_{i=0}^{6} f_i^{m} e_{i\alpha}^{m} \tag{44}$$

$$\rho_{in}^{m} = \sum_{i=0}^{6} f_i^{m} \tag{45}$$

$$f_i^{eq-m}(x,t) = \alpha_i^{m} \rho_{in}^{m} + \alpha_i^{m} \rho_{in\_ini}^{m} \left[\frac{3e_i^{m} u_\alpha^{m}}{c_s^2} + \frac{9(e_{\boldsymbol{i}}^{m} u_\alpha^{mi})^2}{4c_s^4} - \frac{3(u_\alpha^{m})^2}{2c_s^2} \right] \tag{46}$$

$$f_i^{eq-m}(x,t) = \alpha_i^{m} \rho_{in}^{m} + \alpha_i^{m} \rho_{in}^{m} \left[\frac{3e_i^{m} u_\alpha^{m}}{c_s^2} + \frac{9(e_{\boldsymbol{i}}^{m} u_\alpha^{m})^2}{4c_s^4} - \frac{3(u_\alpha^{m})^2}{2c_s^2} \right] \tag{47}$$

where $\alpha_i^{mi} = \frac{1}{6}\delta_{i0} + \frac{1}{72}\delta_{im} + \frac{1}{36}\delta_{in} \quad m = 1 \sim 4 \quad n = 5 \sim 6$

3. Boundary conditions for multiple coupled fields

The extended hybrid cubic lattice D3Q27 model is defined by combined D3Q19 (electric − ionic field) model, D3Q19 (force field) model, D3Q15 (thermal field) model, D3Q13 (Maxwell equation-strong electromagnetic coupled field) model, D3Q13 (electric field) model and D3Q7 (magnetic field) model for multiple coupled fields, the extended multiple coupled pressure and velocity condition and derive the extended distribution functions for every kind of possible case was established, see figure 3.1.

Figure.3.1. Extended boundary for hybrid cubic Lattice D3Q27 multiple coupled fields

The brief presentations of the extended lattice velocity $e_i(X,t)$ (i = 0~26) at position $X(x,y,z)$ and time t , and the distribution functions for hybrid D3Q27 model are given in table.1, where c_{kn}^{l} ($l=1\sim 27,\quad k=1\sim 6,\quad n=1\sim 6$) is coupled coefficient matrix (27×6×6). The extended electronic − ionic distribution functions f_i^{mi} (i=0, 18), flow distribution functions f_i^{f} (i=0, 18), extended thermal distribution functions f_i^{t} (i=0, 15), the extended strong couple electromagnetic distribution functions f_i^{mw} (i=0, 12), the extended electric distribution functions f_i^{e} (i=0, 12) and the extended magnetic distribution functions f_i^{m} (i=0, 7) are listed in Appendix A. More further information about c_{kn}^{l} can be found in Reference[36].

Table.3.1. The lattice velocity e_i (i=0~26) for the multiple coupled fields

3.1 Front-rear flow

As shown in fiugure.3.1a, when the electronic − ionic flow direction is from front to rear, after streaming, the unknown distribution functions are $f_{fr:i}$ (i = 26, 15, 19, 9, 3, 7, 24, 16, 21), on the contrary, after streaming, the unknown distribution functions are $f_{rf:i}$ (i = 22, 17, 23, 10, 4, 8, 20, 18, 25).

PC (pressure condition):

For the front inlet and rear outlet case, the $f_{fr:i}^{p}$ (i=26, 15, 19, 9, 3, 7, 24, 16, 21) can be defined as

$$f_{fr:26}^{p}=f_{13}-\frac{\rho_{in}^{p:t}(u_{fr:x}^{p:t}-u_{fr:y}^{p:t}-u_{fr:z}^{p:t})}{12} \quad (48)$$

$$f_{fr:21}^{p}=f_{10}+\frac{\rho_{in}^{t}(u_{fr:x}^{p:t}+u_{fr:y}^{p:t}-u_{fr:z}^{p:t})}{12} \quad (49)$$

$$f^{p}_{fr:24} = f_{11} + \frac{\rho^{t}_{in}(-u^{t}_{fr:x} + u^{t}_{fr:y} - u^{t}_{fr:z})}{12} \tag{50}$$

$$f^{p}_{fr:19} = f_{8} + \frac{\rho^{p:t}_{in}(u^{p:t}_{fr:x} + u^{p:t}_{fr:y} + u^{p:t}_{fr:z})}{12} \tag{51}$$

$$f^{p}_{fr:9} =$$
$$\frac{\rho^{mi}_{in}u^{mi}_{fr:y} + \rho^{f}_{in}u^{f}_{fr:y}}{6} + \frac{4f_{8} + 4f_{3} - f_{1} + f_{2} - f_{11} + f_{12} - f_{13} + f_{14} + 3\rho^{mw}_{in}(-u^{mw}_{fr:x} + u^{mw}_{fr:y}) + 3\rho^{m}_{in}(-u^{m}_{fr:x} + u^{m}_{fr} }{4} \tag{52}$$

$$f^{p}_{fr:3} = \frac{\rho^{mi}_{in}u^{mi}_{fr:y} + \rho^{mw}_{in}u^{mw}_{fr:y} + \rho^{f}_{in}u^{f}_{fr:y} + \rho^{m}_{in}u^{m}_{fr:y} + 7f_{4} - f_{0} - f_{1} - f_{5} - f_{2} - f_{6}}{3} \tag{53}$$

$$f^{p}_{fr:7} =$$
$$\frac{\rho^{mi}_{in}u^{mi}_{fr:y} + \rho^{f}_{in}u^{f}_{fr:y}}{6} + \frac{3\rho^{p:mw}_{in}(u^{p:mw}_{fr:x} + u^{p:mw}_{fr:y}) + 3\rho^{p:e}_{in}(u^{p:e}_{fr:x} + u^{p:e}_{fr:y}) - 4f_{10} - 4f_{2} + f_{1} - f_{2} + f_{11} - f_{12} + f_{13} - f_{14}}{4} \tag{54}$$

$$f^{p}_{fr:15} =$$
$$\frac{\rho^{p:mi}_{in}u^{p:mi}_{fr:y} + \rho^{p:f}_{in}u^{p:f}_{fr:y}}{6} + \frac{3\rho^{p:mw}_{in}(u^{p:mw}_{fr:y} + u^{p:mw}_{fr:z}) + 3\rho^{p:m}_{in}(u^{p:m}_{fr:y} + u^{p:m}_{fr:z}) + 4f_{18} + 4f_{10} - f_{5} + f_{6} - f_{11} - f_{12} + f_{13} + f_{14}}{4} \tag{55}$$

$$f^{p}_{fr:16} =$$
$$\frac{\rho^{mi}_{in}u^{mi}_{fr:y} + \rho^{f}_{in}u^{f}_{fr:y}}{6} + \frac{3\rho^{p:mw}_{in}(u^{p:mw}_{fr:y} - u^{p:mw}_{fr:z}) + 3\rho^{p:e}_{in}(u^{p:e}_{fr:y} - u^{p:e}_{fr:z}) + 4f_{17} + 4f_{12} - f_{5} + f_{6} - f_{11} - f_{12} + f_{13} + f_{14}}{4} \tag{56}$$

For rear inlet and front outlet case, $f^{p}_{rf:i}$ (i =22, 17, 23, 10, 4, 8, 20, 18, 25) can be defined as

$$f^{p}_{rf:22} = f_{9} - \frac{\rho^{t}_{in}(u^{p:t}_{rf:x} + u^{p:t}_{rf:y} - u^{p:t}_{rf:z})}{12} \tag{57}$$

$$f^{p}_{rf:25} = f_{14} - \frac{\rho^{p:t}_{in}(-u^{p:t}_{rf:x} + u^{p:t}_{rf:y} - u^{p:t}_{rf:z})}{12} \tag{58}$$

$$f^{p}_{rf:23} = f_{12} - \frac{\rho^{p:t}_{in}(-u^{p:t}_{rf:x} + u^{p:t}_{rf:y} - u^{p:t}_{rf:z})}{12} \tag{59}$$

$$f^{p}_{rf:20} = f_{7} - \frac{\rho^{p:t}_{in}(-u^{p:t}_{rf:x} + u^{p:t}_{rf:y} + u^{p:t}_{rf:z})}{12} \tag{60}$$

$$f^{p}_{rf:17} =$$
$$\frac{\rho^{p:mi}_{in}u^{p:mi}_{rf:y} - \rho^{p:f}_{in}u^{p:f}_{rf:y}}{6} + \frac{3\rho^{p:mw}_{in}(u^{p:mw}_{rf:y} - u^{p:mw}_{rf:z}) + 3\rho^{p:e}_{in}(u^{p:e}_{rf:y} - u^{p:e}_{rf:z}) - 3f_{11} + 4f_{16} + f_{5} - f_{6} + f_{12} - f_{13} - f_{14}}{4} \tag{61}$$

$$f^{p}_{rf:4} = \frac{7f_{3} - f_{0} - f_{1} - f_{5} - f_{2} - f_{6} + \rho^{mi}_{in}u^{p;mi}_{rf:y} + \rho^{p:f}_{in}u^{p;f}_{rf:y} + \rho^{p:t}_{in}u^{p;t}_{rf:y} + \rho^{p:m}_{in}u^{p:m}_{u:y}}{3} \tag{62}$$

$$f^{p}_{rf:8} =$$
$$\frac{4f_{9} + 4f_{4} + f_{1} - f_{2} + f_{11} - f_{12} + f_{13} - f_{14} - 3\rho^{p:mw}_{in}(-u^{p:mw}_{rf:x} + u^{p:mw}_{rf:y}) - 3\rho^{p:e}_{in}(-u^{p:e}_{rf:x} + u^{p:e}_{rf:y})}{4} - \frac{\rho^{p:mi}_{in}u^{p:mi}_{rf:y} + \rho^{p:f}_{in}u^{p:f}_{rf:y}}{6} \tag{63}$$

$$f^{p}_{rf:18} = \frac{4f_{15}+4f_{9}-f_{5}+f_{6}-f_{11}-f_{12}+f_{13}+f_{14}-3\rho^{p:mw}_{in}(u^{p:mw}_{rf:y}+u^{p:mw}_{rf:z})-3\rho^{p:e}_{in}(u^{p:e}_{rf:y}+u^{p:e}_{rf:z})}{4}-\frac{\rho^{p:mi}_{in}u^{p:mi}_{rf:y}-\rho^{p:f}_{in}u^{p:f}_{rf:y}}{6} \tag{64}$$

VC (velocity condition):

For the front inlet and rear outlet case, $f^{v}_{fr:i}$ (i=26, 15, 19, 9, 3, 7, 24, 16, 21), can be defined as

$$f^{v}_{fr:26} = f_{13} + \frac{\rho^{v:t}_{in}(-u^{t}_{fr:x}+u^{t}_{fr:y}+u^{t}_{fr:z})}{12} \tag{65}$$

$$f^{v}_{fr:24} = f_{11} + \frac{\rho^{v:t}_{in}(u^{t}_{fr:y}-u^{t}_{fr:x}-u^{t}_{fr:z})}{12} \tag{66}$$

$$f^{v}_{fr:21} = f_{10} + \frac{\rho^{v:t}_{in}(u^{v:t}_{fr:x}+u^{v:t}_{fr:y}-u^{v:t}_{fr:z})}{12} \tag{67}$$

$$f^{v}_{fr:19} = f_{8} + \frac{\rho^{v:t}_{in}(u^{v:t}_{fr:x}+u^{v:t}_{fr:y}+u^{v:t}_{fr:z})}{12} \tag{68}$$

$$f^{v}_{fr:15} = \frac{\rho^{v:mi}_{fr:in}u^{v:mi}_{y}+\rho^{v:f}_{fr:in}u^{v:f}_{y}}{6}-\left(\frac{\rho^{v:mi}_{fr:in}}{\rho^{v:mi}_{fr:in}-3}+\frac{\rho^{v:f}_{fr:in}}{\rho^{v:f}_{fr:in}-3}\right)\left(\frac{f_{6}-4f_{18}-4f_{10}-f_{5}-f_{11}-f_{12}+f_{13}+f_{14}}{2}\right)+\frac{3\rho^{v:mw}_{fr:in}(u^{v:mw}_{fr:y}+u^{v:mw}_{fr:z})+3\rho^{v:e}_{fr:in}(u^{v:e}_{fr:in}+u^{v:e}_{fr:y})}{4} \tag{69}$$

$$f^{v}_{fr:9} = \frac{\rho^{v:mi}_{fr:in}u^{v:mi}_{y}+\rho^{v:f}_{fr:in}u^{v:f}_{y}}{6}+\left(\frac{\rho^{v:mi}_{fr:in}}{\rho^{v:mi}_{fr:in}-3}+\frac{\rho^{v:f}_{fr:in}}{\rho^{v:f}_{fr:in}-3}\right)\left(\frac{4f_{8}+4f_{3}+f_{2}-f_{1}-f_{11}+f_{12}-f_{13}+f_{14}}{2}\right)+\frac{3\rho^{v:mw}_{fr:in}(-u^{v:mw}_{fr:x}+u^{v:mw}_{fr:y})+3\rho^{v:e}_{fr:in}(-u^{v:e}_{fr:in}+u^{v:e}_{fr:x})}{4} \tag{70}$$

$$f^{v}_{fr:3} = \frac{\rho^{v:mi}_{fr:in}u^{v:mi}_{y}+\rho^{v:e}_{fr:in}u^{v:e}_{y}+\rho^{v:t}_{in}u^{v:t}_{fr:y}+\rho^{v:m}_{in}u^{v:m}_{fr:y}+11f_{4}+f_{1}+f_{5}+f_{2}+f_{6}}{3} \tag{71}$$

$$f^{v}_{fr:7} = \frac{\rho^{v:mi}_{fr:in}u^{v:mi}_{y}+\rho^{v:f}_{fr:in}u^{v:f}_{y}}{6}-\left(\frac{\rho^{v:mi}_{fr:in}}{\rho^{v:mi}_{fr:in}-3}+\frac{\rho^{v:f}_{fr:in}}{\rho^{v:f}_{fr:in}-3}\right)\left(\frac{f_{2}-4f_{10}-4f_{2}-f_{1}-f_{11}+f_{12}-f_{13}+f_{14}}{2}\right)+\frac{3\rho^{v:mw}_{fr:in}(u^{v:mw}_{fr:x}+u^{v:mw}_{fr:y})+3\rho^{v:e}_{fr:in}(u^{v:e}_{fr:in}+u^{v:e}_{fr:x})}{4} \tag{72}$$

$$f_{fr:16} = \frac{\rho^{v:mi}_{fr:in}u^{v:mi}_{y}+\rho^{v:f}_{fr:in}u^{v:f}_{y}}{6}+\left(\frac{\rho^{v:mi}_{fr:in}}{\rho^{v:mi}_{fr:in}-3}+\frac{\rho^{v:f}_{fr:in}}{\rho^{v:f}_{fr:in}-3}\right)\left(\frac{4f_{17}+4f_{12}+f_{6}-f_{5}-f_{11}-f_{12}+f_{13}+f_{14}}{2}\right)+\frac{3\rho^{v:mw}_{fr:in}(u^{v:mw}_{fr:y}-u^{v:mw}_{fr:z})+3\rho^{v:e}_{fr:in}(u^{v:e}_{fr:in}-u^{v:e}_{fr:y})}{4} \tag{73}$$

For rear inlet and front outlet case, $f^{v}_{rf:i}$ (i =22, 17, 23, 10, 4, 8, 20, 18, 25) can be defined as

$$f^{v}_{rf:22} = f^{v}_{9} - \frac{\rho^{v:t}_{in}(u^{v:t}_{rf:x}+u^{v:t}_{rf:y}-u^{v:t}_{rf:z})}{12} \tag{74}$$

$$f^{v}_{rf:20} = f_{7} - \frac{\rho^{v:t}_{in}(-u^{v:t}_{rf:x}+u^{v:t}_{rf:y}+u^{v:t}_{rf:z})}{12} \tag{75}$$

$$f^{v}_{rf:23} = f_{12} - \frac{\rho^{v:t}_{in}(-u^{v:t}_{rf:x}+u^{v:t}_{rf:y}-u^{v:t}_{rf:z})}{12} \tag{76}$$

$$f^{v}_{rf:25} = f_{14} - \frac{\rho^{v:t}_{in}(-u^{v:t}_{rf:x}+u^{v:t}_{rf:y}-u^{v:t}_{rf:z})}{12} \tag{77}$$

$$f_{rf:17}^{v} = \frac{\rho_{rf:in}^{v:mi}u_{y}^{v:mi}+\rho_{rf:in}^{v:f}u_{y}^{v:f}}{6}-\left(\frac{\rho_{rf:in}^{v:mi}}{\rho_{rf:in}^{v:mi}-3}+\frac{\rho_{rf:in}^{v:f}}{\rho_{rf:in}^{v:f}-3}\right)\left(\frac{2f_{16}+f_{11}+f_{6}-f_{5}-f_{12}+f_{13}+f_{14}}{2}\right)-\frac{3\rho_{rf:in}^{v:mw}(u_{rf:y}^{v:mw}-u_{rf:z}^{v:mw})+3\rho_{rf:in}^{v:e}(u_{rf:y}^{v:e}-u_{rf:z}^{v:e})}{4} \tag{78}$$

$$f_{rf:10}^{v} = \left(\frac{\rho_{rf:in}^{v:mi}}{2(\rho_{rf:in}^{v:mi}-3)}+\frac{\rho_{rf:in}^{v:e}}{2(\rho_{rf:in}^{v:e}-3)}\right)\left(\frac{2f_{7}+f_{1}+f_{2}-f_{11}+f_{12}-f_{13}+f_{14}}{2}\right)-\frac{\rho_{in}^{v:mi}u_{rf:y}^{v:mi}+\rho_{in}^{v:e}u_{rf:y}^{v:e}}{6}-\frac{3\rho_{rf:in}^{v:mw}(u_{rf:x}^{v:mw}+u_{rf:y}^{v:mw})+3\rho_{rf:in}^{v:e}(u_{rf:x}^{v:e}+u_{rf:y}^{v:e})}{4} \tag{79}$$

$$f_{rf:4}^{v} = \frac{11f_{3}-f_{0}-f_{1}-f_{5}-f_{2}-f_{6}-\rho_{rf:in}^{v:mi}u_{rf}^{v:mi}-\rho_{rf:in}^{v:e}u_{rf}^{v:e}-\rho_{in}^{v:t}u_{rf:y}^{v:t}-\rho_{in}^{v:m}u_{rf:y}^{v:m}}{3} \tag{80}$$

$$f_{rf:8}^{v} = \left(\frac{\rho_{rf:in}^{v:mi}}{\rho_{rf:in}^{v:mi}-3}+\frac{\rho_{rf:in}^{v:f}}{\rho_{rf:in}^{v:e}-3}\right)\left(\frac{2f_{9}-f_{2}+2f_{4}+f_{1}+f_{11}-f_{12}+f_{13}-f_{14}}{2}\right)-\frac{\rho_{rf:in}^{v:mi}u_{y}^{mi}+\rho_{rf:in}^{v:f}u_{y}^{v:f}}{6}-\frac{3\rho_{rf:in}^{v:mw}(-u_{rf:x}^{v:mw}+u_{rf:y}^{v:mw})+3\rho_{rf:in}^{v:e}(-u_{rf:x}^{v:e}+u_{rf:y}^{v:e})}{4} \tag{81}$$

$$f_{rf:18}^{v} = \left(\frac{\rho_{rf:in}^{v:mi}}{\rho_{rf:in}^{v:mi}-3}+\frac{\rho_{rf:in}^{v:f}}{\rho_{rf:in}^{v:f}-3}\right)\left(\frac{2f_{15}+2f_{9}+f_{6}-f_{5}-f_{11}-f_{12}+f_{13}+f_{14}}{2}\right)-\frac{\rho_{rf:in}^{v:mi}u_{y}^{v:mi}+\rho_{rf:in}^{v:f}u_{y}^{v:f}}{6}-\frac{3\rho_{rf:in}^{v:mw}(u_{rf:y}^{v:mw}+u_{rf:z}^{v:mw})+3\rho_{rf:in}^{v:e}(u_{rf:y}^{v:e}+u_{rf:z}^{v:e})}{4} \tag{82}$$

3.2 South-north flow

As shown in fiugure.3.1b, when the extended fluid flow direction is from south to north, after streaming, the unknown distribution functions are $f_{sn:i}$ (i=26, 12, 22, 15, 5, 17, 19, 11, 23), on the contrary, the unknown distribution functions are $f_{ns:i}$ (i =20, 14, 24, 18, 6, 16, 25, 13, 21).

PC:

For the south inlet and north outlet case, $f_{sn:i}^{p}$ (i = 26, 12, 22, 15, 5, 17, 19, 11, 23) can be defined as

$$f_{sn:26}^{p} = f_{13}^{t} - \frac{\rho_{in}^{t}(-u_{sn:x}^{p:t}+u_{sn:y}^{p:t}+u_{sn:z}^{p:t})}{12} \tag{83}$$

$$f_{sn:19}^{p} = f_{8} - \frac{\rho_{in}^{p:t}(-u_{sn:x}^{p:t}-u_{sn:y}^{p:t}+u_{sn:z}^{p:t})}{12} \tag{84}$$

$$f_{sn:26}^{p} = f_{12} - \frac{\rho_{in}^{p:t}(u_{sn:x}^{p:t}-u_{sn:y}^{p:t}+u_{sn:z}^{p:t})}{12} \tag{85}$$

$$f_{sn:22}^{p} = f_{9} - \frac{\rho_{in}^{p:t}(u_{ns:x}^{p:t}-u_{ns:y}^{p:t}+u_{ns:z}^{p:t})}{12} \tag{86}$$

$$f_{sn:12}^{p} = \frac{3\rho_{in}^{p:mw}(-u_{sn:y}^{p:mw}+u_{sn:z}^{p:mw})+3\rho_{in}^{p:e}(-u_{sn:y}^{p:e}+u_{sn:z}^{p:e})-f_{8}+4f_{13}+3f_{7}-f_{1}+f_{2}+f_{9}+f_{10}}{4}+\frac{\rho_{in}^{p:mi}u_{sn:z}^{p:mi}+\rho_{in}^{p:f}u_{sn:z}^{p:f}}{6} \tag{87}$$

$$f_{sn:15}^{p} = \frac{\rho_{in}^{p:mi}u_{sn:z}^{p:mi}+\rho_{in}^{p:f}u_{sn:z}^{p:f}}{6}+\frac{4f_{18}+4f_{10}+f_{3}^{mi}-f_{4}^{mi}+f_{7}^{mi}-f_{8}^{mi}+f_{9}^{mi}-f_{10}^{mi}+3\rho_{in}^{mw}(-u_{sn:x}^{p:mw}+u_{sn:z}^{p:mw})+3\rho_{in}^{p:e}(-u_{sn:x}^{p:e}+u_{sn:z}^{p:e})}{4} \tag{88}$$

$$f^{p}_{sn:5} = \frac{\rho^{p:mi}_{in}u^{p:mi}_{sn:z} + \rho^{p:e}_{in}u^{p:e}_{sn:z} + \rho^{p:m}_{in}u^{p:m}_{sn:z} + 7f_6 - f_0 - f_4 - f_3 - f_2 - f_1}{3} + \frac{3\rho^{p:e}_{in}(u^{p:e}_{sn:y} + u^{p:e}_{sn:z})}{4} \tag{89}$$

$$f^{p}_{sn:17} = \frac{\rho^{p:mi}_{in}u^{p:mi}_{sn:z} + \rho^{p:f}_{in}u^{p:f}_{sn:z}}{6} + \frac{4f_{16} + 4f_{11} - f_3 + f_4 - f_7 + f_8 - f_9 + f_{10} + 3\rho^{p:mw}_{in}(u^{p:mw}_{sn:x} + u^{p:mw}_{sn:z}) + 3\rho^{p:e}_{in}(u^{p:e}_{sn:x} + u^{p:e}_{sn:z})}{4} \tag{90}$$

$$f^{p}_{sn:11} = \frac{\rho^{p:mi}_{in}u^{p:mi}_{sn:z} + \rho^{p:f}_{in}u^{p:f}_{sn:z}}{6} + \frac{4f_{14} + 4f_6 - f^{mi}_1 + f^{mi}_2 - f^{mi}_7 - f^{mi}_8 + f^{mi}_9 + f^{mi}_{10} + 3\rho^{p:mw}_{in}(u^{p:mw}_{sn:y} + u^{p:mw}_{sn:z}) + 3\rho^{p:e}_{in}(u^{p:e}_{sn:y} + u^{p:e}_{sn:z})}{4} \tag{91}$$

For the north inlet and south outlet case, $f^{p}_{ns:i}$ (i =20, 14, 24, 18, 6, 16, 25, 13, 21) can be defined as

$$f^{p}_{ns:20} = f_7 + \frac{\rho^{p:t}_{in}(-u^{p:t}_{ns:x} - u^{p:t}_{ns:y} + u^{p:t}_{ns:z})}{12} \tag{92}$$

$$f^{p}_{ns:21} = f_{10} + \frac{\rho^{p:t}_{in}(u^{p:t}_{ns:x} - u^{p:t}_{ns:y} + u^{p:t}_{ns:z})}{12} \tag{93}$$

$$f^{p}_{ns:24} = f_{11} + \frac{\rho^{p:t}_{in}(u^{p:t}_{ns:x} - u^{p:t}_{ns:y} + u^{p:t}_{ns:z})}{12} \tag{94}$$

$$f^{p}_{ns:25} = f_{14} + \frac{\rho^{p:t}_{in}(-u^{p:t}_{ns:x} + u^{p:t}_{ns:y} + u^{p:t}_{ns:z})}{12} \tag{95}$$

$$f^{p}_{ns:14} = \frac{3\rho^{p:mw}_{in}(u^{p:mw}_{ns:y} + u^{p:mw}_{ns:z}) + 3\rho^{p:e}_{in}(u^{p:e}_{ns:y} + u^{p:e}_{ns:z}) - f_1 + f_2 - f_7 - f_8 + f_9 + f_{10} + 2f_{11} + 2f_5}{4} - \frac{\rho^{p:mi}_{in}u^{p:mi}_{ns:z} + \rho^{p:f}_{in}u^{p:f}_{ns:z}}{6} \tag{96}$$

$$f^{p}_{ns:18} = \frac{2f_{15} + 2f_{10} - f_3 + f_4 - f_7 + f_8 - f_9 + f_{10} + 3\rho^{p:mw}_{in}(-u^{p:mw}_{ns:x} + u^{p:mw}_{ns:z}) + 3\rho^{e:mw}_{in}(-u^{e:mw}_{ns:x} + u^{e:mw}_{ns:z})}{4} - \frac{\rho^{p:mi}_{in}u^{p:mi}_{ns:z} + \rho^{p:f}_{in}u^{p:f}_{ns:z}}{6} \tag{97}$$

$$f^{p}_{ns:6} = \frac{\rho^{p:t}_{in}u^{p:t}_{ns:z} + \rho^{p:m}_{in}u^{p:m}_{ns:z} - \rho^{p:mi}_{in}u^{p:mi}_{ns:z} - \rho^{p:f}_{in}u^{p:f}_{ns:z} - 11f_5 - f_0 - f_4 - f_3 - f_1 - f_2}{3} \tag{98}$$

$$f^{p}_{ns:16} = \frac{2f_{17} + 2f_{12} + f_3 - f_4 + f_7 - f_8 + f_9 - f_{10} - 3\rho^{p:mw}_{in}(u^{p:mw}_{ns:x} + u^{p:mw}_{ns:z}) - 3\rho^{p:e}_{in}(u^{p:e}_{ns:x} + u^{p:e}_{ns:z})}{4} - \frac{\rho^{p:mi}_{in}u^{p:mi}_{sn:z} + \rho^{p:f}_{in}u^{p:f}_{sn:z}}{6} \tag{99}$$

$$f^{p}_{ns:13} = \frac{4f_{12} + 5f_8 + f_1 - f_2 + f_7 - f_9 - f_{10} - 3\rho^{p:mw}_{in}(-u^{p:mw}_{ns:y} + u^{p:mw}_{ns:z}) - 3\rho^{p:e}_{in}(-u^{p:e}_{ns:y} + u^{p:e}_{ns:z})}{4} - \frac{\rho^{p:mi}_{in}u^{p:mi}_{ns:z} + \rho^{p:f}_{in}u^{p:f}_{ns:z}}{6} \tag{100}$$

VC:

For the south inlet and north outlet case, $f^{v}_{sn:i}$ (i = 26, 12, 22, 15, 5, 17, 19, 11, 23) are defined as

$$f_{sn:26}^{v} = f_{13} - \frac{\rho_{in}^{v:t}(-u_{sn:x}^{v:t} + u_{sn:y}^{v:t} + u_{sn:z}^{v:t})}{12} \quad (101)$$

$$f_{sn:19}^{v} = f_{8} - \frac{\rho_{in}^{v}(-u_{sn:x}^{v:t} - u_{sn:y}^{v:t} + u_{sn:z}^{v:t})}{12} \quad (102)$$

$$f_{sn:22}^{v} = f_{9} - \frac{\rho_{in}^{v:t}(u_{sn:x}^{v:t} - u_{sn:y}^{v:t} + u_{sn:z}^{v:t})}{12} \quad (103)$$

$$f_{sn:23}^{v} = f_{12} - \frac{\rho_{in}^{v:t}(u_{sn:x}^{v:t} - u_{sn:y}^{v:t} + u_{sn:z}^{v:t})}{12} \quad (104)$$

$$f_{sn:12}^{v} = \frac{\rho_{sn:in}^{v:mi}u_{z}^{mi} + \rho_{sn:in}^{v:f}u_{z}^{v:f}}{6} - \left(\frac{\rho_{sn:in}^{v:mi}}{\rho_{sn:in}^{v:mi} - 3} + \frac{\rho_{sn:in}^{v:f}}{\rho_{sn:in}^{v:f} - 3}\right)\left(\frac{f_1 - f_2 - f_7 + f_8 - f_9 - f_{10} - 2f_{13}}{2}\right) + \frac{3\rho_{sn:in}^{v:mw}(-u_{sn:y}^{v:mw} + u_{sn:z}^{v:mw}) + 3\rho_{sn:in}^{v:e}(-u_{sn:y}^{v:e} + u_{sn:z}^{v:e})}{4} \quad (105)$$

$$f_{sn:15}^{v} = \frac{\rho_{sn:in}^{v:mi}u_{z}^{mi} + \rho_{sn:in}^{v:f}u_{z}^{f}}{6} + \left(\frac{\rho_{sn:in}^{v:mi}}{2(\rho_{sn:in}^{v:mi} - 3)} + \frac{\rho_{sn:in}^{v:f}}{2(\rho_{sn:in}^{v:f} - 3)}\right)\left(\frac{f_3 - f_4 + f_7 - f_8 + f_9 + f_{10} + 2f_{18}}{2}\right) + \frac{3\rho_{sn:in}^{v:mw}(-u_{sn:x}^{v:mw} + u_{sn:z}^{v:mw}) + 3\rho_{sn:in}^{v:e}(-u_{sn:x}^{v:e} + u_{sn:z}^{v:e})}{4} \quad (106)$$

$$f_{sn:5}^{v} = \frac{\rho_{sn:in}^{v:mi}u_{z}^{v:mi} + \rho_{sn:in}^{v:f}u_{z}^{v:f} - \rho_{in}^{v:t}u_{sn:z}^{v:t} + \rho_{in}^{v:m}u_{sn:z}^{v:m} + 11f_6 + f_0 + f_4 + f_3 + f_2 + f_1}{3} \quad (107)$$

$$f_{sn:17}^{v} = \frac{\rho_{sn:in}^{v:mi}u_{z}^{v:mi} + \rho_{sn:in}^{v:f}u_{z}^{v:f}}{6} - \left(\frac{\rho_{sn:in}^{v:mi}}{\rho_{sn:in}^{v:mi} - 3} + \frac{\rho_{sn:in}^{v:f}}{\rho_{sn:in}^{v:f} - 3}\right)\left(\frac{f_3 - f_4 + f_7 - f_8 + f_9 - f_{10} - 2f_{16} - 2f_{11}}{2}\right) + \frac{3\rho_{sn:in}^{v:mw}(u_{sn:x}^{v:mw} + u_{sn:z}^{v:mw}) + 3\rho_{sn:in}^{v:e}(u_{sn:x}^{v:e} + u_{sn:z}^{v:e})}{4} \quad (108)$$

$$f_{sn:11}^{v} = \frac{\rho_{sn:in}^{v:mi}u_{z}^{v:mi} + \rho_{sn:in}^{v:f}u_{z}^{v:f}}{6} - \left(\frac{\rho_{sn:in}^{v:mi}}{\rho_{sn:in}^{v:mi} - 3} - \frac{\rho_{sn:in}^{v:f}}{\rho_{sn:in}^{v:f} - 3}\right)\left(\frac{f_1 - f_2 + f_7 + f_8 - f_9 - f_{10} - 2f_{14} - 2f_6}{2}\right) + \frac{3\rho_{sn;in}^{v:mw}(u_{sn:y}^{v:mw} + u_{sn:z}^{v:mw}) + 3\rho_{sn;in}^{v:e}(u_{sn:y}^{v:e} + u_{sn:z}^{v:e})}{4} \quad (109)$$

For north inlet and south outlet case, $f_{ns:i}^{v}$ (i =20, 14, 24, 18, 6, 16, 25, 13, 21) are defined as

$$f_{ns:20}^{v} = f_{7} + \frac{\rho_{in}^{v:t}(-u_{ns:x}^{v:t} - u_{ns:y}^{v:t} + u_{ns:z}^{v:t})}{12} \quad (110)$$

$$f_{ns:21}^{v} = f_{10} + \frac{\rho_{in}^{v:t}(u_{ns:x}^{v:t} - u_{ns:y}^{v:t} + u_{ns:z}^{v:t})}{12} \quad (111)$$

$$f_{ns:24}^{v} = f_{11} + \frac{\rho_{in}^{v:t}(u_{ns:x}^{t} - u_{ns:y}^{t} + u_{ns:z}^{t})}{12} \quad (112)$$

$$f_{ns:25}^{v} = f_{14} + \frac{\rho_{in}^{v:t}(-u_{ns:x}^{t} + u_{ns:y}^{t} + u_{ns:z}^{t})}{12} \quad (113)$$

$$f_{ns:14}^{v} = -\frac{\rho_{ns:in}^{v:mi}u_{z}^{v:mi} + \rho_{ns:in}^{v:f}u_{z}^{v:f}}{6} - \left(\frac{\rho_{ns:in}^{v:mi}}{\rho_{ns:in}^{v:mi} - 3} + \frac{\rho_{ns:in}^{v:f}}{\rho_{ns:in}^{v:f} - 3}\right)\left(\frac{f_7 - 2f_{11} - 2f_5 + f_1 - f_2 + f_8 - f_9 - f_{10}}{2}\right) + \frac{3\rho_{ns:in}^{v:mw}(u_{ns:y}^{v:mw} + u_{ns:z}^{v:mw}) + 3\rho_{ns:in}^{v:e}(u_{ns:y}^{v:e} + u_{ns:z}^{v:e})}{4} \quad (114)$$

$$f_{ns:18}^{v} = -\frac{\rho_{ns:in}^{v:mi}u_{z}^{v:mi} + \rho_{ns:in}^{v:f}u_{z}^{v:f}}{6} - \left(\frac{\rho_{ns:in}^{v:mi}}{\rho_{ns:in}^{v:mi} - 3} + \frac{\rho_{ns:in}^{v:f}}{\rho_{ns:in}^{v:f} - 3}\right)\left(\frac{f_7 - 2f_{15} - 2f_{10} - f_3 - f_4 + -f_8 + f_9 - f_{10}}{2}\right) + \frac{3\rho_{ns:in}^{v:mw}(u_{ns:z}^{v:mw} + u_{ns:x}^{v:mw}) + 3\rho_{ns:in}^{v:e}(u_{ns:z}^{v:e} + u_{ns:x}^{v:e})}{4} \quad (115)$$

$$f_{ns:6}^{v} = \frac{f_0 + f_4 + f_3 + f_1 + f_2 - 7f_5 - \rho_{ns:in}^{v:mi}u_{z}^{v:mi} - \rho_{ns:in}^{v:f}u_{z}^{v:f} - \rho_{in}^{v:t}u_{ns:z}^{v:t} - \rho_{in}^{m:t}u_{ns:z}^{m:t}}{3} \quad (116)$$

$$f_{ns:16}^{v} = \left(\frac{\rho_{ns:in}^{v:mi}}{\rho_{ns:in}^{v:mi} - 3} + \frac{\rho_{ns:in}^{v:f}}{\rho_{ns:in}^{v:f} - 3}\right)\left(\frac{2f_{17} + 2f_{12} + f_3 - f_4 + f_7 - f_8 + f_9 - f_{10}}{2}\right) - \frac{\rho_{ns:in}^{v:mi}u_{z}^{v:mi} + \rho_{ns:in}^{v:f}u_{z}^{v:f}}{6} + -\frac{3\rho_{ns:in}^{v:mw}(u_{ns:x}^{v:mw} + u_{ns:z}^{v:mw}) + 3\rho_{ns:in}^{v:e}(u_{ns:x}^{v:e} + u_{ns:z}^{v:e})}{4} \quad (117)$$

$$f_{ns:13}^{v} = \left(\frac{\rho_{ns:in}^{v:mi}}{\rho_{ns:in}^{v:mi} - 3} + \frac{\rho_{ns:in}^{v:f}}{\rho_{ns:in}^{v:f} - 3}\right)\left(\frac{f_1 - f_2 + f_7 + f_8 - f_9 - f_{10} + 2f_{12} + 2f_8}{2}\right) - \frac{\rho_{ns:in}^{v:mi}u_{z}^{v:mi} + \rho_{ns:in}^{v:f}u_{z}^{v:f}}{6} + -\frac{3\rho_{ns:in}^{v:mw}(u_{ns:z}^{v:mw} - u_{ns:y}^{v:mw}) + 3\rho_{ns:in}^{v:e}(u_{ns:z}^{v:e} - u_{ns:y}^{v:e})}{4} \quad (118)$$

3.3 West-east flow

As shown in fiugure.3.1c, when the extended fluid flow direction is from west to east, after streaming, the unknown distribution functions are $f_{we:i}$ (i=23, 11, 19, 8, 1, 7, 25, 13, 21), on the contrary, the unknown distribution functions are $f_{ew:i}$ (i =22, 12, 26, 10, 2, 9, 20, 14, 24).

PC:

For the west inlet and east outlet case, $f^{p}_{we:i}$ (i=23, 11, 19, 8, 1, 7, 25, 13, 21) as defined as

$$f^{p}_{we:23} = f_{12} + \frac{\rho^{p:t}_{in}(u^{p:t}_{we:x} + u^{p:t}_{we:y} - u^{p:t}_{we:z})}{12} \tag{119}$$

$$f^{p}_{we:21} = f_{10} + \frac{\rho^{p:t}_{in}(u^{p:t}_{we:x} - u^{p:t}_{we:y} - u^{p:t}_{we:z})}{12} \tag{120}$$

$$f^{p}_{we:25} = f_{14} + \frac{\rho^{p:t}_{in}(u^{p:t}_{we:x} - u^{p:t}_{we:y} + u^{p:t}_{we:z})}{12} \tag{121}$$

$$f^{p}_{we:19} = f_{8} + \frac{\rho^{p:t}_{in}(u^{p:t}_{we:x} - u^{p:t}_{we:y} - u^{p:t}_{we:z})}{12} \tag{122}$$

$$f_{we:11} = \frac{\rho^{p:mi}_{in}u^{p:mi}_{we:x} + \rho^{p;f}_{in}u^{p:f}_{we:x}}{6} + \frac{4f_{14} + 3f_{6} + f_{5} + f_{15} - f_{16} + f_{17} - f_{18} + 3\rho^{p:mw}_{in}(u^{p:mw}_{we:x} + u^{p:mw}_{we:y}) + 3\rho^{p:e}_{in}(u^{p:e}_{we:x} + u^{p:e}_{we:y})}{4} \tag{123}$$

$$f^{p}_{we:8} = \frac{\rho^{p:mi}_{in}u^{p:mi}_{we:x} + \rho^{p:f}_{in}u^{p:f}_{we:x}}{6} + \frac{4f_{9} + 5f_{4} - f_{3} - f_{15} - f_{16} + f_{17} + f_{18} + 3\rho^{p:mw}_{in}(u^{p:mw}_{we:x} + u^{p:mw}_{we:z}) + 3\rho^{p:e}_{in}(u^{p:e}_{we:x} + u^{p:e}_{we:z})}{4} \tag{124}$$

$$f^{p}_{we:1} = \frac{\rho^{p:mi}_{in}u^{p:mi}_{we:x} + \rho^{p:f}_{in}u^{p:f}_{we:x} + \rho^{p:t}_{in}u^{p:t}_{we:x} + \rho^{p:m}_{in}u^{p:m}_{we:x} - f_{0} - f_{4} - f_{3} - f_{5} - f_{6} + 7f_{2}}{3} \tag{125}$$

$$f^{p}_{we:7} = \frac{\rho^{p:mi}_{in}u^{p:mi}_{we:x} + \rho^{p:f}_{in}u^{p:f}_{we:x}}{6} + \frac{4f_{10} + 4f_{8} + f_{3} - f_{4} + f_{15} + f_{16} - f_{17} - f_{18} + 3\rho^{p:mw}_{in}(u^{p:mw}_{we:x} - u^{p:mw}_{we:y}) + 3\rho^{p:e}_{in}(u^{p:e}_{we:x} - u^{p:e}_{we:y})}{4} \tag{126}$$

$$f^{p}_{we:13} = \frac{\rho^{p:mi}_{in}u^{p:mi}_{we:x} + \rho^{p:f}_{in}u^{p:f}_{we:x}}{6} - \frac{4f_{12} + 4f_{8} + f_{5} - f_{6} + f_{15} - f_{16} + f_{17} - f_{18} + 3\rho^{mw}_{in}(u^{p:mw}_{we:x} - u^{p:mw}_{we:y}) + 3\rho^{e}_{in}(u^{p:e}_{we:x} - u^{p:e}_{we:y})}{4} \tag{127}$$

For the east inlet and west outlet case, $f^{p}_{ew:i}$ (i =22, 12, 26, 10, 2, 9, 20, 14, 24) are defined as,

$$f^{p}_{ew:22} = f^{p:t}_{9} - \frac{\rho^{p:t}_{in}(u^{p:t}_{ew:x} - u^{p:t}_{ew:y} - u^{p:t}_{ew:z})}{12} \tag{128}$$

$$f^{p}_{ew:24} = f_{11} + \frac{\rho^{p:t}_{in}(u^{p:t}_{ew:x} + u^{p:t}_{ew:y} - u^{p:t}_{ew:z})}{12} \tag{129}$$

$$f^{p}_{ew:20} = f_{7} + \frac{\rho^{p:t}_{in}(u^{p:t}_{ew:x} + u^{p:t}_{ew:y} - u^{p:t}_{ew:z})}{12} \tag{130}$$

$$f^{p}_{ew:26} = f_{13} - \frac{\rho^{p:t}_{in}(u^{p:t}_{ew:x} - u^{p:t}_{ew:y} + u^{p:t}_{ew:z})}{12} \tag{131}$$

$$f^{p}_{ew:12} = \frac{\rho^{p:mi}_{in}u^{p:mi}_{ew:x} + \rho^{p:f}_{in}u^{p:f}_{ew:x}}{6} + \frac{4f_{13} + 4f_{7} + f_{5} - f_{6} + f_{15} - f_{16} + f_{17} - f_{18} + 3\rho^{mw}_{in}(u^{p:mw}_{ew:x} - u^{p:mw}_{ew:y}) + 3\rho^{e}_{in}(u^{p:e}_{ew:x} - u^{p:e}_{ew:y})}{4} \tag{132}$$

$$f_{ew:10}^{p:} = -\frac{\rho_{in}^{p:mi} u_{ew:x}^{p:mi} + \rho_{in}^{p:f} u_{ew:x}^{p:f}}{6} + \frac{4f_7 + 4f_1 - f_3 + f_4 - f_{15} - f_{16} + f_{17} + f_{18} - 3\rho_{in}^{p:mw}(u_{ew:x}^{p:mw} - u_{ew:z}^{p:mw}) - 3\rho_{in}^{p:e}(u_{ew:x}^{p:e} - u_{ew:z}^{p:e})}{4} \quad (133)$$

$$f_{ew:2}^{p} = \frac{9f_1 + f_0 + f_4 + f_3 + f_5 + f_6 - \rho_{in}^{p:mi} u_{ew:x}^{p:mi} - \rho_{in}^{p:f} u_{ew:x}^{p:f} - \rho_{in}^{p:t} u_{ew:x}^{p:t} - \rho_{in}^{p:m}}{3} \quad (134)$$

$$f_{ew:9}^{p} = f_8 + f_3 - \frac{\rho_{in}^{p:mi} u_{ew:x}^{p:mi} + \rho_{in}^{p:f} u_{ew:x}^{p:f}}{6} - \frac{-f_3 + f_4 - f_{15} - f_{16} + f_{17} + f_{18} + 3\rho_{in}^{p:mw}(u_{ew:x}^{p:mw} + u_{ew:z}^{p:mw}) + 3\rho_{in}^{p:e}(u_{ew:x}^{p:e} + u_{ew:z}^{p:e})}{4} \quad (135)$$

$$f_{ew:14}^{p} = f_{11} + f_5 - \frac{\rho_{in}^{p:mi} u_{ew:x}^{p:mi} + \rho_{in}^{p:f} u_{ew:x}^{p:f}}{6} - \frac{-f_3 + f_4 - f_{15} - f_{16} + f_{17} + f_{18} - 3\rho_{in}^{p:mw}(u_{ew:x}^{p:mw} + u_{ew:y}^{p:mw}) - 3\rho_{in}^{p:e}(u_{ew:x}^{p:e} + u_{ew:y}^{p:e})}{4} \quad (136)$$

VC:

For the west inlet and east outlet case, $f_{we:i}^{v}$ (i=23, 11, 19, 8, 1, 7, 25, 13, 21), are defined as

$$f_{we:23}^{v} = f_{12} + \frac{\rho_{we:in}^{v:t}(u_{we:x}^{v:t} + u_{we:y}^{v:t} - u_{we:z}^{v:t})}{12} \quad (137)$$

$$f_{we:25}^{v} = f_{14} + \frac{\rho_{we:in}^{v:t}(u_{we:x}^{v:t} - u_{we:y}^{v:t} + u_{we:z}^{v:t})}{12} \quad (138)$$

$$f_{we:21}^{v} = f_{10} + \frac{\rho_{we:in}^{v:t}(u_{we:x}^{v:t} - u_{we:y}^{v:t} - u_{we:z}^{v:t})}{12} \quad (139)$$

$$f_{we:19}^{v} = f_8 + \frac{\rho_{we:in}^{v:t}(u_{we:x}^{v:t} - u_{we:y}^{v:t} - u_{we:z}^{v:t})}{12} \quad (140)$$

$$f_{ew:11}^{v} = \left(\frac{\rho_{ew:in}^{v:mi}}{\rho_{ew:in}^{v:mi} - 3} + \frac{\rho_{ew:in}^{v:f}}{\rho_{ew:in}^{v:f} - 3}\right)\left(\frac{f_{14} + f_5 + f_6 + f_{15} - f_{16} + f_{17} - f_{18}}{2}\right) + \frac{\rho_{ew:in}^{v:mi} u_x^{v:mi} + \rho_{ew:in}^{v:f} u_x^{v:f}}{6} + \frac{3\rho_{we:in}^{v:mw}(u_{we:x}^{v:mw} + u_{we:y}^{v:mw}) + 3\rho_{we:in}^{v:e}(u_{we:x}^{v:e} + u_{we:y}^{v:e})}{4} \quad (141)$$

$$f_{ew:8}^{v:mi} = \left(\frac{\rho_{ew:in}^{v:mi}}{\rho_{ew:in}^{v:mi} - 3} + \frac{\rho_{ew:in}^{v:f}}{\rho_{ew:in}^{v:f} - 3}\right)\left(\frac{2f_9 - f_3 - f_4 - f_{15} - f_{16} + f_{17} + f_{18}}{2}\right) + \frac{\rho_{ew:in}^{v:mi} u_x^{v:mi} + \rho_{ew:in}^{v:f} u_x^{v:f}}{6} + \frac{3\rho_{se:in}^{v:mw}(u_{we:x}^{v:mw} + u_{we:z}^{v:mw}) + 3\rho_{se:in}^{v:e}(u_{we:x}^{v:e} + u_{we:z}^{v:e})}{4} \quad (142)$$

$$f_{ew:1}^{v} = \frac{\rho_{ew:in}^{v:mi} u_x^{v:mi} + \rho_{ew:in}^{v:f} u_x^{v:f} + \rho_{we:in}^{v:t} u_{we:x}^{v:m} + \rho_{we:in}^{v:m} u_{we:x}^{v:m} + 11f_2 + f_0 + f_4 + f_3 + f_5 + f_6}{3} \quad (143)$$

$$f_{ew:7}^{v} = \left(\frac{\rho_{ew:in}^{v:mi}}{\rho_{ew:in}^{v:mi} - 3} + \frac{\rho_{ew:in}^{v:f}}{\rho_{ew:in}^{v:f} - 3}\right)\left(\frac{f_{15} - f_{10} - f_2 + f_3 - f_4 + f_{16} - f_{17} - f_{18}}{2}\right) + \frac{\rho_{ew:in}^{v:mi} u_{ew:x}^{v:mi} + \rho_{ew:in}^{v:f} u_{ew:x}^{v:f}}{6} + \frac{3\rho_{we:in}^{v:mw}(u_{we:x}^{v:mw} - u_{we:z}^{v:mw}) + 3\rho_{we:in}^{v:e}(u_{we:x}^{v:e} - u_{we:z}^{v:e})}{4} \quad (144)$$

$$f_{ew:13}^{v} = \left(\frac{\rho_{ew:in}^{v:mi}}{\rho_{ew:in}^{v:mi} - 3} + \frac{\rho_{ew:in}^{v:f}}{\rho_{ew:in}^{v:f} - 3}\right)\left(\frac{f_3 + 2f_{12} + 2f_8 - f_4 + f_{15} + f_{16} - f_{17} - f_{18}}{2}\right) + \frac{\rho_{ew:in}^{v:mi} u_x^{v:mi} + \rho_{ew:in}^{v:f} u_x^{v:f}}{6} + \frac{\rho_{we:in}^{v:mw}(u_{we:x}^{v:mw} - u_{we:z}^{v:mw}) + \rho_{we:in}^{v:e}(u_{we:x}^{v:e} - u_{we:z}^{v:e})}{4} \quad (145)$$

For the east inlet and west outlet case, $f_{ew:i}^{v}$ (i =22, 12, 26, 10, 2, 9, 20, 14, 24) are defined as,

$$f_{ew:26}^{v} = f_{13} - \frac{\rho_{ew:in}^{v:t}(u_{ew:x}^{v:t} - u_{ew:y}^{v:t} + u_{ew:z}^{v:t})}{12} \quad (146)$$

$$f_{ew:22}^{v} = f_9 - \frac{\rho_{ew:in}^{v:t}(u_{ew:x}^{v:t} - u_{ew:y}^{v:t} - u_{ew:z}^{v:t})}{12} \quad (147)$$

$$f_{ew:24}^{v} = f_{11} + \frac{\rho_{ew:in}^{v:t}(u_{ew:x}^{v:t} + u_{ew:y}^{v:t} - u_{ew:z}^{v:t})}{12} \quad (148)$$

$$f_{ew:20}^{v} = f_7 + \frac{\rho_{ew:in}^{v:t}(u_{ew:x}^{v:t} + u_{ew:y}^{v:t} - u_{ew:z}^{v:t})}{12} \tag{149}$$

$$f_{ew:12}^{v} = \left(\frac{\rho_{we:in}^{v:mi}}{\rho_{we:in}^{v:mi}-3} + \frac{\rho_{we:in}^{v:f}}{\rho_{we:in}^{v:f}-3}\right)\frac{\left(2f_{13} + 2f_7 + f_5 - f_6 + f_{15} - f_{16} + f_{17} - f_{18}\right)}{2} - \frac{\rho_{we:in}^{v:mi}u_x^{mi} + \rho_{we:in}^{v:f}u_x^{v:f}}{6} + \frac{3\rho_{ew:in}^{v:mw}(u_{ew:x}^{v:mw} - u_{ew:y}^{v:mw}) + 3\rho_{ew:in}^{v:e}(u_{ew:x}^{v:e} - u_{ew:y}^{v:e})}{4} \tag{150}$$

$$f_{ew:10}^{v} = \left(\frac{\rho_{we:in}^{v:mi}}{\rho_{we:in}^{v:mi}-3} + \frac{\rho_{we:in}^{v:f}}{\rho_{we:in}^{v:f}-3}\right)\frac{\left(2f_7 + 2f_1 - f_3 + f_4 - f_{15} - f_{16} + f_{17} + f_{18}\right)}{2} - \frac{\rho_{we:in}^{v:mi}u_x^{v:mi} + \rho_{we:in}^{v:f}u_x^{v:f}}{6} - \frac{3\rho_{in}^{v:mw}(u_{ew:x}^{v:mw} - u_{ew:z}^{v:mw}) + 3\rho_{in}^{v:e}(u_{ew:x}^{v:e} - u_{ew:z}^{v:e})}{4} \tag{151}$$

$$f_{ew:2}^{v} = \frac{7f_1 + f_0 + f_4 + f_3 + f_5 + f_6 - \rho_{we:in}^{v:mi}u_x^{v:mi} - \rho_{we:in}^{v:f}u_x^{v:f} - \rho_{ew:in}^{v:t}u_{ew:x}^{t} - \rho_{we:in}^{v:m}u_x^{v:m}}{3} \tag{152}$$

$$f_{ew:9}^{v} = \left(\frac{\rho_{we:in}^{v:mi}}{\rho_{we:in}^{v:mi}-3} + \frac{\rho_{we:in}^{v:f}}{\rho_{we:in}^{v:f}-3}\right)\left(\frac{2f_8 + f_3 + f_4 - f_{15} - f_{16} + f_{17} + f_{18}}{2}\right) - \frac{\rho_{we:in}^{v:mi}u_x^{v:mi} + \rho_{we:in}^{v:f}u_x^{v:f}}{6} + \frac{3\rho_{ew:in}^{v:mw}(u_{ew:x}^{v:mw} + u_{ew:z}^{v:mw}) + 3\rho_{ew:in}^{v:e}(u_{ew:x}^{v:e} + u_{ew:z}^{v:e})}{4} \tag{153}$$

$$f_{ew:14}^{v} = \left(\frac{\rho_{we:in}^{v:mi}}{\rho_{we:in}^{v:mi}-3} + \frac{\rho_{we:in}^{v:f}}{\rho_{we:in}^{v:f}-3}\right)\left(\frac{f_6 - f_{15} + f_{16} - f_{17} + f_{18} + 2f_{11} + f_5}{2}\right) - \frac{\rho_{we:in}^{v:mi}u_x^{v:mi} + \rho_{we:in}^{v:f}u_x^{v:f}}{6} - \frac{3\rho_{in}^{v:mw}(u_{ew:x}^{v:mw} + u_{ew:y}^{v:mw}) + 3\rho_{in}^{v:e}(u_{ew:x}^{v:e} + u_{ew:y}^{v:e})}{4} \tag{154}$$

4. Flow driven pore−crack network model

As shown in figure 3.2, one typical extended 3D flow driven pore−crack networks model for various porosity composites is constructed through digitized technology by using the slices which were scan from the high resolution X-ray CT facility, which domain size is $50 \times 50 \times 100$ mm^3 ($1434 \times 1434 \times 840$ lu^3).

Figure.3.2. Flow driven pore-crack network model

4.1 HHIE−LBM equations for the flow driven pore−crack network problem

Using the boundary conditions in Eqs. (13~83), and the main-part method given by [30, 36], the flow driven pore−crack network problem in various composites can be translate in to a series HHIE-LBM equations, which the unknown functions is extended discontinue displacement ratio functions. After the complicated mathematical derivation, the closed-form formulation of the HHIE-LBM can be expressed as followings.

$$\int_{-\infty}^{+\infty}\left\{\int_{-\infty}^{+\infty}\left[\int_{S^+}\begin{pmatrix} r^{-3}(c_{44}^2 D_0 s_0^2(\delta_{\bar{\alpha}\bar{\beta}} - 3r_{,\bar{\alpha}}r_{,\bar{\beta}}) + (\delta_{\alpha\beta} - 3r_{,\alpha}r_{,\beta})\sum_{i=1}^{6}\rho_i^2 t_i^2)\tilde{\ddot{u}}_\beta(f_{i\to0:26}) + 3r^{-4}r_{,\alpha}\sum_{i=1}^{6}\lambda_{33}s_i^2 t_i^1\tilde{\ddot{u}}_7(f_{i\to0:26}) + \\ +\left(r^{-7}K_{\alpha\beta1} + r^{-5}K_{\alpha\beta2} + r^{-3}K_{\alpha\beta3}\right)\tilde{\ddot{u}}_\beta(f_{i\to0:26}) + \bar{K}_{\alpha\beta}\tilde{\ddot{u}}_\beta(f_{i\to0:26})\end{pmatrix}dS\right]d\tau\right\}d\tau' = -\dot{p}_\alpha \tag{155}$$

$$\int_{-\infty}^{+\infty}\left\{\int_{-\infty}^{+\infty}\left[\int_{S^+}\begin{pmatrix} r^{-2}r_{,\alpha}\sum_{i=1}^{6}A_i^{\Upsilon}t_i^2\rho_i^1\tilde{u}_\alpha(f_{i\to0:26}) + r^{-3}\sum_{n=3}^{6}\sum_{i=1}^{6}\rho_i^m t_i^t\tilde{\ddot{u}}_n(f_{i\to0:26}) + 3r^{-4}\lambda_{3\alpha}r_{,\alpha}\sum_{i=1}^{6}v_i^2\lambda_i^{\vartheta}\rho_i^m\tilde{\ddot{u}}_6(f_{i\to0:26}) \\ +\left(r^{-7}K_{mJ1} + r^{-5}K_{mJ2} + r^{-3}K_{mJ3}\right)\tilde{\ddot{u}}_J(f_{i\to0:26}) + \int_{S^+}\bar{K}_{mJ}\tilde{\ddot{u}}_J(f_{i\to0:26})\end{pmatrix}dS\right]d\tau\right\}d\tau' = -\dot{p}_m \tag{156}$$

$$\int_{-\infty}^{+\infty}\left\{\int_{-\infty}^{+\infty}\left[\int_{S^+}\begin{pmatrix} r^{-2}(\delta_{\alpha\beta} - 3r_{,\alpha}r_{,\beta})\sum_{i=1}^{6}A_i^{\Upsilon}\lambda_{3\beta}t_i^2\tilde{u}_\beta(f_{i\to0:26}) + 3r^{-4}\lambda_{3\alpha}r_{,\alpha}\sum_{i=1}^{6}A_i^{\Upsilon}v_i^2\lambda_i^{\vartheta}\lambda_{33}\rho_i^6\tilde{\ddot{u}}_7(f_{i\to0:26}) \\ +\sum_{i=1}^{6}\left(r^{-7}K_{6J1} + r^{-5}K_{6J2} + r^{-3}K_{6J3}\right)\tilde{\ddot{u}}_J(f_{i\to0:26}) + \sum_{i=1}^{6}\bar{K}_{6J}\tilde{\ddot{u}}_J(f_{i\to0:26})\end{pmatrix}dS\right]d\tau\right\}d\tau' = -\dot{p}_7 \tag{157}$$

where m=4~6, $\dot{p}_i$, $\dot{p}_4(\dot{q}_0)$ $\dot{p}_5(\dot{b}_0)$, $\dot{p}_6(\dot{\vartheta}_0)$, $\dot{p}_7(\dot{b}_0,\dot{\sigma}_{33})$ can be obtained from the solutions for the loads of un-cracked solids. The hypersingular kernel function K_{KIJ} and Cauchy kernel function $\bar{K}_{IJ}$ are given in [36]. It is shown that the time-domain hypersingular integral equations have structures that are similar to those studied by [37-39].

4.2 Pore−crack network propagation parameters

Consider a local coordinate system on an arbitrary crack front in pore-crack networks structure, defined as x_2 x_3, in which the x_1- axis is the tangent line of the crack front at point q_0, the x_2- axis is the internal normal line of the crack plane, and the x_3- axis is the normal of the crack. Then the extended velocity discontinuities gradient of the crack surface near a crack front point $\ddot{\varphi}_0$ can be expressed as

$$\tilde{\dot{U}}_{i,J} = g_k \xi_2^{\lambda_k} \qquad 0 < \mathrm{Re}(\lambda_k) < 1 \tag{158}$$

where g_k are non-zero constants related to point $\ddot{\varphi}_0$, and λ_k represents the singular indices at the front of arbitrary pore/crack around the pore − crack networks, the singular index can be determined by

$$\cot(\lambda_1\pi)=0\ ,\cot(\lambda_2\pi)=0\ ,\ \cot(\lambda_3\pi)=0\ ,\ \cot(\lambda_4\pi)=0\ ,\ \cot(\lambda_5\pi)=0\ ,\ \cot(\lambda_6\pi)=0\ ,\ \cot(\lambda_7\pi)=0 \tag{159}$$

The extended dynamic stress intensity factors are defined as

$$K_1 = \lim_{r\to 0}\sqrt{2r}\sigma_{33}\Big|_{\ddot{\theta}=0}, K_2 = \lim_{r\to 0}\sqrt{2r}\sigma_{31}\Big|_{\ddot{\theta}=0}, K_3 = \lim_{r\to 0}\sqrt{2r}\sigma_{32}\Big|_{\ddot{\theta}=0} \tag{160}$$

$$K_4 = \lim_{r\to 0}\sqrt{2r}D_3\Big|_{\ddot{\theta}=0}, K_5 = \lim_{r\to 0}\sqrt{2r}B_3\Big|_{\ddot{\theta}=0}, K_6 = \lim_{r\to 0}\sqrt{2r}\vartheta_3\Big|_{\ddot{\theta}=0}, K_7 = \lim_{r\to 0}\sqrt{2r}(D_3, B_3)\Big|_{\ddot{\theta}=0} \tag{161}$$

where the extended singular pore stress around the pore-crack network front can be see in the reference [36].

By using the extended multi-scale volume energy density theory [40-42], the extended volume energy density (ESED) function can be defined as,

$$G = \frac{dW}{dV} = \sum_i^4 f(\kappa_i)\left(\frac{dW_i}{dV_i}\right) = \sum_i^4 f(\kappa_i)\left([K]_{1\times 7}[A]_{7\times 7}[K]_{7\times 1}^T\right) \tag{162}$$

where $f(\kappa_i)$, $[K]_{1\times 7}$ and $[A]_{7\times 7}$ are multi-scale intrinsic permeability function coefficient, extended SIFs vector and multiple coupled coefficient matrix, respectively; and can be defined as following

$$f(\kappa_i)=\begin{cases} f(\kappa_1) & \textit{for nano case} \quad 0\le\kappa_1\le 0.001 \\ f(\kappa_2) & \textit{for micro case} \quad 0.001\le\kappa_2\le 0.01 \\ f(\kappa_3) & \textit{for meso case} \quad 0.01\le\kappa_2\le 0.1 \\ f(\kappa_4) & \textit{for macro case} \quad 0.1\le\kappa_2\le 1 \end{cases} \tag{163}$$

$$\kappa_i = \frac{u_i \varphi_i \rho c_s^2 (\tau - 0.5)\Delta t L^2}{\pi(\Psi_{in} - \Psi_{out}) r^2} \quad (164)$$

$$[K]_{1\times 7} = \begin{bmatrix} K_1 & K_2 & K_3 & K_4 & K_5 & K_6 & K_7 \end{bmatrix} \quad (165)$$

The more information about the coefficient matrix $[A]_{7\times 7}$ can be found in reference[43]. The relationship between the fatigue criterion in facture theory and the Richter magnitude scale in geophysics theory can be established by using the extended volume energy density theory[40-42, 44, 45].

5. Numerical solution and discussion

The detail description about pressure and velocity condition on the flow driven pore–crack networks model are shown in figure.3.3, the initial pressure is added to the top (inlet) and bottom (outlet), the initial velocity in z direction is 0.0005785, The pressure and velocity parameters, which are added on the simulate model at the initial time, are shown in the table.2.

Figure.3.3. Pressure and velocity boundary condition for the flow driven pore-crack network model

Table.3.2. Pressure and Velocity condition to the model

5.1 Compliance of boundary condition and convergence of numerical solution

From figure 3.4, we can see that the velocity in x, y and z direction at 30000 time steps possess a stable value in the domain size, the present numerical method for multiple 3D flow driven pore – crack networks is stable and convincing.

Figure. 3.4a Velocity in x direction under 30000 time steps.

Figure. 3.4b Velocity in y direction under 30000 time steps.

Figure. 3.4c Velocity in z direction under 30000 time steps

Figure 3.5 shows the velocity and density (pressure) as function of time step in the core domain, it is shown that the value of velocity and density increase with time step increasing, and increasing gradient is decrease with time step increasing, when time step is bigger than 30000, both velocity and density reach a stable value. This means that we can obtain enough accuracy and stable numerical results by using 30000 time steps, and it can be used as a reference value in engineering practice.

Figure.3.5a. Velocity in x direction as function of time steps. **Figure.3.5b. Velocity in y direction as function of time steps.**

Figure.3.5c. Velocity in z direction as function of time steps **Figure.3.5d. Density as function of time steps.**

The memory and CPU resource, which is used under 30000 time steps, for the numerical simulation is shown in the table.3.3.

Table 3.3. Memory calculation and CPU time

5.2 Fluid velocity and flow distribution

The inlet pressure is 2.3127(minus z direction), the outlet pressure is 3.6873, the dynamic viscosity coefficient is 1/6, the initial fluid velocity in x, y and z direction are 0, 0 and 0.0025cm/s, respectively. The time steps is 80000, the inlet is minus z direction, the fluid velocities is $U_i(x, y, z, t)$, and the radiation distribution for pressure condition in the core area as a function of x, y and z are shown in Figures 6 through 8.

Figure. 3.6a $\dot{U}_{13}$ radiation distributions as function of z in oxy plane Figure. 3.6b $\dot{U}_{12}$ radiation distributions as function of y in oxz plane

Figure. 3.6c $\dot{U}_{11}$ radiation distributions as function of x in oyz plane Figure. 3.7a $\dot{U}_{23}$ radiation distributions as function of z in oxy plane

Figure. 3.7b $\dot{U}_{22}$ radiation distributions as function of y in oxz plane Figure. 3.7c $\dot{U}_{21}$ radiation distributions as function of x in oyz plane

Figure. 3.8a $\dot{U}_{33}$ radiation distributions as function of z in oxy plane Figure. 3.8b $\dot{U}_{32}$ radiation distributions as function of y in oxz plane

Figure. 3.8c $\dot{U}_{31}$ radiation distributions as function of x in oyz plane Figure. 3.9a $\dot{q}_{33}$ radiation distributions as function of z in oxy plane

Figures 3.9, 3.10 and 3.11 show that the variation of flow in x, y and z direction with the position on the core area. The numerical solution agrees well with the analytic solution.

Figure. 3.9b $\dot{q}_{32}$ radiation distributions as function of y in oxz plane **Figure. 3.9c** $\dot{q}_{31}$ radiation distributions as function of x in oyz plane

Figure. 3.10a $\dot{q}_{23}$ radiation distributions as function of z in oxy plane **Figure. 3.10b** $\dot{q}_{22}$ radiation distributions as function of y in oxz plane

Figure. 3.10c $\dot{q}_{21}$ radiation distributions as function of x in oyz plane **Figure. 3.11a** $\dot{q}_{13}$ radiation distributions as function of z in oxy plane

Figure. 3.11b $\dot{q}_{12}$ radiation distributions as function of y in oxz plane **Figure. 3.11c** $\dot{q}_{11}$ radiation distributions as function of x in oyz plane

From the results of figures 3.6 to 3.11, we can obtain that the changing rule of velocity and flow as function of pressure, initial velocity conditions.

5.3 Compare with nuclear magnetic resonance method

In order to further verify the correctness of our numerical method, we compare our numerical results with nuclear magnetic resonance results. A relationship between HHIE–LBM units and SI units is developed by using non-dimensional Reynolds number as a conversion parameters. Nuclear magnetic resonance method is based on real measurements, this relationship allow us to compare velocity magnitude and direction results with those that can occur under real fields conditions for two cases (low case and high case) under compressible and incompressible assumption, respectively.

Figure. 3.12 Lattice Boltzmann model (Lx=100mm, Ly=100mm, Lz=300mm)

Figure. 3.13 Nuclear magnetic model (Lx=100mm, Ly=100mm, Lz=107mm)

Figures 3.12 and 3.13 give the detail domain size and geometric shapes of LBM model and NMR model, respectively. In order to ensure that the domain size and geometric shapes parameter are identical, we subtracted a new domain 100x100x107(from 69 to 176 in z direction on oxy section) from the LBM model. The more detail information about the NMR model is listed in Appendix B.

Figure. 3.14 The contour of $\left|\dot{U}_3\right|$ as the function of z in xoy plane

Figure. 3.15a The vector of $\vec{\dot{U}}_{33}$ as the function of z in oxy plane **Figure. 3.15b** The contour of $\vec{\dot{U}}_{32}$ as the function of y in oxz plane

Figure. 3.15c The contour of $\vec{\dot{U}}_{31}$ as the function of x in oyz plane **Figure. 3.16a** The vector of $\vec{\dot{U}}_{23}$ as the function of z in oxy plane

Figure. 3.16b The vector of $\vec{\dot{U}}_{22}$ as the function of y in oxz plane **Figure. 3.16c** The vector of $\vec{\dot{U}}_{21}$ as the function of x in oyz plane

Figure. 3.17a The vector of $\vec{\dot{U}}_{13}$ as the function of z in oxy plane **Figure. 3.17b** The vector of $\vec{\dot{U}}_{12}$ as the function of y in oxz plane

Figure. 3.17c The vector of $\vec{\dot{U}}_{11}$ as the function of x in oyz plane

Figure 3.14 presents the contour of velocity between the LBM and NMR model. Figures 3.15, 3.16 and 3.17 present the vector of velocity between the LBM and NMR mode. From above results, 6, we can obtain that the vector of velocity in x, y and z direction through different numerical model (LBM and NMR) has the same result.

Figure. 3.18a The vector of $\vec{\dot{U}}_{3i}$ as the function of z in oxy plane for case I

Figure. 3.18b The vector of $\vec{\dot{U}}_{3i}$ as the function of z in oxy plane for case II

Figures 3.18 presents the direction of velocity in x, y and z direction between the LBM and NMR model for incompressible and compressible condition under differential initial pressure and velocity value (case I refer to high initial condition and case II refer to low initial condition) .

Figure. 3.19a The contour of $\dot{U}_i$ as the function of x in oyz plane for case I

Figure. 3.19b The contour of $\dot{U}_i$ as the function of x in oyz plane for case II

Figures 3.19 presents the magnitude of velocity in x, y and z direction between the LBM and NMR model for incompressible and compressible condition under differential initial pressure and velocity value.

Figures 3.20 presents the error analysis between incompressible and compressible condition under different initial pressure and velocity value (case I means high initial condition and case II means low initial condition).

Figure. 3.20 The error analysis of the LBM model for case I and case II

From figure 3.18 and 3.19, we can obtain that the vector of velocity in x, y and z direction through different numerical model (LBM and NMR) has the same result. From figure 3.20, we can see that when we use incompressible distribution function to simulate the fluid flow driven pore-crack problem for porosity composites, the error is less than ±1.0E-3, the HHIE-LBM numerical method is proved correctness and reliability.

5.4 Intrinsic permeability and Reynolds

Based on the Darcy's law, the intrinsic permeability in LBM model and Physical model can be defined as following

$$\kappa_i = \frac{q_i \rho c_s^2 (\tau - 0.5)\Delta t L}{\Delta \Psi} = \frac{u_i \varphi_i \rho c_s^2 (\tau - 0.5)\Delta t L}{\pi(\Psi_{in} - \Psi_{out}) r^2} \qquad \kappa_{i\_physical} = \frac{u_i \varphi_i \rho c_s^2 (\tau - 0.5)\Delta t L}{\pi(\Psi_{in} - \Psi_{out}) r^2} \left(\frac{L_{physical}}{L_{LBM}} \right)^2 \tag{166}$$

The more detailed description is listed in the Appendix C. Take the parameters in table. 3.4 into equation (90), we can obtain the value intrinsic permeability in the core model. Figures 3.21 to 3.22 show the LBM and physical and intrinsic permeability as function of x, y and z coordinate, respectively.

Table 3.4. Parameters for intrinsic permeability

Figure.3.21a Intrinsic permeability in x direction

Figure. 3.21b Intrinsic permeability in y direction

Figure. 3.21c Intrinsic permeability in z direction

Figure. 3.22a Intrinsic physical permeability in x direction

Figure. 3.22b Intrinsic physical permeability in y direction

Figure. 3.22c Intrinsic physical permeability in z direction

5.5 Extended stress intensity and special area

The numerical results in figure 3.23 shows that extended dimensionless extended stress intensity factors varying with x, y and z in the core area, from the figure, we can find the most dangers position in the whole core area, and when the extended stress intensity factor reach the criterion value the area will reach the destroy limit. The relatively specific danger areas are shown in the figure 3.24.

Figure. 3.23a Dimensionless model III SIFs radiation distributions

Figure .3.23b Dimensionless model I SIFs radiation distributions

Figure. 3.23c Dimensionless model II SIFs radiation distributions

Figure. 3.23d Dimensionless electric SIFs radiation distributions

Figure. 3.23e Dimensionless magnetic SIFs radiation distributions

Figure. 3.23f Dimensionless thermal SIFs radiation distributions

Figure. 3.24a Critical areas according to model III SIFs **Figure. 3.24b** Critical area according to model II SIFs

Figure. 3.24c Critical area according to magnetic SIFs **Figure. 3.24d** Critical area according to electric SIFs

Figure. 3.24e Critical areas according to magnetic SIFs **Figure. 3.24f** Critical areas according to thermal SIFs

We can also obtain the relationship between the DSIFs and variously porosity in figures 3.23 and 3.24. The danger area located at the lowest variously porosity areas, when the porosity is fixed, with the extended initial pressure and velocity increased, the extended pore−crack stresses increasing and researching the maximum value; when the extended initial pressure and velocity is fixed, with the porosity decreased, the extended pore-crack stresses increasing and researching the maximum value when porosity decreased to the value of 0.45. This results can help explain the experience results of fluid flow varying mechanism on coseismal slip in references [1, 2].

6. Concluding remarks

In the present article, a 3D fluid flow driven pore − crack network propagation mechanism in various porosity composites under fully coupled hybrid electronic − ionic, thermal, magnetic, electric and force fields was investigated by the hybrid hypersingular integral equation − lattice Boltzmann method (HHIE−LBM). This method has been proposed here for the first time, and the following conclusions can be drawn from our results:

The extended hybrid multiple coupled D3Q27 lattice cubic is created and the extended hybrid electronic − ionic, thermal, electromagnetic (weak and strong coupled cases) and force couple fields pressure and velocity boundary conditions for the HHIE – LBM is established.

The HHIE – LBM is proposed by the authors, and based on the method; the extended 3D flow driven pore – crack networks problem in various porosity composites is translated into a set of coupled HHIE-LBM equations, in which the unknown functions are the extended displacement ratio discontinuities.

The EDSIFs are calculated by using parallel numerical method and visualization results are calculated. The results are presented toward demonstrating the applicability of the proposed method. The relationship between the EDSIFs and differential porosity are discussed, and several rules have been found.

Last, the extended volume energy density function for determining the combine effect of the EDSIFs is derived, and it can be used to describe the pore – crack network propagation mechanism in various porosity composites (different crack scale) under multiple coupled fields (strong and weak case); it establish the relationship between the fatigue criterion in facture theory and the Richter magnitude scale in geophysics theory, which can be utilized to help understand the extended fluid flow mechanism in various porosity composites and analyze the extended fluid flow varying mechanism on coseismal slip.

Acknowledgements

This work was supported by a grant from the National Natural Science Foundation of China (No. D0408/409740594) and this work was also supported by China Postdoctoral Science Foundation (No. 20080430073).

Appendix A

A.1 BC for the electronic and ionic field

A.1.1. Front-rear flow

PC: For the front inlet and rear outlet case, $f_{fr:i}^{mi}$ (i = 15,9,16,3,7) can be defined as,

$$f_{fr:3}^{p:mi} = f_4^{mi} + \rho_{fr:in}^{p:mi} u_{fr:y}^{p:mi} / 3 ,\quad f_{fr:7}^{p:mi} = f_{10}^{mi} + \rho_{fr:in}^{mi} u_{fr:y}^{p:mi} / 6 - c_{fr:1}^{mi} / 4$$

$$f_{fr:9}^{p:mi} = f_8^{mi} + \rho_{fr:in}^{p:mi} u_{fr:y}^{p:mi} / 6 + c_{fr:1}^{p:mi} / 4 ,\quad f_{fr:15}^{p:mi} = f_{18}^{mi} + \rho_{fr:in}^{p:mi} u_{fr:y}^{p:mi} / 6 - c_{fr:2}^{mi} / 4$$

$$f_{fr:16}^{p:mi} = f_{17}^{mi} + \rho_{fr:in}^{p:mi} u_{fr:y}^{p:mi} / 6 + c_{fr:2}^{p:mi} / 4$$

For the rear inlet and front outlet case, $f_{rf:i}^{p:mi}$ (i =17,10,18,4,8) can be defined as

$$f_{rf:4}^{p:mi} = f_3^{mi} - \rho_{rf:in}^{p:mi} u_{rf:y}^{p;mi} / 3 ,\quad f_{rf:10}^{p:mi} = f_7^{mi} - \rho_{rf:in}^{mi} u_{rf:y}^{p:mi} / 6 + c_{fr:1}^{mi} / 4$$

$$f_{rf:8}^{p:mi} = f_9^{mi} - \rho_{rf:in}^{p:mi} u_{rf:y}^{p:mi} / 6 - c_{fr:1}^{mi} / 4 ,\quad f_{rf:18}^{p:mi} = f_{15}^{mi} - \rho_{rf:in}^{p:mi} u_{rf:y}^{p:mi} / 6 + c_{fr:2}^{mi} / 4$$

$$f_{rf:17}^{p:mi} = f_{16}^{mi} - \rho_{rf:in}^{p:mi} u_{rf:y}^{p:mi} / 6 - c_{fr:2}^{p:mi} / 4$$

where

$$c_{fr:\alpha}^{mi} = (f_{14}^{mi} - f_{1}^{mi} + f_{2}^{mi} - f_{11}^{mi} + f_{12}^{mi} - f_{13}^{mi})\delta_{1\alpha} + (f_{6}^{mi} - f_{5}^{mi} - f_{11}^{mi} - f_{12}^{mi} + f_{13}^{mi} + f_{14}^{mi})\delta_{2\alpha}$$

$$u_{fr:y}^{p:mi} = 1 - \left[2(f_{4}^{mi} + f_{8}^{mi} + f_{10}^{mi} + f_{17}^{mi} + f_{18}^{mi}) + f_{0}^{mi} + f_{1}^{mi} + f_{11}^{mi} + f_{5}^{mi} + f_{12}^{mi} + f_{2}^{mi} + f_{14}^{mi} + f_{6}^{mi} + f_{13}^{mi} \right] / \rho_{fr:in}^{p:m}$$

$$u_{rf:z}^{p:mi} = -1 + \left[2(f_{3}^{mi} + f_{7}^{mi} + f_{9}^{mi} + f_{15}^{mi} + f_{16}^{mi}) + f_{0}^{mi} + f_{1}^{mi} + f_{11}^{mi} + f_{5}^{mi} + f_{12}^{mi} + f_{2}^{mi} + f_{14}^{mi} + f_{6}^{mi} + f_{13}^{mi} \right] / \rho_{rf:in}^{p:mi}$$

VC: For the front inlet and rear outlet case, $f_{fr:i}^{v:mi}$ (i=15,9,16,3,7), can be defined as

$$f_{fr:3}^{v:mi} = f_{4}^{mi} + \frac{\rho_{fr:in}^{v:mi} u_{fr:y}^{v:mi}}{3}, \quad f_{fr:7}^{v:mi} = f_{10}^{mi} + \frac{\rho_{fr:in}^{v:mi} u_{fr:y}^{v:mi}}{6} - \frac{\rho_{fr:in}^{v:mi} c_{fr:1}^{mi}}{2(\rho_{fr:in}^{v:mi} - 3)}$$

$$f_{fr:9}^{v:mi} = f_{8}^{mi} + \frac{\rho_{fr:in}^{v:mi} u_{fr:y}^{v:mi}}{6} + \frac{\rho_{fr:in}^{v:mi} c_{fr:1}^{mi}}{2(\rho_{fr:in}^{v:mi} - 3)}, \quad f_{fr:15}^{v:mi} = f_{18}^{mi} + \frac{\rho_{fr:in}^{v:mi} u_{fr:y}^{v:mi}}{6} - \frac{\rho_{fr:in}^{v:mi} c_{fr:2}^{mi}}{2(\rho_{fr:in}^{v:mi} - 3)}$$

$$f_{fr:16}^{v:mi} = f_{17}^{mi} + \frac{\rho_{fr:in}^{v:mi} u_{fr:y}^{v:mi}}{6} + \frac{\rho_{fr:in}^{v:mi} c_{fr:2}^{mi}}{2(\rho_{fr:in}^{v:mi} - 3)}$$

For the rear inlet and front outlet case, $f_{rf:i}^{v:mi}$ (i =17,10,18,4,8) can be defined as

$$f_{rf:4}^{v:mi} = f_{3}^{mi} - \frac{\rho_{rf:in}^{v:mi} u_{rf:y}^{v:mi}}{3}, \quad f_{rf:10}^{v:mi} = f_{7}^{mi} - \frac{\rho_{in}^{v:mi} u_{rf:y}^{v:mi}}{6} + \frac{\rho_{rf:in}^{v:mi} c_{fr\_1}^{mi}}{2(\rho_{rf:in}^{v:mi} - 3)}$$

$$f_{rf:8}^{v:mi} = f_{9}^{mi} - \frac{\rho_{rf:in}^{v:mi} u_{rf:y}^{v:mi}}{6} - \frac{\rho_{rf:in}^{v:mi} c_{fr:1}^{mi}}{2(\rho_{rf:in}^{v:mi} - 3)}, \quad f_{rf:18}^{v:mi} = f_{15}^{mi} - \frac{\rho_{rf:in}^{v:mi} u_{rf:y}^{v:mi}}{6} + \frac{\rho_{rf:in}^{v:mi} c_{fr:2}^{mi}}{2(\rho_{rf:in}^{v:mi} - 3)}$$

$$f_{rf:17}^{v:mi} = f_{16}^{mi} - \frac{\rho_{rf:in}^{v:mi} u_{rf:y}^{v:mi}}{6} - \frac{\rho_{rf:in}^{v:mi} c_{fr:2}^{v:mi}}{2(\rho_{rf:in}^{v:mi} - 3)}$$

where

$$\rho_{fr:in}^{v:mi} = -u_{fr:y}^{v:mi} + 2(f_{4}^{mi} + f_{8}^{mi} + f_{10}^{mi} + f_{17}^{mi} + f_{18}^{mi}) + f_{0}^{mi} + f_{1}^{mi} + f_{11}^{mi} + f_{5}^{mi} + f_{12}^{mi} + f_{2}^{mi} + f_{14}^{mi} + f_{6}^{mi} + f_{13}^{mi}$$

$$\rho_{rf:in}^{v:mi} = -u_{fr:y}^{v:mi} + 2(f_{3}^{mi} + f_{7}^{mi} + f_{9}^{mi} + f_{15}^{mi} + f_{16}^{mi}) + f_{0}^{mi} + f_{1}^{mi} + f_{11}^{mi} + f_{5}^{mi} + f_{12}^{mi} + f_{2}^{mi} + f_{14}^{mi} + f_{6}^{mi} + f_{13}^{mi}$$

A.1.2. South-north flow

PC: For the south inlet and north outlet case, $f_{sn:i}^{p:mi}$ (i = 5,11,12,15,17) can be defined as

$$f_{sn:5}^{p:mi} = f_6^{mi} + \rho_{sn:in}^{p:mi} u_{sn:z}^{p:mi} / 3, \; f_{sn:11}^{p:mi} = f_{14}^{mi} + \rho_{sn:in}^{p:mi} u_{sn:z}^{p:mi} / 6 - c_{sn:1}^{mi} / 4$$

$$f_{sn:12}^{p:mi} = f_{13}^{mi} + \rho_{sn:in}^{p:mi} u_{sn:z}^{p:mi} / 6 - c_{sn:1}^{p:mi} / 4, \; f_{sn:15}^{p:mi} = f_{18}^{mi} + \rho_{sn:in}^{p:mi} u_{sn:z}^{p:mi} / 6 + c_{sn:2}^{p:mi} / 4$$

$$f_{sn:17}^{p:mi} = f_{16}^{mi} + \rho_{sn:in}^{p:mi} u_{sn:z}^{p:mi} / 6 - c_{sn:2}^{p:mi} / 4$$

For the north inlet and south outlet case, $f_{ns:i}^{p:mi}$ (i =6,13,14,16,18) can be defined as

$$f_{ns:6}^{p:mi} = f_5^{mi} - \rho_{ns:in}^{p:mi} u_{ns:z}^{p:mi} / 3, \; f_{ns:14}^{p:mi} = f_{11}^{mi} - \rho_{ns:in}^{p:mi} u_{ns:z}^{p:mi} / 6 - c_{sn:1}^{p:mi} / 4$$

$$f_{ns:13}^{p:mi} = f_{12}^{mi} - \rho_{ns:in}^{p:mi} u_{ns:z}^{p:mi} / 6 + c_{sn:1}^{p:mi} / 4, \; f_{ns:18}^{p:mi} = f_{15}^{mi} - \rho_{ns:in}^{p:mi} u_{ns:z}^{p:mi} / 6 - c_{sn:2}^{mi} / 4$$

$$f_{ns:16}^{p:mi} = f_{17}^{mi} - \rho_{in}^{mi} u_{sn:z}^{p:mi} / 6 + c_{sn:2}^{p:mi} / 4$$

where

$$c_{sn\_\alpha}^{p:mi} = (f_1^{mi} - f_2^{mi} + f_7^{mi} + f_8^{mi} - f_9^{mi} - f_{10}^{mi})\delta_{1\alpha} + (f_3^{mi} - f_4^{mi} + f_7^{mi} - f_8^{mi} + f_9^{mi} - f_{10}^{mi})\delta_{2\alpha}$$

$$u_{sn:z}^{p:mi} = 1 - \left[2(f_6^{mi} + f_{13}^{mi} + f_{14}^{mi} + f_{16}^{mi} + f_{18}^{mi}) + f_0^{mi} + f_4^{mi} + f_3^{mi} + f_{10}^{mi} + f_2^{mi} + f_9^{mi} + f_8^{mi} + f_1^{mi} + f_7^{mi} \right] / \rho_{sn:in}^{p:mi}$$

$$u_{ns:z}^{p:mi} = 1 - \left[2(f_5^{mi} + f_{11}^{mi} + f_{12}^{mi} + f_{15}^{mi} + f_{17}^{mi}) + f_0^{mi} + f_4^{mi} + f_3^{mi} + f_8^{mi} + f_1^{mi} + f_7^{mi} + f_{10}^{mi} + f_2^{mi} + f_9^{mi} \right] / \rho_{ns:in}^{p:mi}$$

VC: For the south inlet and north outlet case, $f_{sn:i}^{v:mi}$ (i = 5,11,12,15,17) can be defined as

$$f_{sn:5}^{v:mi} = f_6^{mi} + \frac{\rho_{sn:in}^{v:mi} u_z^{mi}}{3}, \; f_{sn:11}^{v:mi} = f_{14}^{mi} + \frac{\rho_{sn:in}^{v:mi} u_z^{mi}}{6} - \frac{\rho_{sn:in}^{v:mi} c_{sn\_1}^{mi}}{2(\rho_{sn:in}^{v:mi} - 3)}$$

$$f_{sn:12}^{v:mi} = f_{13}^{mi} + \frac{\rho_{sn:in}^{v:mi} u_z^{mi}}{6} - \frac{\rho_{sn:in}^{v:mi} c_{sn\_1}^{v:mi}}{2(\rho_{sn:in}^{v:mi} - 3)}, \; f_{sn:15}^{v:mi} = f_{18}^{mi} + \frac{\rho_{sn:in}^{v:mi} u_z^{mi}}{6} + \frac{\rho_{sn:in}^{v:mi} c_{sn\_2}^{v:mi}}{2(\rho_{sn:in}^{v:mi} - 3)}$$

$$f_{sn:17}^{v:mi} = f_{16}^{mi} + \frac{\rho_{sn:in}^{v:mi} u_z^{mi}}{6} - \frac{\rho_{sn:in}^{v:mi} c_{sn\_2}^{v:mi}}{2(\rho_{sn:in}^{v:mi} - 3)}$$

For the north inlet and south outlet case, $f_{ns:i}^{v:mi}$ (i =6,13,14,16,18) can be defined as

$$f_{ns:6}^{v:mi}=f_5^{mi}-\frac{\rho_{ns:in}^{v:mi}u_z^{mi}}{3},\ f_{ns:14}^{v:mi}=f_{11}^{mi}-\frac{\rho_{ns:in}^{v:mi}u_z^{mi}}{6}-\frac{\rho_{ns:in}^{v:mi}c_{sn\_1}^{v:mi}}{2(\rho_{ns:in}^{v:mi}-3)},$$

$$f_{ns:13}^{v:mi}=f_{12}^{mi}-\frac{\rho_{ns:in}^{v:mi}u_z^{mi}}{6}+\frac{\rho_{ns:in}^{v:mi}c_{sn\_1}^{v:mi}}{2(\rho_{ns:in}^{v:mi}-3)}$$

$$f_{ns:18}^{v:mi}=f_{15}^{mi}-\frac{\rho_{ns:in}^{v:mi}u_z^{m}}{6}-\frac{\rho_{ns:in}^{v:mi}c_{sn\_2}^{mi}}{2(\rho_{ns:in}^{v:mi}-3)},\ f_{ns:16}^{v:mi}=f_{17}^{mi}-\frac{\rho_{ns:in}^{v:mi}u_z^{mi}}{6}+\frac{\rho_{ns:in}^{v:mi}c_{ns\_2}^{mi}}{2(\rho_{ns:in}^{v:mi}-3)}$$

where

$$\rho_{sn:in}^{v:mi}=u_z^{mi}+2(f_6^{mi}+f_{13}^{mi}+f_{14}^{mi}+f_{16}^{mi}+f_{18}^{mi})+f_0^{mi}+f_4^{mi}+f_3^{mi}+f_{10}^{mi}+f_2^{mi}+f_9^{mi}+f_8^{mi}+f_1^{mi}+f_7^{mi}$$

$$\rho_{ns:in}^{v:mi}=u_z^{mi}+2(f_5^{mi}+f_{11}^{mi}+f_{12}^{mi}+f_{15}^{mi}+f_{17}^{mi})+f_0^{mi}+f_4^{mi}+f_3^{mi}+f_8^{mi}+f_1^{mi}+f_7^{mi}+f_{10}^{mi}+f_2^{mi}+f_9^{mi}$$

A.1.3.West-east flow

PC: For the west inlet and east outlet case, $f_{we:i}^{p:mi}$ (i=1,7,8,11,13) can be defined as

$$f_{we:1}^{p:mi}=f_2^{mi}+\frac{\rho_{in}^{mi}u_{we:x}^{p:mi}}{3},\ f_{we:7}^{p:mi}=f_{10}^{mi}+\frac{\rho_{in}^{mi}u_{we:x}^{p:mi}}{6}-\frac{c_{we\_1}^{mi}}{4},\ f_{we:8}^{p:mi}=f_9^{mi}+\frac{\rho_{in}^{mi}u_{we:x}^{p:mi}}{6}+\frac{c_{we\_1}^{mi}}{4}$$

$$f_{we:11}^{p:mi}=f_{14}^{mi}+\frac{\rho_{in}^{mi}u_{we:x}^{p:mi}}{6}+\frac{c_{we\_2}^{mi}}{4},\ f_{we:13}^{p:mi}=f_{12}^{mi}+\frac{\rho_{in}^{mi}u_{we:x}^{p:mi}}{6}-\frac{c_{we\_2}^{mi}}{4}$$

For the east inlet and west outlet case, $f_{ew:i}^{p:mi}$ (i =2,9,10,12,14) can be defined as,

$$f_{ew:2}^{p:mi}=f_1^{mi}-\frac{\rho_{in}^{mi}u_{ew:x}^{p:mi}}{3}\quad f_{ew:9}^{p:mi}=f_8^{mi}-\frac{\rho_{in}^{mi}u_{ew:x}^{p:mi}}{6}-\frac{c_{we\_1}^{mi}}{4}\quad f_{ew:10}^{p:mi}=f_7^{mi}-\frac{\rho_{in}^{mi}u_{ew:x}^{p:mi}}{6}+\frac{c_{we\_1}^{mi}}{4}$$

$$f_{ew:12}^{p:mi}=f_{13}^{mi}-\frac{\rho_{in}^{mi}u_{ew:x}^{p:mi}}{6}+\frac{c_{we\_2}^{mi}}{4}\quad f_{ew:14}^{p:mi}=f_{11}^{mi}-\frac{\rho_{in}^{mi}u_{ew:x}^{p:mi}}{6}-\frac{c_{we\_2}^{mi}}{4}$$

where

$$c_{we\_\alpha}^{mi}=(-f_3^{mi}+f_4^{mi}-f_{15}^{mi}-f_{16}^{mi}+f_{17}^{mi}+f_{18}^{mi})\delta_{1\alpha}+(f_5^{mi}-f_6^{mi}+f_{15}^{mi}-f_{16}^{mi}+f_{17}^{mi}-f_{18}^{mi})\delta_{2\alpha}$$

$$u_{we:x}^{p:mi}=1-\left[2(f_2^{mi}+f_9^{mi}+f_{10}^{mi}+f_{12}^{mi}+f_{14}^{mi})+f_0^{mi}+f_4^{mi}+f_3^{mi}+f_5^{mi}+f_{17}^{mi}+f_{15}^{mi}+f_{18}^{mi}+f_6^{mi}+f_{16}^{mi}\right]/\rho_{in}^{m}$$

$$u_{ew:x}^{p:mi}=1-\left[2(f_1^{mi}+f_7^{mi}+f_8^{mi}+f_{11}^{mi}+f_{13}^{mi})+f_0^{mi}+f_4^{mi}+f_3^{mi}+f_5^{mi}+f_{17}^{mi}+f_{15}^{mi}+f_{18}^{mi}+f_6^{mi}+f_{16}^{mi}\right]/\rho_{in}^{mi}$$

VC: For the west inlet and east outlet case, $f_{we:i}^{v:mi}$ (i=1,7,8,11,13) can be defined as

$$f_{ew:1}^{v:mi}=f_2^{mi}+\frac{\rho_{ew:in}^{v:mi}u_x^{mi}}{3},\ f_{ew:7}^{v:mi}=f_{10}^{mi}+\frac{\rho_{ew:in}^{v:mi}u_x^{mi}}{6}-\frac{\rho_{ew:in}^{v:mi}c_{we\_1}^{mi}}{2(\rho_{ew:in}^{v:mi}-3)},$$

$$f_{ew:8}^{v:mi}=f_9^{mi}+\frac{\rho_{ew:in}^{v:mi}u_x^{mi}}{6}+\frac{\rho_{ew:in}^{v:mi}c_{we\_1}^{m}}{2(\rho_{ew:in}^{v:mi}-3)},\ f_{ew:11}^{v:mi}=f_{14}^{mi}+\frac{\rho_{ew:in}^{v:mi}u_x^{mi}}{6}+\frac{\rho_{ew:in}^{v:mi}c_{we\_2}^{m}}{2(\rho_{ew:in}^{v:mi}-3)}$$

$$f_{ew:13}^{v:mi}=f_{12}^{mi}+\frac{\rho_{ew:in}^{v:mi}u_x^{mi}}{6}-\frac{\rho_{ew:in}^{v:mi}c_{we\_1}^{mi}}{2(\rho_{ew:in}^{v:mi}-3)}$$

For the east inlet and west outlet case, $f_{ew:i}^{v:mi}$ (i =2,9,10,12,14) can be defined as,

$$f_{we:2}^{v:mi}=f_1^{mi}-\frac{\rho_{we:in}^{v:mi}u_x^{mi}}{3},\ f_{we:10}^{v:mi}=f_7^{mi}-\frac{\rho_{we:in}^{v:mi}u_x^{mi}}{6}+\frac{\rho_{we:in}^{v:mi}c_{we\_1}^{mi}}{2(\rho_{we:in}^{v:mi}-3)}$$

$$f_{we:9}^{v:mi}=f_8^{mi}-\frac{\rho_{we:in}^{v:mi}u_x^{mi}}{6}-\frac{\rho_{we:in}^{v:mi}c_{we\_1}^{mi}}{2(\rho_{we:in}^{v:mi}-3)},\ f_{we:14}^{v:mi}=f_{11}^{mi}-\frac{\rho_{we:in}^{v:mi}u_x^{mi}}{6}-\frac{\rho_{we:in}^{v:mi}c_{we\_2}^{mi}}{2(\rho_{we:in}^{v:mi}-3)}$$

$$f_{we:12}^{v:mi}=f_{13}^{mi}-\frac{\rho_{we:in}^{v:mi}u_x^{mi}}{6}+\frac{\rho_{we:in}^{v:mi}c_{we\_2}^{mi}}{2(\rho_{we:in}^{v:mi}-3)}$$

where

$$\rho_{ew:in}^{v:mi}=u_x^{mi}+\left[2(f_2^{mi}+f_9^{mi}+f_{10}^{mi}+f_{12}^{mi}+f_{14}^{mi})+f_0^{mi}+f_4^{mi}+f_3^{mi}+f_5^{mi}+f_{17}^{mi}+f_{15}^{mi}+f_{18}^{mi}+f_6^{mi}+f_{16}^{mi}\right]$$

$$\rho_{we:in}^{v:mi}=u_x^{mi}+\left[2(f_1^{mi}+f_7^{mi}+f_8^{mi}+f_{11}^{mi}+f_{13}^{mi})+f_0^{mi}+f_4^{mi}+f_3^{mi}+f_5^{mi}+f_{17}^{mi}+f_{15}^{mi}+f_{18}^{mi}+f_6^{mi}+f_{16}^{mi}\right]$$

A.2. BC for the thermal field

A.2.1. Front-rear flow

PC: For the front inlet and rear outlet case, $f_{fr:i}^{p:t}$ (i=3,7,9,12,14) can be defined as

$$f_{fr:3}^{p:t}=f_4^{t}+\frac{\rho_{fr:in}^{p:t}u_{fr:y}^{p:t}}{3},\ f_{fr:7}^{p:t}=f_8^{t}+\frac{\rho_{fr:in}^{p:t}(u_{fr:x}^{p:t}+u_{fr:y}^{p:t}+u_{fr:z}^{p:t})}{12},$$

$$f_{fr:9}^{p:t}=f_{10}^{t}+\frac{\rho_{fr:in}^{p:t}(u_{fr:x}^{p:t}+u_{fr:y}^{p:t}-u_{fr:z}^{p:t})}{12}$$

$$f_{fr:12}^{p:t}=f_{11}^{t}+\frac{\rho_{fr:in}^{p:t}(-u_{fr:x}^{p:t}+u_{fr:y}^{p:t}-u_{fr:z}^{p:t})}{12},\ f_{fr:14}^{p:t}=f_{13}^{t}+\frac{\rho_{fr:in}^{p:t}(-u_{fr:x}^{p:t}+u_{fr:y}^{p:t}+u_{fr:z}^{p:t})}{12}$$

For the rear inlet and front outlet case, $f_{rf:i}^{p:t}$ (i =4,8,10,11,13) can be defined as

$$f_{rf:4}^{p:t} = f_3^t - \frac{\rho_{rf:in}^{p:t} u_{rf:y}^{p;t}}{3}, f_{rf:8}^{p:t} = f_7^t - \frac{\rho_{rf:in}^{p:t}(-u_{rf:x}^{p:t} + u_{rf:y}^{p:t} + u_{rf:z}^{p:t})}{12},$$

$$f_{rf:10}^{p:t} = f_9^t - \frac{\rho_{rf:in}^{p:t}(u_{rf:x}^{p:t} + u_{rf:y}^{p:t} - u_{rf:z}^{p:t})}{12}$$

$$f_{rf:13}^{p:t} = f_{14}^t - \frac{\rho_{rf:in}^{p:t}(-u_{rf:x}^{p:t} + u_{rf:y}^{p:t} - u_{rf:z}^{p:t})}{12}, f_{rf:11}^{p:t} = f_{12}^t - \frac{\rho_{rf:in}^{p:t}(-u_{rf:x}^{p:t} + u_{rf:y}^{p:t} - u_{rf:z}^{p:t})}{12}$$

where

$$u_{fr:x}^{p:t} = \frac{3\rho_{fr:in}^{p:t}}{2}(f_1^t - f_2^t) \quad u_{fr:z}^{p:t} = -1 + \frac{6}{5}(f_5^t - f_6^t + \rho_{fr:in}^{p:t} u_{fr:x}^{p:t} -_{fr:in}^{p:t} u_{fr:y}^{p:t})$$

$$u_{fr:y}^{p:t} = 1 - \left[2(f_4^t + f_8^t + f_{10}^t + f_{11}^t + f_{13}^t) + f_2^t + f_6^t + f_1^t + f_0^t + f_5^t\right] / \rho_{fr:in}^{p:t}$$

$$u_{rf:x}^{p:t} = \frac{3\rho_{rf:in}^{p:t}}{2}(f_2^t - f_1^t) \quad , u_{rf:z}^{p:t} = \frac{6}{5}(f_6^t - f_5^t - \rho_{rf:in}^{p:t} u_{rf:x}^{p:t} + \rho_{rf:in}^{p:t} u_{rf:y}^{p:t})$$

$$u_{rf:y}^{p:t} = 1 - \left[2(f_7^t + f_9^t + f_{12}^t + f_{14}^t + f_3^t) + f_2^t + f_6^t + f_1^t + f_0^t + f_5^t\right] /_{rf:in}^{p:t}$$

VC: For the front inlet and rear outlet case, $f_{fr:i}^{v:t}$ (i=3,7,9,12,14) can be defined as

$$f_{ns:6}^{p:mw} = f_5^{mw} + \frac{3\rho_{ns;in}^{p:mw}(u_{ns:y}^{p:mw} + u_{ns:z}^{p:mw})}{4}, u_{sn:z}^{p:mw} = 2\rho_{sn;in}^{p:mw}(-f_3^{mw} + f_4^{mw} - f_1^{mw} + f_2^{mw}),$$

$$f_{fr9}^{v:t} = f_{10}^t + \frac{\rho_{in}^{v:t}(u_{fr:x}^t + u_{fr:y}^t - u_{fr:z}^t)}{12}$$

$$f_{fr:12}^{v:t} = f_{11}^t + \frac{\rho_{in}^{v:t}(-u_{fr:x}^t + u_{fr:y}^t - u_{fr:z}^t)}{12} \quad , f_{fr:14}^{v:t} = f_{13}^t + \frac{\rho_{in}^{v:t}(-u_{fr:x}^t + u_{fr:y}^t + u_{fr:z}^t)}{12}$$

For the rear inlet and front outlet case, $f_{fr:i}^{v:t}$ (i =17,10,18,4,8) can be defined as

$$f_{rf:4}^{v:t} = f_3^t - \frac{\rho_{in}^{v:t} u_{rf:y}^t}{3} \quad , f_{rf:8}^{v:t} = f_7^t - \frac{\rho_{in}^{v:t}(-u_{rf:x}^t + u_{rf:y}^t + u_{rf:z}^t)}{12}, f_{rf:10}^{v:t} = f_9^t - \frac{\rho_{in}^{v:t}(u_{rf:x}^t + u_{rf:y}^t - u_{rf:z}^t)}{12}$$

$$f_{rf:13}^{v:t} = f_{14}^t - \frac{\rho_{in}^{v:t}(-u_{rf:x}^t + u_{rf:y}^t - u_{rf:z}^t)}{12}, f_{rf:11}^{v:t} = f_{12}^t - \frac{\rho_{in}^{v:t}(-u_{rf:x}^t + u_{rf:y}^t - u_{rf:z}^t)}{12}$$

where

$$\rho_{fr:in}^{v:t} = u_y^t + \left[2(f_4^t + f_8^t + f_{10}^t + f_{11}^t + f_{13}^t) + f_2^t + f_6^t + f_1^t + f_0^t + f_5^t\right],\ u_{rf:x}^t = \frac{3}{\rho_{fr:in}^{v:t} - 3}(f_1^t - f_2^t)$$

$$\rho_{rf:in}^{v:t} = u_y^t + \left[2(f_7^t + f_9^t + f_{12}^t + f_{14}^t + f_3^t) + f_2^t + f_6^t + f_1^t + f_0^t + f_5^t\right],$$

$$f_{ns:10}^{v:mw} = f_{10}^{mw} + \frac{3\rho_{ns:in}^{v:mw}(-u_{ns:x}^{v:mw} + u_{ns:z}^{v:mw})}{4}$$

$$u_{rf:z}^t = \frac{6(f_5^t - f_6^t) - \rho_{rf:in}^{v:t} u_{rf:y}^t + \rho_{rf:in}^{v:t} u_{rf:x}^t}{\rho_{rf:in}^{v:t} - 6}, \qquad u_{fr:z}^t = \frac{6(f_6^t - f_5^t) - \rho_{fr:in}^{v:t} u_{fr:x}^t + \rho_{fr:in}^{v:t} u_{fr}^t}{\rho_{fr:in}^{v:t} - 6}$$

A.2.2. South-north flow

PC: For the south inlet and north outlet case, $f_{sn:i}^{p:t}$ (i=5,7,10,11,14) can be defined as

$$f_{sn:5}^{p:t} = f_6^t - \frac{\rho_{sn:in}^{p:t} u_{sn:z}^{p:t}}{3},\ f_{sn:10}^{p:t} = f_9^t - \frac{\rho_{sn:in}^{p:t}(u_{sn:x}^{p:t} - u_{sn:y}^{p:t} + u_{sn:z}^{p:t})}{12}$$

$$f_{sn:14}^{p:t} = f_{13}^t - \frac{\rho_{sn:in}^{p:t}(-u_{sn:x}^{p:t} + u_{sn:y}^{p:t} + u_{sn:z}^{p:t})}{12},\ f_{sn:7}^{p:t} = f_8^t - \frac{\rho_{sn:in}^{p:t}(-u_{sn:x}^{p:t} - u_{sn:y}^{p:t} + u_{sn:z}^{p:t})}{12}$$

$$f_{sn:11}^{p:t} = f_{12}^t - \frac{\rho_{sn:in}^{p:t}(u_{sn:x}^{p:t} - u_{sn:y}^{p:t} + u_{sn:z}^{p:t})}{12}$$

For the north inlet and south outlet case, $f_{ns:i}^{p:t}$ (i =6,8,9,12,13) can be defined as

$$f_{ns:6}^{p:t} = f_5^t + \frac{\rho_{ns:in}^{p:t} u_{ns:z}^{p:t}}{3},\ f_{ns:9}^{p:t} = f_{10}^t + \frac{\rho_{ns:in}^{p:t}(u_{ns:x}^{p:t} - u_{ns:y}^{p:t} + u_{ns:z}^{p:t})}{12},$$

$$f_{ns:13}^{p:t} = f_{14}^t + \frac{\rho_{ns:in}^{p:t}(-u_{ns:x}^{p:t} + u_{ns:y}^{p:t} + u_{ns:z}^{p:t})}{12},\ f_{ns:8}^{p:t} = f_7^t + \frac{\rho_{ns:in}^{p:t}(-u_{ns:x}^{p:t} - u_{ns:y}^{p:t} + u_{ns:z}^{p:t})}{12}$$

$$f_{ns:12}^{p:t} = f_{11}^t + \frac{\rho_{ns:in}^{p:t}(u_{ns:x}^{p:t} - u_{ns:y}^{p:t} + u_{ns:z}^{p:t})}{12}$$

where

$$u_{sn:y}^{p:t} = \frac{3\rho_{sn:in}^{p:t}}{2}(f_2^t - f_1^t),\ u_{sn:x}^{p:t} = \frac{6}{5}(f_6^t - f_5^t - \rho_{sn:in}^{p:t} u_{s:y}^{p:t} + \rho_{sn:in}^{p:t} u_{sn:z}^{p:t}),\ u_{ns:y}^{p:t} = \frac{3\rho_{ns:in}^{p:t}}{2}(f_1^t - f_2^t)$$

$$u_{sn:z}^{p:t} = 1 - \left[2(f_{12}^t + f_9^t + f_6^t + f_8^t + f_3^t) + f_1^t + f_6^t + f_2^t + f_3^t + f_4^t\right] / \rho_{sn:in}^{p:t}$$

$$u_{ns:x}^{p:t} = \frac{6}{5}(f_3^t - f_4^t + \rho_{ns:in}^{p:t} u_{sn:y}^{p:t} - \rho_{ns:in}^{p:t} u_{sn:z}^{p:t})$$

$$u_{ns:z}^{p:t} = 1 - \left[2(f_{14}^t + f_7^t + f_5^t + f_{10}^t + f_{11}^t) + f_1^t + f_0^t + f_2^t + f_3^t + f_4^t \right] / \rho_{ns:in}^{p:t}$$

VC: For the south inlet and north outlet case, $f_{sn:i}^{v:t}$ (i=5,7,10,11,14) can be defined as

$$f_{sn:5}^{v:t} = f_6^t - \frac{\rho_{sn:in}^{v:t} u_{sn:z}^t}{3}, f_{sn:10}^{v:t} = f_9^t - \frac{\rho_{sn:in}^{v:t}(u_{sn:x}^t - u_{sn:y}^t + u_{sn:z}^t)}{12}$$

$$f_{sn:14}^{v:t} = f_{13}^t - \frac{\rho_{sn:in}^{v:t}(-u_{sn:x}^t + u_{sn:y}^t + u_{sn:z}^t)}{12}, f_{sn:7}^{v:t} = f_8^t - \frac{\rho_{sn:in}^{v:t}(-u_{sn:x}^t - u_{sn:y}^t + u_{sn:z}^t)}{12}$$

$$f_{sn:11}^{v:t} = f_{12}^t - \frac{\rho_{sn:in}^{v:t}(u_{sn:x}^t - u_{sn:y}^t + u_{sn:z}^t)}{12}$$

For the north inlet and south outlet case, $f_{ns:i}^{v:t}$ (i =6,8,9,12,13) can be defined as

$$f_{ns:6}^{v:t} = f_5^t + \frac{\rho_{ns:in}^{v:t} u_{ns:z}^t}{3}, f_{ns:9}^{v:t} = f_{10}^t + \frac{\rho_{ns:in}^{v:t}(u_{ns:x}^t - u_{ns:y}^t + u_{ns:z}^t)}{12}$$

$$f_{ns:13}^{v:t} = f_{14}^t + \frac{\rho_{ns:in}^{v:t}(-u_{ns:x}^t + u_{ns:y}^t + u_{ns:z}^t)}{12}, f_{ns:8}^{v:t} = f_7^t + \frac{\rho_{ns:in}^{v:t}(-u_{ns:x}^t - u_{ns:y}^t + u_{ns:z}^t)}{12}$$

$$f_{ns:12}^{v:t} = f_{11}^t + \frac{\rho_{ns:in}^{v:t}(u_{ns:x}^t - u_{ns:y}^t + u_{ns:z}^t)}{12}$$

where

$$\rho_{ns:in}^{v:t} = u_z^t + \left[2(f_{14}^t + f_7^t + f_5^t + f_{10}^t + f_{11}^t) + f_1^t + f_0^t + f_2^t + f_3^t + f_4^t \right], u_{ns:y}^t = \frac{3}{\rho_{ns:in}^{v:t} - 3}(f_2^t - f_1^t)$$

$$\rho_{sn:in}^{v:t} = u_z^t + \left[2(f_{12}^t + f_9^t + f_6^t + f_8^t + f_3^t) + f_1^t + f_6^t + f_2^t + f_3^t + f_4^t \right], u_{sn:y}^t = \frac{3}{\rho_{sn:in}^{v:t} - 3}(f_1^t - f_2^t)$$

$$u_{ns:x}^t = \frac{6(f_3^t - f_4^t) - \rho_{ns:in}^{v:t} u_{ns:y}^t + \rho_{ns:in}^{v:t} u_{ns:z}^t}{\rho_{ns:in}^{v:t} - 6}, \quad u_{sn:x}^t = \frac{6(f_3^t - f_4^t) - \rho_{sn:in}^{v:t} u_{sn:z}^t + \rho_{sn:in}^{v:t} u_{sn:y}^t}{\rho_{sn:in}^{v:t} - 6}$$

A.2.3.West-east flow

PC: For the west inlet and east outlet case, $f_{we:i}^{p:t}$ (i=1,7,9,11,13) can be defined as

$$f_{we:1}^{p:t} = f_2^t + \frac{\rho_{we:in}^{p:t} u_{we:x}^{p:t}}{3}, f_{we:9}^{p:t} = f_{10}^t + \frac{\rho_{we:in}^{p:t}(u_{we:x}^{p:t} - u_{we:y}^{p:t} - u_{we:z}^{p:t})}{12}$$

$$f_{we:13}^{p:t} = f_{14}^t + \frac{\rho_{we:in}^{p:t}(u_{we:x}^{p:t} - u_{we:y}^{p:t} + u_{we:z}^{p:t})}{12}, f_{we:7}^{p:t} = f_8^t + \frac{\rho_{we:in}^{p:t}(u_{we:x}^{p:t} - u_{we:y}^{p:t} - u_{we:z}^{p:t})}{12}$$

$$f_{we:11}^{p:t} = f_{12}^{t} + \frac{\rho_{we:in}^{p:t}(u_{we:x}^{p:t} + u_{we:y}^{p:t} - u_{we:z}^{p:t})}{12}$$

For the east inlet and west outlet case, $f_{ew:i}^{p:t}$ (i =2,8,10,12,14) can be defined as,

$$f_{ew:2}^{p:t} = f_1^t - \frac{\rho_{ew:in}^{p:t} u_{ew:x}^{p:t}}{3}, f_{ew:10}^{p:t} = f_9^t - \frac{\rho_{ew:in}^{p:t}(u_{ew:x}^{p:t} - u_{ew:y}^{p:t} - u_{ew:z}^{p:t})}{12}$$

$$f_{ew:14}^{p:t} = f_{13}^t - \frac{\rho_{ew:in}^{p:t}(u_{ew:x}^{p:t} - u_{ew:y}^{p:t} + u_{ew:z}^{p:t})}{12}, f_{ew:8}^{p:t} = f_7^t + \frac{\rho_{ew:in}^{p:t}(u_{ew:x}^{p:t} + u_{ew:y}^{p:t} - u_{ew:z}^{p:t})}{12}$$

$$f_{ew:12}^{p:t} = f_{11}^t + \frac{\rho_{ew:in}^{p:t}(u_{ew:x}^{p:t} + u_{ew:y}^{p:t} - u_{ew:z}^{p:t})}{12}$$

where

$$u_{we:x}^{p:t} = 1 - \left[2(f_7^t + f_{11}^t + f_1^t + f_9^t + f_{13}^t) + f_3^t + f_0^t + f_4^t + f_5^t + f_6^t \right] / \rho_{we:in}^{p:t}$$

$$, u_{ew:z}^{p:t} = \frac{3\rho_{ew:in}^{p:t}}{2}(f_4^t - f_3^t)$$

$$u_{ew:x}^{p:t} = 1 - \left[2(f_{14}^t + f_{10}^t + f_2^t + f_{12}^t + f_8^t) + f_3^t + f_0^t + f_4^t + f_5^t + f_6^t \right] / \rho_{ew:in}^{p:t}$$

$$, u_{we:z}^{p:t} = \frac{3\rho_{we:in}^{p:t}}{2}(f_3^t - f_4^t)$$

$$u_{ew:y}^{p:t} = \frac{6}{5}(f_5^t - f_6^t - \rho_{ew:in}^{p:t} u_{ew:z}^{p:t} - \rho_{ew:in}^{p:t} u_{ew:x}^{p:t}) \ , \ u_{we:y}^{p:t} = \frac{6}{5}(f_6^t - f_5^t + \rho_{we:in}^{p:t} u_{we:x}^{p:t} - \rho_{we:in}^{p:t} u_{we:z}^{p:t})$$

VC:

For the west inlet and east outlet case, $f_{we:i}^{v:t}$ (i=1,7,9,11,13) can be defined as

$$f_{we:1}^{v:t} = f_2^t + \frac{\rho_{we:in}^{v:t} u_{we:x}^{t}}{3}, f_{we:9}^{v:t} = f_{10}^t + \frac{\rho_{we:in}^{v:t}(u_{we:x}^{t} - u_{we:y}^{t} - u_{we:z}^{t})}{12}$$

$$f_{we:13}^{v:t} = f_{14}^t + \frac{\rho_{we:in}^{v:t}(u_{we:x}^{t} - u_{we:y}^{t} + u_{we:z}^{t})}{12}, f_{we:7}^{v:t} = f_8^t + \frac{\rho_{we:in}^{v:t}(u_{we:x}^{t} - u_{we:y}^{t} - u_{we:z}^{t})}{12}$$

$$f_{we:11}^{v:t} = f_{12}^t + \frac{\rho_{we:in}^{v:t}(u_{we:x}^{t} + u_{we:y}^{t} - u_{we:z}^{t})}{12}$$

For the east inlet and west outlet case, $f_{ew:i}^{v:t}$ (i =2,8,10,12,14) can be defined as,

$$f_{ew:2}^{v:t}=f_1^t-\frac{\rho_{ew:in}^{v:t}u_{ew:x}^t}{3},\ f_{ew:10}^{v:t}=f_9^t-\frac{\rho_{ew:in}^{v:t}(u_{ew:x}^t-u_{ew:y}^t-u_{ew:z}^t)}{12}$$

$$f_{ew:14}^{v:t}=f_{13}^t-\frac{\rho_{ew:in}^{v:t}(u_{ew:x}^t-u_{ew:y}^t+u_{ew:z}^t)}{12},\ f_{ew:8}^{v:t}=f_7^t+\frac{\rho_{ew:in}^{v:t}(u_{ew:x}^t+u_{ew:y}^t-u_{ew:z}^t)}{12}$$

$$f_{ew:12}^{v:t}=f_{11}^t+\frac{\rho_{ew:in}^{v:t}(u_{ew:x}^t+u_{ew:y}^t-u_{ew:z}^t)}{12}$$

where

$$\rho_{we:in}^{v:t}=u_{we:x}^t+\left[2(f_7^t+f_{11}^t+f_1^t+f_9^t+f_{13}^t)+f_3^t+f_0^t+f_4^t+f_5^t+f_6^t\right],\ u_{we:z}^{v:t}=\frac{3\rho_{we:in}^{v:t}}{2}(f_3^t-f_4^t)$$

$$\rho_{ew:in}^{v:t}=u_{ew:x}^t+\left[2(f_{14}^t+f_{10}^t+f_2^t+f_{12}^t+f_8^t)+f_3^t+f_0^t+f_4^t+f_5^t+f_6^t\right],\ u_{ew:z}^{v:t}=\frac{3\rho_{ew:in}^{v:t}}{2}(f_4^t-f_3^t)$$

$$u_{ew:y}^{v:t}=\frac{6}{5}(f_5^t-f_6^t-\rho_{ewv\backslash:in}^{v:t}u_{ew:z}^t-\rho_{ew:in}^{v:t}u_{ew:x}^t),\ u_{we:y}^{v:t}=\frac{6}{5}(f_6^t-f_5^t+\rho_{we:in}^{v:t}u_{we:x}^t-\rho_{we:in}^{v:t}u_{we:z}^t)$$

A.3. BC for the strong coupled electromagnetic field

A.3.1.Front-rear flow

PC:

For the rear inlet and front outlet case, $f_{rf:i}^{p:mw}$ (i =2,3,10,12) can be defined as

$$f_{rf:12}^{p:mw}=f_{11}^{mw}-\frac{3\rho_{rf:in}^{p:mw}(u_{rf:y}^{p:mw}-u_{rf:z}^{p:mw})}{4},\ f_{rf2}^{p:mw}=f_1^{mw}-\frac{3\rho_{rf:in}^{p:mw}(u_{rf:x}^{p:mw}+u_{rf:y}^{p:mw})}{4}$$

$$f_{rf:10}^{p:mw}=f_9^{mw}-\frac{3\rho_{rf:in}^{p:mw}(u_{rf:y}^{p:mw}+u_{rf:z}^{p:mw})}{4},\ f_{rf:3}^{p:mw}=f_4^{mw}-\frac{3\rho_{rf:in}^{p:mw}(u_{rf:y}^{p:mw}-u_{rf:x}^{p:mw})}{4}$$

where

$$u_{fr:x}^{p:mw}=2\rho_{fr:in}^{p:mw}(-f_5^{mw}+f_6^{mw}-f_7^{mw}+f_8^{mw}),\ u_{fr:z}^{p:mw}=2\rho_{fr:in}^{p:mw}(-f_5^{mw}+f_6^{mw}+f_7^{mw}-f_8^{mw})$$

$$u_{fr:y}^{p:mw}=1-\left[2(f_2^{mw}+f_3^{mw}+f_{10}^{mw}+f_{12}^{mw})+f_8^{mw}+f_5^{mw}+f_0^{mw}+f_6^{mw}+f_7^{mw}\right]/\rho_{fr:in}^{p:mw}$$

$$u_{rf:x}^{p:mw}=2\rho_{rf:in}^{p:mw}(f_5^{mw}-f_6^{mw}+f_7^{mw}-f_8^{mw}),\ u_{rf:z}^{p:mw}=2\rho_{rf:in}^{p:mw}(f_5^{mw}-f_6^{mw}-f_7^{mw}+f_8^{mw})$$

$$u_{rf:y}^{p:mw}=1-\left[2(f_1^{mw}+f_4^{mw}+f_9^{mw}+f_{11}^{mw})+f_8^{mw}+f_5^{mw}+f_0^{mw}+f_6^{mw}+f_7^{mw}\right]/\rho_{rf:in}^{p:mw}$$

VC: For the front inlet and rear outlet case, $f_{fr:i}^{v:mw}$ (i=1,4,9,11) can be defined as

$$f_{fr:1}^{v:mw} = f_2^{mw} + \frac{3\rho_{fr:in}^{v:mw}(u_{fr:x}^{v:mw} + u_{fr:y}^{v:mw})}{4}, f_{fr:9}^{v:mw} = f_{10}^{mw} + \frac{3\rho_{fr:in}^{v:mw}(u_{fr:y}^{v:mw} + u_{fr:z}^{v:mw})}{4}$$

$$f_{fr:4}^{v:mw} = f_3^{mw} + \frac{3\rho_{fr:in}^{v:mw}(-u_{fr:x}^{v:mw} + u_{fr:y}^{v:mw})}{4}, f_{fr:11}^{v:mw} = f_{12}^{mw} + \frac{3\rho_{fr:in}^{v:mw}(u_{fr:y}^{v:mw} - u_{fr:z}^{v:mw})}{4}$$

For the rear inlet and front outlet case, $f_{rf:i}^{v:mw}$ (i =2,3,10,12) can be defined as

$$f_{rf2}^{v:mw} = f_1^{mw} - \frac{3\rho_{rf:in}^{v:mw}(u_{rf:x}^{v:mw} + u_{rf:y}^{v:mw})}{4}, f_{rf:3}^{v:mw} = f_4^{mw} - \frac{3\rho_{rf:in}^{v:mw}(-u_{rf:x}^{v:mw} + u_{rf:y}^{v:mw})}{4}$$

$$f_{rf:10}^{v:mw} = f_9^{mw} - \frac{3\rho_{rf:in}^{v:mw}(u_{rf:y}^{v:mw} + u_{rf:z}^{v:mw})}{4}, f_{rf:12}^{v:mw} = f_{11}^{mw} - \frac{3\rho_{rf:in}^{v:mw}(u_{rf:y}^{v:mw} - u_{rf:z}^{v:mw})}{4}$$

where

$$u_{fr:x}^{v:mw} = \frac{2}{3\rho_{fr:in}^{v:mw} - 2}(-f_5^{mw} + f_6^{mw} - f_7^{mw} + f_8^{mw}), u_{fr:z}^{v:mw} = \frac{2}{3\rho_{fr:in}^{v:mw} - 2}(-f_5^{mw} + f_6^{mw} + f_7^{mw} - f_8^{mw})$$

$$\rho_{fr:in}^{v:mw} = u_{fr:y}^{v:mw} + \left[2(f_2^{mw} + f_3^{mw} + f_{10}^{mw} + f_{12}^{mw}) + f_8^{mw} + f_5^{mw} + f_0^{mw} + f_6^{mw} + f_7^{mw}\right]$$

$$u_{rf:x}^{v:mw} = \frac{2}{3\rho_{rf:in}^{v:mw} - 2}(f_5^{mw} - f_6^{mw} + f_7^{mw} - f_8^{mw}), u_{rf:z}^{v:mw} = \frac{2}{3\rho_{rf:in}^{v:mw} - 2}(f_5^{mw} - f_6^{mw} - f_7^{mw} + f_8^{mw})$$

$$\rho_{rf:in}^{v:mw} = u_{rf:y}^{v:mw} + \left[2(f_1^{mw} + f_4^{mw} + f_9^{mw} + f_{11}^{mw}) + f_8^{mw} + f_5^{mw} + f_0^{mw} + f_6^{mw} + f_7^{mw}\right]$$

A.3.2.South-north flow

PC: For the south inlet and north outlet case, $f_{sn:i}^{p:mw}$ (i=5,8,9,12) can be defined as

$$f_{sn:8}^{p:mw} = f_7^{mw} + \frac{3\rho_{sn;in}^{p:mw}(u_{sn:z}^{p:mw} - u_{sn:y}^{p:mw})}{4}, f_{sn:12}^{p:mw} = f_{11}^{mw} + \frac{3\rho_{sn;in}^{p:mw}(u_{sn:x}^{p:mw} + u_{sn:z}^{p:mw})}{4}$$

$$f_{sn:9}^{p:mw} = f_{10}^{mw} + \frac{3\rho_{sn;in}^{p:mw}(u_{sn:z}^{p:mw} - u_{sn:x}^{p:mw})}{4}, f_{sn:5}^{p:mw} = f_6^{mw} + \frac{3\rho_{sn;in}^{p:mw}(u_{sn:y}^{p:mw} + u_{sn:z}^{p:mw})}{4}$$

For the north inlet and south outlet case, $f_{ns:i}^{p:mw}$ (i =6,7,10,11) can be defined as

$$f_{ns:7}^{p:mw} = f_8^{mw} - \frac{3\rho_{ns;in}^{p:mw}(u_{ns:z}^{p:mw} - u_{ns:y}^{p:mw})}{4}, f_{ns:11}^{p:mw} = f_{12}^{mw} - \frac{3\rho_{ns;in}^{p:mw}(u_{ns:x}^{p:mw} + u_{ns:z}^{p:mw})}{4}$$

$$f_{ns:10}^{p:mw} = f_{10}^{mw} + \frac{3\rho_{ns;in}^{p:mw}(-u_{ns:x}^{p:mw} + u_{ns:z}^{p:mw})}{4}, f_{ns:6}^{p:mw} = f_5^{mw} + \frac{3\rho_{ns;in}^{p:mw}(u_{ns:y}^{p:mw} + u_{ns:z}^{p:mw})}{4}$$

where

$$u_{sn:z}^{p:mw} = 2\rho_{sn;in}^{p:mw}(-f_3^{mw} + f_4^{mw} - f_1^{mw} + f_2^{mw}), \quad u_{sn:x}^{p:mw} = 2\rho_{sn;in}^{p:mw}(-f_3^{mw} + f_4^{mw} + f_1^{mw} - f_2^{mw})$$

$$u_{sn:x}^{p:mw} = 1 - \left[2(f_7^{mw} + f_6^{mw} + f_{10}^{mw} + f_{11}^{mw}) + f_2^{mw} + f_3^{mw} + f_0^{mw} + f_4^{mw} + f_1^{mw}\right] / \rho_{sn;in}^{p:mw}$$

$$u_{ns:z}^{p:mw} = 2\rho_{ns;in}^{p:mw}(f_3^{mw} - f_4^{mw} + f_1^{mw} - f_2^{mw}), \quad u_{ns:x}^{p:mw} = 2\rho_{ns;in}^{p:mw}(f_3^{mw} - f_4^{mw} - f_1^{mw} + f_2^{mw})$$

$$u_{ns:x}^{p:mw} = 1 - \left[2(f_8^{mw} + f_{12}^{mw} + f_9^{mw} + f_5^{mw}) + f_2^{mw} + f_3^{mw} + f_0^{mw} + f_4^{mw} + f_1^{mw}\right] / \rho_{ns;in}^{p:mw}$$

VC:

For the south inlet and north outlet case, $f_{sn:i}^{v:mw}$ (i = 5,8,9,12) can be defined as

$$f_{sn:5}^{v:mw} = f_6^{mw} + \frac{3\rho_{sn;in}^{v:mw}(u_{sn:y}^{v:mw} + u_{sn:z}^{v:mw})}{4}, \ f_{sn:8}^{v:mw} = f_7^{mw} + \frac{3\rho_{sn:in}^{v:mw}(-u_{sn:y}^{v:mw} + u_{sn:z}^{v:mw})}{4}$$

$$f_{sn:9}^{v:mw} = f_{10}^{mw} + \frac{3\rho_{sn:in}^{v:mw}(-u_{sn:x}^{v:mw} + u_{sn:z}^{v:mw})}{4}, f_{sn:12}^{v:mw} = f_{11}^{mw} + \frac{3\rho_{sn:in}^{v:mw}(u_{sn:x}^{v:mw} + u_{sn:z}^{v:mw})}{4}$$

For the north inlet and south outlet case, $f_{ns:i}^{v:mw}$ (i =6,7,10,11) can be defined as

$$f_{ns:7}^{v:mw} = f_8^{mw} - \frac{3\rho_{ns:in}^{v:mw}(-u_{ns:y}^{v:mw} + u_{ns:z}^{v:mw})}{4}, \ f_{ns:11}^{v:mw} = f_{12}^{mw} - \frac{3\rho_{ns:in}^{v:mw}(u_{ns:x}^{v:mw} + u_{ns:z}^{v:mw})}{4}$$

$$f_{ns:10}^{v:mw} = f_{10}^{mw} + \frac{3\rho_{ns:in}^{v:mw}(-u_{ns:x}^{v:mw} + u_{ns:z}^{v:mw})}{4}, f_{ns:6}^{v:mw} = f_5^{mw} + \frac{3\rho_{ns:in}^{v:mw}(u_{ns:y}^{v:mw} + u_{ns:z}^{v:mw})}{4}$$

where

$$u_{sn:z}^{v:mw} = \frac{2}{3\rho_{sn:in}^{v:mw} - 2}(-f_3^{mw} + f_4^{mw} - f_1^{mw} + f_2^{mw}),$$

$$u_{sn:x}^{p:mw} = \frac{2}{3\rho_{sn:in}^{v:mw} - 2}(-f_3^{mw} + f_4^{mw} + f_1^{mw} - f_2^{mw})$$

$$\rho_{sn:in}^{v:mw} = u_{sn:x}^{v:mw} + \left[2(f_7^{mw} + f_6^{mw} + f_{10}^{mw} + f_{11}^{mw}) + f_2^{mw} + f_3^{mw} + f_0^{mw} + f_4^{mw} + f_1^{mw}\right]$$

$$u_{ns:z}^{v:mw} = \frac{2}{3\rho_{ns:in}^{v:mw} - 2}(f_3^{mw} - f_4^{mw} + f_1^{mw} - f_2^{mw}), \quad u_{ns:x}^{v:mw} = \frac{2}{3\rho_{ns:in}^{v:mw} - 2}(f_3^{mw} - f_4^{mw} - f_1^{mw} + f_2^{mw})$$

$$\rho_{ns:in}^{v:mw} = u_{ns:x}^{v:mw} + \left[2(f_8^{mw} + f_{12}^{mw} + f_9^{mw} + f_5^{mw}) + f_2^{mw} + f_3^{mw} + f_0^{mw} + f_4^{mw} + f_1^{mw}\right]$$

A.3.3.West-east flow

PC: For the west inlet and east outlet case, $f_{we:i}^{p:mw}$ (i=1,3,5,7) can be defined as

$$f_{we:1}^{p:mw}=f_2^{mw}+\frac{3\rho_{we:in}^{p:mw}(u_{we:x}^{p:mw}-u_{we:z}^{p:mw})}{4},\ f_{we:3}^{p:mw}=f_4^{mw}+\frac{3\rho_{we:in}^{p:mw}(u_{we:x}^{p:mw}+u_{we:z}^{p:mw})}{4}$$

$$f_{we:7}^{p:mw}=f_8^{mw}+\frac{3\rho_{we:in}^{p:mw}(u_{we:x}^{p:mw}-u_{we:y}^{p:mw})}{4},f_{we:5}^{p:mw}=f_6^{mw}+\frac{3\rho_{we:in}^{p:mw}(u_{we:x}^{p:mw}+u_{we:y}^{p:mw})}{4}$$

For the east inlet and west outlet case, $f_{ew:i}^{p:mw}$ (i =2,4,6,8) can be defined as,

$$f_{ew:2}^{p:mw}=f_1^{mw}-\frac{3\rho_{ew:in}^{p:mw}(u_{ew:x}^{p:mw}-u_{ew:z}^{p:mw})}{4},\ f_{we:4}^{p:mw}=f_3^{mw}+\frac{3\rho_{ew:in}^{p:mw}(u_{ew:x}^{p:mw}+u_{ew:z}^{p:mw})}{4}$$

$$f_{ew:6}^{p:mw}=f_5^{mw}-\frac{3\rho_{ew:in}^{p:mw}(u_{ew:x}^{p:mw}+u_{ew:y}^{p:mw})}{4},f_{ew:8}^{p:mw}=f_7^{mw}+\frac{3\rho_{ew:in}^{p:mw}(u_{ew:x}^{p:mw}-u_{ew:y}^{p:mw})}{4}$$

where

$$u_{we:y}^{p:mw}=2\rho_{we:in}^{p:mw}(-f_{12}^{mw}+f_{11}^{mw}+f_{10}^{mw}-f_9^{mw}),\quad u_{we:z}^{p:mw}=2\rho_{we:in}^{p:mw}(-f_{12}^{mw}+f_{11}^{mw}-f_{10}^{mw}+f_9^{mw})$$

$$u_{we:x}^{p:mw}=1-\left[2(f_2^{mw}+f_4^{mw}+f_6^{mw}+f_8^{mw})+f_9^{mw}+f_{12}^{mw}+f_0^{mw}+f_{11}^{mw}+f_{10}^{mw}\right]/\rho_{we:in}^{p:mw}$$

$$u_{ew:y}^{p:mw}=2\rho_{ew:in}^{p:mw}(f_{12}^{mw}-f_{11}^{mw}-f_{10}^{mw}-f_9^{mw}),\quad u_{ew:z}^{p:mw}=2\rho_{ew:in}^{p:mw}(-f_3^{mw}+f_4^{mw}+f_1^{mw}-f_2^{mw})$$

$$u_{ew:x}^{p:mw}=1-\left[2(f_3^{mw}+f_1^{mw}+f_5^{mw}+f_7^{mw})+f_2^{mw}+f_3^{mw}+f_0^{mw}+f_4^{mw}+f_1^{mw}\right]/\rho_{ew:in}^{p:mw}$$

VC: For the west inlet and east outlet case, $f_{we:i}^{v:mw}$ (i=1,3,5,7) can be defined as

$$f_{we:1}^{v:mw}=f_2^{mw}+\frac{3\rho_{we:in}^{v:mw}(u_{we:x}^{v:mw}-u_{we:z}^{v:mw})}{4},\ f_{we:3}^{v:mw}=f_4^{mw}+\frac{3\rho_{se:in}^{v:mw}(u_{we:x}^{v:mw}+u_{we:z}^{v:mw})}{4}$$

$$f_{we:5}^{v:mw}=f_6^{mw}+\frac{3\rho_{we:in}^{v:mw}(u_{we:x}^{v:mw}+u_{we:y}^{v:mw})}{4},\ f_{we:7}^{v:mw}=f_8^{mw}+\frac{3\rho_{we:in}^{v:mw}(u_{we:x}^{v:mw}-u_{we:y}^{v:mw})}{4}$$

For the east inlet and west outlet case, $f_{ew:i}^{v:mi}$ (i =2,4,6,8) can be defined as,

$$f_{ew:2}^{v:mw}=f_1^{mw}-\frac{3\rho_{ew:in}^{v:mw}(u_{ew:x}^{v:mw}-u_{ew:z}^{v:mw})}{4},f_{ew:4}^{v:mw}=f_3^{mw}+\frac{3\rho_{ew:in}^{v:mw}(u_{ew:x}^{v:mw}+u_{ew:z}^{v:mw})}{4}$$

$$f_{ew:6}^{v:mw}=f_5^{mw}-\frac{3\rho_{ew:in}^{v:mw}(u_{ew:x}^{v:mw}+u_{ew:y}^{v:mw})}{4},f_{ew:8}^{v:mw}=f_7^{mw}+\frac{3\rho_{ew:in}^{v:mw}(u_{ew:x}^{v:mw}-u_{ew:y}^{v:mw})}{4}$$

where

$$u_{we:y}^{v:mw} = \frac{2}{3\rho_{we:in}^{v:mw} - 2}(-f_{12}^{mw} + f_{11}^{mw} + f_{10}^{mw} - f_{9}^{mw}),$$

$$u_{we:z}^{v:mw} = \frac{2}{3\rho_{we:in}^{v:mw} - 2}(-f_{12}^{mw} + f_{11}^{mw} - f_{10}^{mw} + f_{9}^{mw})$$

$$\rho_{we:in}^{v:mw} = u_{we:x}^{v:mw} + \left[2(f_{2}^{mw} + f_{4}^{mw} + f_{6}^{mw} + f_{8}^{mw}) + f_{9}^{mw} + f_{12}^{mw} + f_{0}^{mw} + f_{11}^{mw} + f_{10}^{mw}\right]$$

$$u_{ew:y}^{p:mw} = \frac{2}{3\rho_{ew:in}^{v:mw} - 2}(f_{12}^{mw} - f_{11}^{mw} - f_{10}^{mw} - f_{9}^{mw}),$$

$$u_{ew:z}^{p:mw} = \frac{2}{3\rho_{ew:in}^{v:mw} - 2}(-f_{3}^{mw} + f_{4}^{mw} + f_{1}^{mw} - f_{2}^{mw})$$

$$\rho_{ew:in}^{v:mw} = u_{ew:x}^{p:mw} + \left[2(f_{3}^{mw} + f_{1}^{mw} + f_{5}^{mw} + f_{7}^{mw}) + f_{2}^{mw} + f_{3}^{mw} + f_{0}^{mw} + f_{4}^{mw} + f_{1}^{mw}\right]$$

A.4. BC for magnetic field

A.4.1.Front-rear flow

PC: For the front inlet and rear outlet case, $f_{fr:3}^{p:m}$ can be defined as

$$f_{fr:3}^{p:m} = f_{4}^{m} + \left(\rho_{f:r\,in}^{p:m} - 2f_{4}^{m} - f_{0}^{m} - f_{1}^{m} - f_{5}^{m} - f_{2}^{m} - f_{6}^{m}\right)/3$$

For the rear inlet and front outlet case, $f_{rf:4}^{p:m}$ can be defined as

$$f_{rf:4}^{p:m} = f_{3}^{m} - \left(-\rho_{rf:in}^{p:m} + 2f_{3}^{m} + f_{0}^{m} + f_{1}^{m} + f_{5}^{m} + f_{2}^{m} + f_{6}^{m}\right)/3$$

VC: For the front inlet and rear outlet case, $f_{fr:3}^{v:m}$ can be defined as

$$f_{fr:3}^{v:m} = f_{4}^{m} + u_{f:r\,y}^{v:m}\left(-u_{y}^{m} + 2f_{4}^{m} + f_{0}^{m} + f_{1}^{m} + f_{5}^{m} + f_{2}^{m} + f_{6}^{m}\right)/3$$

For the rear inlet and front outlet case, $f_{rf:4}^{v:m}$ can be defined as

$$f_{rf:4}^{v:m} = f_{3}^{m} - u_{rf:y}^{v:m}\left(-u_{y}^{m} + 2f_{3}^{m} + f_{0}^{m} + f_{1}^{m} + f_{5}^{m} + f_{2}^{m} + f_{6}^{m}\right)/3$$

A.4.2.South-north flow

PC: For the south inlet and north outlet case, $f_{sn:5}^{p:m}$ can be defined as

$$f_{sn:5}^{p:m} = f_{6}^{m} + \left(\rho_{sn:in}^{p:m} - 2f_{6}^{m} - f_{0}^{m} - f_{4}^{m} - f_{3}^{m} - f_{2}^{m} - f_{1}^{m}\right)/3$$

For the north inlet and south outlet case, $f_{ns:6}^{p:m}$ can be defined as

$$f_{ns:6}^{p:m} = f_5^m - \left(\rho_{ns:in}^{p:m} - 2f_5^m - f_0^m - f_4^m - f_3^m - f_1^m - f_2^m\right)/3$$

VC: For the south inlet and north outlet case, $f_{sn:5}^{v:m}$ can be defined as

$$f_{sn:5}^{v:m} = f_6^m + u_{sn:z}^{v:m}\left(u_z^m + 2f_6^m + f_0^m + f_4^m + f_3^m + f_2^m + f_1^m\right)/3$$

For the north inlet and south outlet case, $f_{ns:6}^{v:m}$ can be defined as

$$f_{ns:6}^{v:m} = f_5^m - u_{ns:z}^{v:m}\left(u_z^m + 2f_5^m + f_0^m + f_4^m + f_3^m + f_1^m + f_2^m\right)/3$$

A.4.3.West-east flow

PC: For the west inlet and east outlet case, $f_{we:1}^{p:m}$ can be defined as

$$f_{we:1}^{p:m} = f_2^m + \left(\rho_{we;in}^{p:m} - 2f_2^m - f_0^m - f_4^m - f_3^m - f_5^m - f_6^m\right)/3$$

For the east inlet and west outlet case, $f_{ew:2}^{p:m}$ can be defined as

$$f_{ew:2}^{p:m} = f_1^m - \left(\rho_{ew;in}^{p:m} - 2f_1^m - f_0^m - f_4^m - f_3^m - f_5^m - f_6^m\right)/3$$

VC: For the west inlet and east outlet case, $f_{we:1}^{v:m}$ can be defined as

$$f_{we:1}^{v:m} = f_2^m + u_{we:x}^{v:m}\left(u_x^m + 2f_2^m + f_0^m + f_4^m + f_3^m + f_5^m + f_6^m\right)/3$$

For the east inlet and west outlet case, $f_{ew:2}^{v:m}$ can be defined as

$$f_{ew:2}^{v:m} = f_1^m - u_{ew:x}^{v:m}\left(u_x^m + 2f_1^m + f_0^m + f_4^m + f_3^m + f_5^m + f_6^m\right)/3$$

Appendix B

Figure B.1 The more detail description about the NMR model, equipment and experience illustrative diagram

Appendix C

$$q = \frac{k}{\rho c_s^2(\tau - 0.5)\Delta t}\frac{\Delta\Psi}{L}, k = \frac{q\rho c_s^2(\tau - 0.5)\Delta tL}{\Delta\Psi}$$

$$k = \frac{q\rho c_s^2(\tau - 0.5)\Delta tL}{\Delta\Psi} = \frac{2.75\times 10^{-4} lus^{-1}\cdot ms/lu^3\cdot(1/6)\cdot\Delta ts\cdot 243lu}{0.0034mulu^{-1}s^{-2}} = \frac{2.75\times 10^{-4} lu\cdot ms/lu^3\cdot(1/6)\cdot\Delta ts\cdot 243lu}{0.0034mulu^{-1}s^{-2}} = 3.276lu^2\cdot\Delta t\frac{ms}{mu}$$

$$\mathrm{Re}_{high} = \frac{U_{real}L_{real}}{\nu_{real}} = \frac{2.5\times10^{-4}\,m/s\times5.0\times10^{-2}\,m}{1.0\times10^{-6}\,m^2/s} = 12.5, \mathrm{Re}_{low} = \frac{U_{real}L_{real}}{\nu_{real}} = \frac{1.3\times10^{-4}\,m/s\times5.0\times10^{-2}\,m}{1.0\times10^{-6}\,m^2/s} = 6.5$$

$$U_{LBM}\big|_{high} = \frac{\mathrm{Re}\,\nu_{LBM}}{L_{LBM}} = \frac{12.5\times(1/6)}{180} = 0.01157,$$

$$U_{LBM}\big|_{low} = \frac{\mathrm{Re}\,\nu_{LBM}}{L_{LBM}} = \frac{12.5\times(1/6)}{180} = 0.0060164$$

References

Taira Ta, Silver PG, Niu F, Nadeau RM. Remote triggering of fault-strength changes on the San Andreas fault at Parkfield. Naute 2009;461:636.
Wang C-Y, Manga M, Dreger D, Wong A. Streamflow increase due to rupturing of hydrothermal reservoirs: Evidence from the 2003 San Simeon, California, Earthquake. Geophysical reserch letters 2004;31:doi:10.1029/2004GL020124.
Qian YH, D'Humières D, Lallemand P. Lattice BGK Models for Navier-Stokes Equation. Europhysics letters 1992;17:479.
Zou Q, Hou S, Chen S, Doolen GD. A improved incompressible lattice Boltzmann model for time-independent flows Journal of statistical physics 1995;81:35.
Guo Z, Shi B, Wang N. Lattice BGK model for incompressible Navier-Stokes equation Journal of Computational Physics 2000;165:288.
Noble DR, Chen S, Georgiadis JG. A consistent hydrodynamic boundary condition for the lattice Boltzmann method. physics of fluids 1995;7:203.
Chen S, Martínez D, Mei R. on boundary conditions in lattice boltzmann methods. physics of fluids 1996;8:2527.
Chen S, Doolen GD. lattice boltzmann method for fluid flows. Annual Review of Fluid Mechanics 1998;30:329.
Bear J. The transition zone between fresh and salt waters in coastal aquifers. Ph. D. Thesis 1960;Berkeley: University of California,.
Zou QS, He XY. On pressure and velocity boundary conditions for the lattice Boltzmann BGK model. Physics of Fluids 1997;9:1591.
Maier RS, Bernard RS, Grunau DW. Boundary conditions for the lattice Boltzmann method. Physics of Fluids 1996;8:1788.
Noble DR, Chen SY, Georgiadis JG, Buckius RO. A Consistent Hydrodynamic Boundary-Condition for the Lattice Boltzmann Method. Physics of Fluids 1995;7:203.
Gary D, Doolen. Lattice gas methods: theory, applications, and hardware. Cambridge,Mass.: MIT Press 1991.
He XY, Doolen GD. Thermodynamic foundations of kinetic theory and Lattice Boltzmann models for multiphase flows. Journal of Statistical Physics 2002;107:309.
Gary D, Doolen, Frisch M, Hasslacher B, Orszag S, Wolfram S. Lattice gas methods for partial differential equations. Redwood City, Calif. ; Wokingham : Addison-Wesley 1990;4.
Frisch U, Hasslacher B, pomeau Y. Lattice-gas automata for the Navier-Stokes equation. Phys Rev Lett 1986;56:1505.
Jeremy R, Henderson, Ian G, Main, Calum M, Michael G, Norman. A fracture-mechanical cellular automaton model of seismicity. Pure and applied geophysics 1994;142:545.
Fakhari A, Rahimian MH. Simulation of falling droplet by the lattice Boltzmann method. Communications in Nonlinear Science and Numerical Simulation 2009;14:3046.
Kushch VI, Sevostianov I, Mishnaevsky Jr L. Stress concentration and effective stiffness of aligned fiber reinforced composite with anisotropic constituents. International Journal of Solids and Structures 2008;45:5103.
Kushch VI, Shmegera SV, Sevostianov I. SIF statistics in micro cracked solid: Effect of crack density, orientation and clustering. International Journal of Engineering Science 2009;47:192.
Tan Y-f, Zhou Z-f. Simulation of solute transport in a parallel single fracture with LBM/MMP mixed method. Journal of Hydrodynamics, Ser. B 2008;20:365.
Sih GC. Multiscale evaluation of microstructural worthiness based on the physical-analytical matching (PAM) approach. THEORETICAL AND APPLIED FRACTURE MECHANICS 2006;46:243.
Sih GC, Jones R. Crack size and speed interaction characteristics at micro-, meso- and macro-scale. THEORETICAL AND APPLIED FRACTURE MECHANICS 2003;39:127.
Sih GC, Tang XS. Dual scaling damage model associated with weak singularity for macroscopic crack possessing a micro/mesoscopic notch tip. THEORETICAL AND APPLIED FRACTURE MECHANICS 2004;42:1.
Sih GC, Tang XS. Simultaneous occurrence of double micro/macro stress singularities for multiscale crack model. THEORETICAL AND APPLIED FRACTURE MECHANICS 2006;46:87.
Sih GC, Tang XS. Micro/macro-crack growth due to creep-fatigue dependency on time-temperature material behavior. THEORETICAL AND APPLIED FRACTURE MECHANICS 2008;50:9.
Sih GC, Zuo JZ. Multiscale behavior of crack initiation and growth in piezoelectric ceramics. THEORETICAL AND APPLIED FRACTURE MECHANICS 2000;34:123.
Erdogan F. Mixed boundary value problem in mechanics. Mechanics Today, V4. Nemat-Nasser, S. ed 1978:44~84.
Ioakimidis NI. Application of finite-part integrals to the singular integral equations of crack problems in plane and 3-D elasticity. Acta Mechanica 1982;45:31～47.
Qin TY, Tang RJ. Finite-Part Integral and Boundary-Element Method to Solve Embedded Planar Crack Problems. International Journal of Fracture 1993;60:373.
Zhu, BJ, Qin, TY. Application of hypersingular integral equation method to three-dimensional crack in electromagnetothermoelastic multiphase composites. International Journal of Solids and Structures 2007;44:5994.
Sukop MC, Thorne DT. Lattice Boltzmann Modeling. An Introduction for Geoscientists and Engineers 2005:7.
He XY, Luo LS. Theory of the lattice Boltzmann method: From the Boltzmann equation to the lattice Boltzmann equation. Physical Review E 1997;56:6811.
He XY, Luo LS. Lattice Boltzmann model for the incompressible Navier-Stokes equation. Journal of Statistical Physics 1997;88:927.
Guo ZL, Shi BC, Wang NC. Lattice BGK model for incompressible Navier-Stokes equation. Journal of Computational Physics 2000;165:288.

Zhu B, Qin T. Hypersingular integral equation method for a three-dimensional crack in anisotropic electro-magneto-elastic bimaterials. THEORETICAL AND APPLIED FRACTURE MECHANICS 2007;47:219.
Qin TY, Noda NA. Analysis of a three-dimensional crack terminating at an interface using a hypersingular integral equation method. Journal of Applied Mechanics-Transactions of the Asme 2002;69:626.
Qin TY, Noda NA. Application of hypersingular integral equation method to a three-dimensional crack in piezoelectric materials. Jsme International Journal Series a-Solid Mechanics and Material Engineering 2004;47:173.
T.Y.Qin, Y.S.Yu, N.A.Noda. Finite-part integral and boundary element method to solve three-dimensional crack problems in piezoelectric materials. Int J Solids Struct 2007;In Press, Corrected Proof.
Sih GC. Mechanics of Fracture Initiation and Propagation. Kluwer Academic Publisher 1991.
G.C.Sih, J.Z.Zuo. Multiscale behavior of crack initiation and growth in piezoelectric ceramics. Theoretical and Applied Fracture Mechanics 2000;34:123.
J.Z.Zuo, G.C.Sih. Energy density theory formulation and interpretation of cracking behavior for piezoelectric ceramics. Theoretical and Applied Fracture Mechanics 2000;34:17.
B.J.Zhu. Hypersingular integral equation method to 3D crack in fully coupled electromagnetothermoelastic multiple composites. Dissertation of China Agricultural University 2007;(Ph.D).
Sih GC. A Special Theory of Crack Propagation: Methods of. Analysis and Solutions of Crack Problems. Mechanics of Fracture. G.C. Sih(Ed), Noordhoff International Publishing, Leyden 1973;I:xxv.
Sih GC. A three-dimensional strain energy density theory of crack propagation: three-dimensional of crack problems. Mechanics of Fracture. G.C. Sih(Ed), Noordhoff International Publishing, Leyden 1975;II:xxv.

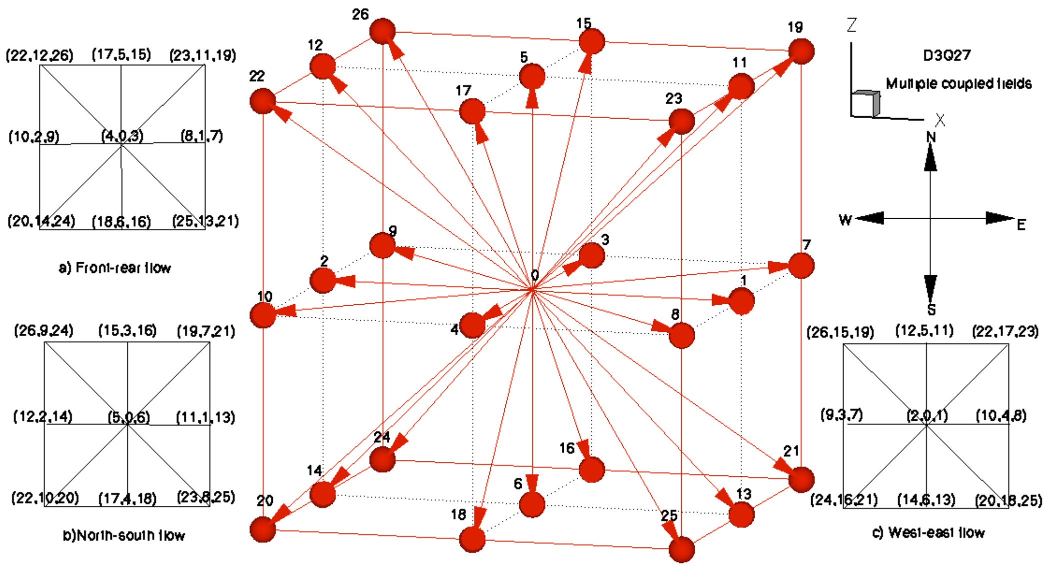

Figure.3.1. Extended boundary for hybrid cubic Lattice D3Q27 multiple coupled fields

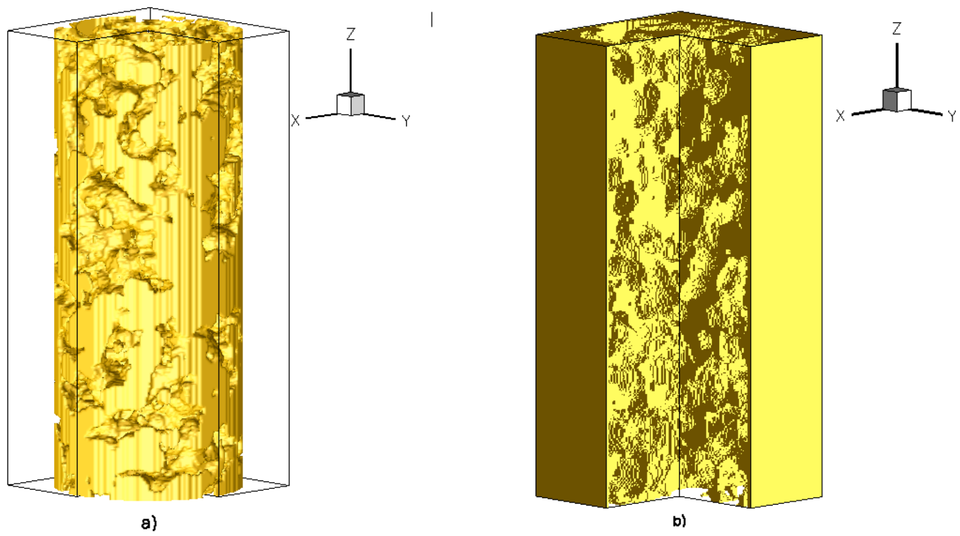

Figure.3.2. Flow driven pore-crack network model

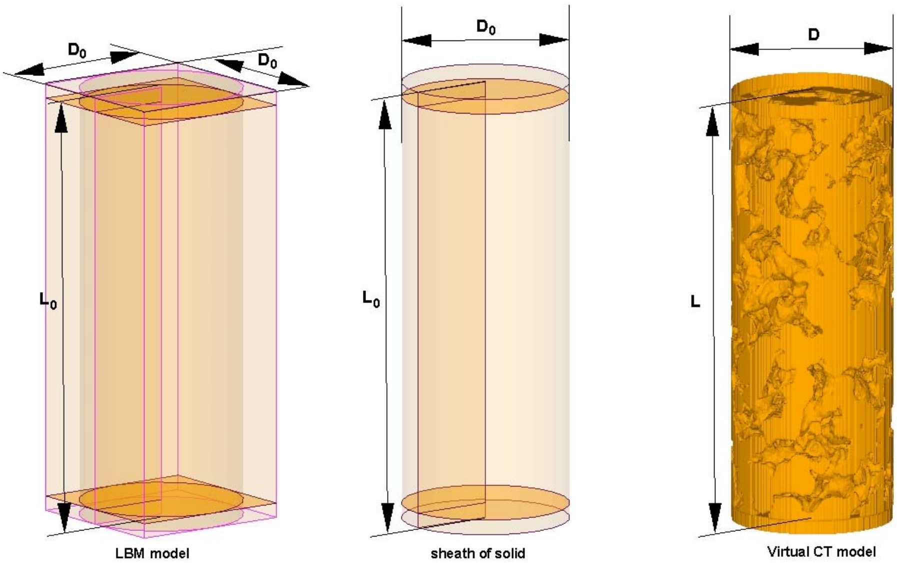

Figure.3.3. Pressure and velocity boundary condition for the flow driven pore-crack network model

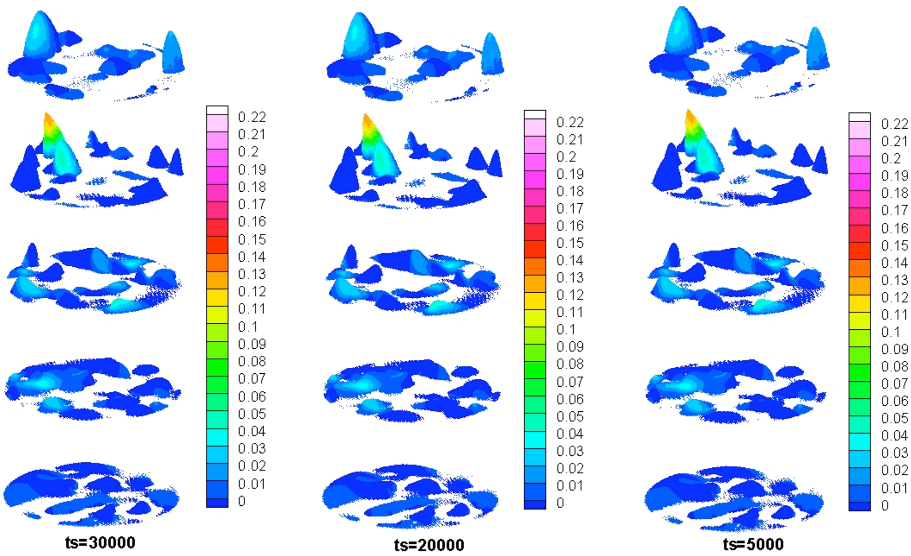

Figure. 3.4a Velocity in x direction under 30000 time steps.

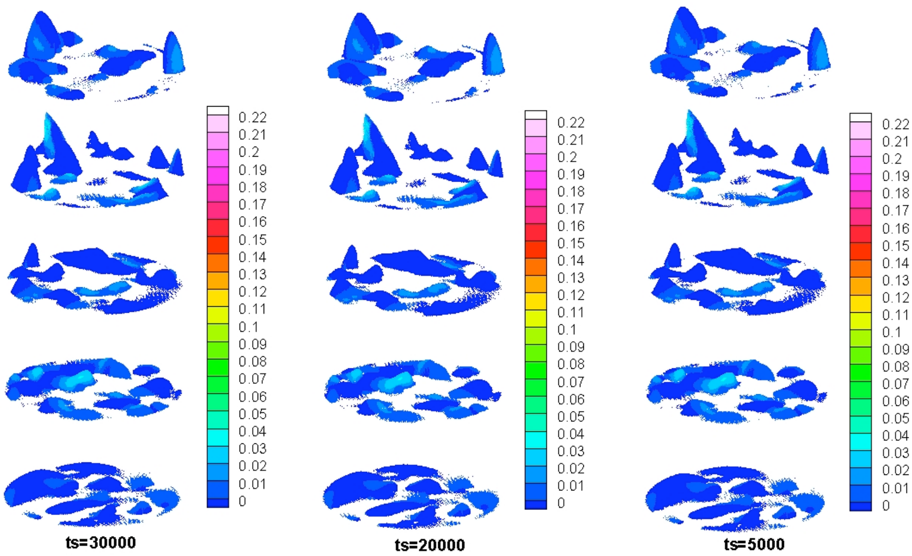

Figure. 3.4b Velocity in y direction under 30000 time steps.

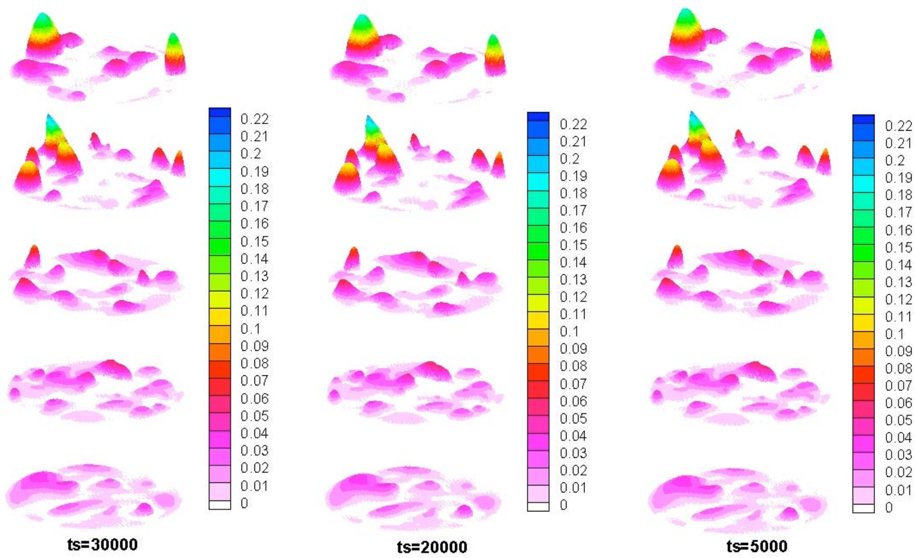

Figure. 3.4c Velocity in z direction under 30000 time steps

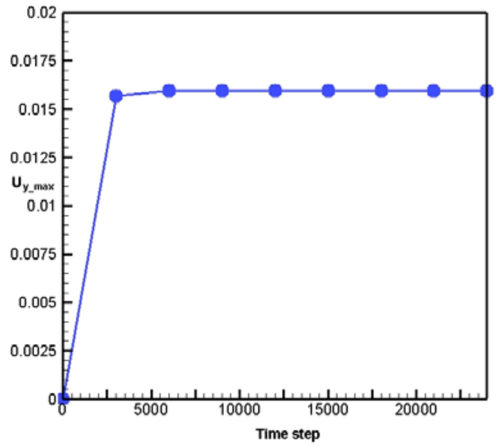

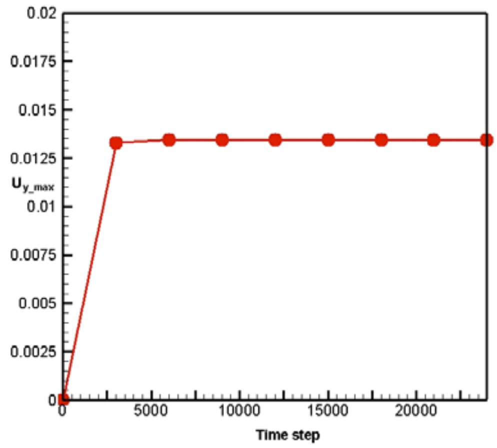

Figure.3.5a. Velocity in x direction as function of time steps. **Figure.3.5b.** Velocity in y direction as function of time steps.

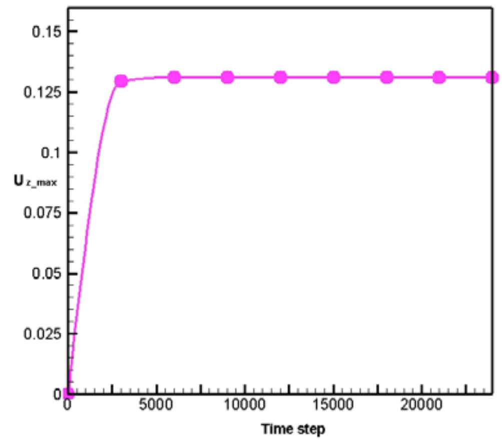

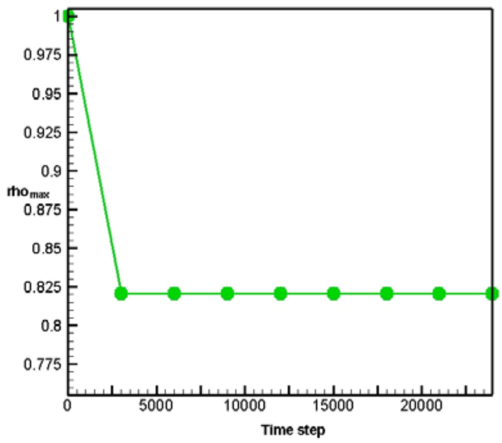

Figure.3.5c. Velocity in z direction as function of time steps **Figure.3.5d.** Density as function of time steps.

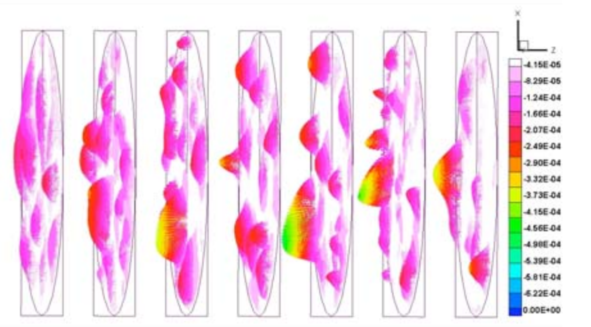

Figure. 3.6a U_3 radiation distributions as function of z in oxy plane

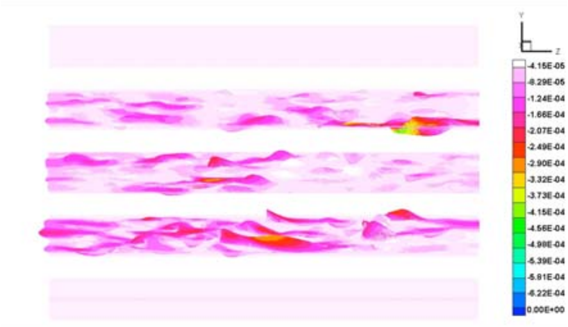

Figure. 3.6b U_3 radiation distributions as function of y in oxz plane

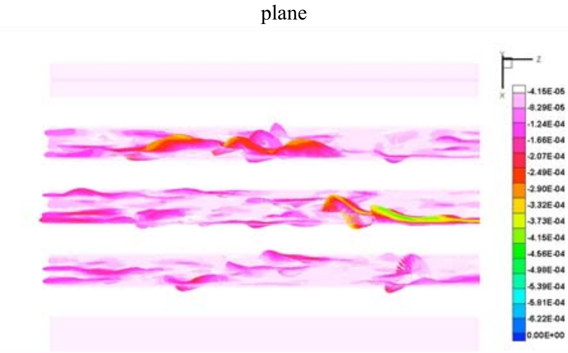

Figure. 3.6c U_3 radiation distributions as function of x in oyz plane

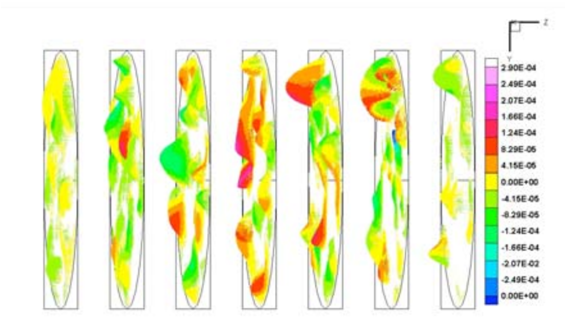

Figure. 3.7a U_2 radiation distributions as function of z in oxy plane

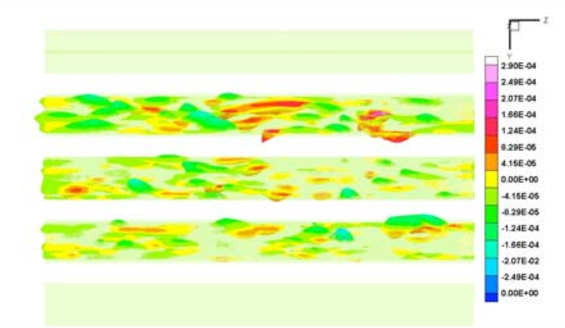

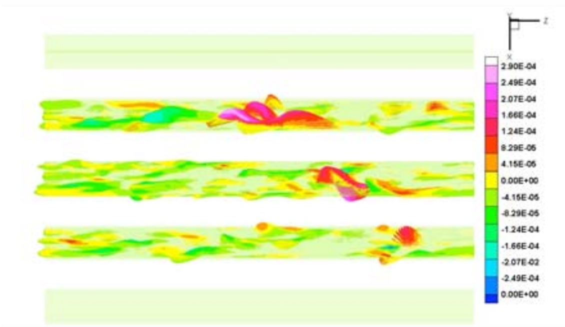

Figure. 3.7b U_2 radiation distributions as function of y in oxz plane **Figure. 3.7c** U_2 radiation distributions as function of x in oyz plane

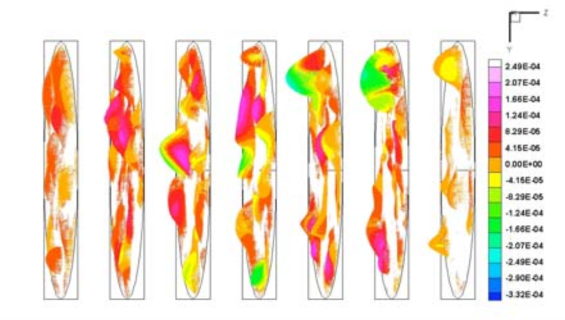

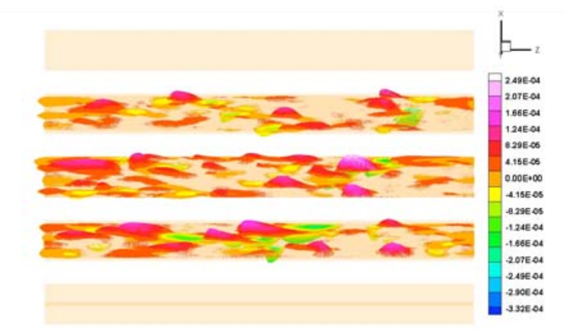

Figure. 3.8a U_1 radiation distributions as function of z in oxy plane **Figure. 3.8b** U_1 radiation distributions as function of x in oyz plane

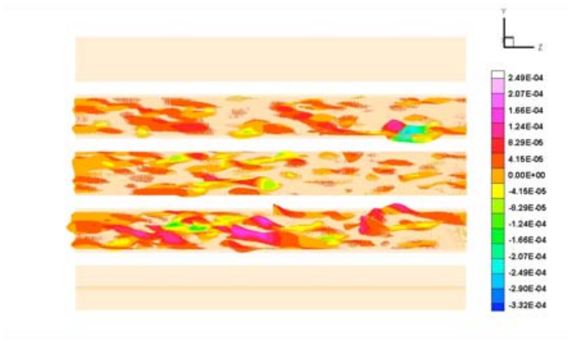

Figure. 3.8c U_1 radiation distributions as function of y in oxz plane

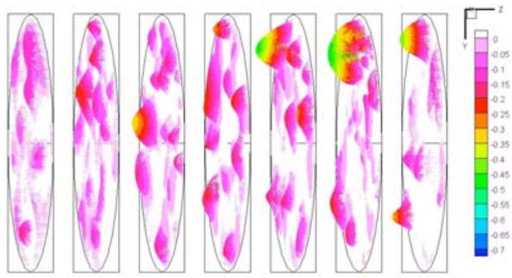

Figure.3.9a q_3 radiation distributions as function of z in oxy plane

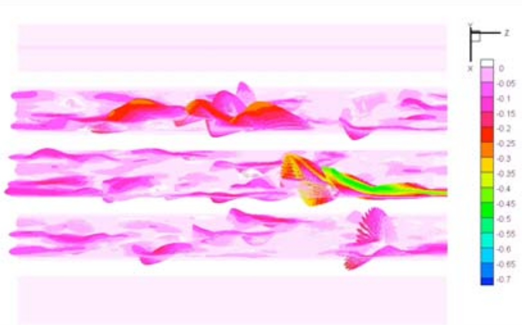

Figure. 3.9b q_3 radiation distributions as function of x in oyz plane

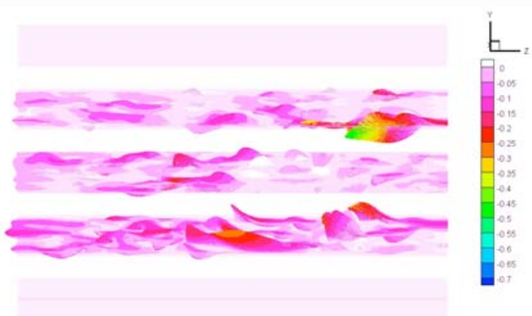

Figure. 3.9c q_3 radiation distributions as function of y in oxz plane

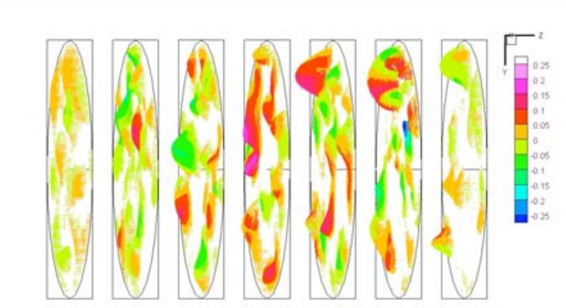

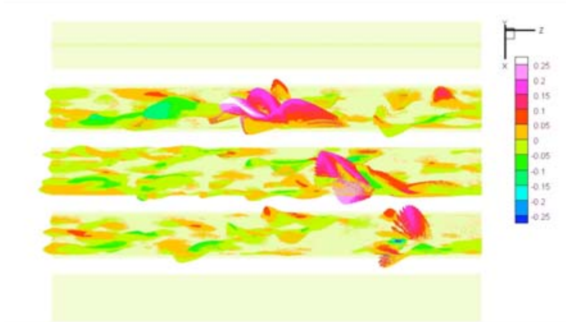

Figure. 3.10a q_2 radiation distributions as function of z in oxy plane **Figure. 3.10b** q_2 radiation distributions as function of x in oyz plane

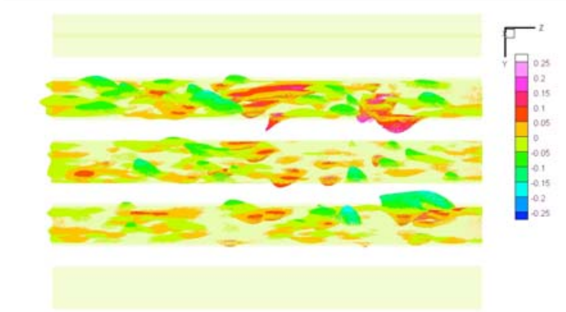

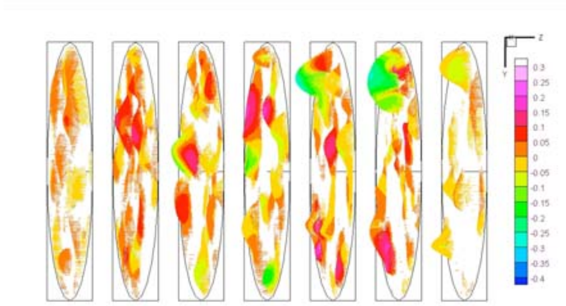

Figure. 3.10c q_2 radiation distributions as function of y in oxz plane **Figure. 3.11a** q_1 radiation distributions as function of z in xoy plane

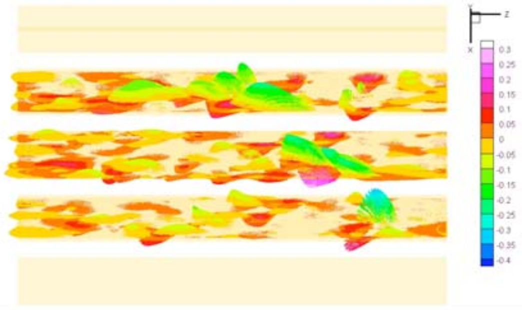

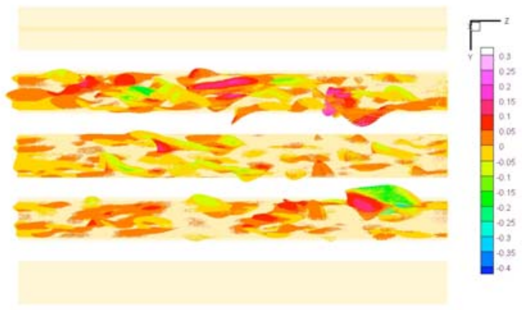

Figure. 3.11b q_1 radiation distributions as function of x in oyz plane **Figure. 3.11c** q_1 radiation distributions as function of y in oxz plane

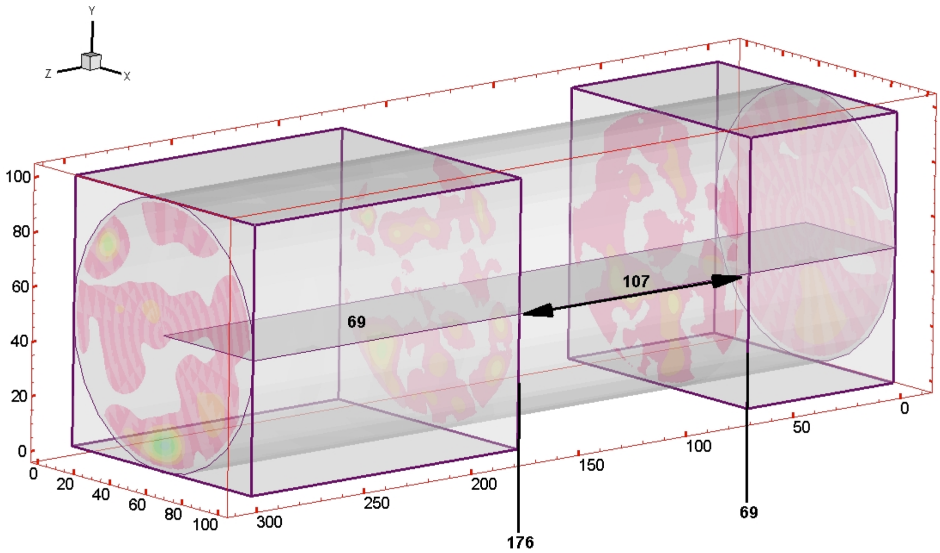

.

Figure. 3.12 Lattice Boltzmann model (Lx=100, Ly=100, Lz=300)

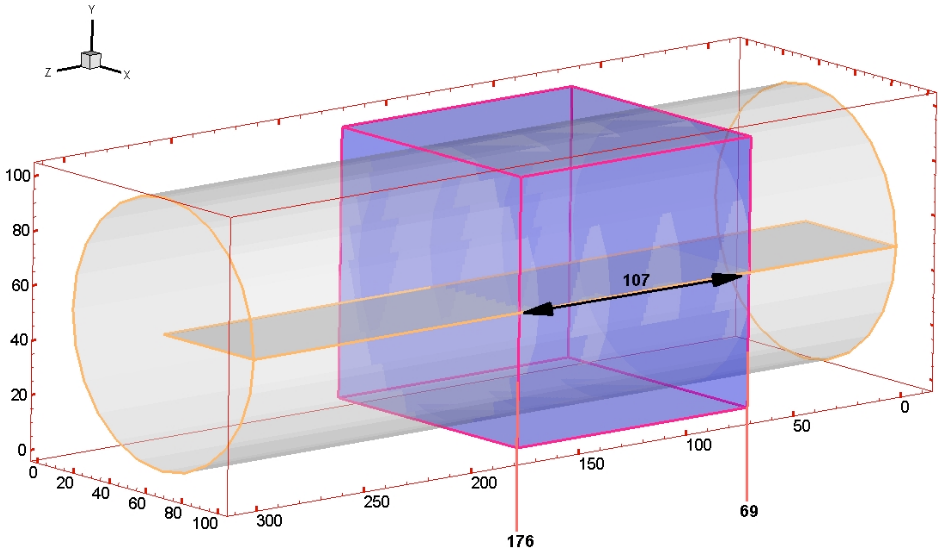

Figure. 3.13 Nuclear magnetic model (Lx=100, Ly=100, Lz=107)

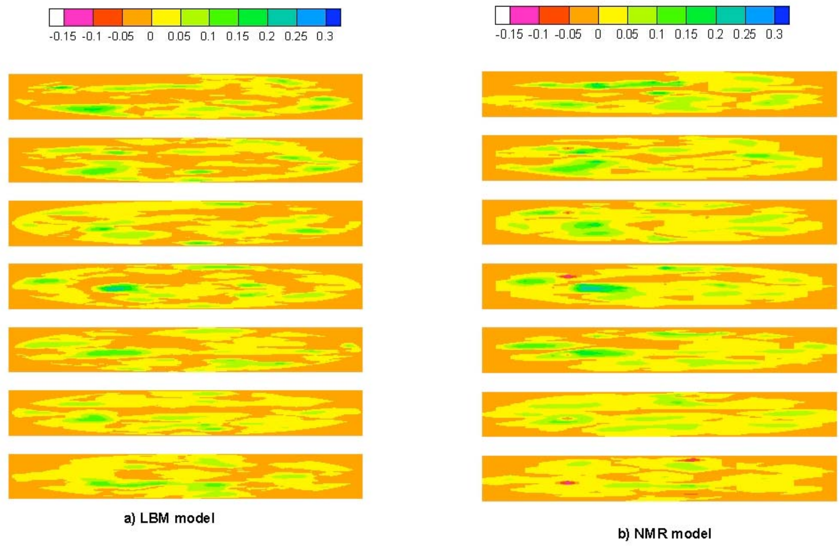

Fiigure. 3.14 The contour of U_3 as the function of z in xoy plane

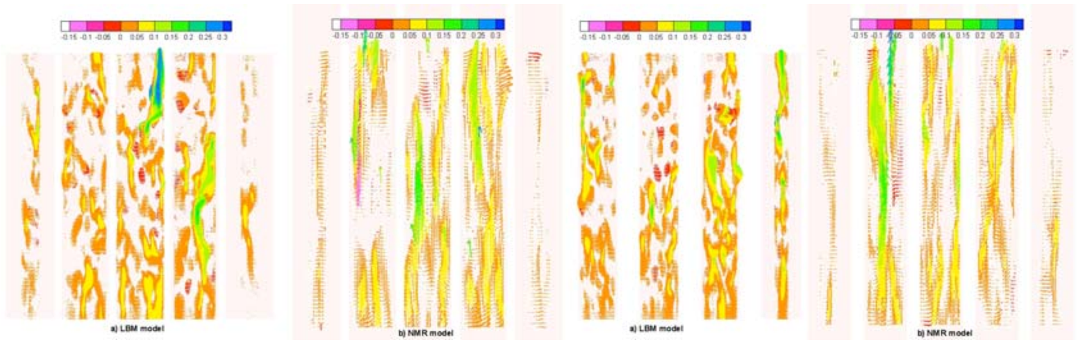

Figure. 3.15a The vector of U_3 as the function of z in oxy plane

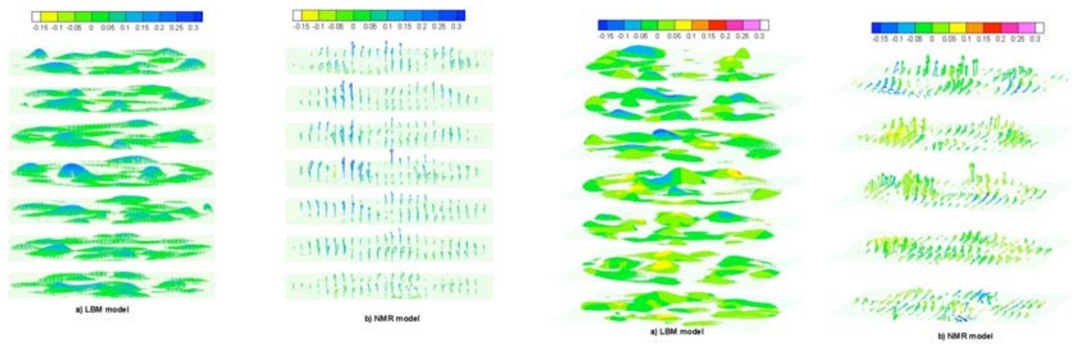

Figure. 3.15b The contour of U_3 as the function of x in oyz plane

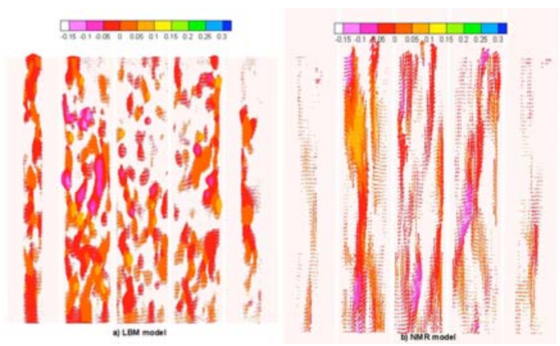

Figure. 3.15c The contour of U_3 as the function of y in oxz plane

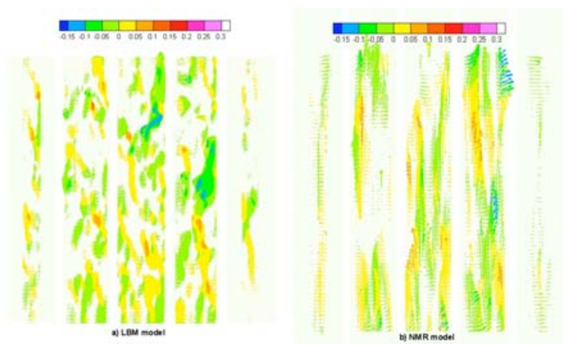

Figure. 3.16a The vector of U_2 as the function of z in oxy plane

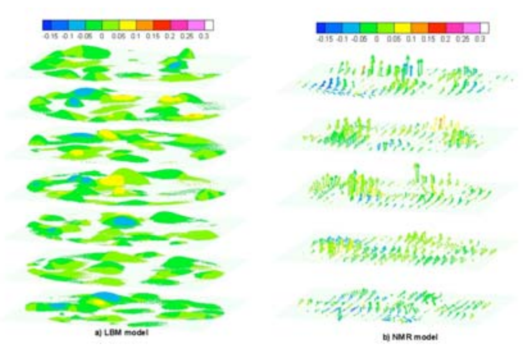

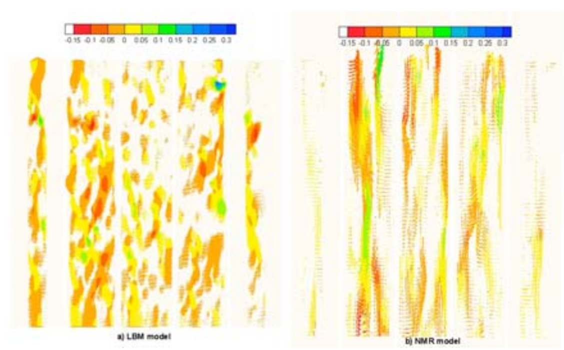

Figure. 3.16b The vector of U_2 as the function of x in oyz plane **Figure. 3.16c** The vector of U_2 as the function of y in oxz plane

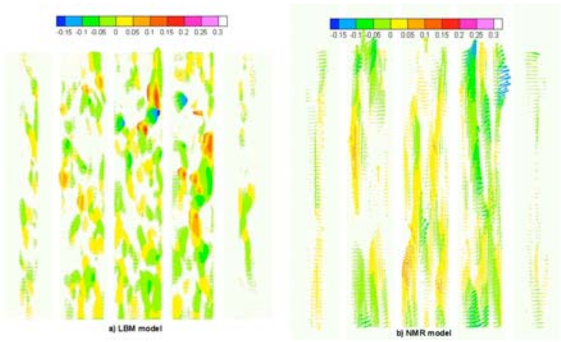

Figure. 3.17a The vector of U_1 as the function of z in oxy plane **Figure. 3.17b** The vector of U_1 as the function of x in oyz plane

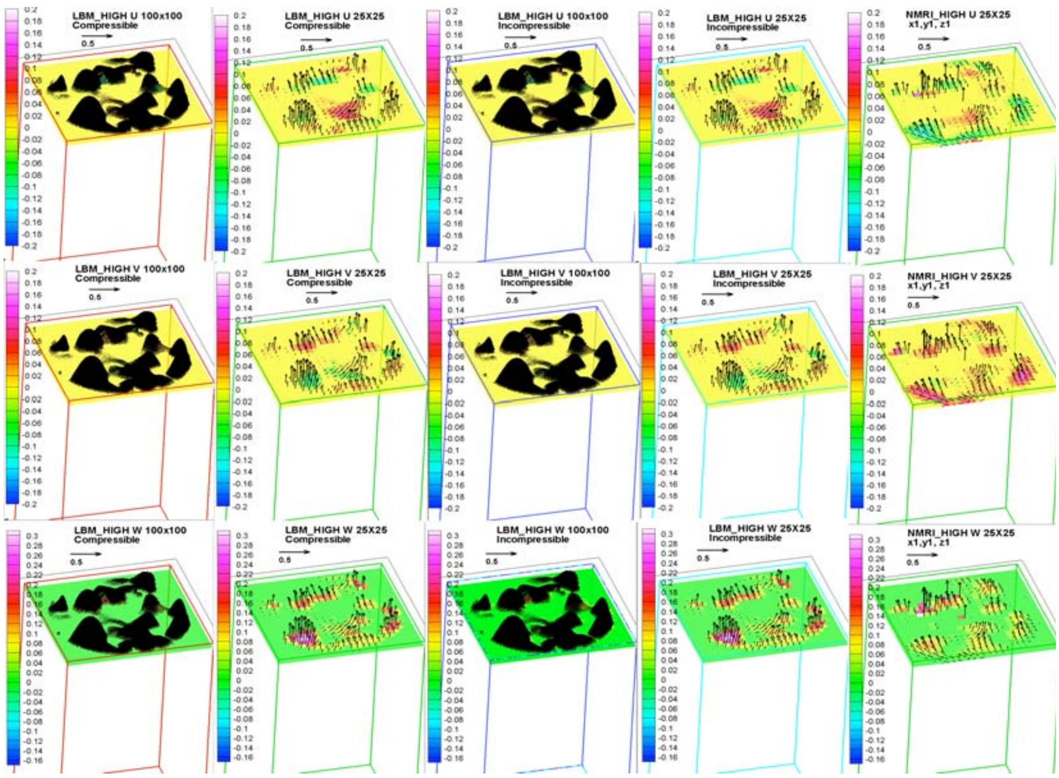

Figure. 3.18a The vector of U_1 as the function of x in oyz plane for case I

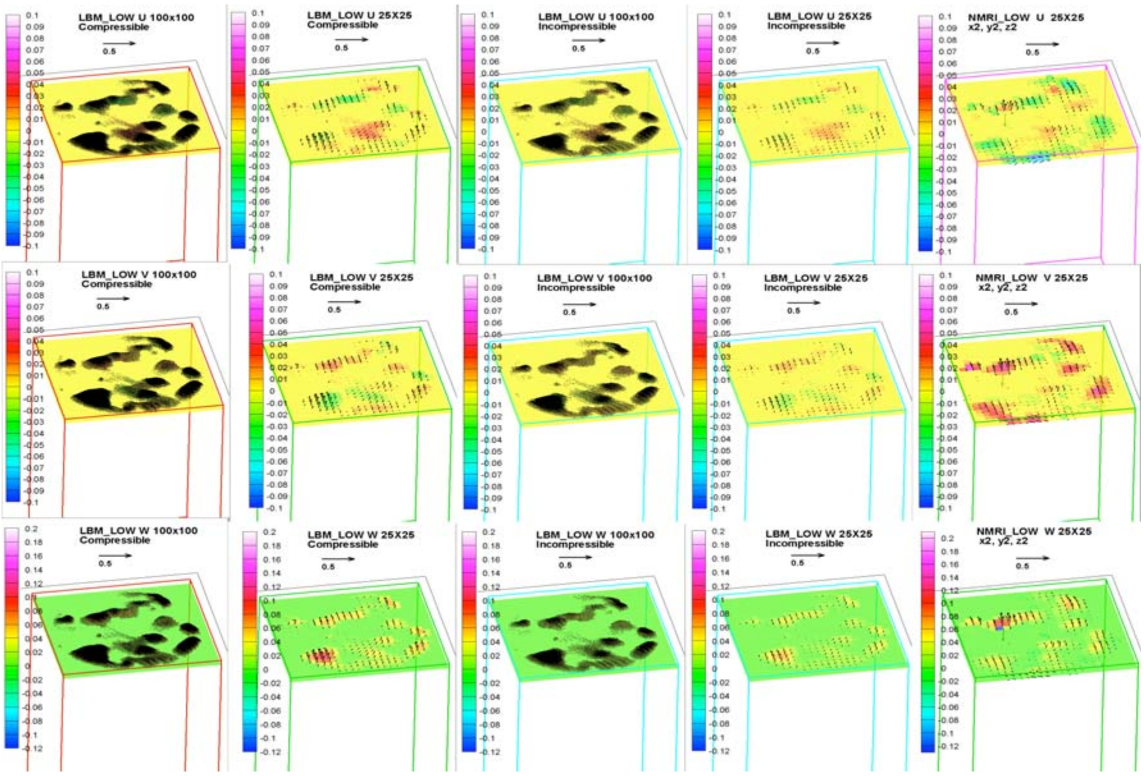

Figure. 3.18b The vector of as the function of x in oyz plane for case II

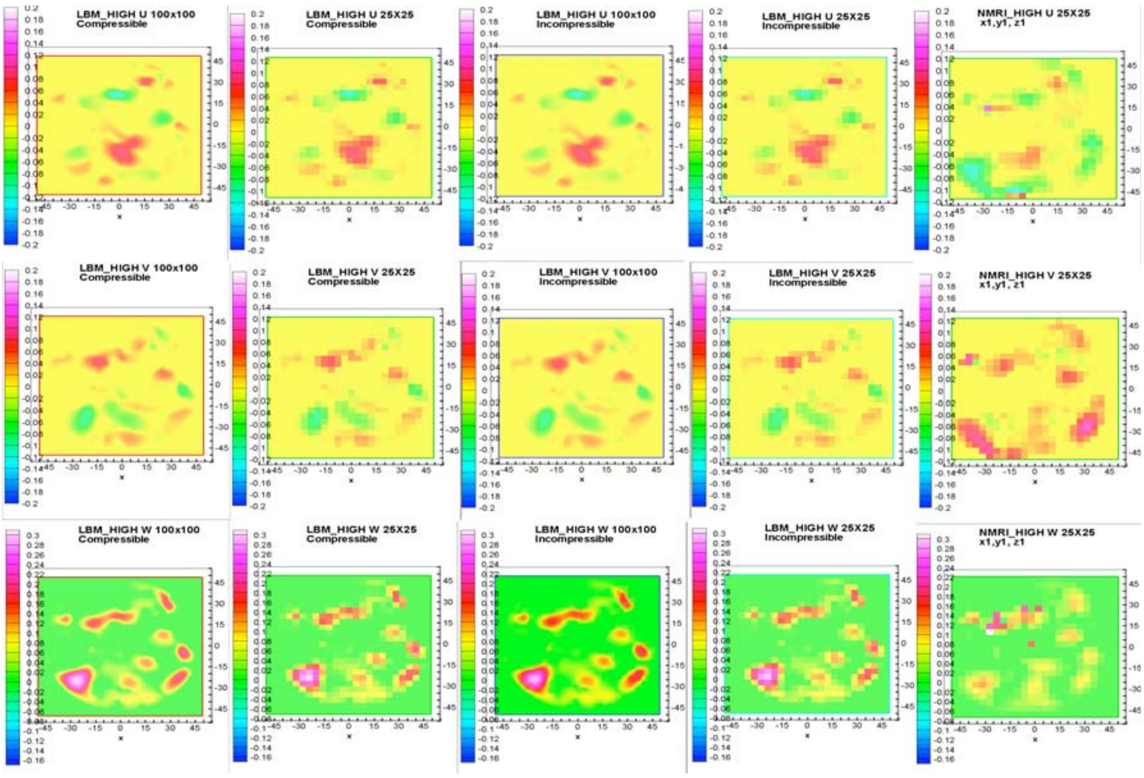

Figure. 3.19a The contour of U_i as the function of x in oyz plane for case I

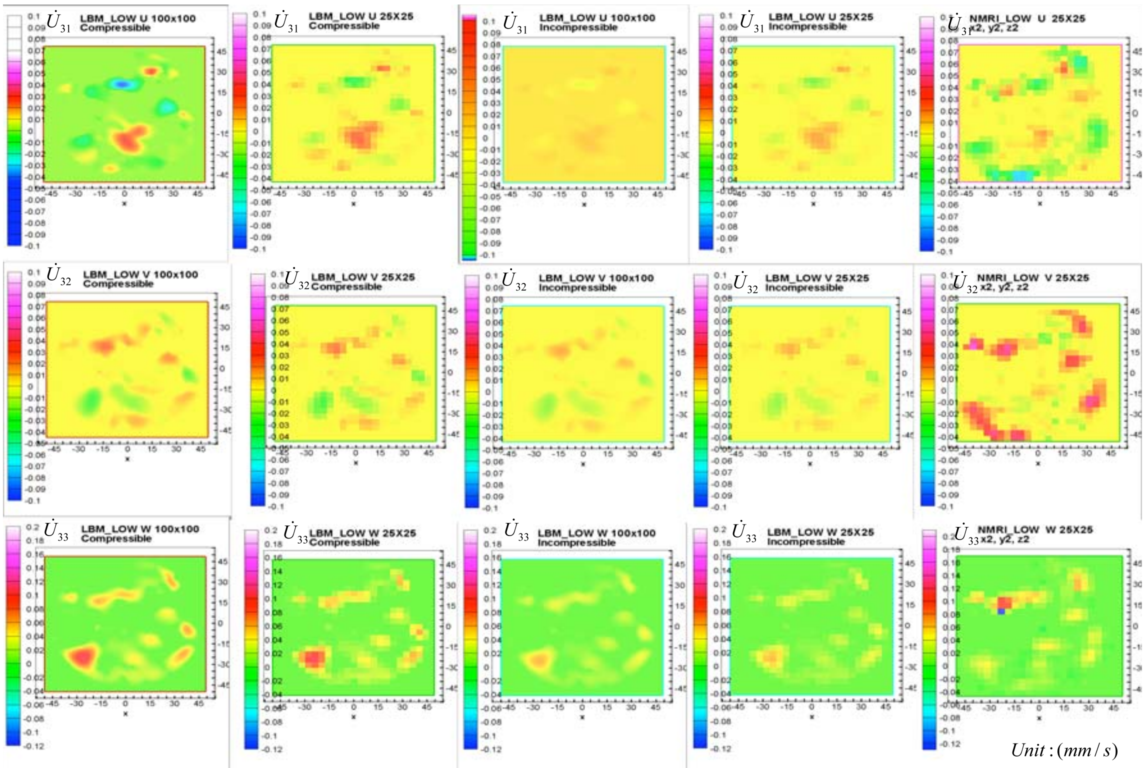

Figure. 3.19b The contour of U_i as the function of x in oyz plane for case II

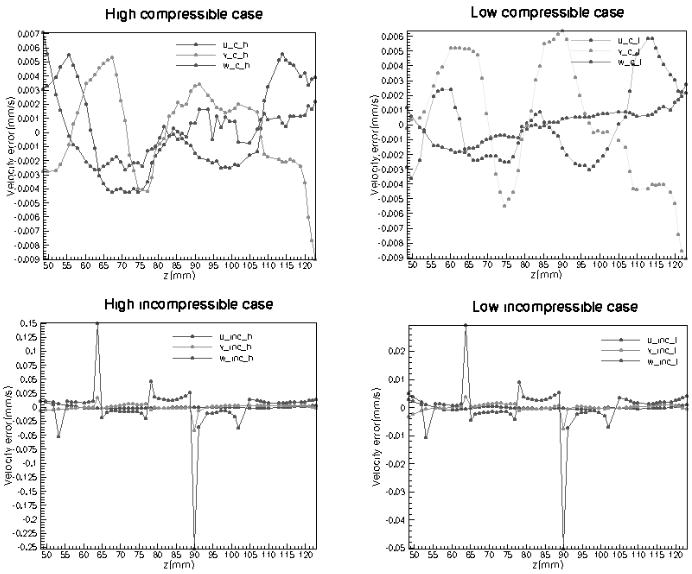

Figure.3.20 The error analysis of the LBM model for case I and case II

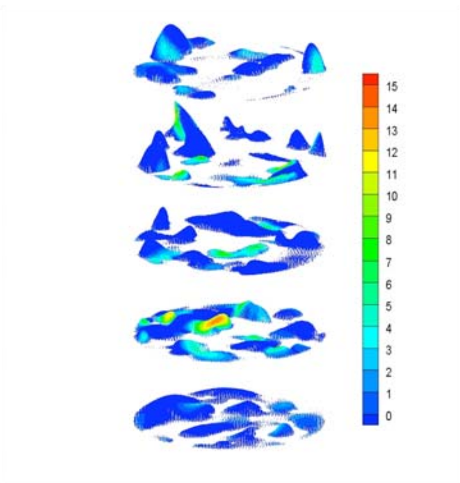

Figure.3.21a Intrinsic permeability in x direction

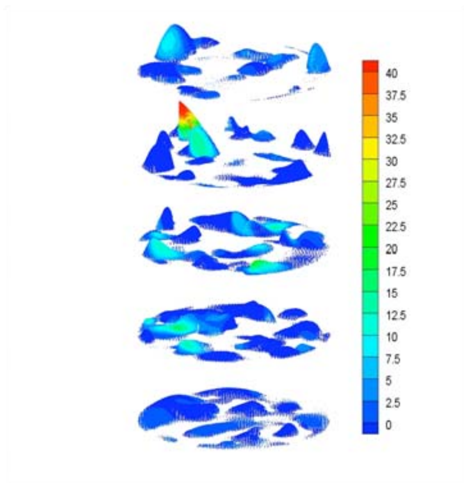

Figure. 3.21b Intrinsic permeability in y direction

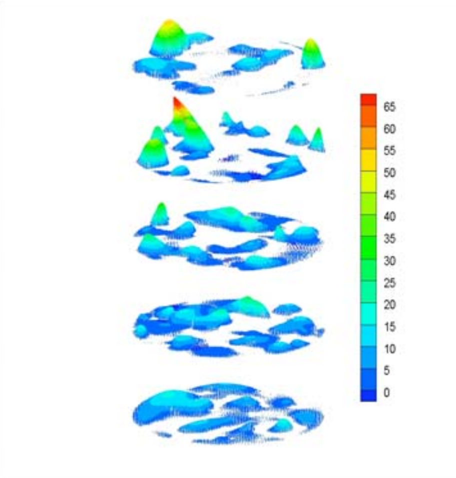

Figure. 3.21c Intrinsic permeability in z direction

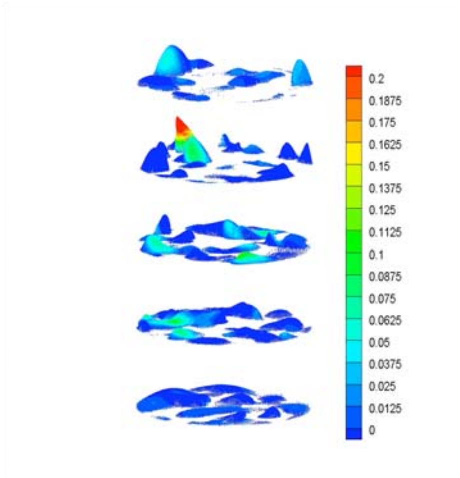

Figure. 3.22a Intrinsic physical permeability in x direction

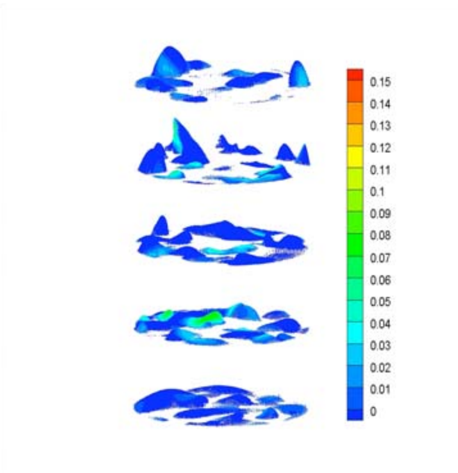

Figure. 3.22b Intrinsic physical permeability in y direction

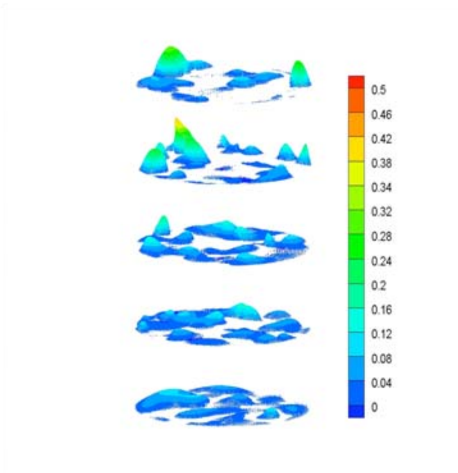

Figure. 3.22c Intrinsic physical permeability in z direction

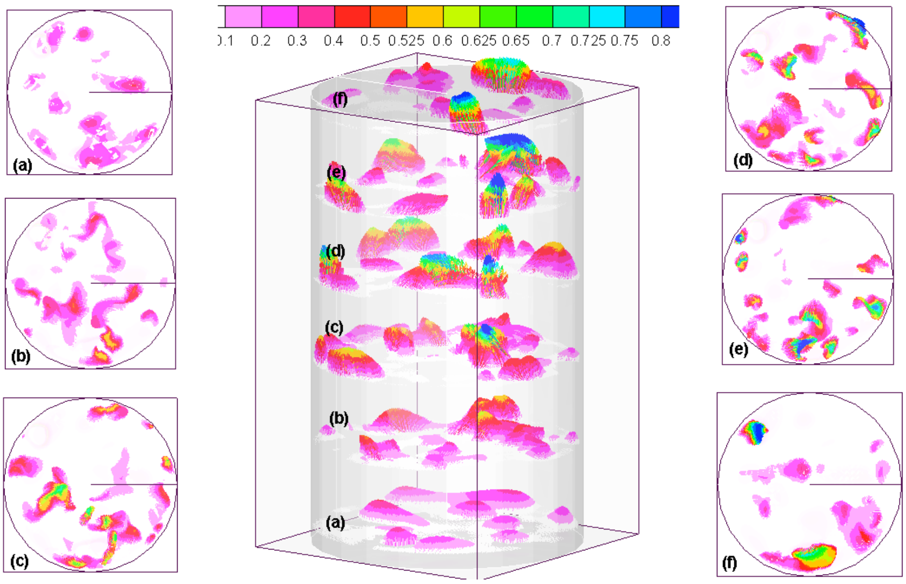

Figure. 3.23a Dimensionless model III SIFs radiation distributions

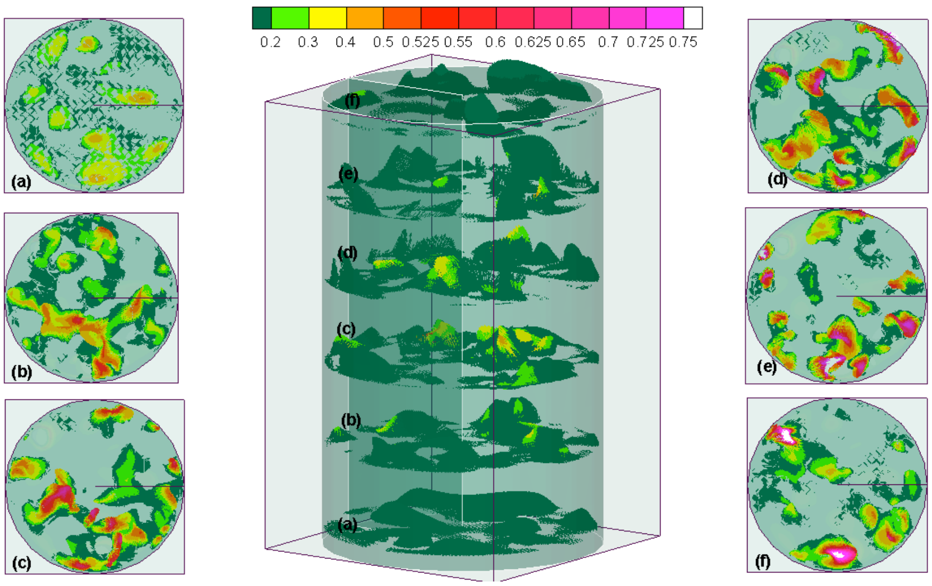

Figure .3.23b Dimensionless model I SIFs radiation distributions

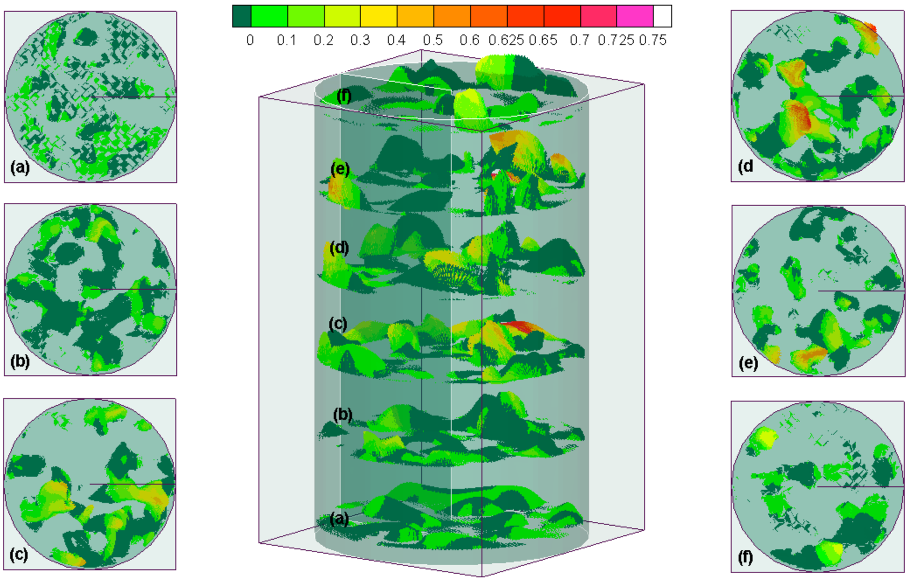

Figure. 3.23c Dimensionless model II SIFs radiation distributions

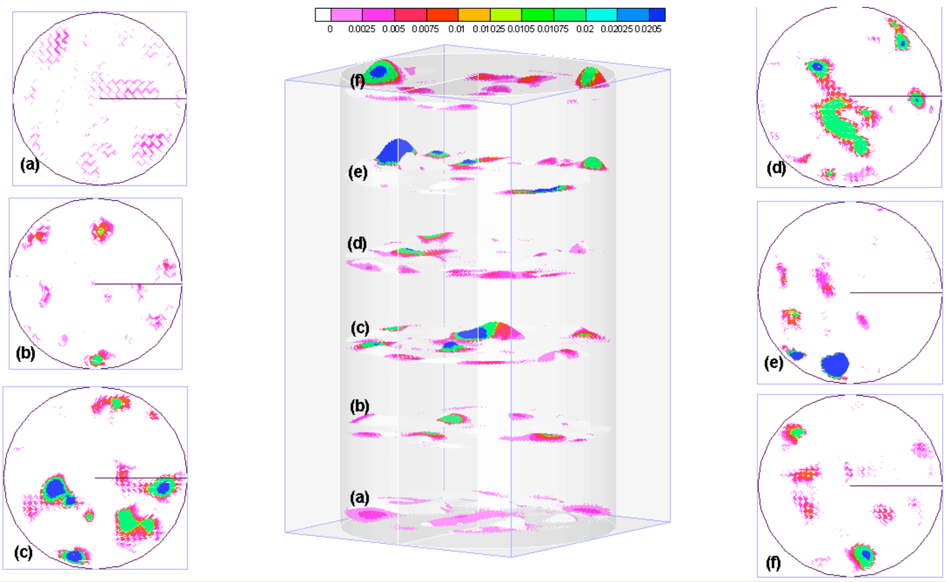

Figure. 3.23d Dimensionless electric SIFs radiation distributions

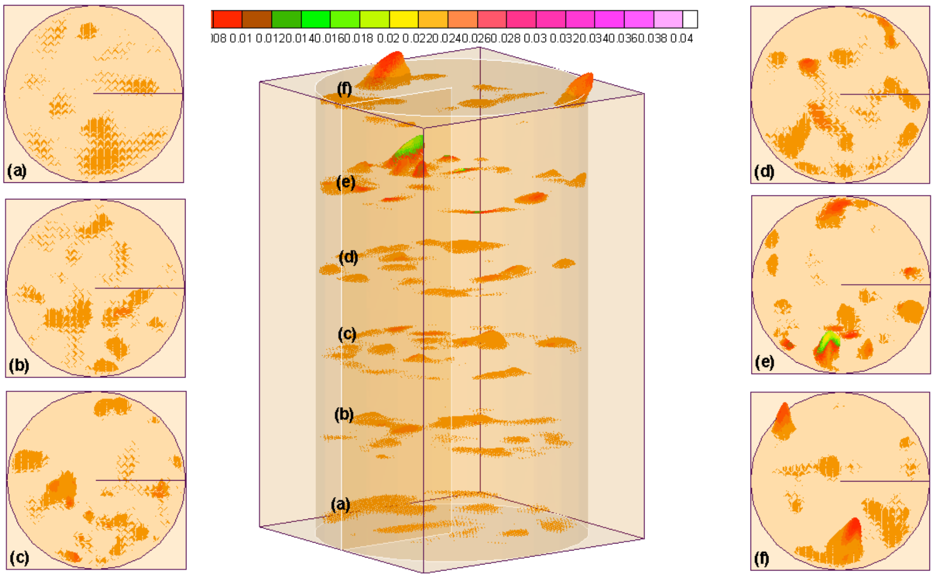

Figure. 3.23e Dimensionless magnetic SIFs radiation distributions

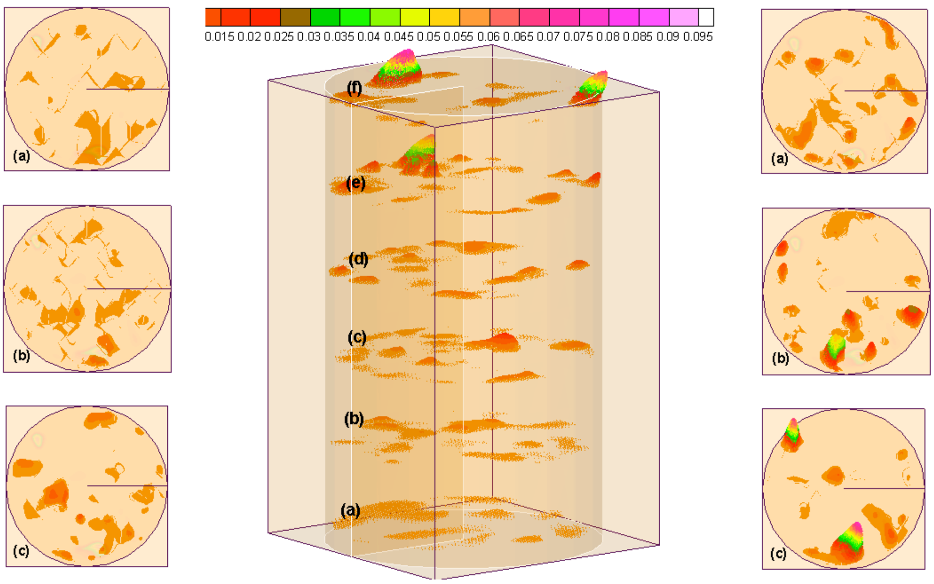

Figure. 3.23f Dimensionless thermal SIFs radiation distributions

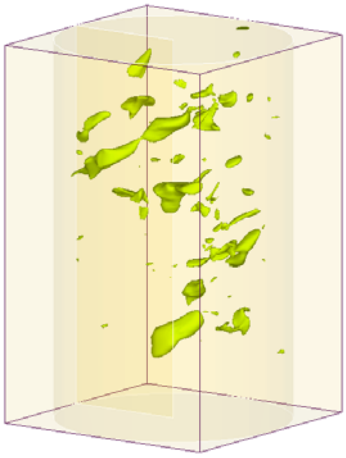
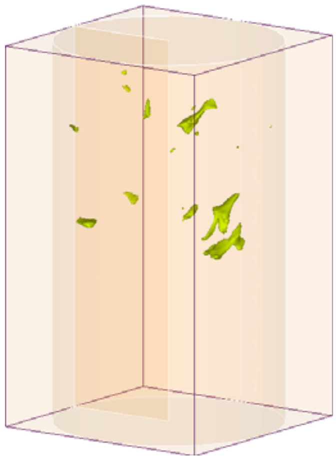

Figure. 3.24a Critical areas according to model III SIFs **Figure. 24b** Critical area according to model II SIFs

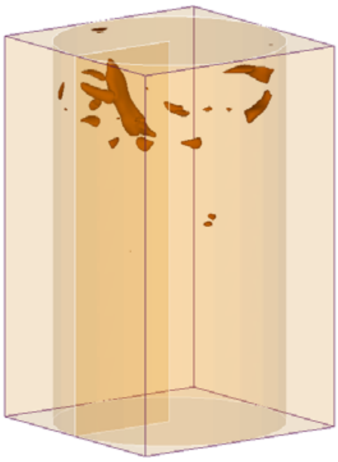
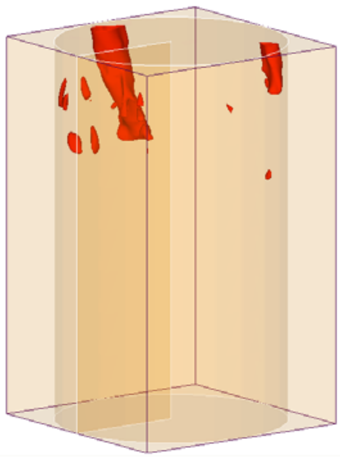

Figure. 3.24c Critical area according to magnetic SIFs **Figure. 24d** Critical area according to electric SIFs

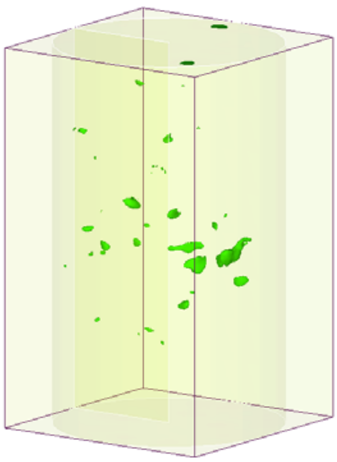
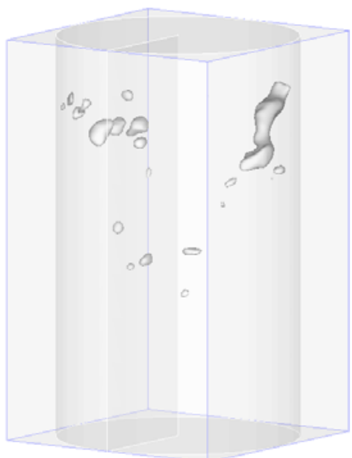

Figure. 3.24e Critical areas according to magnetic SIFs **Figure. 24f** Critical areas according to thermal SIFs

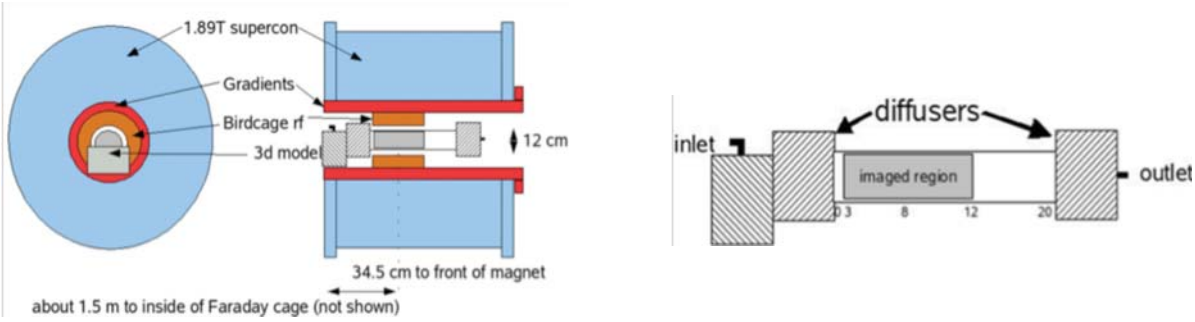

Figure A.1 The more detail description about the NMR model, equipment and experience illustrative diagram

Chapter4: Correlation of reservoir and earthquake by fluid flow driven pore-network crack model

Abstract: Coulomb failure assumptions[1] is used to evaluate the earthquake trigger, and pore pressure [2-5] parts reflect the effect of reservoir which closed to the earthquake slip. Fluid flow driven pore-network crack model[6] is use to study the reservoir and earthquake. Based on the parallel CPU computation and GPU visualization technology, the relationship between the water-drainage sluice process of the Zipingpu reservoir, stress triggers and shadows of 2008 Wenchuan M_s 8.0 earthquake and porosity variability of Longmenshan slip zone have been analyzed and the flow-solid coupled facture mechanism of Longmenshan coseismic fault slip is obtained.

Key words

Zipingpu reservoir, 2008 Wenchuan earthquake, Coulomb failure stress diffusion, Pore stress diffusion, Fluid flow driven pore-network crack model

1. Introduction

A number of factors may contribute to the generation or absence of post-impounding seismicity. Increased vertical stress due to the load of the reservoir and decreased effective stress due to increased pore pressure can modify the stress regime in the reservoir region. The combined effect of increased vertical load and increased pore pressure will have the greatest tendency to increase activity in regions where the maximum compressive stress is vertical[7]. Harsh K.Gupta et.al[8] studied the behavior of earthquakes associated with over a dozen artificial lakes and found that the tremors were initiated or their frequency increased considerably following the lake filling and that their epicenters were mostly located within a distance of 25 km from the lakes.

Zipingpu key water control project is one of the most complex engineering projects in the world for its located on the most complex earthquake fault slips zone in the world (Maximum acceleration value of seismic oscillation is equal to 0.20g[9]). Zipingpu reservoir is located on the Longmenshan earthquake fault slip (below 2km) and the distance between the reservoir and the 2008 Wenchuan M_s 8.0 earthquake initial source within 17 km (Fig.4.1.).

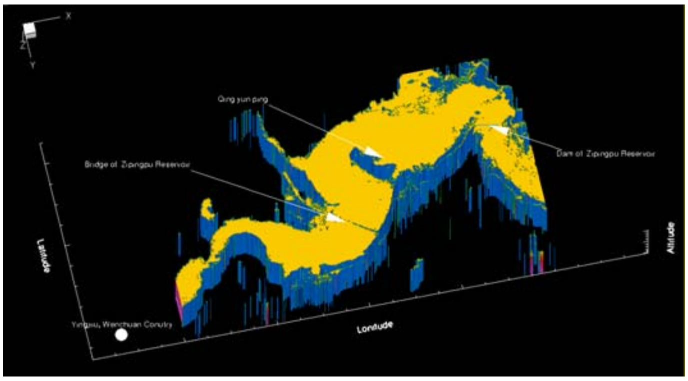

Fig.4.1. Relatively position between Zipingpu reservoir and Earthquake source of Wenchuan M_s 8.0 earthquake

(Zipingpu reservoir [E103°30′18″~E103°34′48″; N31°00′36″~E31°03′00″]; Yingxiu [N30°59′58.56″; E103°29′21.12″)

Longmenshan fault slip of 2008 Wenchuan Ms 8.0 earthquake is obtained by GPS & InSAR inversion technique[10](Fig.4.22.), it composed with two slips and cross-wised Zipingpu reservoir zone. The relationship between the pore stress accumulation of Zipingpu reservoir and the trigging and propagation of the Longmenshan coseismic fault slip because very important for it direction effect the dynamic real-time security evaluation and monitor of Zipingpu key water control project.

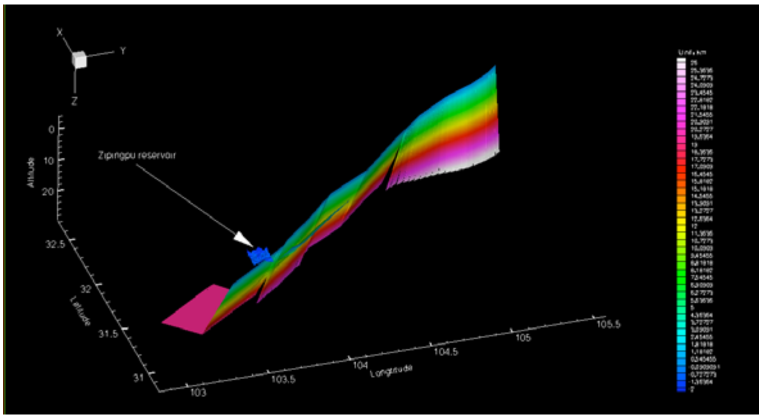

Fig.4.2. Relatively position between Zipingpu reservoir and Longmenshan fault slip of

(Longmenshan fault slip zone [E103.45°~E103.5767°; N30.975°~E31.105°])

Some researches have study 2D coulomb stress caused by reservoir and its effect on the Longmenshan fault [11]. But the natural problem is rather complex than one scale 2D model, and little research about the 3D coulomb stress analysis under different scale has been done because of the current limitations both practical (computing time) and theoretical (3D flow driven pore-crack network theory[6], multiple scale fracture mechanics/physics theory[12-17]) aspect.

In this paper, based on the previous work[6], the relationship between the pore stress accumulation on Zipingpu reservoir and the trigging and propagation mechanism of the Longmenshan coseismic fault slip on scale I and II **[Scale I: 30.976E_31.105E,103.45N_103.577N; Scale**

II:30.7E_31.3E,103.05N_103.76N; Scale III:29E_33E,101N_105N; Scale IV: IN plate and EU plate] have been studied(Fig.3.), and the correlation of Zipingpu reservoir and 2008 Wenchuan M_s 8.0 earthquake by fluid flow driven pore-network crack model had been studied.

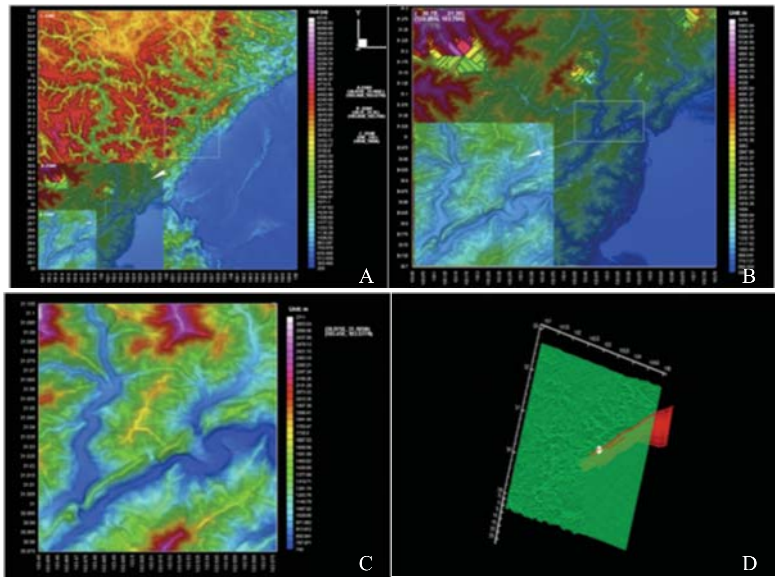

Fig.4.3. Multiple Scale virtual model of Zipingpu reservoir/Longmenshan coseismic fault slip

(A---Scale I; B---Scale II; C---Scale III; D---Relatively position reservoir/slip)

2. Basic equation

In the present paper, summation from 1 to 3 over repeated lowercase, and of 1 to 7 in uppercase, basic strain equation for strain porous elastic media can be defined as

$$\varepsilon_{iJ} = \frac{1}{2G}\left\{\sigma_{iJ} - \frac{v}{1+v}\delta_{iJ}\sigma_{kk} + \frac{3(v_u - v)}{B(1+v)(1+v_u)}\delta_{iJ}p\right\}$$

$$m - m_0 = \left[\frac{3\rho_0(v_u - v)}{2GB(1+v)(1+v_u)}\right]\left(\sigma_{kk} + \frac{3p}{B}\right)$$

$$q_l = -\frac{\rho_0\kappa\partial p}{\partial x_l}$$

Where σ_{iJ}, p, ε_{iJ} and m are represent as the total stress, pore pressure, total strain and fluid mass per unit volume of the medium. The parameters G, v, v_u, m_0, ρ_0, q_l, κ, B are represent as the elastic shear modulus (same for drained (p=constant) and undrained (m=constant) condition), drained condition Poisson's ratio, undrained condition Poisson's ratio, the fluid mass content in the unstressed state, mass density of the pore fluid, the mass flux rate per unit area, the permeability and constant which related to drained and undrained status, respectively.

The equations of motion for a homogeneous, linear elastic and isotropic medium can be defined as

$$(c_P^2 - c_S^2)u_{i,ij} + c_S^2 u_{j,ii} + \frac{f_j}{\rho} - \ddot{u}_j = 0$$

$$G_{ij}(P,Q,t) = P_{ij}(P,Q,t) + S_{ij}(P,Q,t) + PP_{ij}(P,Q,t) + SS_{ij}(P,Q,t) + PS_{ij}(P,Q,t) + SP_{ij}(P,Q,t)$$

Where $G_{ij}(P,Q,t)$ denote the i component of the displacement at point P due to a unite impulsive force at position Q acting j direction at time t.

3. Physical model

As shown in figure.4, Zipingpu key water control project is located on the upstream of Minjiang river, the maximum reservoir storage capacity is 11×10^9 m^3, the adjustable reservoir storage capacity is 8×10^9 m^3, the normal impounded level is 877m, the dam top altitude is 894m and the dam bottom altitude is 728m.The key water control project began Mar.3.2001, stop flow time is Nov.1.2002, storage time is Dec.1.2004 and completed at Dec.1.2006. The total pore stress accumulation time before Wenchuan Ms 8.0 earthquake (May.12.2008) is 3~4 years. In our physical model, we use the 15000 time steps (10 ts/day) to describe the effect of pore stress of reservoir to the Longmenshan fault slip. From the GPS&InSAR inversion technology, the Longmenshan earthquake fault slip is divided into 673 parts.

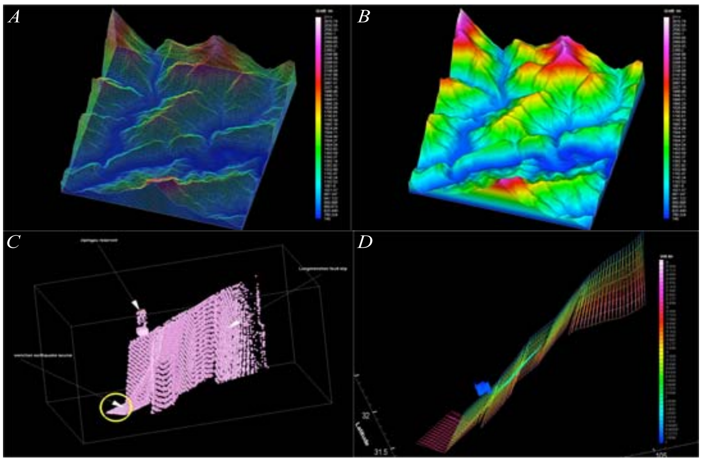

Fig.4.4. Physical Model Zipingpu reservoir and Longmenshan coseismic fault slip

A---Mesh grid of Zipingpu reservoir; B—Physical model of Zipingpu reservoir

C---Physical model of Longmenshan fault slip; D---Detail description of Longmenshan fault slip (composed of 673 parts)

4. Numerical process and discussion

Figure.4.5 shows that the relationship between extended pore strain and stress on Zipingpu reservoir and Longmenshan coseismic fault slip on Scale I under 20000ts. The pore stress accumulation value level is 0.3Mp.

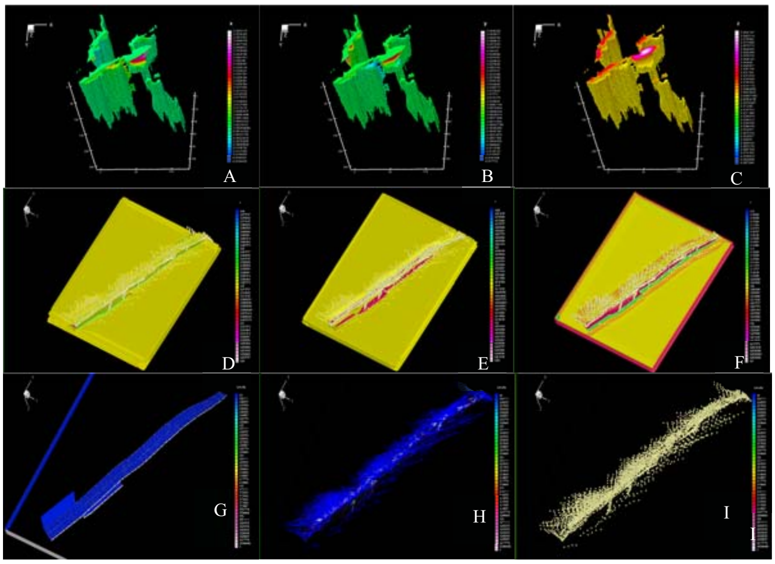

Fig.4.5. Extended pore strain and stress on Zipingpu reservoir and Longmenshan coseismic fault slip on Scale I

A---Reservoir pore strain in x direction; B--Reservoir pore strain in y direction;

C---Reservoir pore strain in z direction; D—Fault slip pore strain in x direction

E---Fault slip pore strain in y direction; F—Fault slip pore strain in z direction;

G---Fault slip pore stress; H---Fault slip flow stream trace; I---Fault slip flow marks

The relationship between extended pore strain and stress on Zipingpu reservoir and Longmenshan coseismic fault slip on Scale II under 20000ts is shown in figure.6. In these scale, we can obtained that in the penetration process, if we defined the fault slip as a fluid-saturated elastic porous media, then the vadose energy (caused by pore pressure and can flow to the fault slip tip) is variable with the undrained or drained zone, more energy is released under drained zone than undrained zone; If the fault slip is a stable creep rupturing process, the criteria energy (strain energy function factors) must increase with the speed of faults spreading.

When penetrate reach a stable stage, the fluid flow pore-network crack function became domain, with the time scale increasing, the micro solid-fluid interface will became weak and blur, the macro phenomenon is the porosity become larger, the strain energy can be released to the faults process decreased with the drained spreading increasing.

The reservoir loading and earthquake trigger relationship is depending on fault slip geometry and character, porosity variability of surrounding geological structure and time and size scale. To Zipingpu reservoir and 2008 Wenchuan earthquake case, porosity and time scale are the key factors.

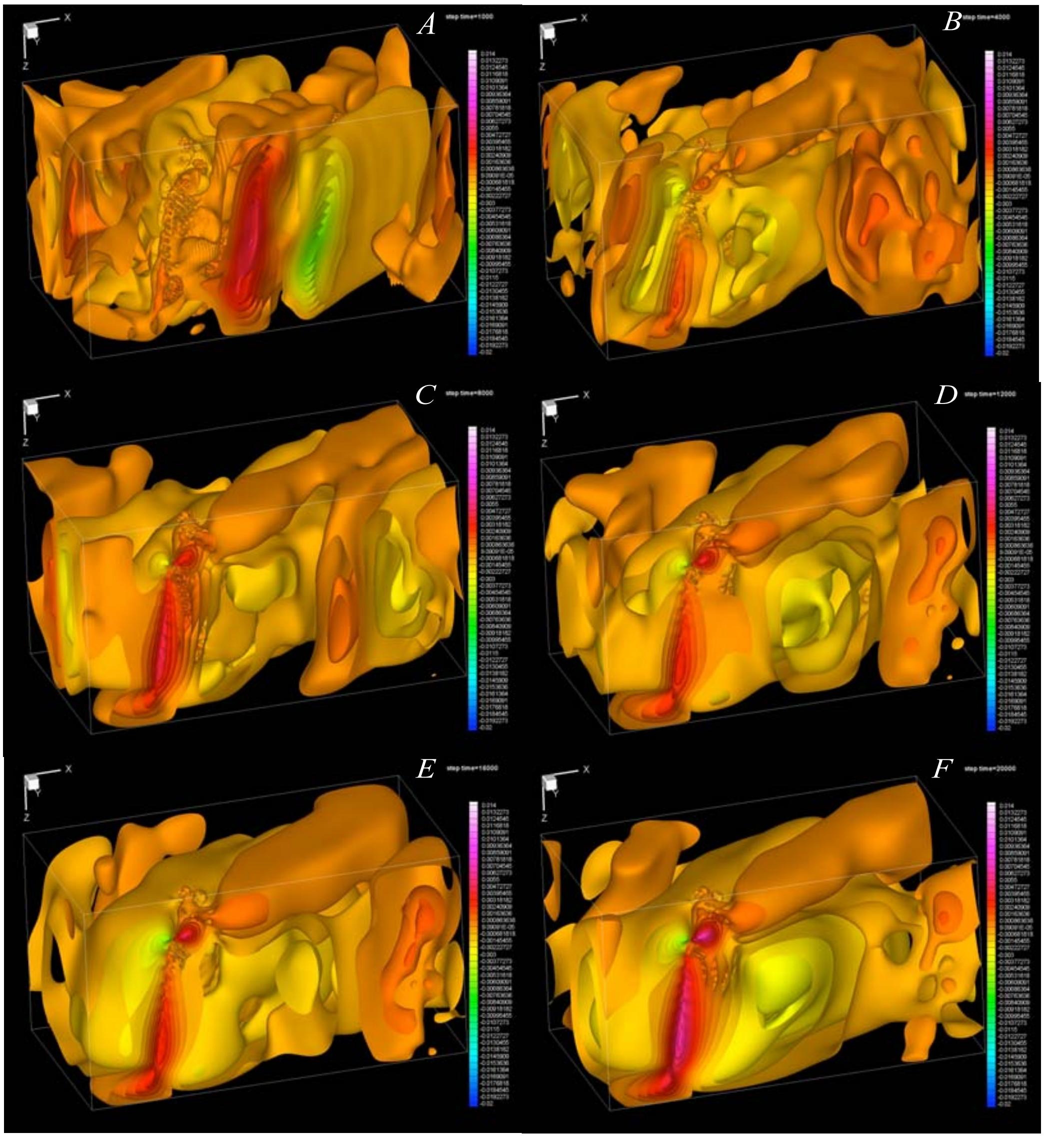

Fig.4.6. Extended pore strain and stress on Zipingpu reservoir and Longmenshan coseismic fault slip on scale II

5. Future work

Because the problem of correlation of reservoir and earthquake is so complex that we can't give a general definite conclusion for all kind of cases by analyze this special case under little changed physical domain scales (Scale I and II) and time domain scales (20000ts). More analysis should be done on multiple physical domain scales and time domain scales. The future work will focus on two things, Using extended coulomb stress to analyze the flow-solid coupled facture mechanism of Longmenshan coseismic fault slip under larger scale (figure4.7 and 4.8). This can provide a combined evaluation of the different effects that can influence reservoir/slip system, and can be further explored to compare the results with other results that have led to negative results [11].

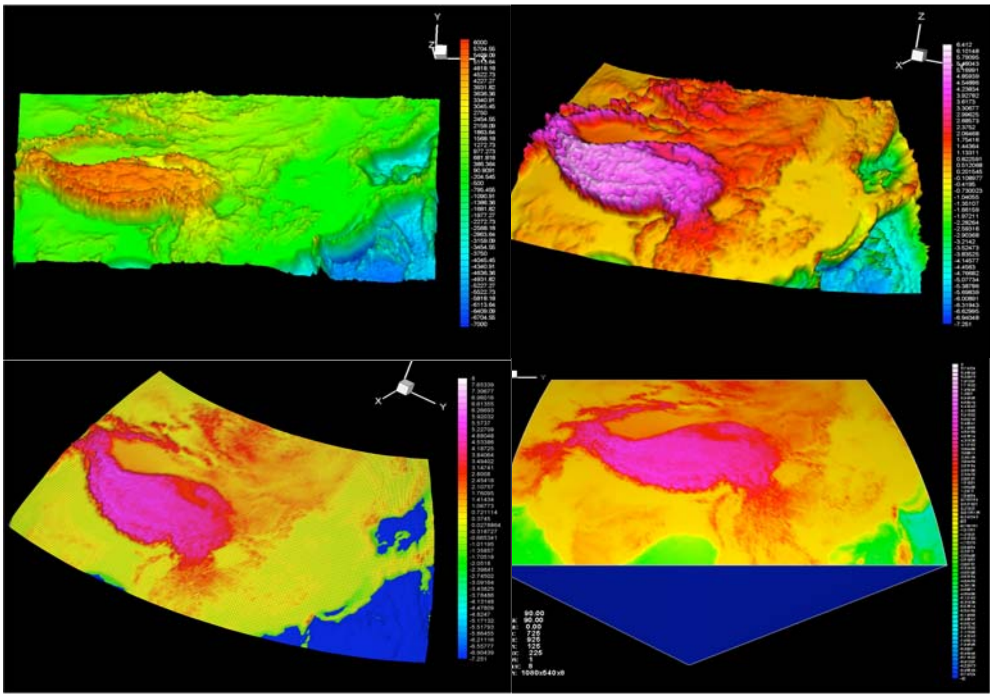

Fig.4.7. Extended pore strain and stress on Zipingpu reservoir and Longmenshan coseismic fault slip on scale III

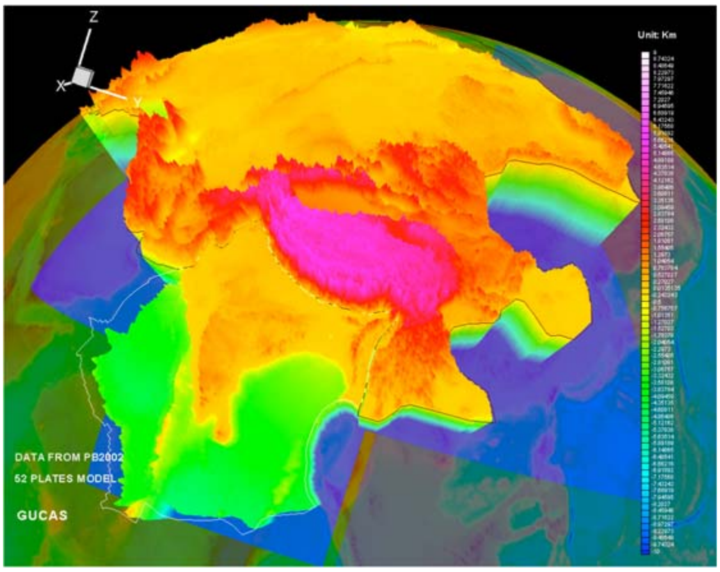

Fig.4.8. Extended pore strain and stress on Zipingpu reservoir and Longmenshan coseismic fault slip on scale IV

Studied Three gorges Dam problem by using same method under different time and physical scale (figure4.9). This can help us understand the general mechanism of reservoir and earthquake and provide some basic theoretical and engineering suggestions to earthquakes associated with artificial lakes/dams.

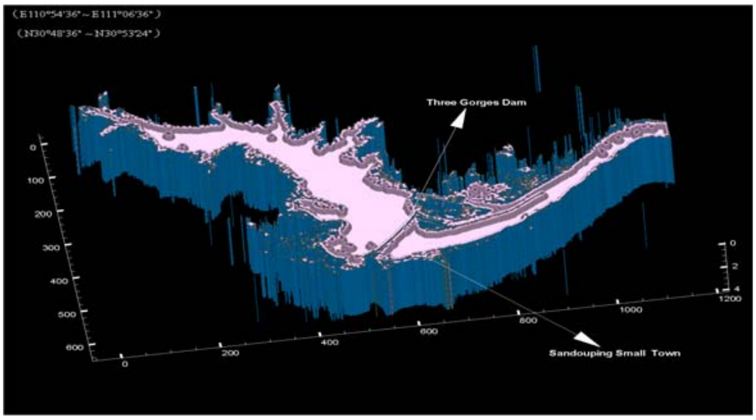

Fig.4.9. Position of Three gorges Dam

(Three gorges Dam Position [E110°54′36″~E111°06′36″; N30°48′36″~E30°53′24″])

Acknowledgements:This work was supported by a grant from the National Natural Science Foundation of China (No. D0408/409740594) and this work was also supported by China Postdoctoral Science Foundation (No. 20080430073).

References

Jaeger JC, N.G.W.Cook. Fundamentals of Rock Mechanics. Methuen 1969;New York:513.

Biot MA. General theory of three-dimensional consolidation. Journal of Applied Physics 1941;12:155.

Biot MA. Theory of elasticity and consolidation for a porous anisotropic solid. Journal of Applied Physics 1955;26:182.

Biot MA. General solutions of the equations of elasticity and consolidation for a porous material. Journal of Applied Physics 1956;78:91.

Biot MA. Nonlinear and semilinear rheology of porous solids. Journal of Geophysics Research 1973;78:4924.

Zhu B, YL.Shi. Three-dimensional flow driven pore-crack networks in porous composites: Boltzmann Lattice method and hybrid hypersingular integrals. Theoretical and applied fracture mechanics 2010;53:9.

Simpson DW. Seismicity changes associated with reservoir loading. Engineering Geology 1976;10:123.

Gupta HK, Rastogi BK, Narain H. common features of reservoir-associated seismic activities. Bulletin of the seismological society of america 1972;62:481.

Seismic safety evaluation of composite report of zipingpu key water control project on minjiang river in sichuan provience. Earthquake prediction research institute of the China seismological bureauEarthquake disaster prevention center of P.R.China 2009.

Shen Z-K, Sun J, Zhang P, Wan Y, Wang M, Bürgmann R, Zeng Y, Gan W, Liao H, Wang Q. Slip maxima at fault junctions and rupturing of barriers during the 2008 Wenchuan earthquake. Nature Geoscience 2009;2:718~724.

Ge s, Liu M, Lu N, Godt JW, Luo G. Did the Zipingpu Reservoir trigger the 2008 Wenchuan earthquake? Geophysical research letters 2008;36:1.

Sih GC. Multiscale evaluation of microstructural worthiness based on the physical-analytical matching (PAM) approach. Theoretical and applied fracture mechanics 2006;46:243.

Sih GC, Jones R. Crack size and speed interaction characteristics at micro-, meso- and macro-scale. Theoretical and applied fracture mechanics 2003;39:127.

Sih GC, Tang XS. Dual scaling damage model associated with weak singularity for macroscopic crack possessing a micro/mesoscopic notch tip. Theoretical and applied fracture mechanics 2004;42:1.

Sih GC, Tang XS. Simultaneous occurrence of double micro/macro stress singularities for multiscale crack model. Theoretical and applied fracture mechanics 2006;46:87.

Sih GC, Tang XS. Micro/macro-crack growth due to creep-fatigue dependency on time-temperature material behavior. Theoretical and applied fracture mechanics 2008;50:9.

Sih GC, Zuo JZ. Multiscale behavior of crack initiation and growth in piezoelectric ceramics. Theoretical and applied fracture mechanics 2000;34:123.

致 谢

本人在中国科学院研究生院博士后研究期间，导师石耀霖院士对我进行了悉心指导。导师渊博的知识、敏锐的科学洞察力、对科学方向的精准把握、严谨的科学态度、一丝不苟的治学精神和充沛的科研精力深深影响着我。例如：因为科研需要，有时把阶段结果发给导师已经是深夜或凌晨，但是经过导师修改，修正后的意见大多都能在发出去几个小时返回给我，这种治学精神和充沛的科研精力让我感到羞愧，也正是这种治学精神不断激励我，在自己想偷懒时，给我鼓励，让我坚持下来。

感谢薛昌明教授(G.C.Sih)对我科研工作提出的建议，使我能够在断裂力学领域把握最新研究动态，并将自己的理论研究与实际应用结合起来。

感谢中国科学院研究生院各位老师，特别是人事处负责博士后管理的周晓慧老师，在我出国期间给了我太多帮助，使我能在科研最困难和最紧张时能够坚持下来。

感谢为我提供科研经费支持的全国博士后基金委员会和国家自然科学基金委员会各位老师，您们的支持，使的科研活动能够正常进行下去 。

感谢妻子于冬梅博士多年来始终如一的理解、帮助和支持。

作者：朱伯靖

2010年9月

博士后期间部分发表论文

1.BJ Zhu, YL Shi. 2010. Three-dimensional flow driven pore-crack networks in porous composites: Boltzmann Lattice method and hybrid hypersingular integrals. Theoretical and Applied Fracture, 53(1), 9-41 （SCI&EI)

2. BJ Zhu, YL Shi, TY Qin, MC Sukop, SH Yu and YB Li. 2009. Mixed-mode stress intensity factors of 3D interface crack in fullycoupled belectromagnetothermoelastic multiphase composites. International Journal of Solids and Structures, 46(13): 2669-2679. （SCI&EI)

3. BJ Zhu, YL. Shi, MC Sukop, YB Li and TY Qin. 2009. Analysis of 3D fluid driven crack propagation problem in co-seismic slipunder P- and S- waves by hybrid hypersingular integral method. Computer Methods in Applied Mechanics and Engineering,198(30-32): 2446-2469.

4. BJ Zhu, TY Qin. 2009. 3D modeling of crack growth in electro-magneto-thermo-elastic coupled viscoplastic multiphase composites.Applied mathematical modeling, 33(2): 1014-1041.

博士后期间获得资助情况

主持：

2008.4-2010.4博士后基金委第44批一等资助： 同震断层电磁破坏机理研究（5万） 20080372

2009.4-2011.4博士后基金委第二批特别资助： 基于并行WHIE—LBM法的流体驱动同震断层广义电磁破坏机理研究（10万)

2010.1-2013.1国家自然科学基金面上：基于并行WHIE-LBM法的孕震、同震广义电磁破坏机理研究（40万）D0408/40974059

2009.1-2010.1中国地震局. 玉龙雪山地质构造_横向课题（9万）

2009.12-2011.1中国地震局. 汶川地震断层ABAQUS有限元模拟_横向课题（9万）

参与：

2009.1-2011.1国家自然科学基金面上项目：磁电热弹多场耦合材料断裂研究（31万)
10872213/A020302

2007.5-2010.5美国自然科学基金项目：并行LBM法的迈阿密地区地下水渗流问题研究